Mechanical metamaterials

Richard Craster[1,2], **Sébastien Guenneau**[2], **Muamer Kadic**[3] and **Martin Wegener**[4,*]

[1] Department of Mathematics, Imperial College London, London SW7 2AZ, United Kingdom
[2] UMI 2004 Abraham de Moivre-CNRS, Imperial College, London SW7 2AZ, United Kingdom
[3] Institut FEMTO-ST, UMR 6174, CNRS, Université de Bourgogne Franche-Comté, Besançon, France
[4] Institute of Applied Physics and Institute of Nanotechnology, Karlsruhe Institute of Technology (KIT), 76128 Karlsruhe, Germany

E-mail: martin.wegener@kit.edu

Abstract

Mechanical metamaterials, also known as architected materials, are rationally designed composites, aiming at elastic behaviors and effective mechanical properties beyond ('meta') those of their individual ingredients—qualitatively and/or quantitatively. Due to advances in computational science and manufacturing, this field has progressed considerably throughout the last decade. Here, we review its mathematical basis in the spirit of a tutorial, and summarize the conceptual as well as experimental state-of-the-art. This summary comprises disordered, periodic, quasi-periodic, and graded anisotropic functional architectures, in one, two, and three dimensions, covering length scales ranging from below one micrometer to tens of meters. Examples include extreme ordinary linear elastic behavior from artificial crystals, e.g. auxetics and pentamodes, 'negative' effective properties, behavior beyond classical linear elasticity, e.g. arising from local resonances, chirality, beyond-nearest-neighbor interactions, quasi-crystalline mechanical metamaterials, topological band gaps, cloaking based on coordinate transformations and on scattering cancelation, seismic protection, nonlinear and programmable metamaterials, as well as space-time-periodic architectures.

Keywords: metamaterials, cloaking, homogenisation, topological crystals, space-time media, pentamode, auxetics.

Contents

* Author to whom any correspondence should be addressed.

1. Introduction

For centuries, technological progress has been driven by new capabilities to handle, process, and apply novel materials. The impact of materials upon human civilisation has been profound as demonstrated by the naming of eras of humankind after materials: Stone Age, Copper Age, Bronze Age, Iron Age, Glass Age, Silicon Age, ... This line-up raises the question: what comes next? The Metamaterial Age?

So far, the properties of all materials have been derived mainly from the atoms the materials are composed of. Clearly, mechanical properties, e.g. the strength of metallic alloys, also sensitively depend on how the atoms are arranged; they depend on crystallinity, defects, grain boundaries etc as encompassed by the field of physical metallurgy [1]. Furthermore, starting with graphene, current activities on two-dimensional (2D) crystals and stacks thereof [2] demonstrate that there may still be plenty of room to explore ever-new arrangements of atoms. However, all of this research uses the atoms that nature has provided to us.

This review on mechanical metamaterials addresses a radically different approach that is based on creating our own artificial atoms with designed and tailored properties. These artificial atoms or building blocks are composed of millions or trillions of real atoms and can exhibit mechanical, optical, or transport properties that ordinary atoms just do not have (see[5]). Thereby, desired behavior and functionalities can be built into the unit cells of artificial crystals, artificial quasicrystals or artificial amorphous arrangements called metamaterials. The Greek prefix 'meta' highlights the aim of this exercise, namely that the effective properties of such metamaterials should go beyond those of their ingredients, qualitatively or quantitatively.

The notion of metamaterials was coined in the context of electromagnetism about two decades ago, followed by a surge of interest in metamaterials driven both by theoretical and experimental advances [5]. As a result, electromagnetic and optical metamaterials have reached a certain maturity; many reviews are available [6–10]. The successes and promise of the optical and electromagnetic metamaterials have stimulated major interest in mechanical metamaterials starting only about one decade ago, although it should be said that isolated precursors have been around for centuries already. Prominent examples are laminates, e.g. periodic arrangements of layers of wood with alternating orientation: today, laminates are still a paradigm in the field of metamaterials. Broadly speaking, they offer anisotropic properties from isotropic ingredients. Progressing from periodicity in only one dimension for laminates to more complex architectures with two- and three-dimensional (3D) periodicity offers a yet much wider design space.

So far, much of the research in the field of mechanical metamaterials has been driven by mere scientific curiosity. What properties are possible? What are fundamental bounds? Where is the end of our imagination? However, now this field has considerably expanded to encompass many domains, the quest for real-world applications becomes pressing. We will mention some applications in this review, but the current status is that applications, in the sense of products, are still sparse. However there is future promise: an entire field of applications may arise in the context of 3D additive manufacturing also known as 3D printing: 2D graphical inkjet printers achieve a multitude of colors by using designed microstructured ink dot patterns from only three color-cartridges. If the observer zooms out, he or she does not resolve the dot patterns but rather perceives an effective homogeneous color; this dot-patterning technique is known as dithering. By analogy, microstructured 3D metamaterials may become the meta-inks of the future. By microstructuring only a finite number of materials from 'cartridges' in a 3D printer, thousands of effective mechanical (and other) material properties may become accessible. Within this vision, this review is essentially a manual for future meta-inks for 3D printing.

[5] Some interesting publications [3, 4] consider crystals with a much lower number of atoms within the unit cell, allowing for operation at THz frequencies. Such crystals stress the difference between crystals with large unit cells and metamaterials.

This review is organized as follows. The goal of metamaterials is to obtain certain desired effective mechanical material behaviors or properties. Therefore, the first crucial scientific question that arises to researchers in the field is: how do we grasp the notion of 'mechanical properties' precisely and mathematically? Unfortunately, there is not yet a unique answer to this question. Neither is there a general unifying scheme that would allow us to grasp all behaviors found for metamaterials up to this point. We are, in fact, far from that. The issue is that researchers regularly come up with ever-new behaviors that defeat previous material categorization schemes. While these developments make the field interesting and lively, they also make it hard for newcomers. Section 2 gives introductory guidelines concerning effective-medium descriptions of the linear elastic properties of homogeneous media. While such descriptions have emerged from the (quasi-)static regime, they are also applicable in the dynamic case for not-too-large frequencies and not-too-small wavelengths.

The second crucial question arising for researchers in the field is the connection between structure and properties of a metamaterial. This connection has two directions and is discussed in section 3, again emphasizing linear elastic properties. The so-called 'forward' direction is to obtain the effective properties for a given metamaterial structure. In regard to effective-medium descriptions, this step is referred to as 'homogenization': laminates are a paradigm. The reverse direction or 'inverse problem' is to derive the metamaterial structure from some predefined targeted metamaterial properties. Both directions are not fully solved yet. This should not surprise us though as the inverse problem has not yet been solved for ordinary materials either, despite of many decades of research.

Section 4 addresses experiments on metamaterials. We provide an overview on what has been accomplished in terms of effectively homogeneous mechanical metamaterials, ranging from the micrometer scale to the macroscale.

Section 5 discusses architectures composed of graded metamaterial distributions, with an emphasis on structures designed by using coordinate transformations. This overview includes various cloaking devices, for example aiming at protecting sensitive infrastructure, such as a nuclear power plant, against seismic earthquake waves. We conclude in section 6.

2. Effective-medium descriptions

Why do we need effective-medium descriptions in the context of mechanical metamaterials?

First, we need to describe the mechanical properties of the constituent material(s) the metamaterial is composed of in order to describe the behavior of the metamaterial. Common constituent materials are elastic solids such as metals or polymers, fluids, or gases. Most fluids and gases are well approximated by the Helmholtz pressure equation (see section 2.1). If an additional solid constituent of the metamaterial is sufficiently rigid, the solid merely provides a (Neumann) boundary condition for the gas or fluid. Hence, the properties of the solid drop out. Most elastic solids are well approximated by classical Cauchy elasticity (see section 2.2). Often, the interface of the solid to the gas in the voids of the solid can be treated by a traction-free boundary condition; hence, the gas drops out. However, there are metamaterial architectures for which the interplay of a gas/fluid in the pores of a solid and the elastic behavior of the solid itself plays a crucial role. In this case, the coupled problem of poroelasticity (see section 2.6) is the adequate starting point for designing the metamaterial.

Second, once the metamaterial has been designed, manufactured, and characterized, one may want to map its properties onto linear elastic effective-medium parameters. Sometimes, the three aforementioned continuum descriptions (see sections 2.1, 2.2 and 2.6) are sufficient for doing that. However, there are plenty of exceptions. For example, any chiral or non-reciprocal behavior cannot be captured by either of the three, but is covered by Eringen micropolar or micromorphic elasticity (see section 2.3). As another example, mathematically, the Navier equation and Cauchy elasticity are strictly scale invariant. Physically, this means that the associated static properties do not depend on the number of metamaterial unit cells in a specimen of fixed size. In situations connected to some sort of characteristic length, scale invariance is effectively broken for metamaterials. Depending on the application, such effects are captured by micropolar elasticity, by Willis elasticity (see section 2.4), and by strain-gradient theories (see section 2.5).

2.1. Acoustics for gases and fluids

In ordinary gases under ambient conditions, the ideal-gas equation connects the pressure P to the mass density ρ. For linear acoustic waves in gases or fluids, the local pressure field can often be expressed as a small pressure modulation $\tilde{P} \ll P_0$ imposed on a constant background pressure P_0. As derived in many textbooks dating back to Lord Rayleigh and more recent monographs [11–14], conservation of mass and momentum leads to the wave equation, which can be expressed in the frequency domain as

$$\frac{\partial}{\partial x_i}\left(\rho^{-1}\frac{\partial}{\partial x_j}\tilde{P}\right) + B^{-1}\omega^2\tilde{P} = 0. \tag{1}$$

Here, ω is the angular frequency, x_i ($i = 1,2,3$) are the components of the position vector in three dimensions, and B is the bulk modulus, which equals the inverse of the compressibility κ of the gas or fluid. For ideal gases and fluids, B and ρ are positive and constant to first approximation and the Newton–Laplace formula [15] leads to a positive and constant speed of sound (or phase velocity) $c_\mathrm{p} = \sqrt{B/\rho}$.

More generally, for metamaterials, the bulk modulus must be positive in the static limit [16] from thermodynamic arguments; a similar argument applies to the static mass density [17]. However in the dynamic regime, $B = B(\omega)$ and $\rho = \rho(\omega)$ are generally frequency dependent and no bounds exist [16, 18, 19]. Therefore, for example, the effective metamaterial mass density can become negative in some frequency range.

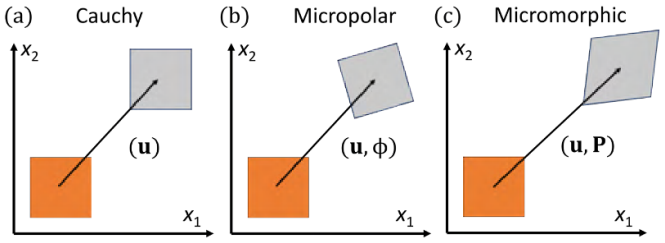

Figure 1. Elasticity models: (a) Cauchy elasticity has a single displacement field $\mathbf{u}$ (3 degrees of freedom). (b) A micropolar model has a displacement field $\mathbf{u}$ + a rotation field Φ (6 degrees of freedom). (c) Micromorphic model has 3 (components of displacement field $\mathbf{u}$) + 9 (components of micro-distortion tensor $\mathbf{P}$) leading to 12 degrees of freedom.

Moreover, if the structure of the metamaterial is anisotropic, the effective wave behavior can deviate from being isotropic as well. This may lead to an anisotropic mass density tensor with components ρ_{ij} replacing the ordinary scalar mass density ρ. We will return to the anisotropic mass density tensor in section 2.4. The ability to create materials with negative effective physical, and designed anisotropic tensorial properties, i.e. mass density in this case, are key elements that endow metamaterials with novel behavior that can be exploited.

2.2. Classical elasticity

2.2.1. Cauchy elasticity. In the 19th Century, in order to describe the continuous deformations of a body, Augustin-Louis Cauchy introduced the idea of continuum mechanics [20, 21], which describes fictitious continua instead of collections of atoms or points. The continuous aspect is the key ingredient in the theory. It means that there is no length scale to start with. This theory makes sense if and only if the considered samples consist of a large number of atoms [22, 23]. If the sample size is even remotely comparable to the constituent atomic size, such a model is not truly valid and then atomistic mechanics or molecular dynamics [24, 25] approaches are more suitable; we will return to this aspect in section 2.3.

In linear Cauchy elasticity, starting from Newton's law and using the Einstein summation convention, we express the constitutive law, Hookes law, between the components of the stress tensor σ_{ij} and the components of the strain tensor ϵ_{ij} by

$$\sigma_{ij} = C_{ijkl}\epsilon_{kl}, \tag{2}$$

where C_{ijkl} are the components of the elasticity tensor. First, the strain tensor is symmetric,

$$\epsilon_{ij} = \frac{\partial u_j}{\partial x_i} + \frac{\partial u_i}{\partial x_j}, \tag{3}$$

by definition, with $\mathbf{u} = (u_1, u_2, u_3)$ being the displacement field (see figure 1(a)). Second, using the principle of conservation of angular momentum, the stress tensor is also symmetric

$$\sigma_{ij} = \sigma_{ji}. \tag{4}$$

Hence the elasticity tensor $\mathbf{C}$ is also symmetric and the anisotropy of the elastic crystal is represented by a 4th order tensor [26].

The monograph [26] gives the anisotropic elastic derivations which we follow here: the symmetry of the stress and strain tensors result in the conditions $C_{ijkl} = C_{klij} = C_{jikl} = C_{ijlk}$. In the most anisotropic case, that is a triclinic crystal, the elasticity tensor can have up to 21 independent non-zero coefficients. Using the standard Voigt notation for tensors with the following choice of reduced indices:

ij	11	22	33	23 or 32	13 or 31	12 or 21
α	1	2	3	4	5	6

one can write the most anisotropic elasticity tensor, triclinic, in a matrix form for any linear elastic medium as

$$C^{\text{ani}}_{\alpha\beta} = \begin{bmatrix} C_{11} & C_{12} & C_{13} & C_{14} & C_{15} & C_{16} \\ C_{12} & C_{22} & C_{23} & C_{24} & C_{25} & C_{26} \\ C_{13} & C_{23} & C_{33} & C_{34} & C_{35} & C_{36} \\ C_{14} & C_{24} & C_{34} & C_{44} & C_{45} & C_{46} \\ C_{15} & C_{25} & C_{35} & C_{45} & C_{55} & C_{56} \\ C_{16} & C_{26} & C_{36} & C_{46} & C_{56} & C_{66} \end{bmatrix}. \tag{5}$$

For the cubic case, we have only three independent elements, and the elasticity tensor takes the form

$$C^{\text{cub}}_{\alpha\beta} = \begin{bmatrix} C_{11} & C_{12} & C_{12} & 0 & 0 & 0 \\ C_{12} & C_{11} & C_{12} & 0 & 0 & 0 \\ C_{12} & C_{12} & C_{11} & 0 & 0 & 0 \\ 0 & 0 & 0 & C_{44} & 0 & 0 \\ 0 & 0 & 0 & 0 & C_{44} & 0 \\ 0 & 0 & 0 & 0 & 0 & C_{44} \end{bmatrix}. \tag{6}$$

Let us compute its eigenvalues for the isotropic case, i.e. $C_{11} = B + 4G/3$, $C_{12} = B - 2G/3$ and $C_{44} = G$, with the bulk modulus B and the shear modulus G. We can express the previous tensor with its diagonalized form [18] as

$$C^{\text{iso}}_{\alpha\beta} = \mathbf{P} \begin{bmatrix} 3B & 0 & 0 & 0 & 0 & 0 \\ 0 & 2G & 0 & 0 & 0 & 0 \\ 0 & 0 & 2G & 0 & 0 & 0 \\ 0 & 0 & 0 & G & 0 & 0 \\ 0 & 0 & 0 & 0 & G & 0 \\ 0 & 0 & 0 & 0 & 0 & G \end{bmatrix} \mathbf{P}^{-1}, \tag{7}$$

with

$$\mathbf{P} = \begin{bmatrix} 1/\sqrt{3} & \sqrt{2/3} & 0 & 0 & 0 & 0 \\ 1/\sqrt{3} & -1/\sqrt{6} & -1/\sqrt{2} & 0 & 0 & 0 \\ 1/\sqrt{3} & -1/\sqrt{6} & 1/\sqrt{2} & 0 & 0 & 0 \\ 0 & 0 & 0 & 1 & 0 & 0 \\ 0 & 0 & 0 & 0 & 1 & 0 \\ 0 & 0 & 0 & 0 & 0 & 1 \end{bmatrix}.$$

Later this explicit form of eigenvalues will be used in section 4.1.1 to justify the origin and the behavior of the

extreme classes of pentamode and auxetic metamaterials, respectively. We particularly note two special cases of isotropic media. If the shear modulus becomes negligible, $G \to 0$, the material has five small eigenvalues and is thus soft with respect to five modes of deformation, i.e. it can resist to only one (hydrostatic pressure like a fluid); such a medium has been coined pentamode for this aspect by Milton and Cherkaev back in 1995 [27] (see also Sigmund [28]). For the opposite limit, if the bulk modulus is small, $B \to 0$, only one eigenvalue $\to 0$ and thus this material is called unimode and the unique mode of deformation (five times degenerated) is pure dilation [29].

In the elastodynamic case, starting from Newton's law, we obtain

$$\frac{\partial \sigma_{ji}}{\partial x_j} = \rho \frac{\partial^2 u_i}{\partial t^2}. \tag{8}$$

This equation can be transformed into Fourier space using a time-harmonic dependence $e^{(i\omega t)}$ we have

$$\frac{\partial \sigma_{ji}}{\partial x_j} = -\rho \omega^2 u_i. \tag{9}$$

If the material is isotropic and homogeneous then (9) can be entirely written in terms of displacement in the compact form

$$(\lambda + 2G)\nabla\nabla \cdot \mathbf{u} - G\nabla \times \nabla \times \mathbf{u} = -\rho\omega^2 \mathbf{u}, \tag{10}$$

where $\nabla = (\partial/\partial x_1, \partial/\partial x_2, \partial/\partial x_3)^T$ and $\lambda = B - 2G/3$; this equation clearly shows the decoupling between the compressional and the shear aspects of the elastic waves [30]. The first term of the equation depends on the bulk and shear moduli, whereas the second term is just shear dependent. This is most readily seen by taking the limit as $G \to 0$ where we obtain a fluid-like behavior (see section 2.1). However if B is strictly zero, both contributions remain. In the dynamic case, this is equivalent to saying that transverse waves with velocity $c_t = \sqrt{G/\rho}$ vanish in the pentamode case. The compression or longitudinal wave with velocity $c_l = \sqrt{(B + 4G/3)/\rho} \to c_l = \sqrt{(4G/3)/\rho}$ will not vanish though and will always stay larger than the shear wave velocity. Alternatively, this decoupling into shear and compression can be seen using vector calculus taking the divergence or curl of equation (10). We will return to these aspects in section 4.1.1.

2.2.2. Coupling to stimuli. For almost 20 years, most metamaterials have been treated as time-independent periodic structures in 3D space. More recently, scientists have additionally started considering time dependences [31]. If all parts of a metamaterial are subject to the same temporal modulation, one often loosely speaks of four-dimensional ('4D') architectures with time acting as the fourth dimension. If the modulation of the properties of the constituent material(s) of the metamaterial is periodic in space and time, one speaks of space-time metamaterials. In either case, changes of the constituent material(s) properties need to be mediated by an external stimulus [32]. Many physical fields can serve as stimulus, including electric fields, magnetic fields, pressure fields, temperature

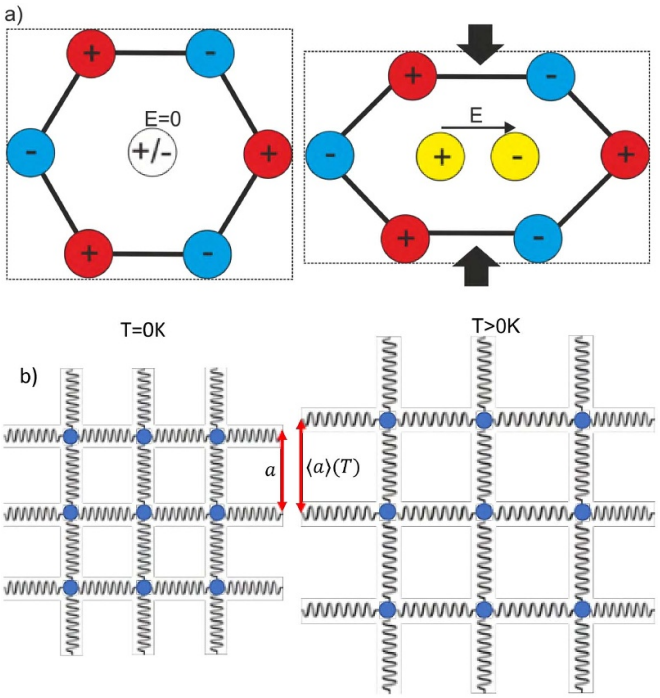

Figure 2. Illustration of two mechanisms leading to stimulus-responsive mechanical behavior. (a) Piezoelectric effect. (b) The nuclei in a solid experience a potential $V(\boldsymbol{u})$ around their rest positions with respect to their neighbors that can be Taylor-expanded according to $V(u) = \frac{1}{2}Du^2 - gu^3 + \cdots$, with displacement u *(for simplicity, out-of-plane i.e. scalar)*, Hooke's spring constant D, and nonlinearity factor g. This potential corresponds to a nonlinear spring with force $F(u) = -Du + \frac{1}{3}gu^2$. At zero temperature, $T = 0$, the nuclei sit in their potential minima and the displacement is zero, $u = 0$. At finite temperatures $T > 0$, the classical thermal expectation value of the displacement approximately follows $\langle u \rangle \propto gT$ [34, 35]. For Lennard–Jones or Born–Mayer type binding potentials, $g > 0$ holds true and the displacement is positive, i.e. $\langle u \rangle > 0$. Thus, the distance between nuclei $\langle a \rangle(T)$ increases versus temperature, also leading to a volume increase versus temperature.

fields, etc. In what follows, we focus on two examples, namely electric fields and temperature.

The piezoelectric effect has widespread applications in many areas outside the field of metamaterials. It couples mechanical fields and electric fields (see figure 2(a)) in materials. This means that an applied external electric field can induce a mechanical deformation in the material ('inverse' or Lippman effect) or, vice versa, that a deformation leads to an electric field within the material ('direct' effect); the theory is outlined in several textbooks, for instance in [33]. Both directions of coupling are summarized by the equations

$$\begin{aligned} \epsilon_{ij} &= s_{ijkl}\sigma_{kl} + d_{kij}E_k \\ D_i &= d_{ijk}\sigma_{jk} + \varepsilon_{ij}E_j, \end{aligned} \tag{11}$$

where s_{ijkl} are the elements of compliance matrix, the inverse of the elasticity tensor. d_{ijk} are the elements of the matrix for the direct piezoelectric effect, the d_{kij} form the matrix for the inverse piezoelectric effect. Importantly, $\mathbf{d}$ is symmetric with respect to the last two indices, i.e. $d_{ijk} = d_{ikj}$. From standard

electromagnetism, the electric displacement field $\mathbf{D}$ is connected to the electric field vector $\mathbf{E}$ by the permittivity matrix ε via $D_i = \epsilon_0 \varepsilon_{ij} E_j$. For example, in Voigt notation, the direct piezoelectric tensor of the widespread piezoelectric material lead zirconate titanate ($PbZr_xTi_{1-x}O_3$) has the form

$$d = \begin{bmatrix} 0 & 0 & 0 & 0 & d_{15} & 0 \\ 0 & 0 & 0 & d_{24} & 0 & 0 \\ d_{31} & d_{32} & d_{33} & 0 & 0 & 0 \end{bmatrix}. \tag{12}$$

Next, we consider thermo-mechanical effects. An elastic body subject to a change in temperature leads to a volumetric force via the modified constitutive equation (with an additional term added to equation (2)):

$$\sigma_{ij} = C_{ijkl}(\epsilon_{kl} - \alpha_{kl}\Delta T) \tag{13}$$

where α is the (isotropic) thermal volume expansion coefficient and ΔT a change of temperature, T. For $\alpha > 0$, an increase of temperature, $\Delta T > 0$, leads to an expansion of the volume of the overall solid. Likewise, $\alpha > 0$ and $\Delta T < 0$, or $\alpha < 0$ and $\Delta T > 0$ lead to a contraction. In general, thermal expansion of materials can be anisotropic, in which case the scalar α has to be replaced by a matrix. This includes, for example, the possibility of positive thermal expansion in one direction and negative thermal expansion (contraction) in the orthogonal directions. For metamaterials, highly anisotropic effective behavior can occur, e.g. for laminates (see section 3.1.2).

Light [36] and gravity [37] can also serve as stimuli for stimulus-responsive mechanical behavior. However, their relative amplitudes are extremely small, making their use almost impossible.

2.3. Eringen micropolar/micromorphic elasticity

In the preceding section, we have assumed that the strain, stress, and elasticity tensors are symmetric. However, in crystalline structures, these symmetries are not always given. Chirality is an example. An object is chiral if it cannot be superimposed onto its mirror image. Chiral mechanical behavior of materials and metamaterials is not captured Cauchy elasticity, which is constructed for infinitesimal but symmetric volume elements. In sharp contrast, micropolar continuum theory takes into account additional rotational degrees of freedom, allowing to grasp effects of chirality.

In micropolar elasticity, derived by Eringen in the seventies [38], the rotational degrees of freedom are described by the components of the rotation vector ϕ_i, which come in addition to the components of the displacement vector, u_i. The new micropolar strain tensor and the curvature tensor, respectively, are defined by [38]

$$\varepsilon_{ij} = \frac{\partial u_j}{\partial x_i} + \zeta_{jik}\phi_k \tag{14}$$

$$\kappa_{ij} = \frac{\partial \phi_i}{\partial x_j}. \tag{15}$$

Here, ζ_{ijk} represents the Levi-Civita tensor. Importantly, the new micropolar strain tensor is no longer symmetric and the generalized Navier equations read

$$\frac{\partial \sigma_{ji}}{\partial x_j} = \rho \frac{\partial^2 u_i}{\partial t^2} \tag{16}$$

$$\frac{\partial m_{ji}}{\partial x_j} + \epsilon_{ijk}\sigma_{jk} = \rho J \frac{\partial^2 \phi_i}{\partial t^2}. \tag{17}$$

Here, the J is the micro-inertia per unit density and the m_{ij} are the components of the couple stress tensor. Again, the stress tensor is generally no longer symmetric [39, 40].

Now, e.g. following Chen *et al* [40] the stress and couple stress tensors are given by:

$$\sigma_{ij} = \frac{\partial w}{\partial \varepsilon_{ij}} = C_{ijkl}\varepsilon_{kl} + D_{ijkl}\kappa_{kl} \tag{18}$$

$$m_{ij} = \frac{\partial w}{\partial \kappa_{ji}} = A_{jikl}\kappa_{kl} + D_{klji}\varepsilon_{kl}. \tag{19}$$

Only for the special case of $A_{ijkl} = D_{ijkl} = 0$, and $C_{ijkl} = C_{klij} = C_{jikl}$, do the C_{ijkl} reduce to the components of the classical Cauchy elasticity tensor. $\mathbf{D}$ is a fourth-order pseudo-tensor, which reverses its sign under a space-inversion operation. This fact is a necessary prerequisite to capture chiral effects within an effective-medium description.

Next, we turn to the kinematics of micromorphic continua. This is one step further away from Cauchy elasticity, as depicted in the right panel of figure 1. There are a rich variety of micromorphic elasticity theories, and we shall restrict ourselves to the energetic description presented in [41]. The importance of such enriched continuum models lies in their richer kinematics with respect to the classical macroscopic displacement field alone, which is related to the possibility of describing the motions of the microstructure inside the unit cell of a composite medium, such as a metamaterial.

We introduce the micro-distortion tensor $\mathbf{P}$ as shown in figure 1. We are specifically interested in the relaxed micromorphic model in [41], which requires six constitutive parameters in the isotropic case (μ_e, λ_e, μ_{micro}, λ_{micro}, μ_c, L_c). The first two parameters are related to the usual Lamé elastic parameters, the next two to microscopic effects, and μ_c to a form of rotational coupling. L_c is the characteristic length intrinsically related to nonlocal effects. The occurrence of non-zero characteristic lengths in micropolar and micromorphic elasticity indicates broken scale invariance. This means that many effective properties, for example the Young's modulus, are no longer constant for a given material, but rather depend on the number of unit cells in a crystalline metamaterial. We will come back to such effects in section 4.1.5. A version of a relaxed anisotropic micromorphic model is discussed in [42].

The counterpart of (16) and (17) takes the form

$$\begin{aligned} \mathrm{Div}\,\tilde{\sigma} &= \rho \frac{\partial^2 \mathbf{u}}{\partial t^2} + \mathrm{Div}\mathcal{I} \\ \tilde{\sigma} - \mathbf{s} - \mathrm{Curl}\,\mathbf{m} &= \eta \frac{\partial^2 \mathbf{P}}{\partial t^2}, \end{aligned} \tag{20}$$

where η is the free micro-inertia density and $\mathrm{Div}\mathcal{I} := (\nabla\cdot\mathcal{I}_1, \nabla\cdot\mathcal{I}_2, \nabla\cdot\mathcal{I}_3)^T$ and $\mathrm{Div}\,\tilde{\sigma}$ are rank-1 tensors with

$$\begin{aligned}\mathcal{I} &= \bar{\eta}_1 \mathrm{dev\,sym}\frac{\partial^2\nabla\mathbf{u}}{\partial t^2} + \bar{\eta}_2 \mathrm{skew}\frac{\partial^2\nabla\mathbf{u}}{\partial t^2} \\ &\quad + \frac{1}{3}\bar{\eta}_3 \mathrm{Tr}\frac{\partial^2\nabla\mathbf{u}}{\partial t^2} \\ \tilde{\sigma} &= 2\mu_e \mathrm{sym}\,(\nabla\mathbf{u} - \mathbf{P}) + \lambda_e \mathrm{Tr}\,(\nabla\mathbf{u} - \mathbf{P})\,\mathbf{I} \\ &\quad + 2\mu_c \mathrm{skew}\,(\nabla\mathbf{u} - \mathbf{P})\,.\end{aligned} \tag{21}$$

Here, $\bar{\eta}_i$, $i = 1,2,3$ are the gradient micro-inertia densities, $\mathbf{I}$ is the identity tensor, the subscripts dev, skew and sym denote the deviatoric (trace-free), skew symmetric, symmetric and trace (spherical) parts of a tensor, respectively. Finally,

$$\begin{aligned}\mathbf{s} &= 2\mu_{\mathrm{micro}}\,\mathrm{sym}\,(\mathbf{P}) + \lambda_{\mathrm{micro}}\,\mathrm{Tr}\,(\mathbf{P})\,\mathbf{I} \\ \mathbf{m} &= \mu_e L_c^2\,\mathrm{Curl}\,\mathbf{P}\end{aligned} \tag{22}$$

where $\mathrm{Curl}\,\mathbf{P} := ((\nabla\times\mathbf{P}_1)^T, (\nabla\times\mathbf{P}_2)^T, (\nabla\times\mathbf{P}_3)^T)^T$ is the rank-2 dislocation density tensor and $\mathrm{Curl}\,\mathbf{m} := ((\nabla\times\mathbf{m}_1)^T, (\nabla\times\mathbf{m}_2)^T, (\nabla\times\mathbf{m}_3)^T)^T$.

2.4. Willis elasticity

Dynamic homogenization of inhomogeneous elastodynamic media is rooted in the work of the British mathematician John Willis in the early 80s. Here, we present the basic ideas that have led to the derivation by Willis of the eponymous elastodynamic equations using so-called ensemble-averaging techniques for random media. If one applies asymptotic homogenization as illustrated in figure 3 to a periodic structure consisting of random media, it leads to homogenized Willis equations with the same structure, but with artificial anisotropy. Asymptotic homogenization theories are further described below. For now, we briefly present dynamic homogenization using ensemble averaging.

It is useful to recast the equation of motion (8) as

$$\frac{\partial\sigma_{ij}}{\partial x_j} + f_i = \frac{\partial p_i}{\partial t}\,, \tag{23}$$

where the stress tensor σ is related to the strain tensor ε via the elasticity tensor $\mathbf{C}$ in (2). The latter is related to the displacement vector field $\mathbf{u}$, see (3). Besides, $\mathbf{f}$ is the body force vector and $\mathbf{p}$ is the momentum vector

$$p_i = \rho\frac{\partial u_i}{\partial t}\,. \tag{24}$$

We now wish to average the equations of motion and find the constitutive parameters that relate the averaged field variables $\langle\sigma\rangle$, $\langle\varepsilon\rangle$, $\langle\mathbf{p}\rangle$ and $\langle\frac{\partial\mathbf{u}}{\partial t}\rangle$. Following Willis, the homogenization procedure can be derived for random composites. Random composites represent families whose physical properties vary not only with position but also with a parameter α (labeling the realisation of the random medium), which is a member of a sample space $\mathcal{A}$ (space of all outcomes), over which a probability measure $\mathcal{P}$ is defined (with values in $[0,1]$). This approach amounts to solving many problems over a domain defined, for each problem, by materials with elastic properties given by the elasticity tensor $\mathbf{C}(\mathbf{x},\alpha)$ and the mass density $\rho(\mathbf{x},\alpha)$. Each problem has the same body force, initial conditions, transmission conditions and outgoing wave condition. This leads to the point-wise solution $\mathbf{u}(\mathbf{x},\alpha)$ (and other derived field variables) for each problem. The cornerstone of John Willis's theory, is so-called ensemble average of a physical quantity Φ, which is defined over the sample space $\mathcal{A}$ by:

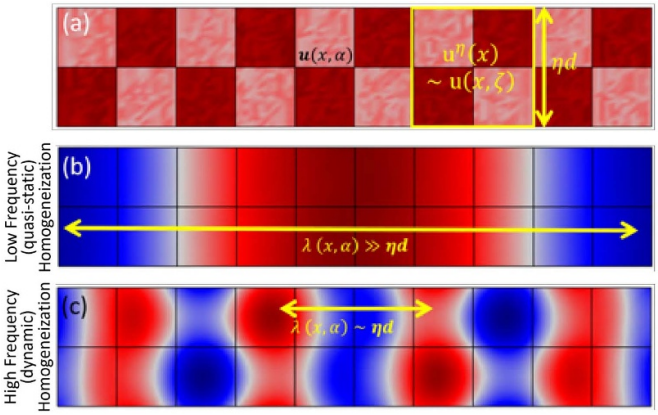

Figure 3. Schematic classification of asymptotic homogenization theories in periodic structures (a) and link with ensemble averaging of random media: in the low frequency regime when $\omega d/v \ll 1$, the wave wavelength λ is much larger than the lattice periodicity ηd, and one can apply low frequency (quasi-static) homogenization (b); in the high-frequency (Bragg) regime when $\omega d/v \sim 1$, the wavelength λ is close to the lattice periodicity ηd, and one should apply some high frequency (dynamic) homogenization (c). Each cell consists here of two types of random media. Elastic properties of these random media are deduced from ensemble averaging that leads to the Willis equation (28) in the dynamic regime.

$$\langle\Phi\rangle(\mathbf{x}) = \int_{\mathcal{A}} \Phi(\mathbf{x},\alpha)\,\mathcal{P}(\mathrm{d}\alpha). \tag{25}$$

This notion of mean is more general than that used in the sequel for periodic structures (see section 3.1.1), proves also useful in the homogenization of disordered structures (see section 3.1.3), and it is from this definition (25) that extraordinary elastodynamic properties can emerge for a complex medium.

Ensemble averaging the equation of motion (23), one gets

$$\frac{\partial\langle\sigma\rangle_{ji}}{\partial x_j} + f_i = \frac{\partial\langle p\rangle_i}{\partial t}\,, \tag{26}$$

and similarly ensemble averaging the strain made symmetric with (3) leads to

$$\langle\epsilon\rangle_{ij} = \frac{\partial\langle u\rangle_j}{\partial x_i} + \frac{\partial\langle u\rangle_i}{\partial x_j} \tag{27}$$

which can be solved if the ensemble averages of stress and momentum are related to the ensemble averages of strain and

velocity through appropriate homogenized relations. Coupled homogenized constitutive relations emerge [43]

$$\begin{aligned}\langle\sigma\rangle &= \mathbf{C}^{\text{eff}} \otimes \langle\epsilon\rangle + \mathbf{S}^{\text{eff}} \otimes \left\langle \frac{\partial}{\partial \mathbf{x}} \mathbf{u} \right\rangle \\ \langle\mathbf{p}\rangle &= \overline{\mathbf{S}}^{\text{eff}} \otimes \langle\epsilon\rangle + \rho^{\text{eff}} \otimes \left\langle \frac{\partial}{\partial \mathbf{x}} \mathbf{u} \right\rangle\end{aligned}, \tag{28}$$

where $\otimes$ represents convolution in space and time and $\overline{\mathbf{S}}^{\text{eff}}$ denotes the complex conjugate of $\mathbf{S}^{\text{eff}}$.

A material exhibiting the coupled constitutive relation (28), which is a generalization of the classical elastic constitutive relation, is known as a Willis material. It is interesting to note [44] that a periodic composite formed using Willis materials, using some asymptotic homogenization theory, will lead to a Willis material. Willis equations are said to satisfy a property known as G-closure [16].

2.5. Strain-gradient theories

Mindlin and Tiersten [45] and Koiter [46] developed the initial version of a couple stress theory, in which the deformation is completely specified by the continuous displacement field. This theory is implicitly based on the rigid body portion of motion of infinitesimal elements of matter at each point of the continuum. Therefore, in this theory, the internal stresses are exactly the force- and couple-stress tensors introduced by Cosserat and Cosserat [47]. Each of them has at most 9 independent components. However, Eringen [48] realized that there were some pitfalls in the couple stress theory. Instead of resolving the inconsistencies in the framework of this theory, researchers turned to other theories, such as micropolar theories that we discussed previously, but also to higher-gradient theories, such as strain-gradient theories [49].

The spirit of such theories, see e.g. [50–56], is usually to take some asymptotic expansions (akin to Taylor series) in the unknown of the governing equation. In order to do that, it is customary to introduce a slow variable $\mathbf{x} = (x_1, x_2, x_3)$ and a fast variable $\mathbf{y} = (x_1/\eta, x_2/\eta, x_3/\eta)$, where η is a small positive parameter related to the size of a microstructural element that is repeated periodically within a composite, such as shown in figure 3. The fast variable will capture the fast oscillations of the displacement field and its derivatives. Here, we give the recipe for an order 2 strain-gradient theory. We consider the following ansatz for the displacement field

$$\mathbf{u}^{\eta}(\mathbf{x}) = \mathbf{u}^0(\mathbf{x}) + \eta \mathbf{u}^1(\mathbf{x}, \mathbf{y}) + \eta^2 \mathbf{u}^2(\mathbf{x}, \mathbf{y}) + O(\eta^2) \tag{29}$$

where the Bachmann–Landau big O notation means that the left and right members of the equation are asymptotically equal if η is very small.

We then write the following ansatz for $\mathbf{u}^1$

$$\mathbf{u}^1(\mathbf{x}, \mathbf{y}) = \mathbf{U}^1(\mathbf{x}) + H_{ikl}(\mathbf{y}) \epsilon_{kl}(\mathbf{u}^0(\mathbf{x})) \tag{30}$$

where $\epsilon_{kl}(\mathbf{u}^0(\mathbf{x})) = 1/2\left(\partial_{x_k} u_l^0 + \partial_{x_l} u_k^0\right)$ and H_{ikl} is a rank-3 tensor, which is symmetric with respect to the last two indices. Similarly, for $\mathbf{u}^2$, we write

$$\begin{aligned}\mathbf{u}^2(\mathbf{x}, \mathbf{y}) = \mathbf{U}^2(\mathbf{x}) &+ H_{ikl}(\mathbf{y}) \epsilon_{kl}(\mathbf{U}^1(\mathbf{x})) \\ &+ P_{ijkl}(\mathbf{y}) \epsilon_{kl}(\partial_{x_j} \mathbf{u}^0(\mathbf{x}))\,,\end{aligned} \tag{31}$$

where the P_{ijkl} are the components of a rank-4 tensor that is symmetric with respect to the last two indices, but not necessarily with respect to the first two indices. This means that one can have $P_{ijkl} \neq P_{jikl}$ and $P_{ijkl} \neq P_{klij}$, depending on the microstructure.

In order to deduce the effective equations, one then introduces the mean operator over a unit cell $Y = [0,1]^3$, which is a counterpart to ensemble averaging (25) for periodic structures

$$\langle\Phi\rangle(\mathbf{x}) = \int_Y \Phi(\mathbf{x}, \mathbf{y})\, \mathrm{d}\mathbf{y}. \tag{32}$$

This notion of mean is specially designed for periodic structures and will be used exclusively in the sequel.

Plugging ansatz (29)–(31) in (9) and collecting the terms of same power of η in (9), we get

$$\begin{aligned}&C^0_{ijmn} \epsilon_{mn}(\partial_{x_j} \langle\mathbf{u}\rangle(\mathbf{x})) + \eta C^1_{ijkmn} \epsilon_{mn}(\partial_{x_k} \partial_{x_j} \langle\mathbf{u}\rangle(\mathbf{x})) \\ &\quad + \eta^2 C^2_{ijprmn} \epsilon_{mn}(\partial_{x_r} \partial_{x_p} \partial_{x_j} \langle\mathbf{u}\rangle(\mathbf{x})) \\ &\quad + \omega^2 \{\rho_0 \langle u_i\rangle(\mathbf{x}) \\ &\quad + \eta \langle \rho(\mathbf{y}) H_{ikl}(\mathbf{y})\rangle \epsilon_{kl}(\langle\mathbf{u}\rangle(\mathbf{x})) \\ &\quad + \eta^2 \rho(\mathbf{y}) P_{ijkl}(\mathbf{y}) \epsilon_{kl}(\partial_{x_j} \langle\mathbf{u}\rangle(\mathbf{x}))\} = 0\,,\end{aligned} \tag{33}$$

which is an enriched governing equation valid for the averaged macroscopic field, with first and second-order corrections to the classical Cauchy elasticity tensor, as well as to the density.

Such strain-gradient theories are a quest to better encapsulate the different size effects in materials such as that initiated in [57], but they can lead to very complicated governing equations, since one can add further and further high-order corrections to the elasticity tensor and density. Important applications of size-effects are in strengthening of polycrystalline materials (i.e. solids that are composed of many crystallites of varying size and orientation, such as metals, ceramics, rocks) by grain refinement or by dispersion hardening. The strength of the polycrystals in these cases is improved by reducing the size of the microstructural constituents of the materials, namely, the grain size or the size of second phase particles. These effects (of which the well-known Hall–Petch effect is an example [58, 59]) are well described by dislocation theories for crystalline materials. These theories are beyond the scope of the present review, but they represent interesting potential extensions that may be relevant for mechanical metamaterials.

However, one should be aware that they sometimes lead to inconsistent generalized continuum equations [60, 61]. There is a vast literature on this topic and we refer the reader, e.g. to the review article [62] for further details. Such theories also

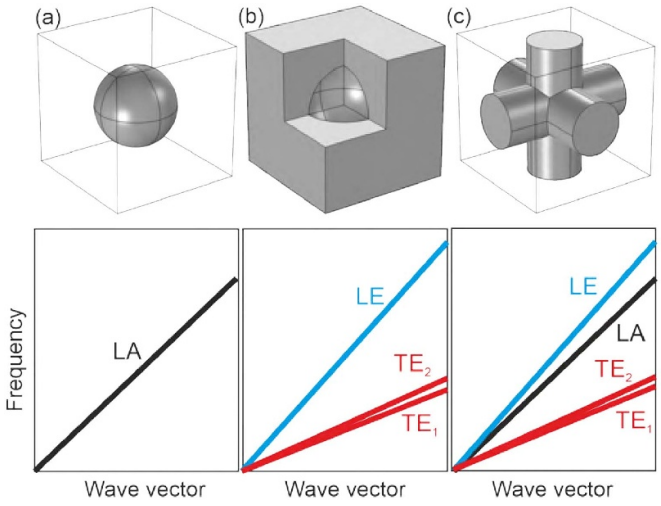

Figure 4. Unit cell of a fluid containing a solid inclusion (a), a solid with a fluid inclusion (b), and two continuous phase composites made of a solid and a fluid (c). Corresponding schematic dispersion relation. LA refers to longitudinal acoustic, LE to longitudinal elastic, and TE transverse elastic. Note that the latter composite supports four acoustical modes instead of three in Cauchy elasticity.

touch upon the bulk and surface effects in the elastic properties of solids [63].

2.6. Coupled acoustic-elastic problems

As seen in the previous sections, a solid subjected to a force is described by the Navier equation while the fluids are governed by the Helmholtz scalar equation (see section 2.1). When the two share an interface, the pressure in the fluid is continuous with the normal traction in the solid, or $T_{ij}n_j = -pn_i$ where $\mathbf{T} = \mathbb{C} : \nabla\mathbf{u}$ is the stress tensor and $\mathbf{n}$ is the normal to the interface entering the fluid. Second, the normal acceleration is continuous and proportional to the gradient of pressure in the fluid according to

$$\mathbf{n} \cdot \left(\rho^{-1}\nabla p\right) = -\mathbf{n} \cdot \frac{\partial^2 \mathbf{u}}{\partial t^2}\,, \tag{34}$$

where the normal $\mathbf{n}$ now enters the solid.

More generally, solid or liquid media containing solid or liquid inclusions are called poroelastic media. Many different approximate models have been used. We distinguish between three cases (see figure 4):

- (i) A liquid contains solid dispersed inclusions.
- (ii) A continuous solid contains liquid inclusions.
- (iii) A liquid and solid phase intermix continuously. Two continuous media coexist.

In the first case, it can be naively understood that any fluid containing solid inclusions will still behave as a fluid as long as it is not too saturated by the solid parts. This leads to a single acoustical mode (figure 4(a)). In the second case of a solid containing liquid inclusions, the effective properties are homogenised to an effective solid with lower stiffness than that of the host material. Globally, it will support two transverse waves and one longitudinal wave (figure 4(b)). Finally, the perhaps most interesting case (figure 4(c)) is if both phases are continuous through the material. With the addition of elastic waves the two previous properties will add up and we have 4 possible propagating acoustical modes in this composite (2 transverse elastic, 1 longitudinal elastic, and 1 longitudinal acoustic); this last case will be further discussed in section 4.1.3.

This is encompassed within the framework of a more general description of fluid–solid coupled systems: in the 1950s Biot [64, 65] embarked upon a study of the deformations of porous solids motivated by problems from geophysics involving soil and rock mechanics; the extraction of oil and gas from porous oil reservoirs being a typical application of poroelasticity. Ignoring elastic waves, one can envisage the porous medium as a fluid saturated porous sponge with an elastic skeleton and fluid filled interconnected pores. The fluid pressure obeys a diffusion-law and is also coupled to the dilatation of the solid skeleton, conversely the elastic material is coupled to fluid pressure and the resulting system is fully coupled; a review in the geophysics setting is given in [66].

3. Structure-property relations

The relation between structure and properties is a core problem for materials in general and metamaterials in particular. This relation has two directions, the forward problem and the inverse problem. In the forward problem, one starts from a given microstructure of the metamaterial and would like to derive its effective properties. These effective parameters refer to a fictitious effective homogeneous medium that approximately (!) behaves like the heterogeneous metamaterial. Therefore, this step is often referred to as homogenization. Precisely, the effective metamaterial properties are described by the material parameters that occur in the effective-medium descriptions that we have outlined in section 2. Thus, as a first step of the forward problem, one must choose an appropriate effective-medium description. As described in sections 3.1.1 and 3.1.3, the following mathematical steps in homogenization depend on the contrast of the ingredient material parameters, the considered frequency range, whether the metamaterial structure is periodic or quasi-periodic, and on whether the problem is time-dependent. In the inverse problem, a ‘user’ defines certain wanted effective material parameters and asks for a microstructure that exhibits these effective parameters. The inverse problem touched upon in section 3.2 is much harder to solve and typically requires solving the forward problem many times.

3.1. Forward problems

Deriving the homogenized anisotropic Cauchy elasticity tensor is a well-known result of homogenization theory [67–70]. The homogenization of the Eringen micropolar elasticity equations proceeds in the same way but is more involved, so we refer the reader to [71] for further details on the micropolar case.

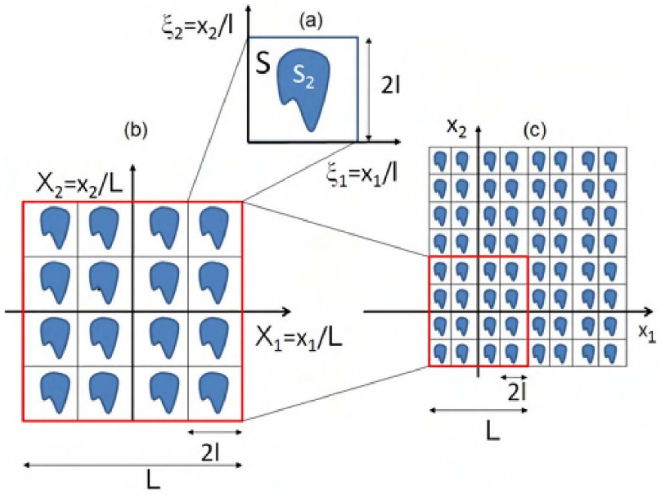

Figure 5. Low and high frequency homogenisation principles: an elementary cell (a) of sidelength $2l$, modeled by a fast oscillating variable $\boldsymbol{\xi}$, is repeated periodically within a supercell (b) of sidelength L, modeled by a slow variable $\mathbf{X}$, which is itself repeated periodically in space (c). One then assumes that the parameter $\epsilon = l/L$ is small, and its vanishing limit thereafter studied. The leading order, homogenised, term of Floquet–Bloch eigenfields within the crystal are then sought as $u_0(\mathbf{X},\boldsymbol{\xi}) = f_0(\mathbf{X})U_0(\boldsymbol{\xi};\Omega_0)$, wherein f_0 accounts for variations of the fields on the order of the supercells, and U_0 captures their fast oscillations in the much smaller cells, when either periodic or anti-periodic conditions are enforced on the cells: Perturbing away from these standing waves of frequency Ω_0 allows for a complete reconstruction of the Bloch spectrum and associated Floquet–Bloch eigenfields.

3.1.1. Low-frequency homogenization. We consider a sequence of problems parametrized by a small positive parameter η that denotes the ratio of periodic cell's size to wavelength:

$$\begin{cases} -\frac{\partial}{\partial x_j}\left(\sigma_{ij}^{\eta}(\mathbf{u}(\mathbf{x}))\right) = \omega^2\rho\left(\frac{\mathbf{x}}{\eta}\right)u_i^{\eta}(\mathbf{x}) & , \\ \sigma_{ij}^{\eta}(\mathbf{u}(\mathbf{x})) = C_{ijkl}\left(\frac{\mathbf{x}}{\eta}\right)e_{kl}^{\eta}(\mathbf{u}(\mathbf{x})) & , \\ e_{kl}^{\eta}(\mathbf{u}(\mathbf{x})) = \frac{1}{2}\left(\frac{\partial u_k\left(\frac{\mathbf{x}}{\eta}\right)}{\partial x_l} + \frac{\partial u_l\left(\frac{\mathbf{x}}{\eta}\right)}{\partial x_k}\right) & , \end{cases} \tag{35}$$

where $i,j,k,l = 1,2,3$, $\mathbf{x} = (x_1,x_2,x_3)$. Note that $C_{ijkl}(\mathbf{y})$ is fully symmetric and is periodic of period 1 in y_1, y_2 and y_3. This means that $C_{ijkl}(\frac{\mathbf{x}}{\eta})$ is periodic of period η in all three directions.

We would like to consider the limit when the parameter η goes to zero in the above system, which is known as the long-wavelength limit. This also means that the periodic structure will be filled by a large number of small elementary cells in the homogenization limit: indeed, during the homogenization process (see figure 5), each small elementary cell Y is rescaled by the parameter η according to $\eta Y = [0;\eta]^3$, where $\eta \ll 1$, and their number scales as η^{-3}.

We consider the following two-scale asymptotic expansion of the displacement field [67]:

$$\mathbf{u}^{\eta}(\mathbf{x}) = \mathbf{u}^0(\mathbf{x}) + \eta\mathbf{u}^1(\mathbf{x},\mathbf{y}) + \eta^2\mathbf{u}^2(\mathbf{x},\mathbf{y}) + \cdots \tag{36}$$

where $\mathbf{u}^i(\mathbf{x},\mathbf{y})$ is 1-periodic in the microscopic variable $\mathbf{y} = (y_1,y_2,y_3)$ (so is 1-periodic in y_1, y_2 and y_3).

We can deduce [68, 70], the homogenized Navier problem as:

$$\begin{cases} -\frac{\partial}{\partial x_j}\left(\sigma_{ij}^H(\mathbf{u}^0(\mathbf{x}))\right) = \omega^2\langle\rho\rangle u_i^0(\mathbf{x}) & , \\ \sigma_{ij}^H(\mathbf{u}^0(\mathbf{x})) = C_{ijkl}^H e_{kl}(\mathbf{u}^0(\mathbf{x})) & , \\ e_{kl}(\mathbf{u}^0(\mathbf{x})) = \frac{1}{2}\left(\frac{\partial u_k^0}{\partial x_l} + \frac{\partial u_l^0}{\partial x_k}\right) & , \end{cases} \tag{37}$$

where C_{ijkl}^H denotes the homogenized elasticity tensor given by

$$C_{ijmh}^H = \frac{1}{|Y|}\int_Y C_{ijkl}(\mathbf{y})\left(\delta_{km}\delta_{lh} + e_{kly}(w^{mh}(\mathbf{y}))\right)\mathrm{d}\mathbf{y} \tag{38}$$

where $|Y|$ denotes the cell volume (or its area for a configuration in two dimensions, see section 3.1.2), and the subscript y in the coefficients of the strain tensor indicates partial derivatives therein are with respect to the microscopic variable. So-called potentials w^{kl} are given by the annex problem posed on the periodic cell Y:

$$-\frac{\partial}{\partial y_j}\left(C_{ijkl}(\mathbf{y})\frac{\partial}{\partial y_l}w^{kl}(\mathbf{y})\right) = \delta_{mk}\delta_{hl}\left(\frac{\partial}{\partial y_j}C_{ijmh}(\mathbf{y})\right), \tag{39}$$

with $w^{kl}(\mathbf{y})$, 1-periodic in y_1, y_2 and y_3.

We note that if the elastic medium does not depend upon the third variable y_3, then the volume integral in (38) simplifies; this is the case for the laminates of the next section.

3.1.2. Laminates. Let us first consider the anti-plane shear case. Indeed, for the case of laminates, the anti-plane and in-plane problems decouple [16]. Consider a 2D periodic laminate with an anisotropic shear modulus $\mu_{ij}(y_1,y_2)$, $i,j = 1,2$, and a unit cell $Y = [0,1]^2$. The cell contains a layered medium which is periodic along y_1 and constant along y_2 (so periodic in y_2 as well). In that case (39) takes the form

$$-\frac{\partial}{\partial y_j}\left(\mu_{jl}(\mathbf{y})\frac{\partial}{\partial y_l}w^k(\mathbf{y})\right) = \delta_{mk}\left(\frac{\partial}{\partial y_j}\mu_{jm}(\mathbf{y})\right), \tag{40}$$

with $w^k(\mathbf{y})$, 1-periodic in y_1 and y_2. The components of the homogenized shear modulus of the laminate are given by the anti-plane shear part of the homogenized elasticity tensor

$$\mu_{ij}^H = \frac{1}{|Y|}\int_Y C_{ijkl}(\mathbf{y})\left(\delta_{km}\delta_{lh} + e_{kly}(w^{mh}(\mathbf{y}))\right)\mathrm{d}\mathbf{y}\,, \tag{41}$$

which are

$$\begin{aligned}
\mu^h_{11} &= \left(\frac{1}{|Y|}\int_Y \mu_{11}^{-1}(y_1,y_2)\,\mathrm{d}y_1\mathrm{d}y_2\right)^{-1}\\
&:= \langle \mu_{11}^{-1}\rangle_Y^{-1}\\
\mu^h_{22} &= \langle \mu_{22}\rangle_Y - \langle \mu_{21}\mu_{12}\mu_{11}^{-1}\rangle_Y\langle \mu_{11}^{-1}\rangle_Y^{-1}.\\
&\quad + \langle \mu_{21}\mu_{11}^{-1}\rangle_Y\langle \mu_{12}\mu_{11}^{-1}\rangle_Y\langle \mu_{11}^{-1}\rangle_Y^{-1}\\
\mu^h_{21} &= \langle \mu_{21}\mu_{11}^{-1}\rangle_Y\langle \mu_{11}^{-1}\rangle_Y^{-1}\\
\mu^h_{12} &= \langle \mu_{12}\mu_{11}^{-1}\rangle_Y\langle \mu_{11}^{-1}\rangle_Y^{-1}
\end{aligned} \tag{42}$$

We note here that the homogenized matrix is not symmetric, which reflects the fact that the principal axes for anisotropy might not be in general aligned with the y_1 and y_2 axes. Upon rotation, the matrix becomes symmetric. We also note that if $\mu_{11}=\mu_{22}=\mu$, where μ is the Lamé constant for an isotropic elastic medium and $\mu_{12}=\mu_{21}=0$, then we retrieve the well-known formula $\mu^h_{11}=\langle\mu^{-1}\rangle_Y^{-1}$ and $\mu^h_{22}=\langle\mu\rangle_Y$.

We now move to the in-plane part of the homogenized elasticity tensor. In that case, we need to solve $(A2)$ and find 16 unknown functions w^{kl} and using the expression for the homogenized elasticity tensor C^H_{ijkl} we are led to the Backus formula [73]; solutions to $(A2)$ are found analytically, resulting in explicit formulas for the effective elastic tensor [16, 74]:

$$\begin{aligned}
&c^h_{11} = \langle 1/(\lambda+2\mu)\rangle^{-1}, c^h_{55}=c^h_{66}=\langle 1/\mu\rangle^{-1},\\
&c^h_{44} = \langle\mu\rangle, c^h_{12}=c^h_{13}=\langle\lambda/(\lambda+2\mu)\rangle\langle 1/(\lambda+2\mu)\rangle^{-1},\\
&c^h_{23} = \langle 2\mu\lambda/(\lambda+2\mu)\rangle + \langle\lambda/(\lambda+2\mu)\rangle c^h_{12},\\
&c^h_{22} = c^h_{33} = \langle 4\mu(\lambda+\mu)/(\lambda+2\mu)\rangle + \langle\lambda/(\lambda+2\mu)\rangle c^h_{12},
\end{aligned} \tag{43}$$

where λ and μ are Lamé's constants for isotropic materials ($\lambda+2\mu=c_{11}$, $\mu=c_{66}$). It is also possible to deduce analytic formulae when the layers are anisotropic, but such formulas are more complex [69, 75].

Backus's formulae were first derived in the framework of layered soils in geophysics but they have been used in a number of studies in phononic crystals and metamaterials. We show in figure 6 finite element computations of so-called slowness curves that exemplify the potential anisotropy of a laminate.

However, strict periodicity might be hard to achieve in practice, due to unavoidable imperfections during the fabrication process of mechanical metamaterials at the small scale. On the other hand, large scale metamaterials such as seismic metamaterials (see section 5.7) consist of a periodic assembly of boreholes or concrete columns embedded or above a soil that is inherently a disordered medium. Or one might wish to depart from the strictly periodic case to achieve certain effects such as in graded metamaterials (see section 5). Fortunately, much of what has been done in sections 3.1.1 and 3.1.4 can be extended to random media, provided certain assumptions are made (in passing aforementioned compensated compactness method [76, 77], also known as translation method breaks free from periodicity assumption in a more abstract mathematical setup).

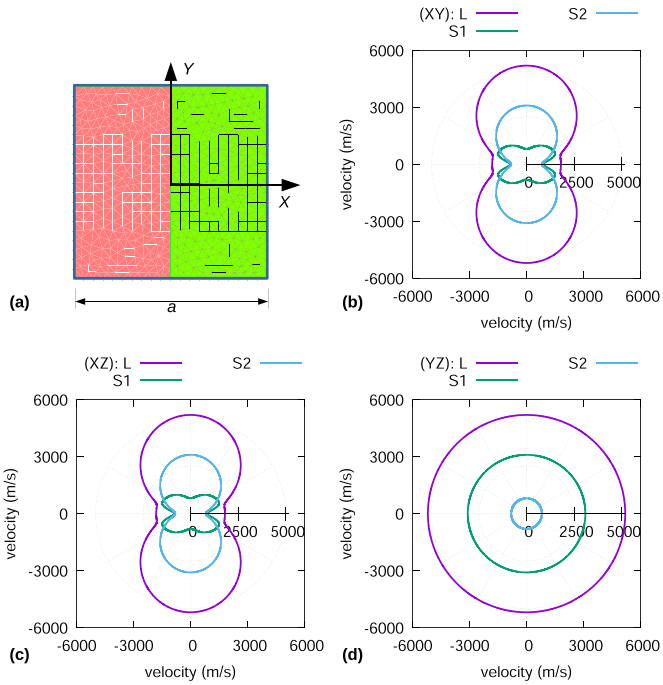

Figure 6. (a) A periodic cell of a laminate made of an alternation of layers of steel and epoxy with equal thickness. (b)–(d) Cross-sections of the three effective velocity surfaces through the symmetry planes of the crystal. Reprinted from [72], with the permission of AIP Publishing.

3.1.3. Disordered crystals. There is a vast amount of literature on homogenization of random media, and we refer the reader to the classical textbook [69], representative work [78–90] and references therein for general results. Not surprisingly, the fully probabilistic homogenization approach recovers the periodic case [91]. However, following [92], we can generalize our results for low frequency homogenization of periodic structures to random structures with little effort when the elasticity tensor and the density satisfy certain ergodicity assumptions. Indeed, the asymptotic analysis of section 3.1.1 carries through with little adjustments, provided we adopt the mathematical framework introduced forty years ago in [92], see also supplemental materials.

The homogenized system has the same expression (37) as in the periodic case, but the homogenized elasticity tensor C^H_{ijkl} is given by the ergodic limit:

$$\begin{aligned}
C^H_{ijmh} = \lim_{T\to\infty}\frac{1}{(2T)^3}\int_{[-T,T]^3} & C_{ijkl}(\mathbf{y},\alpha)\\
&\times\left(\delta_{km}\delta_{lh}+e_{kly}(w^{mh}(\mathbf{y},\alpha))\right)\mathrm{d}\mathbf{y}\,,
\end{aligned} \tag{44}$$

with $T>0$ and α labelling the realization of the random medium. Similarly, section 3.1.2 carries through, replacing the mean over Y by the above ergodic mean.

The counterpart of annex problem (39) is

$$\begin{aligned}
\lim_{T\to\infty}\frac{1}{(2T)^3}\int_{[-T,T]^3}\Big(& C_{ijkl}(\mathbf{y},\alpha)\frac{\partial}{\partial y_l}w^{kl}(\mathbf{y},\alpha)\\
&+ C_{ijmh}(\mathbf{y},\alpha)\delta_{mk}\delta_{hl}\Big)\frac{\partial}{\partial y_j}\phi(\mathbf{y},\alpha)\,\mathrm{d}\mathbf{y}=0,
\end{aligned} \tag{45}$$

and is posed in the whole space $\mathbb{R}^3$. In practice, effective properties of disordered crystals are deduced by considering large enough cells. The fact that the annex problem for a disordered crystal is posed on the whole space $\mathbb{R}^3$, and cannot be reduced to a problem posed on a periodic cell Y as in the periodic case has far reaching consequences for numerical implementation. Truncations of problem (45) have to be considered, typically on large domains and using periodic boundary conditions. This could be viewed as a supercell approach of homogenization. The actual homogenized coefficients are only captured in the asymptotic regime. Important theoretical questions about the quality and the rate of the convergence in terms of the truncation size arise and are addressed in [93–96]. One should bear in mind that the rate of convergence in L^2 norm of $\mathbf{u}^\eta$ to the leading term $\mathbf{u}^0$ of the asymptotic expansion (36) scales as η in the periodic one-dimensional (1D) case and as $\sqrt{\eta}$ in the disordered case 1D. In practice if a supercell cell consists of N layers of the 1D disordered medium this means that the truncation error is on the order of $N^{-1/2}$. Thus, for 100 layers, the error is about $\sqrt{0.01} = 0.1$, and one would need to consider a larger supercell with 10^4 layers to ensure a vanishingly small error of about 0.01; this should be compared with the periodic case for which 100 layers would suffice.

Positioned between periodic and random media are quasicrystals. So-called quasi-crystals require a special treatment to avoid resorting to an annex problem on a cell with size tending to infinity, and thus escaping the associated truncation issues, as we shall now see.

3.1.4. Quasi-crystals. Homogenization of almost periodic partial differential operators was performed in an abstract functional space framework by the Russian mathematician Kozlov back in 1979 [97] and subsequently by [98–105]. Extending the two-scale convergence method introduced by Nguetseng [106] and further developed by Allaire [107] (see [108] for a comprehensive survey), it was shown in [109] that quasicrystals derived from a cut-and-projection of a periodic structure in a higher dimensional space (a method introduced by the physicists Duneau and Katz in 1985 [110]) can be replaced by an effective anisotropic medium described in a Fourier space; this inspired [111, 112]. Irrational (cut-and-project) differential operators introduced in [113] allow us to proceed with the asymptotic analysis of the Navier system for quasi-periodic (cut-and-project) structures, in the similar way to what was done for the periodic case in section 3.1.1. We introduce the mapping (a lifting of space) $\mathbf{R}$ from physical space $\mathbb{R}^3$ to higher dimensional space $\mathbb{R}^m$ with $m > 3$, which fulfills the criterion

$$\mathbf{R}^T \underline{\mathbf{k}} \neq 0 \ , \ \forall \mathbf{k} \in \mathbb{Z}^m \setminus \{\mathbf{0}\} \ . \tag{46}$$

This criterion means that the entries of $\mathbf{R}$ are incommensurate, such as those for typical quasicrystals generated by the cut-and-projection, see figure 7.

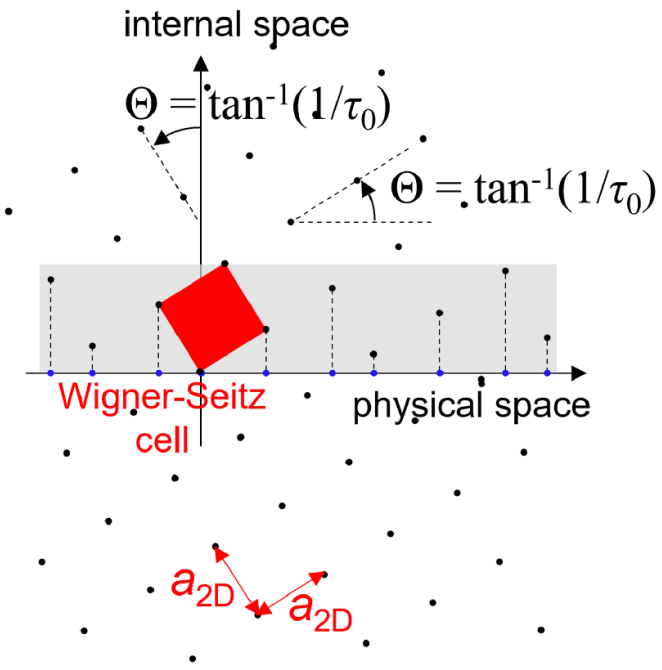

Figure 7. Illustration of the cut-and-project method for generating a 1D quasicrystal from a 2D square lattice of dots. The 2D lattice is rotated by angle Θ, which is connected to the golden number τ_0, and part of the lattice is projected onto the horizontal 'physical space' axis. The blue dots form the 1D quasicrystal.

We now consider the sequence of problems

$$\begin{cases} -\dfrac{\partial}{\partial x_j}\left(\sigma_{ij}^\eta(\mathbf{u}(\mathbf{x}))\right) = \omega^2 \rho\left(\dfrac{\mathbf{Rx}}{\eta}\right) u_i^\eta(\mathbf{x}) & , \\ \sigma_{ij}^\eta(\mathbf{u}(\mathbf{x})) = C_{ijkl}\left(\mathbf{x}, \dfrac{\mathbf{Rx}}{\eta}\right) \mathrm{e}_{kl}^\eta(\mathbf{u}(\mathbf{x})) & , \\ e_{kl}^\eta(\mathbf{u}(\mathbf{x})) = \dfrac{1}{2}\left(\dfrac{\partial u_k^\eta(\mathbf{x})}{\partial x_l} + \dfrac{\partial u_l^\eta(\mathbf{x})}{\partial x_k}\right) & , \end{cases} \tag{47}$$

which is the counterpart of (35) in the periodic case.

Asymptotic expansion of fast oscillatory displacement field $\mathbf{u}_\eta(\mathbf{x})$ solution of the above has the form

$$\begin{aligned} \mathbf{u}_\eta(\mathbf{x}) = \mathbf{u}^0(\mathbf{x}, \mathbf{R}(\mathbf{x})/\eta) + \eta \mathbf{u}^1(\mathbf{x}, \mathbf{R}(\mathbf{x})/\eta) \\ + \eta^2 \mathbf{u}^2(\mathbf{x}, \mathbf{R}(\mathbf{x})/\eta) + \cdots \ , \end{aligned} \tag{48}$$

where $\mathbf{u}^i : \Omega_f \times Y^m \longmapsto \mathbb{C}^3$ is a smooth function of $3+m$ variables, independent of η, such that $\forall \mathbf{x} \in \Omega_f$, $\mathbf{u}^i(\mathbf{x}, \cdot)$ is Y^m-periodic in $\mathbb{R}^m$, with $Y^m = [0,1]^m$.

We note that the rescaled gradient acting on two-scale functions $\mathbf{u}^i$ is such that

$$\begin{aligned} \nabla\, \mathbf{u}^i(\mathbf{x}, \mathbf{R}(\mathbf{x})/\eta) = \nabla_{\mathbf{x}}\, \mathbf{u}^i(\mathbf{x}, \mathbf{R}(\mathbf{x})/\eta) \\ + \eta^{-1} \nabla_{\mathbf{R}}\, \mathbf{u}^i(\mathbf{x}, \mathbf{R}(\mathbf{x})/\eta) \ , \end{aligned} \tag{49}$$

where the so-called cut-and-projection operator $\nabla_{\mathbf{R}}\, \mathbf{u}^i(\mathbf{x}, \mathbf{y}) = \mathbf{R}^T \nabla_{\mathbf{y}}\, \mathbf{u}^i(\mathbf{x}, \mathbf{y})$; the rescaled divergence and curl have similar expressions.

One can then carry out asymptotic analysis of the Navier system in the same way as is done for the periodic case. We can thus write the homogenized Navier equation as follows [113]:

$$\begin{cases} -\dfrac{\partial}{\partial x_j}\left(\sigma_{ij}^H(\mathbf{u}^0(\mathbf{x}))\right) = \omega^2\langle\rho\rangle u_i^0(\mathbf{x}) & , \\ \sigma_{ij}^H(\mathbf{u}^0(\mathbf{x})) = C_{ijkl}^H e_{kl}(\mathbf{u}^0(\mathbf{x})) & , \\ e_{kl}(\mathbf{u}^0(\mathbf{x})) = \dfrac{1}{2}\left(\dfrac{\partial u_k^0}{\partial x_l} + \dfrac{\partial u_l^0}{\partial x_k}\right) & , \end{cases} \tag{50}$$

which is identical to (37) except that now the homogenized elasticity tensor is given by

$$C_{ijrh}^H = \frac{1}{|Y^m|}\int_{Y^m} C_{ijkl}(\mathbf{y})\left(\delta_{kr}\delta_{lh} + \sum_{p=1}^{m} R_{pl} e_{kpy}(w^{rh}(\mathbf{y}))\right) \mathrm{d}\mathbf{y}\,. \tag{51}$$

where $w^{rh}(\mathbf{y})$ are Y^m-periodic functions given by cell problems in higher-dimensional space

$$\begin{aligned} &-\sum_{p=1}^{m} R_{pj}\frac{\partial}{\partial y_p}\left(C_{ijkl}\sum_{q=1}^{m} R_{ql}(\mathbf{y})\frac{\partial}{\partial y_q} w^{rh}(\mathbf{y})\right) \\ &\quad = \delta_{rk}\delta_{hl}\left(\sum_{p=1}^{m} R_{pj}\frac{\partial}{\partial y_p} C_{ijrh}(\mathbf{y})\right). \end{aligned} \tag{52}$$

These annex problems are counterpart of (39) in the periodic case.

An alternative way to homogenize quasicrystals is to proceed with periodic rational approximants in the physical space as was done in [114]. This amounts to considering larger and larger periodic cells in the quasiperiodic medium, until the error in the homogenized coefficients is small enough. This approach can be mathematically justified using the formalism discussed in section 3.1.3, see [92].

Another homogenization problem of particular interest for metamaterials is that of periodic media with highly contrasted phases that we address next.

3.1.5. High-contrast homogenization. Until now, we assumed that the contrast in material parameters was moderate, and thus the main effect of homogenization was to bring some artificial anisotropy in the governing equations i.e. to make some material parameters matrix valued. We would like now to achieve dispersive (i.e. frequency dependent) parameters.

To illustrate this, following [115], we consider a 3D phononic crystal with a periodic cell shown in figure 8 (upper left panel), which consists of a sphere S filled with a fluid of density ρ_i surrounded by a fluid of density ρ_e. The associated irreducible Brillouin zone ΓXMU is shown in upper right panel. When we increase the contrast between ρ_i and ρ_e, we note the appearance of low frequency localized modes inside the spheres of the array (Mie resonances).

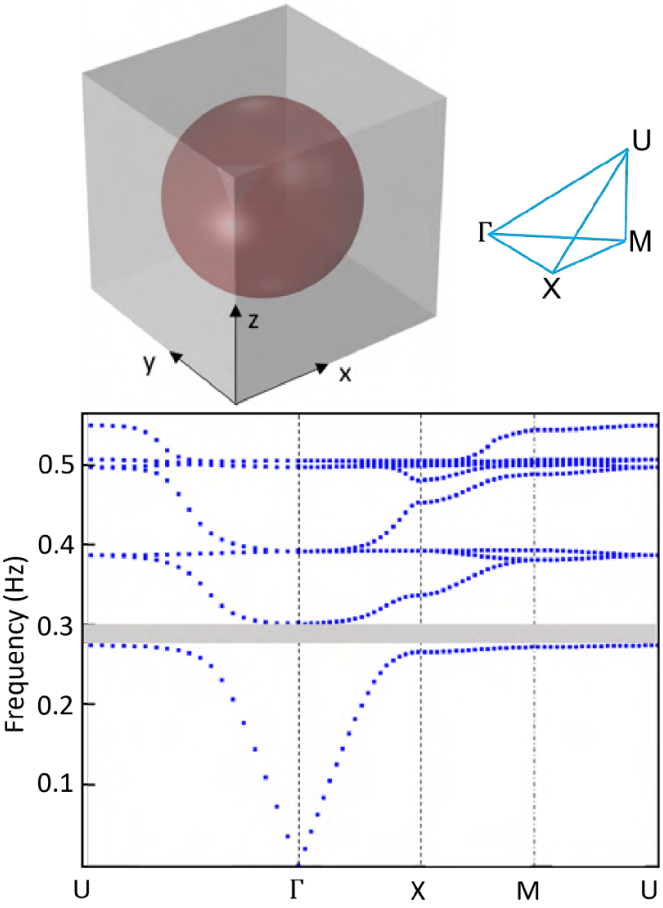

Figure 8. (Top left) Periodic cell Y of sidelength 1m with a spherical inclusion S of radius $r = 0.4$ m. (Top right) First Brillouin zone $U\Gamma XM$. (Bottom) Dispersion curves for densities $\rho_i = 20\,\mathrm{kg\,m^{-3}}$ and $\rho_e = 1\,\mathrm{kg\,m^{-3}}$. The bulk modulus is taken to be equal to 1 Pa.

To model the appearance of the low-frequency stop band in figure 8 and identify the associated effective medium we start with the scalar wave equation (1) which we recast as [116]

$$-\nabla\cdot\rho_\eta^{-1}\nabla p_\eta = k^2 p_\eta\,. \tag{53}$$

thus assuming that the medium is heterogeneous isotropic with a density $\rho_i = \rho_e(\rho_r/\eta)$ in the spherical inclusions S and ρ_e outside the inclusions (ρ_i and ρ_e are in units of $\mathrm{kg\,m^{-3}}$, whereas ρ_r is a relative density without any physical units), and a wavenumber $k = \omega\sqrt{\rho_e}/\sqrt{B}$ with ω the angular wave frequency ($\mathrm{rad\,s^{-1}}$) and B the bulk modulus (identical inside and outside inclusions in units of Pa).

Let us denote $\chi_\eta = \rho_\eta^{-1}\nabla u_\eta$, so that the Helmholtz equation (53) is now recast into the following coupled system:

$$-\nabla\cdot\chi_\eta = k^2 p_\eta\,,\ \rho_\eta^{-1}\nabla p_\eta = \chi_\eta\,. \tag{54}$$

We proceed with the asymptotic analysis by considering the ansatz:

$$\begin{aligned} p_\eta(x) &= p_0(\mathbf{x},\mathbf{x}/\eta) + \eta p_1(\mathbf{x},\mathbf{x}/\eta) + \cdots, \\ \chi_\eta(x) &= \chi_0(\mathbf{x},\mathbf{x}/\eta) + \eta\chi_1(\mathbf{x},\mathbf{x}/\eta) + \cdots, \end{aligned} \tag{55}$$

where the pairs (p_j, χ_j) of successive terms for the ansatz of the pressure field and its gradient (flux) are periodic with respect to the second variable.

In [116], (55) are plugged into (54) and the following homogenized macroscopic equation is then deduced

$$\nabla_{\mathbf{x}} \cdot [\rho_{\text{hom}}^{-1} \nabla_{\mathbf{x}} (\kappa_{\text{hom}} p_{\text{hom}})] + k^2 p_{\text{hom}} = 0 \,, \tag{56}$$

where the effective density can be expressed as:

$$\rho_{\text{hom}} = \rho_e \int_{Y \setminus S} (1 + A_{\text{hom}}(\mathbf{y}))\, \mathrm{d}\mathbf{y} \,. \tag{57}$$

with $A_{\text{hom}}(\mathbf{y}) = \nabla_{\mathbf{y}} \psi_j$ where the ψ_j, $j = 1,2,3$, are solutions (defined up to an additive constant) of the annex problem:

$$\Delta_{\mathbf{y}} \cdot \psi_j = 0 \text{ in } Y \setminus S \,, \; \mathbf{n} \cdot \nabla_{\mathbf{y}} \psi_j = -n_j \text{ on } \partial S \,, \tag{58}$$

with $\mathbf{n} = (n_1, n_2, n_3)$ the unit outward normal to ∂S.

Thus far, there is no real surprise in the effective model, as it has been known for over four decades now that the homogenization of periodic structures brings some artificial anisotropy in various physical contexts, see e.g. [117, 118] for Maxwell's equations, that have been extended to the bianisotropic and chiral cases [119–121] for which correspondences can be drawn with elasticity equations [122, 123].

However, the expression for the effective parameter κ_{hom} that appears in (56) is given by

$$\kappa_{\text{hom}}^{-1}(k) = 1 - k^2 \sum_{n=1}^{\infty} \frac{1}{k^2 - k_n^2} \left(\int_Y \phi_n(\mathbf{y})\, \mathrm{d}\mathbf{y} \right)^2 \,, \tag{59}$$

and one notes it is frequency dependent and can take negative values near resonances k_n. These Mie resonances that appear as flat bands (often seen in the close frequency neighborhood of a band with vanishing group velocity at the Γ point in figure 8) are associated with an eigenvalue problem posed on the sphere S: in order to draw the function $\kappa_{\text{hom}}^{-1}(k)$ in (59), one looks for eigenvalues and orthonormal eigenfunctions (k_n, ϕ_n), $n \geqslant 1$, satisfying the following Laplace eigenvalue problem with homogeneous Dirichlet boundary conditions:

$$\nabla^2 \phi + k^2 \rho_r \phi = 0, \text{ in } S, \; \phi = 0, \text{ on } \partial S. \tag{60}$$

This function $\kappa_{\text{hom}}^{-1}(k)$ in (59) was first introduced in the context of high-contrast homogenization theory by Zhikov [124, 125], and then applied to artificial magnetism in high-contrast dielectric crystals by Bouchitté and Felbacq [116]. We further point out some earlier work by Auriault on high-contrast homogenization in the context of the heat [126], and elasticity [127–129], equations.

The effective parameter κ_{hom} takes negative values inside the stop band of the periodic structure, so in the frequency range between 0.28 and 0.3 Hz in figure 8. Indeed, (56) only has propagating solutions when κ_{hom} is positive.

One can similarly derive a high-contrast version of (37) and (38), see [130, 131] for a comprehensive derivation. Such dynamic effects in the low frequency homogenization regime can be observed in highly anisotropic fibres and in reinforced

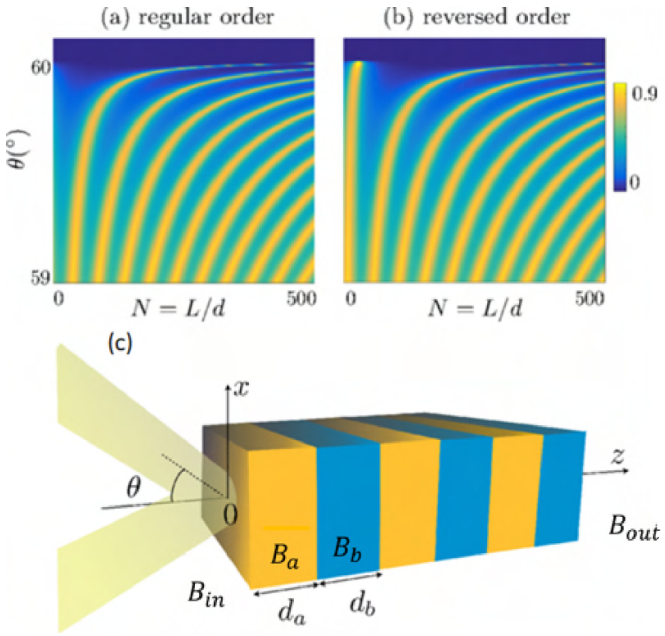

Figure 9. Discrete transmission spectra for a plane pressure wave propagating in a fluid with density ρ_{in} and compressibility B_{in} incident upon a stack of fluidic layers with identical density $\rho = \rho_{\text{in}}$ and an alternation of compressibilities (a) $B_a = 1/5 B_{\text{in}}$, $B_b = B_{\text{in}}$ and (b) for the reversed order $B_a = B_{\text{in}}$, $B_b = 1/5 B_{\text{in}}$. (c) Schematics of the layered fluid of finite length along the z direction. The structured fluid is embedded in a fluid with $B_{\text{in}} = B_{\text{out}}$ and $\rho_{\text{in}} = \rho_{\text{out}}$ corresponding to regular order (a). The multilayer structure is illuminated by the plane wave near the critical angle of total reflection ($d = d_a + d_b$ is the period). The length of the stack of layers is $L = Nd$ and it varies with d increment, N being an integer. The discrepancy in transmission for cases (a) and (b) is noted when N is small i.e. when the number of cells is small, and is attributed to boundary layer effects. Note that the same spectra would be obtained in the regular and reversed orders for structures starting with an half layer of fluid a or b. Reprinted (figure) with permission from [147], Copyright (2018) by the American Physical Society.

fibres in elasticity [132–141]. We note that the homogenization formalism for disordered crystal described in section 3.1.3 can be adapted to the high-contrast case (aka double porosity), and it similarly leads to dispersive effective parameters. Some general mathematical framework can also be found in [142].

On the other hand, it is well known that truncation of a periodic structure has an impact on its dynamic effective properties, see e.g. [143–147]. Such finite size effects of periodic structures appear both in scattering, and eigenvalue, problems. Section 3.1.6 presents high-order homogenization for a scattering problem. This is yet another way to achieve frequency dependent effective parameters. This does not require some high contrast in material parameters, but this requires higher order asymptotic corrections as we shall now see.

3.1.6. High-order homogenization. There is a vast literature on the importance of finite size effects for effective medium parameters of periodic structures in scattering problems, see e.g. [146–153].

We note in figure 9 that the transmission properties of a scalar pressure wave highly depend upon the incident angle

of the wave incident on the layered fluid, as well as on the order upon which one assembles layers in the finite stack. It is deduced from asymptotic homogenization, see appendix A in [147], that the effective medium associated with the stack of layers in figure 9 is accurately described by

$$\left\{\begin{array}{l} \Delta P+\omega^2\rho B_{\rm eff}^{-1}(k)P=0\,,\\ \frac{\partial P}{\partial z}(x,0^+)-\frac{\partial P}{\partial z}(x,0^-)=\omega^2\rho d B_{\rm int}^{-1}P(x,0)\,,\\ \frac{\partial P}{\partial z}(x,L^+)-\frac{\partial P}{\partial z}(x,L^-)=\omega^2\rho d B_{\rm out}^{-1}P(x,L) \end{array}\right. \tag{61}$$

where L is the structure extent and d is the thickness of the periodic cell. The effective bulk modulus is given by

$$B_{\rm eff}^{-1}(k)=\langle B^{-1}\rangle+\frac{\omega^2}{12}\rho(B_a^{-1}-B_b^{-1})^2\frac{d_a^2d_b^2}{d^2} \tag{62}$$

where $d=d_a+d_b$ and

$$\langle B^{-1}\rangle=\frac{d_aB_a^{-1}+d_bB_b^{-1}}{d}\,. \tag{63}$$

The importance of the dynamic correction to the usual effective medium formula which assumes $\omega=0$ (so-called quasi-static approximation) has been experimentally studied in [154].

Obviously, the high-order homogenized problem (61) is different if we consider a fluid with varying density ρ instead of compressibility B. In that case, one gets some anisotropic effective density with a dynamic correction. Similarly, the high-order homogenization of a stack of elastic layers with same configuration as in figure 9 has been performed in [155, 156] and it leads to the following homogenized equation of the Willis type:

$$C_{ijkl}^{\rm eff}\frac{\partial^2u_l}{\partial x_i\partial x_k}+{\rm i}\omega(S_{ijl}^{\rm eff}-S_{ilj}^{\rm eff})\frac{\partial u_l}{\partial x_i}+\omega^2\rho_{jl}^{\rm eff}u_l=0\,, \tag{64}$$

with $C^{\rm eff}$ the effective rank-4 elasticity tensor, $S^{\rm eff}$ the effective rank-3 coupling Willis tensor and $\rho^{\rm eff}$ the rank-2 effective density tensor. The expressions of the (symmetric) tensors in (64) depend upon the frequency and wavenumber and can be found in [155, 156]. Importantly, in the zero frequency limit, the effective coupling tensor $S^{\rm eff}$ vanishes. The coupling coefficients that relate particle momentum and stress are unknown in standard Cauchy models of solids. The Willis coupling tensor plays the similar role to the magneto-optic tensor for bianisotropic media [148]. Such correspondences between equations of electromagnetics and elastodynamics have proved extremely fruitful in the development of graded metamaterials, as we shall see in section 5.

Effect of weak disorder [157] and quasi-periodicity [158] have been studied for effective medium parameters of scattering problems. Finite size effects on effective properties play also a prominent role in the context of chiral elastic metamaterials in the static regime [159], and some are discussed in section 4.1.5.

3.1.7. High-frequency homogenization. The homogenization models described thus far keep the wave frequency fixed, while the small parameter tends to zero, and thus the essence of the highly oscillating fields characteristic of higher Bloch modes associated with the second and higher bands in figure 8 cannot be captured. Whilst high-order homogenization allows one to asymptotically reconstruct the first (acoustic) band in figure 8 by adding corrective terms to the leading order homogenization, that encapsulate effective dispersion effect, it breaks down at the first stop band, see e.g. [160–162]. There is however a remedy to this pitfall. Back in 1926, the physicists Wentzel, Kramers and Brillouin independently developed the famous WKB method [163–165] (apparently unaware of the work of the British mathematician Jeffreys [166]) to approximate solutions of linear partial differential equations such as the Schrodinger equation in quantum mechanics. The WKB method has been employed notably to study wave propagation in waveguides with a slow variation compared to the wave wavelength in [167, 168]. This slow variation allows for the appearance of localized eigenstates unveiled by an asymptotic analysis rooted in WKB theory [169–172]. Multi-layered acoustic and elastic waveguides with a slow variation along their main axis have also been studied in a series of papers [173–176] that did not make the connection with asymptotic methods for high-frequency waves in infinite perfectly periodic media introduced in [67] in conjunction with Floquet–Bloch theory. Indeed, when an otherwise perfectly periodic lattice is perturbed, it is well known from chemists, engineers and applied physicists [177–192] as well as theoretical physicists and applied mathematicians [193–206], that some strongly localized defect states can occur in diverse physical systems, these defect states exponentially decay with distance from the defect. In wave systems, this behavior bears some resemblance with the trapped modes observed in a slowly varying waveguide. This similarity was actually exploited in a theory of high frequency homogenization proposed in [207], wherein the complete spectrum of Bloch modes, can be captured by an asymptotic theory by scaling the wave frequency as the inverse of the small parameter (and thus considering the high-frequency regime). Even at leading order, fields oscillate on the microscale, which motivate a WKB ansatz in the classical textbook by Bensoussan *et al* [67]. Intuitively, this does not play well with what homogenization should do. However, for fields oscillating at the microscale, the variation of the solution from one periodicity cell to the next can be very small. High-frequency homogenization (aka homogenization near a neighborhood of an edge gap in the context of approximation of operator resolvent [208, 209]) was developed to model such a situation. One wishes to replace the complex microstructured medium with an effective (possibly anisotropic and nonlocal) medium even when the wavelength and microstructure are of similar scales. We shall see that HFH can not only reproduce dispersion curves asymptotically, but also obtain envelope functions of the resulting fields and treat localized defect modes and other features due to local non-periodic material changes or boundaries, with these effects coming through in extra forcing terms within the continuum partial differential equations and effective boundary conditions. We start with a

doubly periodic structure made of a square lattice of identical cells (the case of a triply periodic structure carries through *mutatis mutandis*). The square periodic cell contains a hole and its sidelength is $2l$ (assumption of equal length lattice vectors and a square lattice can be removed). The periodic cell defines the length scale for the micro-scale of the structure. A metamaterial sample can be made of many hundreds of such elementary cells. We introduce a macro-scale length denoted by L which is a characteristic overall dimension of the metamaterial sample: The ratio of these scales, $\eta \equiv l/L$, is assumed to be small, see also figure 5. Each cell is identical in geometry and the material within each cell is characterized by two periodic functions, in $\boldsymbol{\xi} \equiv (x_1/l, x_2/l)$, namely $a(\boldsymbol{\xi})$ and $\rho(\boldsymbol{\xi})$; for instance, these are shear modulus (stiffness) and density for anti-plane shear waves in isotropic heterogeneous solids.

3.1.7.1. Acoustic case. We consider the scalar wave equation, with a time harmonic dependence $\exp(-i\omega t)$, ω being the angular wave frequency. We further non-dimensionalize physical parameters as follows: $a \equiv a_0 \hat{a}(\boldsymbol{\xi})$, $\rho \equiv \rho_0 \hat{\rho}(\boldsymbol{\xi})$ and $\mathbf{x} = l\hat{\mathbf{x}}$ where $c_0 = \sqrt{a_0/\rho_0}$ is the characteristic wave speed. This leads to the resulting equation of study where the hat decoration has been removed:

$$l^2 \nabla_{\boldsymbol{x}} \cdot [a(\boldsymbol{\xi}) \nabla_{\boldsymbol{x}} u(\boldsymbol{x})] + \Omega^2 \rho(\boldsymbol{\xi}) u(\boldsymbol{x}) = 0, \tag{65}$$

with $\Omega = \frac{\omega l}{c_0}$, on $-\infty < x_1, x_2 < \infty$, Ω is the non-dimensional frequency and u is the out-of-plane displacement in elasticity. The two scale nature of the problem is incorporated using the small and large length scales to define two new independent coordinates namely $\mathbf{X} = \boldsymbol{x}/L$, and $\boldsymbol{\xi} = \boldsymbol{x}/l$. Equation (65) then becomes,

$$\begin{aligned} &\nabla_{\boldsymbol{\xi}} \cdot [a(\boldsymbol{\xi}) \nabla_{\boldsymbol{\xi}} u(\mathbf{X}, \boldsymbol{\xi})] + \Omega^2 \rho(\boldsymbol{\xi}) u(\mathbf{X}, \boldsymbol{\xi}) \\ &\quad + \eta [2a(\boldsymbol{\xi}) \nabla_{\boldsymbol{\xi}} + \nabla_{\boldsymbol{\xi}} a(\boldsymbol{\xi})] \cdot \nabla_{\mathbf{X}} u(\mathbf{X}, \boldsymbol{\xi}) \\ &\quad + \eta^2 a(\boldsymbol{\xi}) \nabla^2_{\mathbf{X}} u(\mathbf{X}, \boldsymbol{\xi}) = 0. \end{aligned} \tag{66}$$

Standing waves occur when there are periodic (or anti-periodic) boundary conditions across the elementary cell (in the $\boldsymbol{\xi}$ coordinates) and these standing waves encode the local information about the multiple scattering that occurs by the neighboring cells. The asymptotic technique is then a perturbation about these standing wave solutions. As these are associated with periodic and anti-periodic boundary conditions, which are respectively in-phase and out-of-phase waves across the cell, the conditions in $\boldsymbol{\xi}$ on the edges of the cell, ∂S_1, are known:

$$u|_{\xi_i=1} = \pm u|_{\xi_i=-1} \quad \text{and} \quad u_{,\xi_i}|_{\xi_i=1} = \pm u_{,\xi_i}|_{\xi_i=-1}, \tag{67}$$

where the subscript $,\xi$ denotes partial derivatives with respect to the variable ξ and with the $+,-$ for periodic or anti-periodic cases respectively. We now pose an ansatz for the field and the frequency,

$$\begin{aligned} u(\mathbf{X}, \boldsymbol{\xi}) &= u_0(\mathbf{X}, \boldsymbol{\xi}) + \eta u_1(\mathbf{X}, \boldsymbol{\xi}) + \eta^2 u_2(\mathbf{X}, \boldsymbol{\xi}) + \ldots, \\ \Omega^2 &= \Omega_0^2 + \eta \Omega_1^2 + \eta^2 \Omega_2^2 + \ldots \end{aligned} \tag{68}$$

The $u_i(\mathbf{X}, \boldsymbol{\xi})$'s adopt the boundary conditions (67) on the edge of the cell. An ordered set of Equations emerge indexed with their respective power of η, and are treated in turn, see [207]:

$$\frac{\partial}{\partial \xi_i}\left(a \frac{\partial}{\partial \xi_i} u_0\right) + \Omega_0^2 \rho u_0 = 0, \tag{69}$$

$$\begin{aligned} \frac{\partial}{\partial \xi_i}\left(a \frac{\partial}{\partial \xi_i} u_1\right) + \Omega_0^2 \rho u_1 = &-\frac{\partial}{\partial X_i}\left(2a \frac{\partial}{\partial \xi_i} u_0 + u_0 \frac{\partial}{\partial \xi_i} a\right) \\ &- \Omega_1^2 \rho u_0, \end{aligned} \tag{70}$$

$$\begin{aligned} \frac{\partial}{\partial \xi_i}\left(a \frac{\partial}{\partial \xi_i} u_2\right) + \Omega_0^2 \rho u_2 = &-a \frac{\partial^2}{\partial X_i^2} u_0 \\ &- \frac{\partial}{\partial X_i}\left(2a \frac{\partial}{\partial \xi_i} u_1 + u_1 \frac{\partial}{\partial \xi_i} a\right) \\ &- \Omega_1^2 \rho u_1 - \Omega_2^2 \rho u_0. \end{aligned} \tag{71}$$

The leading order equation (69) does not depend upon the slow, long scale, variable $\mathbf{X}$. Physically, its solution is a standing wave on the periodic cell, with eigenfrequency Ω_0 with associated eigenmode consisting of a fast oscillating function $U_0(\boldsymbol{\xi}; \Omega_0)$, modulated by a long scale function $f_0(\mathbf{X})$:

$$u_0(\mathbf{X}, \boldsymbol{\xi}) = f_0(\mathbf{X}) U_0(\boldsymbol{\xi}; \Omega_0). \tag{72}$$

To keep things simple, we assume isolated eigenfrequencies (repeated eigenvalues will be dealt with in the sequel). The overarching goal is to derive a partial differential equation with an effective (matrix valued) coefficient for the unknown f_0 at the macroscopic scale. However, unlike for low frequency homogenization, coefficients are integrated, not averaged, quantities and in this way the microscopic scale is restored.

3.1.7.2. Elastic case. Before we proceed with the derivation of the long scale, high-frequency, effective equation for the unknown f_0, we would like to present the elastic counterpart of the acoustic case. We consider a linear isotropic elastic medium with the Cauchy stress (see (2)) related to the elastic displacements via the constitutive relation

$$\sigma_{ij} = \mu\left(\frac{\partial}{\partial x_j} u_i + \frac{\partial}{\partial x_i} u_j\right) + \lambda \delta_{ij} \frac{\partial}{\partial x_k} u_k. \tag{73}$$

with $\mathbf{x} = (x_1, x_2)$ and μ, λ the Lamé parameters and $,x_j$ denoting differentiation with respect to variable x_j.

We consider the elastodynamic wave equation (8), with a time-harmonic dependence $\exp(-i\Omega t)$ assumed, and thus

$$\frac{\partial}{\partial x_j} \sigma_{ij} + \rho \Omega^2 u_i = 0, \tag{74}$$

with ρ the density. To identify the high-frequency effective medium description of the periodic structure we follow the methodology given in [210]. From the microscopic and macroscopic scale separation, we deduce the leading order solution

$$u_{0_i} = f_0(\mathbf{X}) U_{0_i}(\boldsymbol{\xi}; \Omega_0). \tag{75}$$

wherein $U_{0_i}(\boldsymbol{\xi};\Omega_0)$ depends only on the fast (microscopic) variable. This short-scale, fast oscillating, displacement field U_{0_i} is modulated by a long-scale, unknown, scalar function $f_0(\mathbf{X})$. We stress that $U_{0_i}(\boldsymbol{\xi};\Omega_0)$ is different for each standing wave frequency Ω_0. It might seem counter-intuitive to consider a scalar function f_0 in (75) and one could opt for two different scalar functions f_{0_1}, f_{0_2} multiplying each displacement field U_{0_1} and U_{0_2}. In a potential formulation, f_{0_1}, f_{0_2} would stand for the shear and compressional potentials, and this seems a natural thing to do. However, upon inspection for self-consistency one finds that $f_{0_1} = f_{0_2}$.

Going back to (73), from the microscopic displacement, U_{0_i}, we define a stress field $S_{0_{ij}}(\boldsymbol{\xi};\Omega_0)$ as

$$S_{0_{ij}} = \mu\left(\frac{\partial}{\partial\xi_j}U_{0_i} + \frac{\partial}{\partial\xi_i}U_{0_j}\right) + \lambda\delta_{ij}\frac{\partial}{\partial\xi_k}U_{0_k} \tag{76}$$

and deduce the leading order counterpart of (74)

$$\frac{\partial}{\partial\xi_j}S_{0_{ij}} + \rho\Omega_0^2 U_{0_i} = 0 \tag{77}$$

for the microscopic scale. This equation can be solved, subject to some boundary conditions, to extract the displacements U_{0_i} and stresses $S_{0_{ij}}$; some illustrative example are given in the section on Bloch dispersion curves.

As in the earlier sections, one moves up the hierarchy of equations arriving at a solvability equation for the longscale function [207] as

$$\begin{aligned}
&\frac{\partial^2}{\partial X_k\partial X_j}f_0\int_S \mu\Bigg(U_{0_i}\left(\frac{\partial}{\partial\xi_j}U_{1_{ik}} + \frac{\partial}{\partial\xi_i}U_{1_{jk}}\right)\\
&\quad - U_{1_{ik}}\left(\frac{\partial}{\partial\xi_j}U_{0_i} + \frac{\partial}{\partial\xi_i}U_{0_j}\right)\\
&\quad + \lambda\left(\frac{\partial}{\partial\xi_i}U_{1_{ik}}U_{0_j} + U_{0_k}U_{0_j} - U_{1_{kj}}\frac{\partial}{\partial\xi_i}U_{0_i}\right)\Bigg)\mathrm{d}S\\
&\quad + \frac{\partial^2}{\partial X_j^2}f_0\int_S \mu U_{0_i}U_{0_i}\mathrm{d}S + \frac{\partial^2}{\partial X_i\partial X_j}f_0\int_S \mu U_{0_i}U_{0_j}\mathrm{d}S\\
&\quad + f_0\Omega_2^2\int_S \rho U_{0_i}U_{0_i}\mathrm{d}S = 0.
\end{aligned} \tag{78}$$

One notes the presence of rank-2 tensor functions $U_{1_{ij}}$ arising from the first order solution $u_{1_i} = \frac{\partial}{\partial X_j}f_0(\mathbf{X})U_{1_{ij}}(\boldsymbol{\xi};\Omega_0)$. The important point about the solvability equation is that the short-scale is completely absent, it has been integrated out and is encapsulated within coefficients of a rank-2 tensor T_{ij} in

$$T_{ij}\frac{\partial^2 f_0}{\partial X_i\partial X_j} + \Omega_2^2 f_0 = 0. \tag{79}$$

We will verify this using non-trivial examples later where we use equation (79) to find asymptotic dispersion curves for perfectly periodic Floquet–Bloch problems and compare with full numerical solutions. We stress that we have reduced the complexity of the elasticity problem described by (73) and (74) to solving the scalar PDE (79). If we were to perform our analysis in a three-dimensional elastic periodic setting (e.g. a cubic array of rigid or traction-free spheres), the derivation of (79) would apply *mutatis mutandis* with i,j ranging from 1 to 3 and the Bloch vector now describing the edges of a tetrahedron. Similar theories for long wave wavelength near cut-off frequencies in elastic composite materials have been independently developed by Nemat-Nasser *et al* [211], and by Boutin *et al* [212, 213], that also produce dynamic effective elastic parameters at high-frequencies.

3.1.7.3. Long wave zero frequency limit. It is well known [67, 199, 214] that the slope of the lowest dispersion curve near the origin (i.e. in the neighborhood of the Γ point of the irreducible Brillouin zone), such as shown in figure 8, leads to the quasi-static effective medium description of a periodic structure. Assuming some traction free boundary conditions on the holes of the periodic structure, allows wave propagation at frequencies of the order of $\Omega^2 \sim O(\eta^2)$. However, assuming clamped boundary conditions is fundamentally different since the periodic structure now exhibits a zero-frequency stop-band such as shown in figure 10. This disallows a long-wave low frequency solution, that persists in the limit of asymptotically small clamped inclusions [210, 215, 216], and this has potential applications in shielding elastic waves of very long wavelengths (e.g. seismic waves) [217]. This is known as the problem of non-commuting limits for the acoustic band in the physics community [218] and a singularly perturbed problem in the applied mathematics community [132, 133, 219–223]. Physicists consider there is a competition between the limits taken for a vanishing Bloch wavenumber in the reciprocal space and an increasing contrast between material parameters within inclusions and surrounding medium when studying the quasi-static limit in a band diagram associated with a periodic structure with clamped inclusions such as in figure 10. Applied mathematicians point out that the asymptotic model for clamped inclusions can be recast as a PDE with the small parameter factor of a Laplacian of a highly oscillating function, in which case the small parameter cannot be approximated by setting its value to zero. As a salient consequence the homogenized solution for such a singularly perturbed problem cannot be uniformly approximated by the usual asymptotic expansion (36). We refer the reader to a comprehensive literature in [224–228] for asymptotic expansions devoted to singularly perturbed problems arising in physical and engineering sciences.

However, if the periodic structure consists of traction-free inclusions, the leading order equation emerging from the long wave zero frequency limit of HFH, is $\sigma_{ij,\xi_j} = 0$ and it admits two independent solutions for $u_i = f_0^{(l)}(\mathbf{X})U_{0_i}^{(l)}$, with $U_{0_i}^{(l)}$ being constants. These constant solutions are plugged back into the first order equation to yield $\Omega_1 = 0$. One can then solve for $u_{1_i} = f_{0,X_j}^{(l)}U_{1_{ij}}^{(l)}$ where the first order equation is the same as the leading order with the boundary conditions replaced by $\sigma_{1_{ij}}n_j = 0$. Finally Ω_2 is obtained and using that $\Omega_0 = \eta\Omega_2$ provides the linear asymptotics for the lowest bands around the Γ point (for a doubly periodic structure, there are two distinct acoustic branches for pressure (P) and shear (S) in-plane elastic waves due to their different wavespeed, unlike for the

Table 1. The first seven standing wave frequencies for a square cell with clamped holes of radius $r = 0.4$ at wavenumber $\boldsymbol{\kappa} = (\pi/2, 0)$ at X, cf figure 10, together with associated values for T_{11} and T_{22}. The above coefficients are used in figure 12.

Ω_0	T_{11}	T_{22}
2.112	−0.1826	2.470
3.3317	1.6246	−2.4885
3.5485	−196.4900	−0.1476
3.6216	200.6397	−0.6115
4.3847	1.0742	4.9378
4.5952	−28.7271	4.0614
4.6258	27.4797	0.2967

anti-plane shear case that can be treated independently and has only one acoustic band see [134, 140, 141, 214, 229–233]).

3.1.7.4. Effective equation. Going back to macroscopic coordinates equation (78) provides us with the effective medium equation which is scalar irrespective of whether we consider anti-plane or in-plane elastic waves in the 2D case. This effective equation entails a bulk envelope wave propagation law for both scalar and vector elasticity

$$T_{ij}\frac{\partial^2}{\partial x_i \partial x_j} f_0 + \frac{\Omega^2 - \Omega_0^2}{l^2} f_0 = 0, \tag{80}$$

where $l = 1$ is the short characteristic length taken as half the length of a square cell. Rearranging terms in equation (80) leads to the effective wave velocity expressed as the tensor

$$c_{ij} = \frac{\Omega^2 l^2}{\Omega^2 - \Omega_0^2} T_{ij}, \tag{81}$$

within the effective equation

$$c_{ij}\frac{\partial^2}{\partial x_i \partial x_j} f_0 + \Omega^2 f_0 = 0. \tag{82}$$

One should note that (81) shows not only the dependence of the effective velocity on the T_{ij} coefficients, but also on the perturbation away from the standing wave. The effective medium is often strongly anisotropic elliptic (figure 11(a)) or even hyperbolic (figure 11(b)) causing the occurrence of highly directive effects.

3.1.7.5. Bloch dispersion curves. The spirit of HFH is that is allows for an effective medium description of a periodic structure at any frequency, so well beyond classical, low frequency, homogenization. In order to check the accuracy of the asymptotic algorithm, asymptotic dispersion curves are computed with HFH and compared against full numerical simulations performed with finite elements. This is done here for elasticity, and we consider normalized elastic Lamé parameters λ, μ as $2.3, 1$ respectively, and similarly for the density $\rho = 1$, in all of the following computations as typical material values. These are typical normalized parameters for elastic media with a Poisson ratio close to 0.35, for instance fused silica, which is drilled to fabricate photonic crystal fibres (with

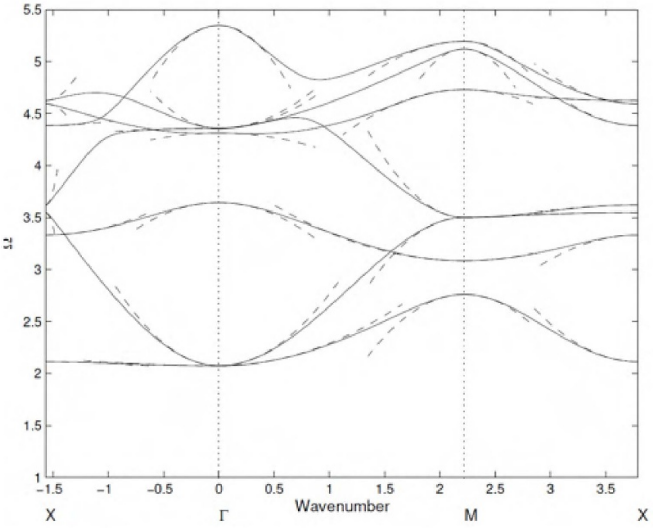

Figure 10. Bloch dispersion curves and HFH asymptotics for clamped cylinders of radius 0.4 in an elementary cell of side 2 The solid lines are from finite element numerical simulations and the dashed lines are from the HFH. Reprinted from [210], Copyright (2014), with permission from Elsevier.

physical units $\rho = 2.2 \times 10^3$ kg·m^{-3}, $\lambda = 31.15 \times 10^9$ Pa, $\mu = 16.05 \times 10^9$ Pa) [234, 235].

Typical Bloch dispersion curves, with both the HFH asymptotics (dashed lines) and numerical simulations from finite elements (solid lines) shown are plotted in figure 10 for vanishingly small cylindrical inclusions of radius 0.01 in a square array of side 2. This figure shows the appearance of a zero-frequency stop band, in common with Dirichlet inclusions in the acoustic/polarized electromagnetic analogues, see [216, 218]. There is no such cut-off for traction-free inclusions (not shown) that share features with the analogous Neumann case for out-of-plane elasticity at low frequencies, i.e. there is a low-frequency linear response when inclusions are not clamped. The zero-frequency stop-band behavior of the clamped inclusions completely derails the classical low frequency Bloch-wave homogenisation approach of effective media that requires low frequencies and long waves and the microstructured medium to produce some effective parameters. As can be seen in figure 10, HFH solves the conundrum of non-commuting limits [218, 220] as its asymptotics accurately represent the dispersion curves close to the edges of the Brillouin zone for clamped holes, including at the Γ point for the lowest band.

It is remarkable that in figure 10 the HFH asymptotics (dashed lines) based upon the scalar f_0 equation capture the detailed behavior of the dispersion curves computed with finite elements for the full vector Navier system (solid lines). Besides from obvious advantages in terms of computational resources, the power of HFH is that it allows us to replace a microstructured medium by an effective dispersive medium (frequency and Bloch wavenumber dependent) well beyond the quasi-static limit. Thanks to HFH, elastic properties of the periodic structure are encapsulated at all frequencies within the coefficients T_{ij} in the PDE for f_0 (or by the coefficients in the coupled cases of repeated roots). The

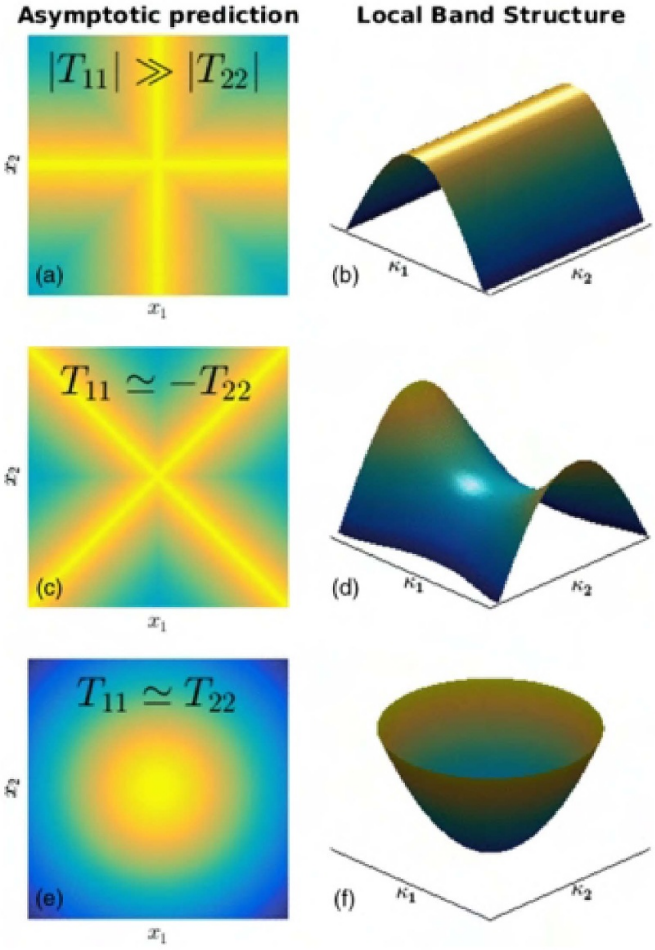

Figure 11. Asymptotic prediction of the local mode structure and respective dispersion surfaces: Coefficients of effective tensor govern the parabolic ($|T_{11}| \gg |T_{22}|$), hyperbolic ($T_{11}T_{22} < 0$), or elliptic ($T_{11}T_{22} > 0$) character of equation (80) and capture the extreme anisotropic features of waves propagating within a doubly periodic medium shown in (a), (c) and (e). The corresponding local dispersion surfaces are shown in (b), (d) and (f). Reprinted (figure) with permission from [236], Copyright (2017) by the American Physical Society..

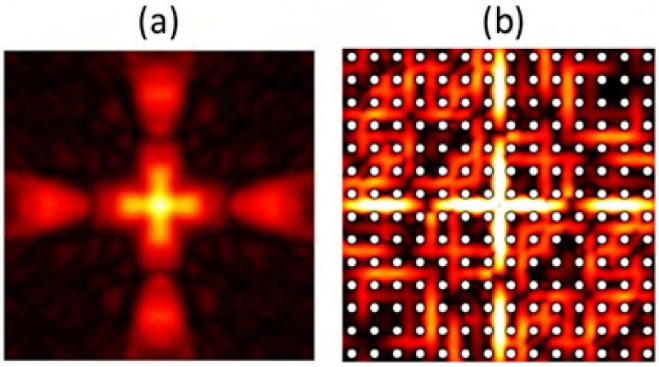

Figure 12. Directive emission in horizontal and vertical directions, caused by a point compressive source at frequency $\Omega = 2.19$, in a doubly periodic array of square cells with circular holes of radius $r = 0.4$, clamped at their surface. See figure 10 first band at point X. Panel (b) shows FEM calculations and panel (a) reproduces the effects by HFH with $T_{11} = -0.18255$ and $T_{22} = 2.46973$ (see table 1). Effective equation (80) has a parabolic character since $|T_{11}| \ll |T_{22}|$, and wavefield pattern is consistent with panels (a) and (b) in figure 11. Reprinted from [210], Copyright (2014), with permission from Elsevier.

parabolic ($|T_{11}| \gg |T_{22}|$), hyperbolic ($T_{11}T_{22} < 0$), or elliptic ($T_{11}T_{22} > 0$) character of equation (80) then guides one to anticipate or predict particular features such as some highly-directional wave patterns in figure 12. The cross effect is predicted by the T_{ij} coefficients where one is of order one while the other is nearly null and vice versa, depending on which point of the Brillouin zone is considered, $X(\pi/2, 0)$ or $\Gamma(0, \pi/2)$. Some of the dispersion curves nearly touch in figure 10, in which case a refined asymptotic ansatz need be implemented, that can be found in [237, 238], and also in a precursor study on long-wave high-frequency motion of elastic layers [239].

3.1.7.6. Elastic plates [236]. High-frequency homogenization has been developed for various periodic wave systems, including thin elastic plates, within which propagation of flexural waves is governed by the fourth-order Kirchhoff–Love equation [240]. Unexpectedly, the effective equation is again (80). Some experiments have been led for flexural waves in a Duraluminium plate clamped with screws on a square periodic lattice with [236]. Although the clamped area is localized to the pin positions, the screws are not precisely pointlike as pins, and so their clamping area is accounted for in the theory. Wavefield pattern predicted by HFH at , and confirmed by finite difference time domain simulations, see figure 13.

HFH has proved to be a useful tool to help design topological insulators for elastic thin plates [241, 242]. Extension to non-linear interface models are desirable as HFH might be employed to greatly simplify the numerical models [243].

There is ongoing work on extension of HFH to quasi-crystals using the same approach of irrational (cut-and-project) operators as for the low frequency case discussed in section 3.1.4. Development of HFH for quasi-periodic media may have an important impact in the elastic metamaterial community. Indeed, it has been numerically established in [114] that highly non trivial rational approximants of certain quasiperiodic mechanical metamaterials can display simultaneously chiral and isotropic features in the homogenization regime (see section 4.1.1).

Periodic and quasi-periodic media can be considered as members of a larger class of random media. Homogenization theory for random media is a well developed field of mathematics that can be performed within some asymptotic framework similar to what we have discussed in section 3.1.3 in the tracks of [92]. Adapting to HFH [92] would require considering some larger and larger cell (whose size tends to infinity) with boundary conditions as in (67). Thus, numerically one would solve the problem on a large enough cell (hence with some truncation error to estimate). However, there are powerful mathematical tools from measure and probability theory that can handle very complex homogenization problems, and we refer to [69, 244, 245] and references therein.

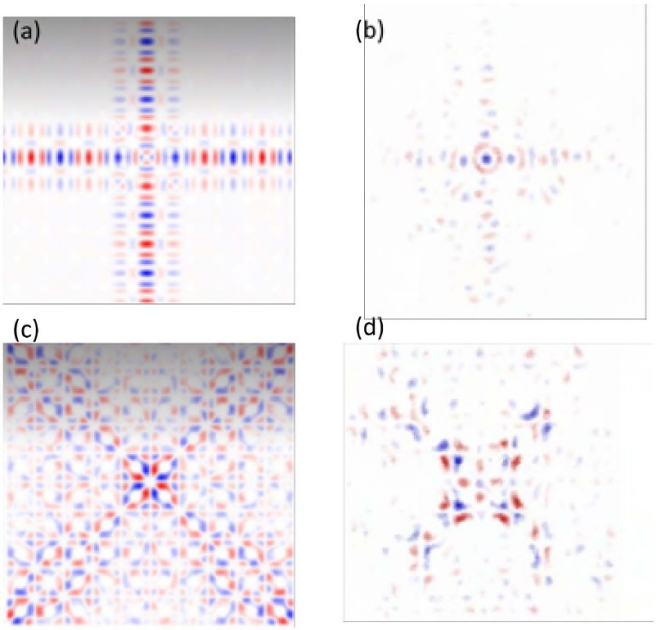

Figure 13. Comparison between HFH (left) and experiments (right): snapshots of flexural wavefield evolution from a pulse excitation at the center of a periodically pinned Duraluminiun plate, with central frequency Ω given by HFH when equation (80) has a parabolic character (a), (b) and an hyperbolic character (c) and (d). Note tha similarity between (a) and (c) and same in figure 11. Reprinted (figure) with permission from [236], Copyright (2017) by the American Physical Society.

Finally, it would be interesting to develop an HFH theory for high-contrast media. Indeed, low frequency homogenization for high-contract periodic structures as discussed in section 3.1.5 only works near resonances. This corresponds to frequencies close to flat bands, for a Bloch wavenumber at the high-symmetry point Γ in figure 8 (with no phase-shift in the periodic cell). It would be useful to understand the nature of the effective medium for other frequencies and Bloch wavenumbers in order to better exploit the physics of such high-contrast phononic crystals. Extending HFH to absorptive, dispersive and visco-elastic periodic structures [246–252] is also highly desirable, and similarly for quasi-periodic structures. HFH has been also implemented in the context of transient [243] and travelling [253] waves. There is actually a renewed interest in the interplay between space and time in dynamic metamaterials as we shall now see.

3.1.8. Space-time homogenization. Thus far, homogenization was merely concerned with some periodicity, or quasi-periodicity, of the space variables. There is however, another important class of metamaterials, known as space-time media. As is fairly usual in physics, such space-time media were introduced quite a while back, but it is only recently that researchers started to realize the full extent of their capabilities. Let us look at what we can achieve in terms of effective properties, when there is periodicity not only in space but also in the time variable.

3.1.8.1. Acoustic case. We now consider a sequence of acoustic hyperbolic problems depending upon the small positive parameter η in the following way: One considers a displacement field u_η which is a function on $\mathbb{R}\times[0,T]$ solution of

$$\begin{cases} \frac{\partial}{\partial x}\left(a(\frac{x-c_1t}{\eta})\frac{\partial}{\partial x}u_\eta(x,t)\right) \\ -\frac{1}{c^2}\frac{\partial}{\partial t}\left[\rho(\frac{x-c_1t}{\eta})\frac{\partial}{\partial t}u_\eta(x,t)\right]=0 \\ u_\eta(x,0)=\overline{u}_\eta(x) \end{cases} \tag{83}$$

where c and $a(\frac{x-c_1t}{\eta})$ and $\rho(\frac{x-c_1t}{\eta})$ respectively denote the speed of sound in air, the stiffness and density in the space-time layered medium, which is subject to a periodic modulation of speed c_1. In other words, the stiffness a and the density ρ are 1 periodic functions of x and they are $1/c_1$ periodic functions of t. This model might be debatable from a physical standpoint [254], but parameters a and ρ could alternatively be replaced by the shear modulus and inverse of bulk modulus, respectively, in the context of anti-plane shear elastic waves [255, 256].

From now on we assume a normalized wavespeed $c=1$ $\mathrm{m}\cdot\mathrm{s}^{-1}$ in (83) and we consider the following ansatz for the displacement field

$$\begin{aligned} u_\eta(x,t)=u_0\left(x,t,\frac{x-c_1t}{\eta}\right)+\eta u_1\left(x,t,\frac{x-c_1t}{\eta}\right) \\ +\eta^2u_2\left(x,t,\frac{x-c_1t}{\eta}\right)+\cdots \end{aligned} \tag{84}$$

where $u_i(x,t,\cdot)$ is 1-periodic in $\mathbb{R}$.

We consider the coordinate system $(y,x_2,x_3,t)=(x_1-c_1t,x_2,x_3,t)$, in the moving frame attached to the modulated medium. We note that the partial derivatives in the moving frame can be expressed as $(\partial_x,\partial_t)=(\partial_y,-c_1\partial_y+\partial_t)$.

In a way similar to what is usually done for homogenization of unmodulated periodic media we replace the partial differential operator acting on the space x_1 variable by the two-scale operator $\frac{\partial}{\partial x}:=\frac{\partial}{\partial x}+\frac{c_1}{\eta}\frac{\partial}{\partial y}$, but moreover we do the same for the partial differential operator acting on the time variable t, so that $\frac{\partial}{\partial t}:=\frac{\partial}{\partial t}-\frac{c_1}{\eta}\frac{\partial}{\partial y}$. These two scale operators are combined with the asymptotic expansion of the displacement u_η. Assuming that the terms of the development of the powers higher than two are bounded, we can write:

$$\begin{aligned} &\eta^{-2}\left(\frac{\partial}{\partial y}a\frac{\partial}{\partial y}u_0-c_1^2\frac{\partial}{\partial y}\left[\rho\frac{\partial}{\partial y}u_0\right]\right) \\ &+\eta^{-1}\left(\frac{\partial}{\partial y}a\frac{\partial}{\partial y}u_1+\frac{\partial}{\partial y}a\frac{\partial}{\partial x}u_0+\frac{\partial}{\partial x}a\frac{\partial}{\partial y}u_0\right. \\ &\left.-c_1^2\frac{\partial}{\partial y}\left[\rho\frac{\partial}{\partial y}u_1\right]+c_1\frac{\partial}{\partial y}\rho\left[\frac{\partial}{\partial t}u_0\right]+c_1\frac{\partial}{\partial t}\rho\left[\frac{\partial}{\partial y}A_0\right]\right) \\ &+\eta^0\left(\frac{\partial}{\partial x}a\frac{\partial}{\partial x}u_0+2\frac{\partial}{\partial y}a\frac{\partial}{\partial x}u_1+\frac{\partial}{\partial y}a\frac{\partial}{\partial y}u_2-\frac{\partial^2}{\partial t^2}\left[\rho u_0\right]\right. \\ &\left.-c_1^2\frac{\partial^2}{\partial y^2}\left[\rho u_2\right]+2c_1\frac{\partial}{\partial y}\frac{\partial}{\partial t}\left[\rho u_1\right]\right)=o(\eta) \end{aligned} \tag{85}$$

In a neighborhood of $\eta=0$, we express the vanishing of the coefficients of successive powers of $\frac{1}{\eta}$ which leads to three equations.

The homogenized equation is (using $\langle . \rangle$ to write the mean)

$$\begin{aligned}
&\frac{\partial^2}{\partial t^2}u_0\left(c_1^2\left\langle\frac{1}{c_1^2-a\rho^{-1}}\right\rangle^2\left\langle\frac{\rho^{-1}}{c_1^2-a\rho^{-1}}\right\rangle^{-1}\right.\\
&\left.-\left\langle\frac{a}{c_1^2-a\rho^{-1}}\right\rangle\right)+2c_1\frac{\partial^2}{\partial t\partial x}u_0\left(\left\langle\frac{a\rho^{-1}}{c_1^2-a\rho^{-1}}\right\rangle\right.\\
&\left.\times\left\langle\frac{1}{c_1^2-a\rho^{-1}}\right\rangle\left\langle\frac{\rho^{-1}}{c_1^2-a\rho^{-1}}\right\rangle^{-1}-\left\langle\frac{a}{c_1^2-a\rho^{-1}}\right\rangle\right).\\
&+\frac{\partial^2}{\partial x^2}u_0\left(\left\langle\frac{a\rho^{-1}}{c_1^2-a\rho^{-1}}\right\rangle^2\left\langle\frac{\rho^{-1}}{c_1^2-a\rho^{-1}}\right\rangle^{-1}\right.\\
&\left.-c_1^2\left\langle\frac{a}{c_1^2-a\rho^{-1}}\right\rangle\right)=0
\end{aligned}\tag{86}$$

One can see that when $c_1>0$, the usual wave equation has some additional term mixing partial derivatives in space and time, that can be interpreted as a dissipative term, aka scalar Willis coupling [255] in acoustics and Fresnel drag in electromagnetics [257]. Note that both parameters entering the wave equation need be time-modulated to achieve non-reciprocal effects in the homogenization limit. Further note that with small adjustments, the above derivation follows through for the time-modulated heat equation, for which non-reciprocity is also achieved in the homogenization regime [258], and exciting effects such as asymmetric heat diffusion can be observed [259].

This problem was first addressed by Lurie back in 1997 [260]; Lurie wrote a comprehensive textbook on time modulated media [261]. Homogenization of a larger class of periodic multiscale space-time media has also been carried out [262–265]. Let us now move to the more involved case of the linear elasticity equations.

3.1.8.2. Elastodynamic case. We now consider the two-scale homogenization of the vector Navier system of a time-modulated layered medium. For this we need a fixed space-time Cartesian coordinate system $(\mathbf{x},t)=(x_1,x_2,x_3,t)$ and a time modulated layered periodic medium. The propagation is assumed along the direction x_1 of stacking of layers. In what follows, the subscript denotes dependence of the field upon the periodicity η in the space-time variable x_1-c_1t, where c_1 is the modulation speed along x_1. We mostly follow the same lines as the derivation of Nassar *et al* [266]. One considers a displacement field $\mathbf{u}_\eta$ which is a function on $\mathbb{R}^3\times[0,T]$ solution of

$$\begin{cases}\nabla\cdot\left[\mathbb{C}\left(\dfrac{x_1-c_1t}{\eta}\right):\nabla\mathbf{u}_\eta\right]=\dfrac{1}{c^2}\dfrac{\partial}{\partial t}\left[\rho\left(\dfrac{x_1-c_1t}{\eta}\right)\dfrac{\partial}{\partial t}\mathbf{u}_\eta\right],\\ \mathbf{u}_\eta(\mathbf{x},0)=\overline{\mathbf{u}}_\eta(\mathbf{x}),\end{cases}$$

where $\mathbb{C}(\frac{x_1-c_1t}{\eta})$ and $\rho(\frac{x_1-c_1t}{\eta})$ respectively denote the rank-4 elasticity tensor and density. These parameters are 1 periodic functions of x_1 and $1/c_1$ periodic functions of t.

From now on we assume that $\mathbb{C}_0=\mathbf{I}$ and by linearity of the Navier equations one can choose $\rho_0=1$. We consider the following ansatz for the vector displacement field

$$\begin{aligned}\mathbf{u}_\eta(\mathbf{x},t)=\mathbf{u}_0\left(\mathbf{x},t,\frac{x_1-c_1t}{\eta}\right)+\eta\mathbf{u}_1\left(\mathbf{x},t,\frac{x_1-c_1t}{\eta}\right)\\+\eta^2\mathbf{u}_2\left(\mathbf{x},t,\frac{x-c_1t}{\eta}\right)+\cdots\end{aligned}\tag{87}$$

where $\mathbf{u}_i(\mathbf{x},t,\cdot)$ is 1-periodic in $\mathbb{R}$.

The homogenized constitutive equations are, as first derived in [266],

$$\begin{aligned}\Sigma&=\mathbb{C}_{\text{eff}}:\nabla\mathbf{u}_0+\mathbf{S}^1_{\text{eff}}\cdot\frac{\partial}{\partial t}\mathbf{u}_0\\ \Pi&=\mathbf{S}^2_{\text{eff}}:\nabla\mathbf{u}_0+\rho_{\text{eff}}\cdot\frac{\partial}{\partial t}\mathbf{u}_0\end{aligned}\tag{88}$$

where the rank-4 homogenized elasticity tensor $\mathbb{C}_{\text{eff}}$, the rank-3 homogenized coupling Willis tensors $\mathbf{S}^1_{\text{eff}}$ and $\mathbf{S}^2_{\text{eff}}$ and the rank-2 homogenized density tensor are given by:

$$\begin{aligned}\mathbb{C}_{\text{eff}}&=\langle\mathbb{C}:\mathbf{n}\otimes\mathbf{M}\rangle\cdot\langle\mathbf{M}\rangle^{-1}\cdot\langle\mathbf{M}\otimes\mathbf{n}:\mathbb{C}\rangle\\&\quad-\langle\mathbf{C}:\mathbf{n}\otimes\mathbf{M}\otimes\mathbf{n}:\mathbb{C}\rangle+\langle\mathbb{C}\rangle\,,\\ \mathbf{S}^1_{\text{eff}}&=c_1\langle\mathbb{C}:\mathbf{n}\otimes\mathbf{M}\rangle\cdot\langle\mathbf{M}\rangle^{-1}\cdot\langle\rho\mathbf{M}\rangle\\&\quad-c_1\langle\rho\mathbb{C}:\mathbf{n}\otimes\mathbf{M}\rangle\,,\\ \mathbf{S}^2_{\text{eff}}&=-c_1\langle\rho\mathbf{M}\rangle\cdot\langle\mathbf{M}\rangle^{-1}\cdot\langle\mathbf{M}\otimes\mathbf{n}:\mathbb{C}\rangle\\&\quad+c_1\langle\rho\mathbf{M}\otimes\mathbf{n}:\mathbb{C}\rangle\,,\\ \rho_{\text{eff}}&=\langle\rho\rangle\mathbf{I}-c_1^2\langle\rho\mathbf{M}\rangle\cdot\langle\mathbf{M}\rangle^{-1}\cdot\langle\rho\mathbf{M}\rangle\\&\quad+c_1^2\langle\rho^2\mathbf{M}\rangle\,,\end{aligned}\tag{89}$$

which couple stress to velocity and momentum to strain, when the speed of modulation $c_1>0$.

The fact that (89) has the same structure as the Willis's equation (28) opens a door on non reciprocal wave phenomena via a different mechanism to that previously observed in non modulated metamaterials [267]. Also worth mentioning is the reiterated homogenization of the parabolic equation with fast oscillating diffusivity in space and time across different scales [262]. Indeed, space-time thermal metamaterials are or current interest [258, 259].

Thus far, we derived effective properties using some averaging and asymptotic techniques. However, for non-periodic structures, or dispersive/resonant periodic structures, solving the annex problem becomes more involved, or asymptotic homogenization might break down, and thus other effective medium approaches such as so-called parameter retrieval become handy.

3.1.9. Parameter retrieval. For centuries, people were knocking on, or shaking, opaque boxes to find out if they were full or empty. This very particular way of sending a signal onto

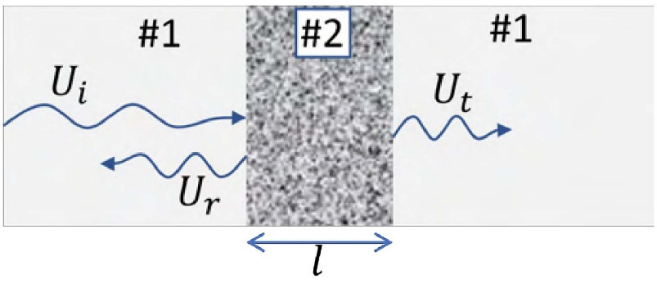

Figure 14. Reflection and transmission through a slab (of a thickness l) depicted by #2 from a homogeneous medium denoted by #1. Here we consider only a normal incidence.

an object and looking at the reflected and eventually transmitted sound has been generalized in 1D via the S-matrix formalism. It is used in many fields of physics. When the problem does not suffer too much from the boundary effects, it is easily applicable to acoustic problems and we will first write down how to retrieve effective parameters of a slab (with unknown acoustic properties) from a reflection and transmission measurements. However, such technique is less convenient for solids as the measurement techniques are far more complex and require many directions of observation for anisotropic media. In addition, the high-dimensional complexity of the rank-4 elasticity tensor and mass density (a rank-2 tensor in general case) drives us to present a less complex way to uncover all parameters.

Let's start with a slab of a thickness l shown in figure 14 with unknown properties such as the density, ρ, and the bulk modulus, B. We first define the effective impedance of a material denoted ♯i (see figure 14) by $Z_i = \rho_i c_i = \rho\sqrt{B_i/\rho_i}$ and $k_i = \omega/c_i$. Here, ω is the angular frequency and c_i the phase velocity.

An incident wave is partially transmitted and partially reflected as illustrated in figure 14. The simple measurement of the reflection, R and transmission coefficient, T can be directly connected to the slab properties [18] by:

$$R = \frac{(Z_2^2 - Z_1^2)\sin k_2 d}{(Z_2^2 + Z_1^2)\sin k_2 d + 2\mathrm{i} Z_1 Z_2 \cos k_2 l} \tag{90}$$

$$T = \frac{2\mathrm{i} Z_1 Z_2}{(Z_2^2 + Z_1^2)\sin k_2 d + 2\mathrm{i} Z_1 Z_2 \cos k_2 l}. \tag{91}$$

Measuring R and T, one can retrieve the slab properties and thus identify the effective parameters of the material. We should note that the retrieved parameters do not necessary need to be constant. However once we diverge from the long wavelength limit, it is not so easy and practical to identify from the measurement which parameters are frequency dependent (mass density or the bulk modulus).

A similar technique is often used in elasticity, however, one has to keep in mind that longitudinal and transverse waves must be used to probe the samples. In addition, inherent anisotropy makes the experiments more difficult as these require multiple angles of excitation and measurement of the transmission and reflection. Such experiments require the use of three elastic media in order to sandwich the unknown material.

Additional techniques based on the acoustic measurements are easier. Leymarie *et al* [268] show that under many wavefront reconstructions combined with some objective function optimisation, one can reconstruct the full elasticity tensor.

In section 3.1, we have discussed direct homogenization problems, whereby we derive the effective properties associated with a given periodic, quasi-periodic or random medium. However, in practice, one may wish to work out what is the microstructure that would achieve some prerequisite effective properties. This is a shift of paradigm known as inverse homogenization which is related to inverse problems.

3.2. *Inverse problems*

There is a vast amount of literature on inverse homogenization, and we refer the reader to the seminal works [269–272] as well as to the classical textbooks [273, 274].

In brief, the problem of optimal design, such as shape or topology optimization, of structures is defined by three ingredients

- a model (typically a partial differential equation) to evaluate (or analyze) for instance the acoustical, electromagnetic, thermal or mechanical behavior of a structure,
- an objective function which has to be minimized or maximized, or sometimes several objectives (also called cost functions),
- and a set of admissible designs which precisely define the optimization variables, including possible constraints.

Problems of optimal design can concern a certain parametric optimization of material parameters, for instance the geometric properties of the constituent material(s) to achieve a desired behavior. A typical optimization problem in elasticity includes an objective function defined as

$$F(\mathbf{u}(\rho,\lambda,\mu,\omega),\rho,\lambda,\mu,\omega),$$

where $\mathbf{u}$ is the displacement that satisfies a governing equation (for instance equation (9)), ρ, λ and μ are the density and Lamé parameters of the elastic medium (representing the material distribution inside the medium), and ω is the angular frequency of a vibration. This function F represents the quantity that is being minimized for best performance of the desired structured medium. For example, F can be the compliance, and minimizing F maximizes the stiffness of the medium (in which case ω is irrelevant).

A design domain Ω indicates the admissible area/volume within which the design can exist (depending upon whether the desired medium is 2D or 3D). Regions or components in the model that cannot be modified during the course of the optimization are considered as non-design regions, and are just left aside.

The optimization problem can be written as:

$$\begin{aligned} &\underset{\rho,\lambda,\mu,\omega}{\text{minimize}} \;\; F = \int_\Omega f(\mathbf{u}(\rho,\lambda,\mu,\omega),\rho,\lambda,\mu,\omega)\mathrm{d}V \\ &\text{subject to} \;\; G_j(\mathbf{u}(\rho,\lambda,\mu,\omega),\rho,\lambda,\mu,\omega) \leqslant 0 \end{aligned} \tag{92}$$

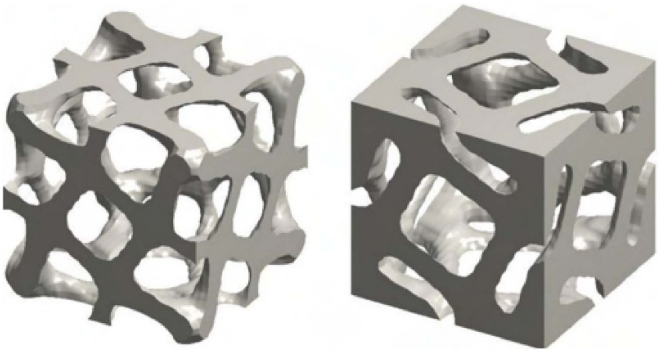

Figure 15. Topology optimization: two different chiral cubic unit cells (cf figure 22) optimized for different effective elastic properties. Note that the topology of the two architectures is distinct, i.e. the number of holes is different. Reprinted from [275], Copyright (2019), with permission from Elsevier.

with $j = 0, \ldots, m$. We thus minimize in the design space Ω the quantity F over the set of parameters $\rho, \lambda, \mu, \omega$ (in certain parameter space) subject to the $m+1$ constraints G_j.

For instance, one can consider simply optimizing a static problem with $F(\mathbf{u}(\rho), \rho)$, with $\rho = \text{const.}$ in the constituent material and 0 in air (or vacuum), in which case we can consider the constraint $G_0(\rho) = \int_\Omega \rho \mathrm{d}V - V_0 \leqslant 0$, and m other characteristics that the solution must satisfy through the constraints $G_j(\mathbf{u}(\rho), \rho) \leqslant 0, j = 1, \ldots, m$. This could, for example, correspond to the maximum amount of material to be distributed in a given area/volume (so with an area/volume constraint V_0) and the number of air holes (the latter being related to topological properties of the medium).

This is a rather general setup and we would like to discuss specific types of optimization problems.

In practice, let us emphasize that shape (geometric) optimization corresponds to designs obtained from an initial guess by moving the boundary of the reference medium without change of its topology (so excluding due the generation of new boundaries).

On the other hand, if we now assume the reference domain for a membrane is denoted by Ω, with a boundary made of three disjoint parts $\partial\Omega = \Gamma \cup \Gamma_D \cup \Gamma_N$ (with Γ_D and Γ_N denoting some clamped and stress-free parts of the boundary, respectively). A result of topology optimization,in which both the shape and the topology of the admissible designs can vary without any explicit or implicit restrictions, is illustrated in figure 15.

The last category in the above is, of course, the most general but also the most difficult to perform. We recall that two shapes share the same topology if there exists a continuous deformation from one to the other. In two dimensions, topology is completely characterized by the number of holes that correspond to Betti numbers [276] (or, equivalently, of connected components of the boundary). In three dimensions, matters are more complicated. Indeed, the topology of a set in three dimensions is not only determined by the number of holes, but it also depends on the number and intricacy (knotedness) of handles or loops.

A conceptually distinct approach for solving the inverse problem is machine learning [277, 278]. Herein, one trains a (deep) neural network with a large number of solutions of the forward problem. After appropriate training, the network is able to solve the forward problem efficiently. Dedicated networks can also be able to solve the inverse problem [279–281]. Concerning machine learning for mechanical metamaterials, a limited number of publications has been published. For example, the inverse problem has approximately been solved in two dimensions and for isotropic elastic properties within Cauchy elasticity [282, 283]. The 3D Cauchy problem and the inverse problem for generalized effective-medium elasticity theories has not been addressed so far. In any case, one should be aware that machine learning requires a very large overhead for training the neural network. Thereafter, any individual inverse problem can be solved in essentially no time. Therefore, machine learning makes sense if one aims at solving the inverse problem for many different parameters, whereas topology optimization is better for solving the inverse design problem only once or a few times. We shall come back to artificial neural networks in section 5.3 in the context of designing cloaks.

4. Metamaterials

More than three Centuries ago, Robert Hooke formulated what is now known as Hooke's law by elegantly stating: 'as the extension, so the force'. In essence, section 3. presents various examples of generalizations of Hooke's law in the sense of extreme, 'negative', isotropic, highly anisotropic, highly dissipative, chiral, non-reciprocal, and active linear elastic behavior (section 4.1), reversible nonlinear behavior (section 4.2), and irreversible nonlinear behavior (section 4.3).

4.1. Linear elasticity

In section 4.1, we review metamaterial architectures with an unusual resonant or off-resonant response that is proportional to the force or torque applied to them. Such behaviors clearly also change the elastic wave propagation in these structures, that is, they determine the metamaterial phonon modes and dispersion relations.

4.1.1. Extreme properties. In this subsection, we summarize extreme metamaterial properties in the sense of classical Cauchy elasticity (see section 2.1), including auxetic, pentamode, isotropic, and ultra-light weight bulk behavior. We also briefly touch upon extreme surface properties.

The vast majority of mechanical metamaterials investigated so far has been periodic, i.e. crystalline. The reason is that periodicity eases the theoretical treatment (e.g. via periodic boundary conditions) as well as the experimental manufacturing. Notable exceptions from periodicity are early works on auxetic foams [284] and recent publications on 3D quasi-crystalline structures [114]. In general, crystalline mechanical metamaterials exhibit a strongly anisotropic behavior. This statement

holds true even for cubic symmetry and within the long-wavelength limit, for which optical metamaterials, acoustic metamaterials, diffusive metamaterials, as well as transport metamaterials exhibit isotropic effective properties [21]. The particular behavior of mechanical metamaterials in this regard can be traced back to shear forces and compression forces acting at the same time, leading to the simultaneous presence of transversely and longitudinally polarized elastic waves in the dynamic case.

Two polar opposite limiting cases of classical Cauchy elasticity are auxetics [29, 284–294] and pentamodes [27, 28, 295–298]. For auxetics, the shear forces dominate. Precisely, for simplicity assuming a 3D isotropic response, the shear modulus G is much larger than the bulk or compression modulus B, i.e. $G/B \gg 1$. Equivalently, the Poisson's ratio approaches $\nu \to -1$ from above. Such extreme auxetic metamaterials with $\nu_{\text{eff}} \to -1$ have also been referred to as dilational metamaterials [29], because their only mode of deformation is an overall size change without any changes in shape. In contrast, for pentamode metamaterials [27], the compression forces effectively dominate, thus $B_{\text{eff}}/G_{\text{eff}} \gg 1$ or $\nu_{\text{eff}} \to 0.5$ from below. In this limit, the behavior of an elastic solid approaches that of a gas or fluid, which exhibits zero shear forces. Loosely speaking, a pentamode metamaterial is 'more rubbery' than rubber.

In crystalline metamaterials, the Poisson's ratio is generally not isotropic. Thus, the scalar Poisson's ratio has to be replaced by the Poisson tensor, describing this anisotropy. Remarkably, in three dimensions, the Poisson tensor converges towards the unity matrix times a scalar in the two limits of $\nu_{\text{eff}} \to -1$ and $\nu_{\text{eff}} \to +0.5$, i.e. the Poisson's ratio becomes isotropic for ideal dilational and ideal pentamode metamaterials. However, even for $\nu_{\text{eff}} \to +0.5$ from below, the remaining small shear forces are anisotropic and, hence, the transverse metamaterial phonons have an anisotropic dispersion relation [299].

Figure 16 illustrates cubic-symmetry examples of 3D dilational metamaterials and 3D pentamode metamaterials made by 3D additive manufacturing of polymers. In both cases, the key are 'hinge' regions the size of which is very small compared to the unit cell size. Ideally, the hinges should be points at which two elements touch. However, this ideal would lead to an unstable structure. Experimental characterizations have been published in [300–302]. Bimode metamaterials [27, 303] are the 2D counterpart of 3D pentamode metamaterials. Generalizations to intentionally anisotropic versions of pentamode/bimode metamaterials have been discussed, too [19]. We will come back to cloaks based on pentamode metamaterials in section 5.

It has been argued mathematically [16, 27], that any Cauchy elasticity tensor can be constructed based on pentamode metamaterials. An alternative general procedure has been proposed by Milton *et al.* but can only be applied for very small deformations [304]. The strategy is to find six pentamode structures each supporting a stress represented by a vector $\mathbf{v}_i$, $i = 1, \ldots, 6$, and to tune them so that their respective effective elasticity tensors are nearly $C^{(i)}_{\text{eff}} = \Lambda_i \mathbf{v}_i \otimes \mathbf{v}_i$. The six pentamodes are then successively superimposed

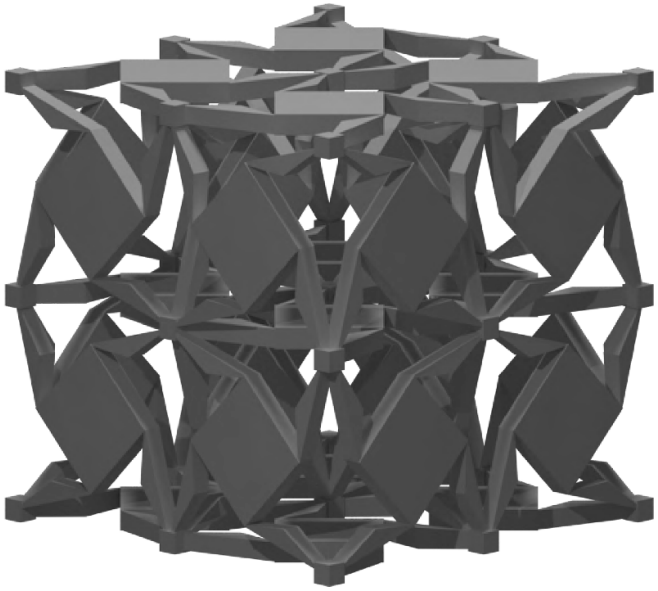

Figure 16. Unit cell of a dilational metamaterial. Under any uniaxial compression, the material shrinks in the orthogonal directions. Inspired from [286].

(avoiding some overlapping), and elastic interactions between pentamodes are minimized in such a way that the resulting metamaterial is described by an effective tensor given by the sum of the six $C^{(i)}_{\text{eff}}$. This effective tensor approximates the desired elasticity tensor (see [304] and also foreword in [305] for further details). Camar-Eddine and Seppecher [306] also proved the realizability of any elasticity tensor as a corollary of their far more general characterization of all possible linear elastic behaviors, including non-local ones. The proof goes from the continuum to the discrete (spring networks) back to the continuum. Their microstructures are, however, intricate with infinitely many scales, and with infinitely thin members that buckle at infinitesimal loading. For the discrete elastodynamic case all possible time-dependent linear behaviors have been characterized [307], which should be an ingredient in the extension of Camar-Eddine and Seppecher's result [306] to linear elastodynamics. Nevertheless, we are not aware of an established general rational strategy for obtaining a specific metamaterial microstructure that yields a desired Cauchy elasticity tensor after homogenization (with generally 21 independent nonzero scalar parameters, see 2.2). Obtaining such strategy appears important for applications; therefore, it represents a relevant future avenue.

An alternative to the general strategy proposed by Milton are 3D cubic-symmetry unit cells designed by topology optimization, yielding an isotropic achiral static elastic metamaterial behavior despite the crystallinity [308]. This includes the possibility of isotropic auxetics [308]. However, the obtained isotropy is somewhat similar to an accidental degeneracy in quantum mechanics, in that fabrication imperfections in the making of this specially shaped unit cell immediately lead to deviations from an isotropic behavior. Isotropic linear elastic behavior is also well established in disordered foams [284],

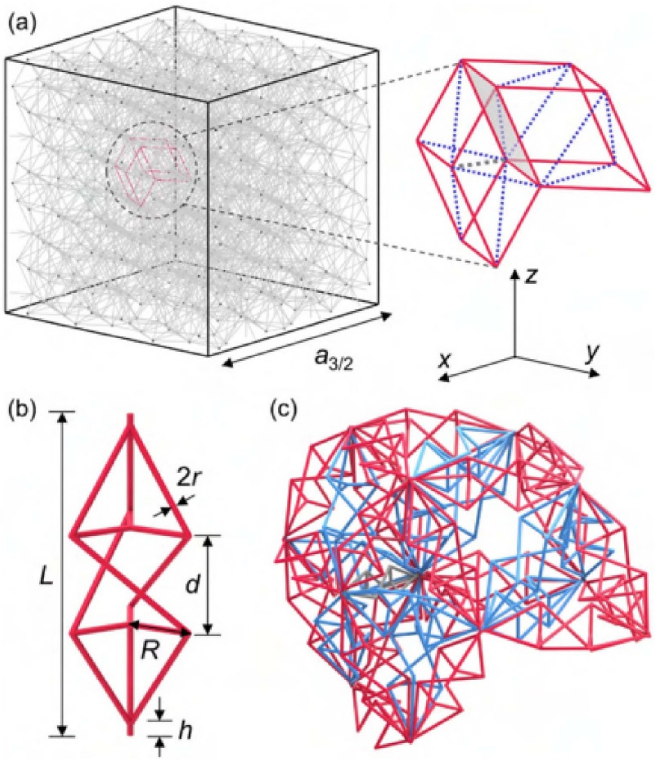

Figure 17. (a) Illustration of the an approximant of a 3D icosahedral quasicrystalline metamaterial. The black points result from the cut-and-project method. The enlarged area highlights three types of segments between these points, i.e. the edges (red), the face diagonals (blue dotted) of the two types of rhombohedra, and the shortest body diagonals (gray dashed) of the thinner rhombohedra. (b) Each red uniaxial chiral rod from (a) is replaced by the new chiral metarod with threefold rotational symmetry. (c) Resulting chiral architecture corresponding to the enlarged region in (a). Reprinted (figure) with permission from [114], Copyright (2020) by the American Physical Society.

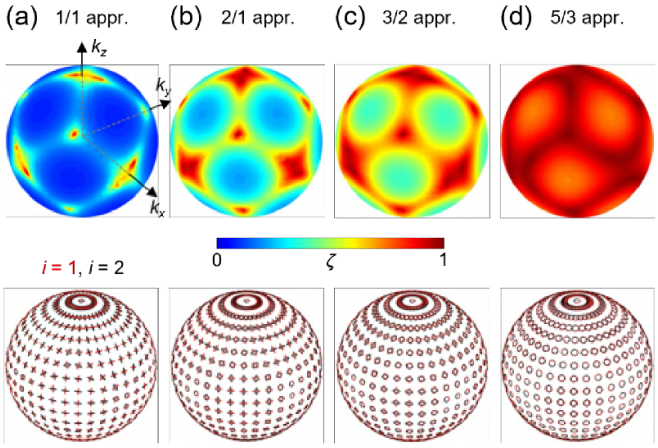

Figure 18. Calculated results for increasing order (from left to right) of 3D quasicrystal approximants for at fixed low value or wavevector (dashed gray lines in figures 2 and 2). Different approximants are used: (a) $q/p = 1/1$, (b) $q/p = 2/1$, (c) $q/p = 3/2$, and (d) $q/p = 5/3$. The first row exhibits the polarization degree, ζ, on a false-color scale. $\zeta = 0$ corresponds to linear polarization and $\zeta = 1$ to circular polarization. The second row shows real-space trajectories of the phonon displacement vector versus time (mean over one periodic cell), i.e. a circle corresponds to circular phonon polarization, an ellipse to elliptical polarization, and a line to linear polarization. Reprinted (figure) with permission from [114], Copyright (2020) by the American Physical Society.

including auxetic foams [284]. Here, the structure of the foam is far from being isotropic locally. Isotropy is rather achieved on average in terms of position and orientation, for example if a wave propagates over a distance of many characteristic voids in a foam. In that sense, isotropy in foams is statistically robust against fabrication tolerances and imperfections. While many types of foams can be fabricated inexpensively in large volumes, it should be noted that their properties are not fully controlled by a rational design procedure.

Therefore, we have recently considered [114] periodic approximants of 3D quasi-crystalline mechanical metamaterial architectures as an alternative (see figure 17). Here, the aimed-at extreme classical property is isotropy. In the spirit of the cut-and-project method [309, 310], 3D quasi-crystals can be derived from a simple-cubic 6D crystal lattice of points (with lattice constant a_{6D}) that is rotated by an angle connected to the golden number $\tau = \left(1+\sqrt{5}\right)/2 \approx 1.6180$ [114]—the most irrational number in mathematics [311]. Subsequently, parts of the rotated lattice are projected onto three dimensions. Periodic approximations of quasi-crystals, so-called approximants, can be obtained by replacing the golden number by fractions of successive Fibonacci numbers $F_0 = 0,\ F_1 = 1,\ F_2 = 1,\ F_3 = 2,\ F_4 = 3,\ F_5 = 5,\ F_6 = 8, \ldots$ according to $\tau \to F_{n+1}/F_n$, which is motivated by the limit $\tau = \lim_{n\to\infty} F_{n+1}/F_n$. A finite integer $n \geqslant 1$ for the fractions $F_{n+1}/F_n = 1/1,\ 2/1,\ 3/2,\ 5/3, \ldots$ leads to a periodic cubic crystal with lattice constant $a_n = 2a_{6D}\left(F_{n+1}\tau + F_n\right)/\sqrt{1+\tau^2}$. Clearly, this lattice constant rapidly increases with increasing approximant order n. For example, for the $5/3$ approximant, we obtain $a_3 \approx 11.6\ a_{6D}$. To arrive at a concrete architecture, rules are needed how to connect the resulting fictitious lattice points with each other within the unit cell. Our rules [114] have been motivated by achieving a large local coordination number to obtain good angle averaging. The discussed 3D quasi-crystal lattice is composed of two types of rhombohedra [114], in analogy to 2D Penrose tilings composed of two types of 2D tiles [312]. Two lattice points are connected by a thin cylindrical rod on the edges of the rhombohedra, on the face diagonals of the two types of rhombohedra, and on the shortest body diagonals of the thinner rhombohedra. Figure 18 shows the results of calculations illustrating how isotropy and insensitivity with respect to transverse polarization (cf first two bands) is approached for the three lowest metamaterial phonon bands versus increasing approximant order. For sufficiently long wavelengths, the two lowest transverse bands become nearly degenerate, and this architecture can be described by using only a scalar effective shear modulus G_{eff}, an effective scalar bulk modulus B_{eff}, and an effective mass density ρ_{eff}. As in disordered foams, the structure of the quasi-crystal is far from being isotropic locally. Isotropy is rather achieved on average. For 3D quasi-crystals, one can go beyond the discussed *achiral* behavior towards

chiral isotropic properties. We will come back to this aspect in section 4.1.5.

As another aspect, the static mass density, ρ, of ordinary bulk materials is important for many applications, for example in aviation. The metamaterial quasi-static effective mass density is defined by

$$\rho_{\text{eff}} = \frac{m}{V_{\text{eff}}}$$

with the mass m of the involved constituent material and the effective metamaterial volume V_{eff}, i.e. the volume enclosed by the outer boundaries of the metamaterial structure (*cf.* section 4.1.3). For example, ultra-light metallic metamaterials based on hollow beams with values as low as $\rho_{\text{eff}} = 0.9\,\text{kg}\,\text{m}^{-3}$ have been realized [313] (not counting the air mass in the voids or pores). For comparison, the mass density of air under ambient conditions is $\rho_{\text{air}} \approx 1.2\,\text{kg}\,\text{m}^{-3}$.

Finally, various types of extreme effective surface properties have been reported by using artificial periodic lattices of rationally designed unit cells, albeit often not under the name 'metamaterial'. For example, effective superoleophobic surface properties [314] have been realized experimentally. These lattices are repellent towards low-surface-tension liquids. As another example, inspired by the Salvinia effect [315, 316], extreme effective air-holding surface properties have been demonstrated that might find applications in reducing the mechanical friction between the ship wall of large ships and water.

4.1.2. Tailored properties. In the preceding subsection, we have seen that most crystalline materials and metamaterials exhibit an anisotropic elastic behavior. However, for cloaking applications (see section 5) tailored anisotropy and especially extremely large anisotropies are needed. Such behavior can be achieved by laminates, which are a paradigmatic class of metamaterial [16]. The simplest laminate is a periodic stack of plates with alternating properties. Whereas each plate by itself may be homogeneous and isotropic, the alternation introduces an effective metamaterial anisotropy. For example, an alternation of rubber and metal plates is compliant for loading normal to the plates, and stiff in the orthogonal directions. The degree of effective metamaterial anisotropy can be tailored by the choice of the two constituent materials and their relative thicknesses (cf section 3.1.2). The two layers of the laminate can also be made from two different pentamode metamaterials (see section 4.1.1) or other elastic metamaterials, which allows for obtaining highly anisotropic effective properties from just a single constituent material and voids within [27]. The individual laminate layers may also be laminates with inclined stacking directions, leading to hierarchical laminates [16].

4.1.3. Negative effective properties. In ordinary materials, the bulk modulus B, which is equal to the inverse of the compressibility $\kappa = B^{-1}$, and the mass density ρ are positive definite quantities. In contrast, the unit cell of metamaterials can be designed to exhibit low-frequency local resonances; a paradigm being the acoustic Helmholtz resonator [317]. If the corresponding wavelengths are sufficiently large compared with the unit-cell size, these resonances can be cast into frequency-dependent effective-medium behaviors $B_{\text{eff}}(\omega)$ and $\rho_{\text{eff}}(\omega)$. As for any harmonic-oscillator resonance, the system response exhibits a 180° phase shift above the respective eigenfrequency. This means that $B_{\text{eff}}(\omega)$ and $\rho_{\text{eff}}(\omega)$ can become negative in a certain frequency interval. If appropriately designed, these frequency intervals overlap. As a result, for airborne or waterborne sound, the effective phase velocity of sound c_{p}, with $c_{\text{p}}^2 = B_{\text{eff}}(\omega)/\rho_{\text{eff}}(\omega)$ hence $c_{\text{p}} = \pm\sqrt{B_{\text{eff}}(\omega)\rho_{\text{eff}}(\omega)}$, becomes negative [318]. A variety of such resonant structures has been presented [319, 320]. However, due to the resonant nature and due to the Kramers–Kronig relations based on causality, the frequency-dependent real parts of $\rho_{\text{eff}}(\omega)$ and $B_{\text{eff}}(\omega)$ unavoidably come along with a finite imaginary parts. In passive media, this imaginary part leads to wave attenuation, which is often unwanted—unless the goal is to attenuate sound, ideally without reflection at the interface to the attenuating medium. We will come back to sound dissipation and its limits in section 4.1.4. If the frequency intervals of negative response of $B_{\text{eff}}(\omega)$ and $\rho_{\text{eff}}(\omega)$ do not overlap, the phase velocity becomes imaginary where $B_{\text{eff}}(\omega) < 0$ or $\rho_{\text{eff}}(\omega) < 0$, respectively, leading to low-frequency stop bands connected with evanescent waves [321–325]. A simple example is a lattice of soft rubber balls with a high mass-density metal core [326]. The rubber shell acts as a soft Hooke's spring and the metal core as a mass of a simple mass-spring oscillator. This result was initially misinterpreted as negative elastic modulus and explained at a later stage as a negative effective mass density [327]. Frequency stop bands and band gaps can alternatively be realized by exploiting Bragg resonances, which was one of the early goals of the more mature field of phononic crystals [11, 328].

Negative phase velocities have also been reported for back-folded longitudinal acoustic bands in labyrinthine metamaterials [320] when the effective elastic modulus and density are both negative [329]. In essence, winding channels defined by rigid walls inside of the metamaterial unit cell effectively delay the propagation of airborne sound in two or three dimensions. However, it has also been pointed out that defining the sign of the phase velocity for higher bands, which are back-folded by Bragg reflection/diffraction, is possible, but generally ambiguous [330]. Nevertheless, labyrinthine metamaterials offer the possibility of off-resonant isotropic acoustic wave speeds slower than the speed of sound in air under ambient conditions by factors as large as 8 (= effective acoustical refractive index n_{eff}) in the 1–4 kHz regime [330]—which is an extreme and otherwise unavailable property by itself. On the basis of labyrinthine metamaterials, flat acoustic lenses have been realized [331] and many types of diffractive acoustic elements are conceivable in analogy to diffractive optical elements [332].

While the nonlinear stress–strain curve of materials and metamaterials can exhibit regions of negative differential slope (see section 4.2), the static linear-elastic compressibility κ of ordinary materials is always positive. Broadly speaking, being

a response function, $\kappa(\omega = 0) = B^{-1}(\omega = 0)$, which is given by

$$\kappa = -\frac{1}{V}\left(\frac{\partial V}{\partial P}\right)_T,$$

just cannot be negative due to causality for arbitrary boundary conditions. For special boundary conditions [333], a positive effective compressibility may be possible. From an energetic viewpoint, $\kappa < 0$ is analogous to a negative passive Hooke's spring constant, which violates energy conservation. In a thermodynamic sense, the compressibility cannot be negative either because unstable behavior would result. This means that an increasing hydrostatic pressure P exerted onto an ordinary material always leads to a reduction of the material's volume V. This includes the possibility that a material behaves anisotropically and expands along one direction, while the overall volume shrinks. Such behavior is sometimes referred to as negative linear compressibility [334, 335]. An ordinary sponge or foam would also shrink in response to an increased hydrostatic pressure. However, caution needs to be exerted because such systems must be considered as poroelastic (cf section 2.6). Here, the single compressibility κ of ordinary materials has to be replaced by two generally different compressibilities, the jacketed and the unjacketed compressibility [336]. The unjacketed compressibility, which we here refer to as effective compressibility for consistency of nomenclature,

$$\kappa_{\text{eff}} = -\frac{1}{V_{\text{eff}}}\left(\frac{\partial V_{\text{eff}}}{\partial P}\right)_T$$

relates to the effective volume V_{eff} of the structure, i.e. the volume enclosed by the outer boundaries of the structure. An observer not resolving or not noticing the porosity would perceive and measure the effective volume V_{eff} rather than the volume V of the material the foam is composed of. Neither thermodynamics, nor causality, nor energetics forbids $\kappa_{\text{eff}} < 0$ in the static regime ($\omega = 0$).

What metamaterial architectures enable such unusual behavior? Interestingly, obtaining $\kappa_{\text{eff}} < 0$ from a metamaterial is intimately related to obtaining a negative effective thermal expansion coefficient, $\alpha_{\text{eff}} < 0$, from constituents with $\alpha > 0$. Early metamaterial suggestions [337] referred to thermal expansion. The effective metamaterial thermal expansion coefficient is given

$$\alpha_{\text{eff}} = +\frac{1}{V_{\text{eff}}}\left(\frac{\partial V_{\text{eff}}}{\partial T}\right)_P.$$

An arbitrary porous structure composed of only a single material with bulk thermal expansion coefficient α and (evacuated) voids within leads to $\alpha_{\text{eff}} \equiv \alpha$. This finding is boring yet remarkable because all other effective mechanical properties, such as the mass density or elastic moduli, change when microstructuring a bulk host material.

Therefore, corresponding metamaterials need more than just a single constituent material. Figure 19 shows a motif and its application for 1D, 2D, and 3D metamaterials. These architectures are composed of three ingredients, namely two dissimilar bulk materials and the voids within. The voids, which

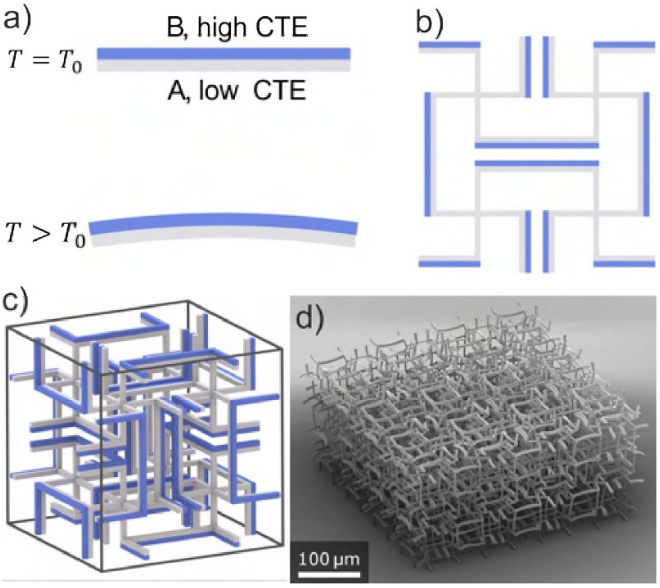

Figure 19. Principle of bi-material based metamaterials (see [338]): (a) illustration of a simple bi-material beam having two different coefficient of thermal expansion (CTE) and leading to a bending upon a change of temperature. (b) A 2D metamaterial made of only positive CTE but leading to an effective negative CTE. (c) A 3D version of (c). Corresponding fabricated structure. Reproduced from [335]. CC BY 4.0.

can be filled with a gas/liquid or which could be evacuated, are a quintessential part of the metamaterial and are hence sometimes counted as a third 'material'. The mechanism illustrated in figure 19 is based on bi-material beams. Upon increasing the temperature, the two materials of the beam expand differently, leading to a bending of the beam (see [338]). If the (positive) compressibilities of the two materials in the bi-material beam are different, the beam would also bend when exposed to an increasing hydrostatic pressure. The shown unit cells can translate this bending into an effective reduction of the metamaterial lattice constant, a, in one, two, or three dimensions. In a cubic-symmetry crystal, this reduction of the lattice constant can be made identical for all three dimensions, leading to an isotropic reduction of the effective volume V_{eff} given by $V_{\text{eff}} = N_x N_y N_z\, a^3$. Here, N_x, N_y, and N_z are the numbers of the unit cells in the x-, y-, and z-direction, respectively. For example, for a cubic crystal in 3 dimensions, this leads to

$$\alpha_{\text{eff}} = +\frac{3}{a}\left(\frac{\partial a}{\partial T}\right)_P \quad \text{and} \quad \kappa_{\text{eff}} = -\frac{3}{a}\left(\frac{\partial a}{\partial P}\right)_T.$$

It has been shown that, at least mathematically, any sign and magnitude of κ_{eff} (and hence of α_{eff}) from $-\infty$ to $+\infty$ can be achieved by varying the ratio of the length of the lever arms L and the beam heights h [335] (see figure 19). Therefore, the behavior is conceptually unbounded.

We note in passing that the same sign-reversal mechanism can also be exploited for other material behaviors. If, for example, the two constituent materials in figure 19 swell differently when exposed to a solvent that penetrates into these materials, the metamaterial effectively shrinks rather

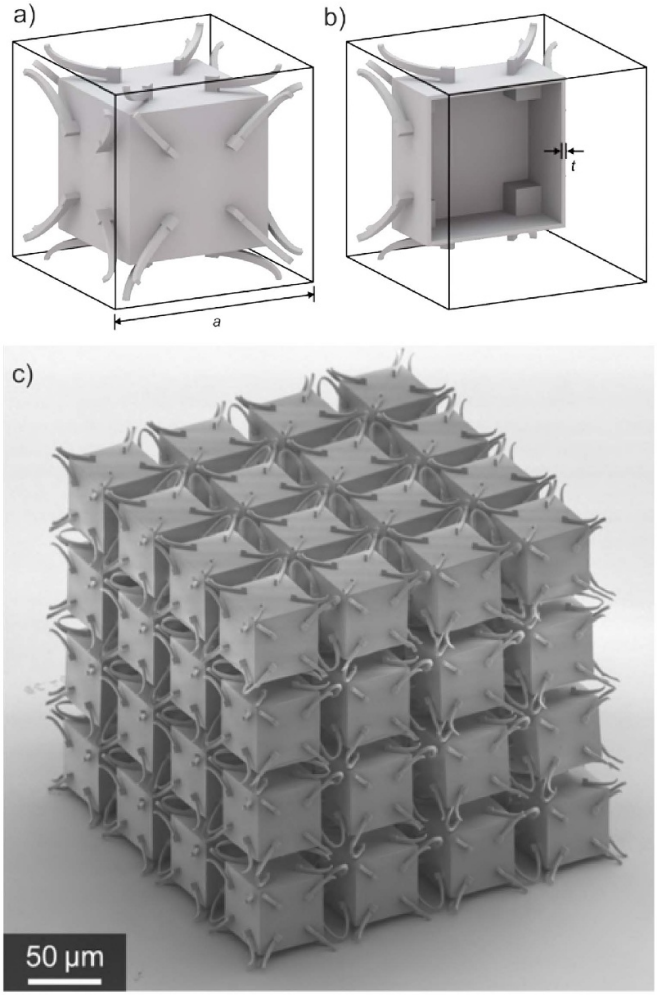

Figure 20. Unit cell of a poroelastic metamaterial (a) and the cut version showing the inside in (b). (c) Corresponding fabricated metamaterial. Reproduced from [335]. CC BY 4.0.

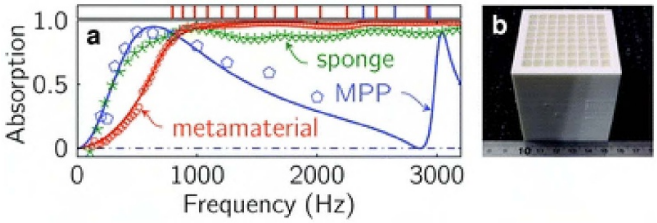

Figure 21. (a) Absorption comparison between conventional acoustic absorption materials and the designed broadband metamaterial. (b) A photo image of the metamaterial unit with a thickness of 5.63 cm. Reproduced from [357] with permission from the Royal Society of Chemistry.

than swells [335]. It could also be designed for fixed effective volume. Likewise, the sign of volume-magnetostriction, a shrinkage of the material (e.g. Invar) volume when exposed to a static magnetic field, could also be reversed in sign or enhanced in magnitude. Thermal-expansion metamaterials can be divided into bending-dominated [339–349] and stretching-dominated architectures [350–356]. Figure 19 shows 3D bending-dominated microstructured metamaterials that have been manufactured and successfully characterized. Sign reversal of thermal expansion ($\alpha_{\text{eff}} < 0$) has been achieved by adjusting the cross-linking density and hence $\alpha_2 > \alpha_1 > 0$ of the two involved polymers by locally changing the laser power during 3D printing. $\alpha_{\text{eff}} > \alpha_2 > \alpha_1$ has been achieved, too. Using the same architecture for $\kappa_{\text{eff}} < 0$ should be possible, but leads to extremely small effects as the compressibilities of ordinary elastic materials are small and the compressibility differences between them is yet smaller. The different structures in figure 20 containing hollow volumes are based on replacing one of the two materials by a gas such as air, the compressibility of which is orders of magnitude larger than that of solids. The walls of the hollow and sealed volumes serve to keep the gas in position. Optimizing the behavior has led to the different solutions shown in figure 20. Negative effective compressibility as well as large positive effective compressibility has been achieved experimentally [335]. Furthermore, it has been shown by numerical calculations that the positive effective metamaterial compressibility can even exceed the compressibility of air ($\kappa = \left(10^5\ \text{Pa}\right)^{-1} = \left(1\ \text{bar}\right)^{-1}$) under ambient conditions [334]. Zero static effective compressibility is a possible special intermediate case [334, 335].

4.1.4. Extreme sound dissipation. In section 4.1.1, we have mentioned that the fundamental principle of causality, i.e. the fact that we cannot change the past, connects the real and imaginary parts of elastic properties, e.g. of the effective bulk modulus, connected to local resonances within the metamaterial unit cell. As usual, finite imaginary parts lead to an exponential decay of the wave amplitude. While often undesirable, such behavior is wanted for noise protection of airborne sound. However, noise absorption is only useful if large absorption coincides with little reflection from the metamaterial surface. Zero reflection requires matching the effective metamaterial impedance, Z_{eff}, to the impedance of air $Z = \rho c_{\text{p}} = \sqrt{\rho B}$. Under ambient conditions, we have $Z = 400\ \text{Ns}\,\text{m}^{-3}$. Near a resonance, the condition $Z_{\text{eff}} = Z$ can be met by frequency-dependent metamaterial effective quantities $\rho_{\text{eff}}(\omega)$ and $B_{\text{eff}}(\omega)$. However, for just a single Lorentzian resonance, perfect absorption near 100% can only be achieved over a fairly limited frequency range, whereas audible sound covers many octaves in frequency. Using the rationally designed distribution of folded Fabry–Pérot resonators with different resonance frequencies within one metamaterial unit cell depicted in figure 21 nearly perfect absorption of airborne sound has been obtained experimentally over almost three octaves in frequency from 500 to 3000 Hz [357]. The absorber thickness has been about 11 cm. While this thickness may still be considered as too large for widespread applications on room walls, it should be mentioned that this value is close to the minimum-thickness limit determined by causality [357, 358]. For lower frequencies, hence larger wavelengths, the thickness-limit increases further. Previous and further work on perfect sound absorbers can be found in [359–366].

Active metamaterials discussed in section 4.1.10 are an approach for noise dissipation or cancelation, which is different from the extreme passive structures presented in this subsection.

4.1.5. Chiral properties. In this subsection, we present linear elastic results that go beyond classical Cauchy elasticity in the sense of chirality (compare sections 2.1, 2.2 and 2.6). Static structural chirality requires broken space-inversion symmetry, the absence of mirror planes, and no rotation-reflection symmetries [21]. Time-inversion symmetry may still hold true though, but can also be broken independently (cf section 4.1.6).

One consequence of chirality in metamaterials in the quasi-static limit is the conversion of an axial push or force onto a beam, leading to an axial strain ϵ_{zz}, into a twist around the pushing axis, with twist angle φ. Such behavior might be useful for converting a linear motion of a piezoelectric actuator into an angular variation. This example is well suited to highlight that such behavior beyond classical Cauchy elasticity is inherently connected to the loss of scale invariance, that is, to finite-sample-size effects. Size matters [367]. Consider a 3D metamaterial composed of $N_x N_y N_z$ unit cells total. All dimensions shall follow $N_x \propto N_y \propto N_z \propto N$, where N is successively increased. A simple reasoning based on different contributions to the linear-elastic energy [159] leads to the following behavior of the twist angle

$$\frac{\varphi\,(N)}{\epsilon_{zz}} = \frac{\varphi(1)}{\epsilon_{zz}} \cdot \frac{N N_c^2}{N^2 + N_c^2}$$

versus integer $N > 1$. Interestingly, this expression contains only two parameters. First, the twist angle $\varphi(1)$, which is merely a prefactor and which is obviously a property of an individual unit cell, $N = 1$. Second, the non-integer parameter N_c, which determines the shape of $\varphi\,(N)$ versus N. When multiplied with the metamaterial lattice constant, this parameter corresponds to a characteristic length. It describes the coupling between the different chiral metamaterial unit cells. For $N \gg N_c$, this formula leads to an asymptotic behavior $\varphi\,(N)/\epsilon_{zz} \propto 1/N$, which, for $N \to \infty$, brings us back to Cauchy elasticity, for which $\varphi/\epsilon_{zz} \equiv 0$. As $1/N$ is proportional to the surface-to-volume ratio, this term indicates the importance of the sample surface [368]. In the opposite limit of $N \ll N_c \gg 1$, the twist angle increases according to $\varphi\,(N)/\epsilon_{zz} \propto N$. The twist angle peaks at $N = N_c$. If N_c is on the order of $N_c \approx 1$ or < 1, no maximum of $\varphi\,(N)/\epsilon_{zz}$ versus integer N occurs and one gets a monotonously decaying behavior versus $N \geqslant 1$.

A gallery of possible (static) chiral unit cells is shown in figure 22. Later, topology optimization has led to modified motifs [369]. From the start, a goal has been to make φ/ϵ_{zz} and N_c as large as possible. Early experimental work corresponded to $\varphi/\epsilon_{zz} \approx 2^\circ\,\%^{-1}$ and $N_c \approx 1.7$ [368]. A few years later, specially tailored metamaterial unit cells in regard to the coupling yielded N_c on the order of 10 at slightly larger starting values of φ/ϵ_{zz} [368, 369], in agreement between numerical

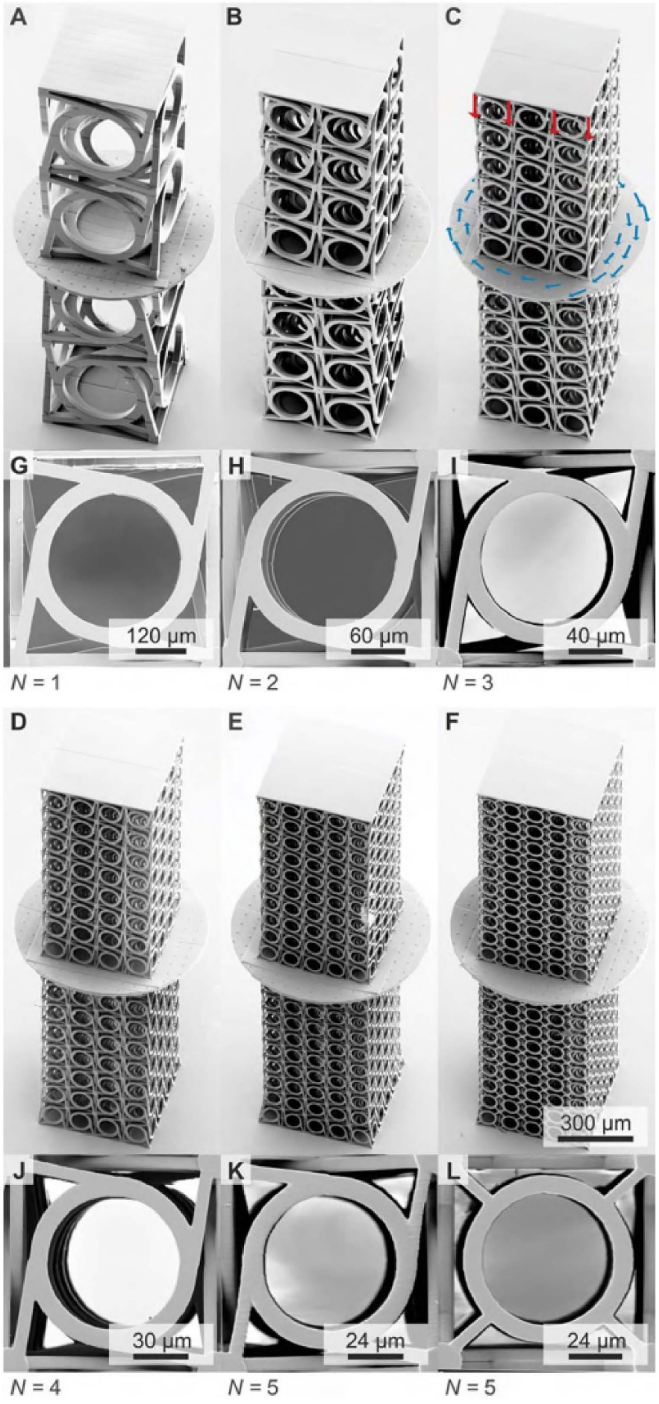

Figure 22. Gallery of electron micrographs of mechanical metamaterials fabricated using 3D laser microprinting. The structures are chiral, except for the achiral controls in panels F and L. From [159]. Reprinted with permission from AAAS.

microstructure calculations, the above simple model, numerical solutions of Eringen micropolar continuum elasticity (cf section 2.3), and experiments. Manufactured 3D metamaterial samples with $N = 27$ ($N_x N_y N_z = 118\,098 > 10^5$ unit cells total) delivered twist angles larger than $\varphi/\epsilon_{zz} \approx 4^\circ\,\%^{-1}$. For

the structures investigated, large characteristic lengths have always been connected with large geometrical nonlinearities [368]. Large tailorable characteristic lengths have also been studied in achiral mechanical metamaterials [370], where they are again connected to pronounced size effects [367].

All behaviors discussed for the chiral linear-elastic regime are qualitatively well described by Eringen micropolar elasticity. However, it has been pointed out that cutting through unit cells at the sample surface leads to appreciably large effects that cannot be grasped by any bulk continuum description [40]. Here, generalized effective-medium theories combining bulk and surface contributions would be required to arrive at an improved description. Steps in this direction have been taken [40], albeit without chirality.

In addition to the quasi-static case discussed thus far, chirality strongly influences the metamaterial phonon dispersion relations. In a chiral medium, the phonon modes are chiral, too. For a finite-size specimen, one generally gets four phonon branches emerging from the Γ-point: two transverse modes, one longitudinal mode, and one twist mode. Chirality mixes the twist mode and the longitudinal mode [371]. This mixing is the dynamic counterpart of the quasi-static push-to-twist conversion discussed above. Furthermore, chirality mixes the two transverse modes, generally leading to new eigenstates with elliptical polarization [40, 159]. If the phonon wave vector has a three-fold or higher rotational symmetry axis, one obtains left-handed and right-handed chiral phonons, which are the counterpart of circular polarization of light in optics. The phonon wave vector forms an axis around which the unit cell's center of mass orbits in circles around its rest position. In a cubic metamaterial crystal, chiral phonons occur along the three principal cubic directions with three-fold rotational symmetry, and along the three space diagonals with four-fold rotational symmetry. In a 3D chiral quasi-crystal [114], chiral phonons can occur along any wave-vector direction, making the chiral behavior effectively isotropic. Here, the required structure symmetry is not provided locally, but on average over the course of phonon propagation [114].

The fingerprint of chiral metamaterial phonons is acoustical activity [372–374]. As for its counterpart, optical activity [375–377], an incident linear polarization needs to be decomposed into the left- and right-handed circularly polarized eigenstates in this case. These eigenstates propagate with different phase velocities, c_+ and c_-, say along the z-direction, with $\overrightarrow{k} = (0,0,k_z)$. Therefore, the incident linear polarization rotates over the course of phonon propagation over length L_z by an angle ϑ given by

$$\vartheta = \left(\frac{\omega}{c_+} - \frac{\omega}{c_-} \right) \frac{L_z}{2} = \Delta k_z(\omega) \frac{L_z}{2} \ .$$

Here, $\Delta k_z(\omega)$ is the wave-number difference between the two modes at angular frequency ω. The effects of acoustical activity have been observed years ago in ordinary crystals such as quartz [372–374], but they have been very small there and could not be tuned to operation frequencies of interest.

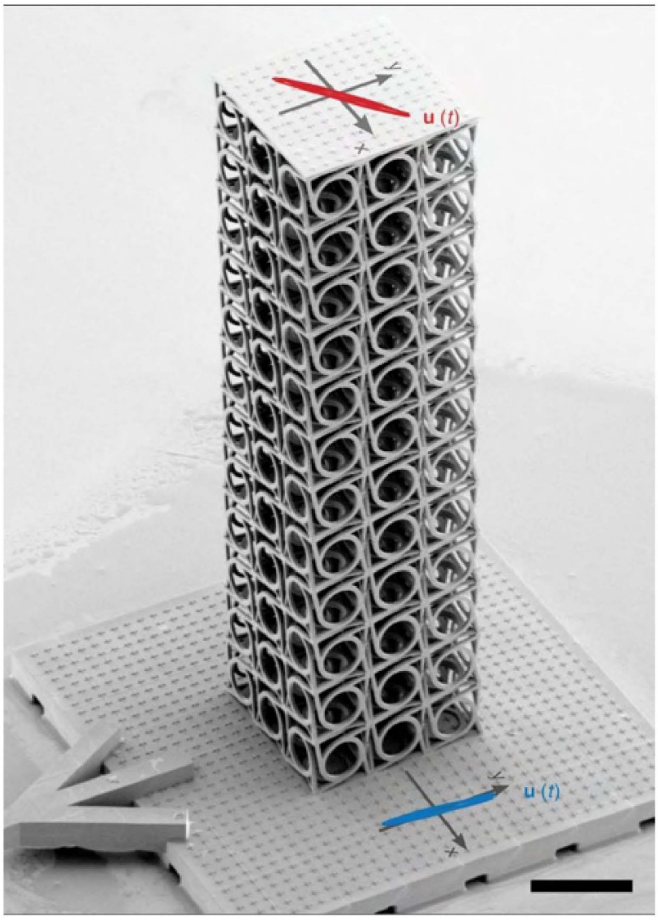

Figure 23. Oblique-view electron micrograph of a $3 \times 3 \times 12$ unit-cells metamaterials. A piezoelectric transducer is used to excites the sample. A polarisation measurement experiment is carried out using cross-correlation imaging on the top of the sample. Reproduced from [371]. CC BY 4.0.

In metamaterials, any wanted operation frequency can be accessed by choosing the metamaterial lattice constant appropriately. Experimentally [368], in metamaterial beams and for propagation along a metamaterial-beam axis, rotation angles ϑ as large 22 degrees per unit cell have been found in ring-like architectures at 180 kHz frequency (cf figure 23) and 30 degrees per unit cell at 100 kHz frequency in twisted-rod architectures (cf figure 24). To convert the polarization from one linear transverse orientation to the orthogonal one, a 90° rotation is needed. The fundamental upper limit is 90 degrees per lattice constant a_z due to $|\Delta k_z| \leqslant \pi / a_z$ [369]. As for the quasi-static case (see above), pronounced sample-size effects have been found experimentally [371], i.e. the rotation angles ϑ depend on N. However, large effects of acoustical activity can remain in the bulk limit of $N \to \infty$ [371] as the wavelength, $\lambda = 2\pi / k_z$, is no longer necessarily large compared to the lattice constant a_z, as is the case in the quasi-static limit. Therefore, Cauchy elasticity does not apply. However, acoustical activity, including metamaterial crystal anisotropies [40], can be well described by micropolar continuum elasticity [38] (cf section 2.3).

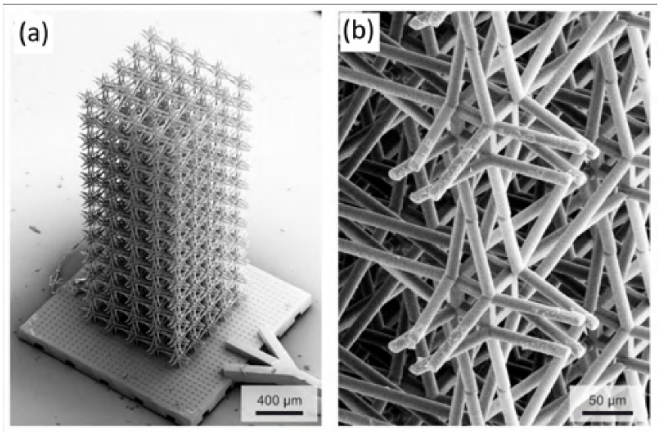

Figure 24. (a) Electron micrographs of rod-based chiral mechanical metamaterials. (b) A zoom in the structure shown in (a). Reproduced from [369]. CC BY 4.0.

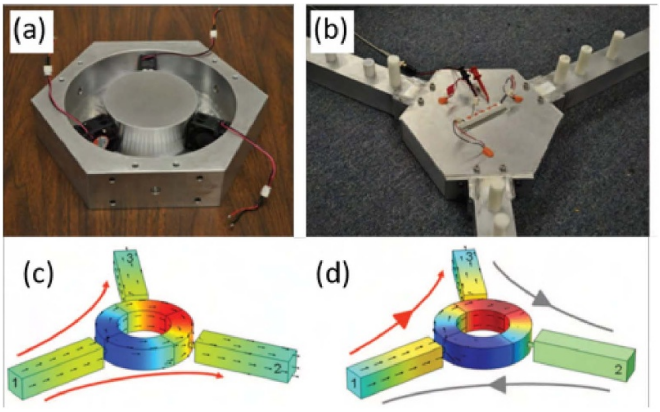

Figure 25. (a) Photograph of part of the interior of one unit cell of a non-reciprocal acoustic metamaterial containing a fan blowing air in the circular channel. The lid is intentionally taken off. (b) Photograph of what could be one metamaterial unit cell. (c) Acoustical-wave propagation without air circulation by the fan. Here, the wave impinging from the left equally splits to the left and right (or clockwise and counter-clockwise). (d) When the fan is activated, the symmetry is broken and the wave predominantly exits at the upper port. Such a circulator device can be used for isolation. From [383]. Reprinted with permission from AAAS.

4.1.6. Nonreciprocal behavior. In the previous subsection, we have discussed chirality, which requires broken space-inversion symmetry. At first sight, the effects of broken time-inversion symmetry can be similar to those of broken space-inversion symmetry, yet they are conceptually different.

For wave propagation in a linear-elastic lossless material that is not subject to temporal modulation (cf section 4.1.10), both, broken space-inversion symmetry and broken time-inversion symmetry, can lead to a frequency splitting of previously degenerate modes. Furthermore, both can lead to circularly polarized eigenmodes (chiral phonons). Thus, both can lead to a rotation of an incident linear polarization. However, for acoustical activity (see section 4.1.5), when going from $t \to -t$ (time inversion) or from $\overrightarrow{k} \to -\overrightarrow{k}$ (reflection of the wave), the reciprocity condition

$$\omega_{\pm}\left(-\overrightarrow{k}\right) = \omega_{\mp}\left(+\overrightarrow{k}\right)$$

holds true, because a left-handed transverse chiral phonon (index '+') turns into a right-handed chiral phonon (index '−') and vice versa when reversing the propagation direction—simply because the handedness is defined with respect to the propagation direction. Therefore, the polarization rotation angle ϑ is reversed, $\vartheta \to -\vartheta$, when reversing the propagation direction, $\overrightarrow{k} \to -\overrightarrow{k}$. Wave propagation is reciprocal—as for optical activity in optics. This behavior no longer holds true for broken time-inversion symmetry. As an extreme case, one may get $\vartheta \to +\vartheta$ for $\overrightarrow{k} \to -\overrightarrow{k}$, which would be the immediate mechanical counterpart of Faraday rotation in presence of a static longitudinal magnetic field in optics [378]. This direct counterpart has not yet been observed in mechanical metamaterials. Yet, there are other interesting possibilities that have.

For example, time-inversion symmetry in mechanics can be broken by a permanently rotating mechanical element within each metamaterial unit cell. Such a 'spinner' may rotate clockwise or counter-clockwise and is therefore analogous to aligned spins or permanent magnetic moments in ordinary magnetic materials, in which time-inversion symmetry is broken. Hence, the behavior becomes non-reciprocal. Designs and band-structure calculations for spinner-based chiral metamaterials, which break time-inversion and space-inversion symmetry, have been presented [379, 380]. For elastic wave propagation, the resulting behaviors include negative refraction [381] and one-way flexural waves [380]. Corresponding experimental demonstrations are elusive though. A potential application of gyro-elastic beams might lie in the vibration reduction of long flexural systems [382]. Micropolar elasticity (see section 2.1.4) should be able to grasp such linear-elastic non-reciprocal effects.

For longitudinal airborne sound waves, a clockwise or counter-clockwise rotation or spinning can be introduced by a constant circulating air flow in a ring cavity with rigid walls, e.g. by motor-driven fans built into in a sub-wavelength metamaterial unit cell [383] (see figure 25). The air flow leads to a Doppler frequency shift that depends on the sound propagation direction [383]. Likewise, an observer listening to airborne sound sitting on a bicycle driving with constant velocity $|v|$ in the same $(+v)$, or opposite $(-v)$ direction as the sound wave experiences a Doppler frequency shift $\Delta f \propto \mp v$. The ring cavity introduces a resonance acting as a spectral filter. reference [383] has pointed out the analogy to the electronic Zeeman effect (see figure 25): the acoustical frequency splitting is proportional to the constant velocity $|v|$ of the circulating air flow, just like the electronic Zeeman energy splitting [384] is proportional to the applied constant magnetic field $|\mathbf{B}|$. On this basis, acoustical isolation has been demonstrated experimentally, with up to 40 dB isolation at around 800 Hz frequency [383]. Such non-reciprocal acoustical-metamaterial unit cells also allow for obtaining topological band gaps and corresponding protected edge states, which we discuss in section 4.1.9.

We will address further approaches for obtaining non-reciprocal metamaterial dynamic behavior in the context of active metamaterials in section 4.1.10.

We note in passing that diode-like behavior for airborne sound can also be achieved by reciprocal metamaterials without any active (cf section 4.1.6), moving, or rotating parts [385]. Here, the underlying mechanism is asymmetric conversion between an even and an odd acoustic-waveguide mode. Using a quasi-1D metamaterial, the authors demonstrated, by calculation and experiment, highly asymmetric sound propagation with respect to the forward and backward directions in a narrow frequency range centered at about 2.3 kHz. This behavior is reciprocal and obeys time-inversion symmetry.

So far, in this subsection, we have discussed the dynamic case. The Maxwell–Betti definition applies to the static case in mechanics [386]. In 1D form, it states that a material is reciprocal if

$$F_{\mathrm{L}} u_{\mathrm{R}} = F_{\mathrm{R}} u_{\mathrm{L}}.$$

Here, F_{L} (F_{R}) is the force in the positive (negative) x-direction applied to the left-hand side (right-hand side) of a material, leading to a displacement u_{R} (u_{L}) in the positive (negative) x-direction on its right-hand side (left-hand side). For this definition to make sense, the material needs to be anchored at some point; otherwise the applied force leads to an overall translation of the material's center of mass. In the linear-elastic regime, the Maxwell–Betti condition is always fulfilled due to Hooke's law with $|F(u_x)| = |F(-u_x)|$. This means that every linear-elastic metamaterial is reciprocal in the static regime. For an arrangement (material and anchoring) that is symmetric with respect to swapping left (L) and right (R), the Maxwell–Betti condition is fulfilled by symmetry, even within the nonlinear-elastic regime. However, for asymmetric (meta)materials in the nonlinear-elastic regime, the behavior can be non-reciprocal according to Maxwell–Betti. The experiments in [387] have shown a quasi-1D asymmetric nonlinear buckling mechanical metamaterial composed of ten unit cells as an example, for which the non-reciprocal effects are pronounced. We will come back to nonlinear buckling metamaterials with $|F(u_x)| \neq |F(-u_x)|$ in section 3.2. Possibly, static non-reciprocal nonlinear mechanical metamaterial behavior can be applied in terms of force isolation [387].

4.1.7. Inertial resonators. In the previous two subsections, we have discussed chirality and non-reciprocal behavior in metamaterials. We would like now to discuss some design of mechanical metamaterials reminiscent of the former, although the effect we are after here is rather a local resonance within each unit cell, that does not induces necessarily some chirality or non-reciprocity. So-called inertial resonators (IRs), such as in figure 26, see [388, 389] make possible a class of standing waves in a periodic system containing inclusions with the structured coating. The vibration modes in the simplified mechanical model in figure 26(b) are obtained via the introduction of the rotation angle $\delta(t)$. Let u_r and u_δ denote the radial and tangential displacements on the contour of the void. Direct derivation shows that the rotational motion of the core region is governed by the differential equation [388]

$$\frac{d^2}{dt^2}\delta + \omega_0^2 \delta = \frac{\omega_0^2}{R_i \cos\eta}(u\delta \sin\alpha - u_r \cos\alpha) \tag{93}$$

with geometrical parameters α, η, and R_i defined in figure 26(b) and vibration frequency

$$\omega_0 = 2\sqrt{\frac{\kappa}{M}}\cos\eta. \tag{94}$$

Here M is the mass of the central core region, $\kappa = EA/l$ is the total longitudinal stiffness of inclined bars, E is Young's modulus, l is the beam length, and $A = NA_s$ is the total cross-sectional area of the N bars with the cross section A_s and thickness s. We note that ω_0 vanishes when the connecting bars become radial, which corresponds to the degenerate case, where flexural deformation of the bars has to be taken into account, and the eigenfrequency of the corresponding vibration mode is substantially reduced.

However, with a bit more work, in the degenerate case it is found that the natural frequency ω_0 of the system in figure 26(a) is [388]

$$\omega_0 = \sqrt{\cos^2\eta + \frac{s^2}{3l^2}\left(3\sin^2\eta + 3\frac{l}{R_i}\sin\eta + l^2 R_i^2\right)} \times \sqrt{2\frac{\kappa}{M}}. \tag{95}$$

The eigenfrequencies, estimated in (94) and (95), can be efficiently tuned by changing geometric and material parameters of the composite, such as relative inclinations, number, and cross section of the beams. The asymptotic estimate (95) predicts with a good accuracy the frequency corresponding to a localized rotational mode within a square array of IRs. Although the formulas (94) and (95) are derived on the basis of an asymptotic model of a single resonator, this is exactly what is required for analysis of a standing wave on an elementary cell of a doubly periodic structure. The vibration modes for such a standing wave are localized, so that on the boundary of the elementary cell of periodicity the amplitude of displacements is negligibly small compared to the displacement amplitude within the rotational resonator. Interestingly, a similar design was proposed in the context of acoustic metamaterials displaying frequency dispersive effective density and bulk modulus [390].

A 3D counterpart of the previous IRs has been experimentally validated in [391]. A photographic image of the unit cell is shown in figure 27(a). A steel cylinder, with a radius $r = 15.8$ mm and height $h = 37.6$ mm, is coated with silicone rubber. The cylinder's axial direction is defined as the z-axis, and the xy-plane is parallel to the end surfaces. The silicone layers on the top and at the bottom of the steel cylinder are both 1 mm in thickness; whereas the silicone covering the curvilinear side has a thickness of 5 mm. The silicone-coated steel cylinder is then cast inside an epoxy cube with each side $a = 60$ mm. The physics of this unit cell can be understood

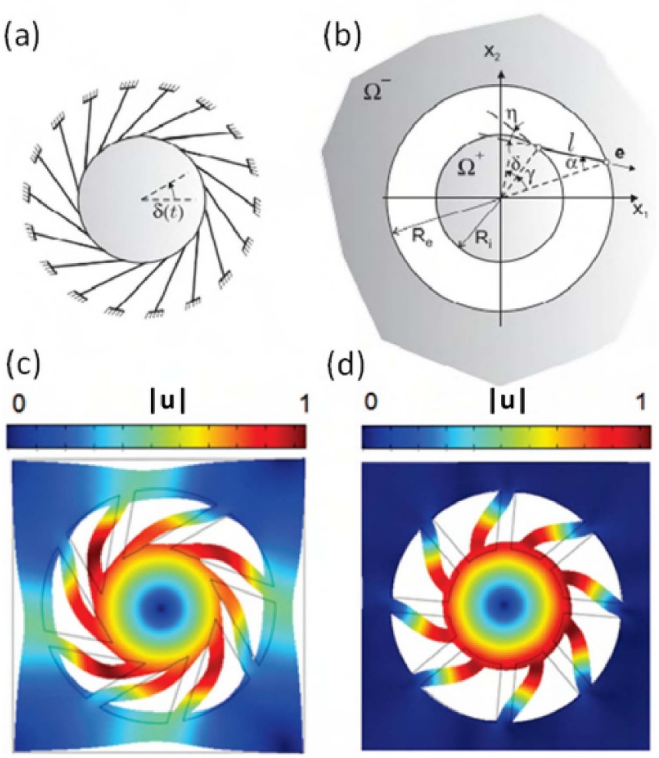

Figure 26. Structural interface for a circular inclusion Ω^+ in a continuum medium Ω^-. The beams have length $l = \sqrt{R_i^2 + R_e^2 - 2R_eR_i\cos\gamma}$, thickness s, and relative inclination $\eta = \pi/2 - \gamma - \alpha$. (a) Simplified model for the asymptotic approximation. (b) Detail of the geometrical parameters. (c), (d) The unit cell and its rotational eigenmodes for the case of ligaments with large (c) and small (d) inclination. Reprinted (figure) with permission from [388], Copyright (2013) by the American Physical Society.

with a simple mass-spring-mass model, as shown in the inset of figure 27(a). Here the steel cylinder and the epoxy cladding mostly have the role of two block masses, M1 and M2, which interact through compression and expansion of the silicone rubber that acts as springs. Owing to the difference in the silicone's thickness, the spring constants in relevant positions are different (denoted by K for the side, and K′ for top and bottom, respectively).

4.1.8. Rotons. In the absence of local resonances, usual transverse or longitudinal acoustic phonon dispersion relations emerge from zero frequency at zero wave vector with constant phase velocity, and bend over towards the edge of the first Brillouin zone. It has been shown theoretically [392, 393] that two distinct mechanisms in metamaterials can drastically modify this behavior in that a minimum of $\omega(\vec{k})$ occurs for the lowest band at some finite wave vector within the first Brillouin zone. Such roton minimum is known from the dispersion relation in superfluid helium [394] and other correlated quantum systems at low temperatures [395]. It is connected to a region

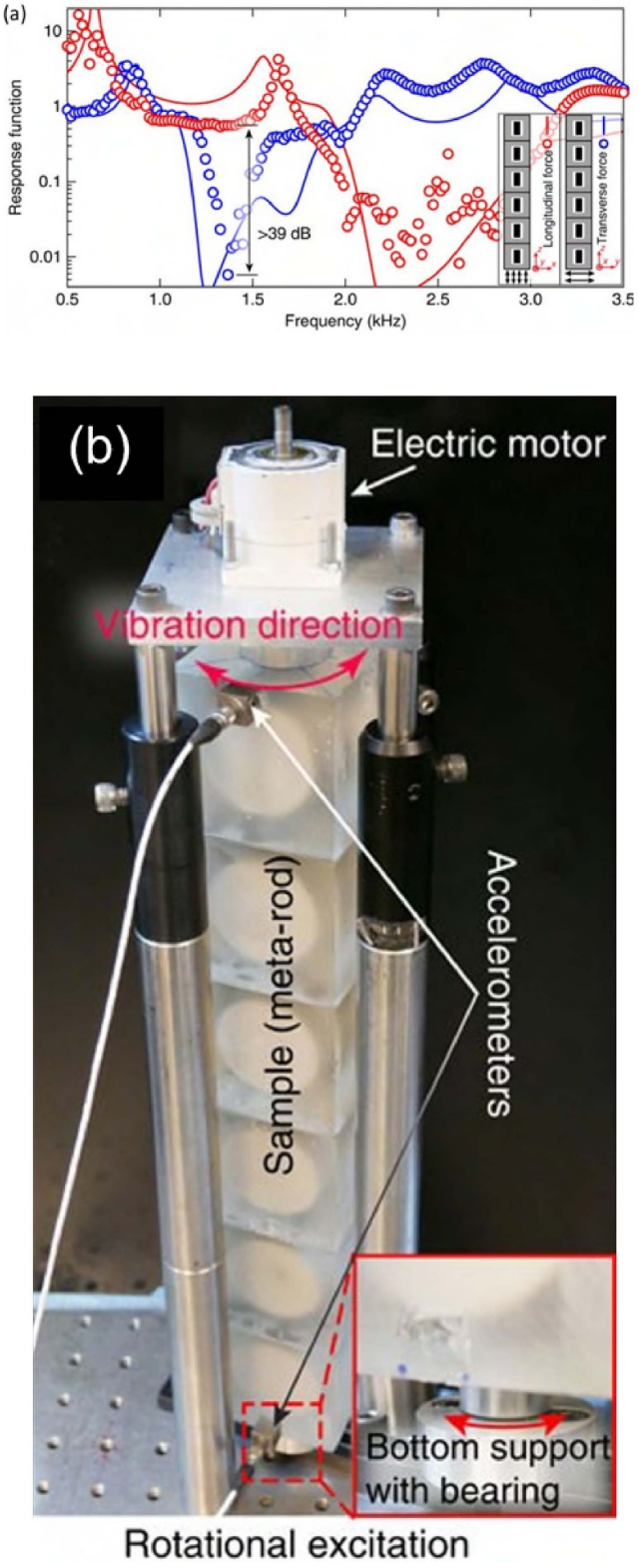

Figure 27. (a) Measured response functions of longitudinal and flexural waves. A bandgap for flexural waves is seen in 1.2–1.6 kHz, which overlaps with longitudinal waves passband. (b) An electromagnetic shaker is used for transverse excitation which exerts a torque pulse on the meat beam composed here of few unit cells. Reproduced from [391]. CC BY 4.0.

for which the phonon group velocity vector $\vec{v}_{gr}$ and the phonon phase velocity vector $\vec{v}_p$ point in opposite directions, i.e. $\vec{v}_{gr} \cdot \vec{v}_p < 0$. This behavior can effectively be described by a negative refractive index. However, one should be clear that the roton dispersion relation in this region has three different solutions for a given frequency ω and for a given propagation direction, associated to three different wavelengths and three different refractive indices. One of the two suggested mechanisms [392] is based on chirality and has explicitly been worked out on the level of Eringen micropolar elasticity. Experiments are elusive. The other mechanism [393] is based on sufficiently strong third-nearest-neighbor interactions in addition to the usual nearest-neighbor interactions among metamaterial unit cells. This non-local [393] mechanism does not require chirality, but can be combined with chirality [393]. It has been argued that, in this case, strain-gradient theory is able to qualitatively grasp the roton behavior on the level of effective media [396]. Experiments have recently been performed [396] on (achiral) metamaterials supporting airborne longitudinal pressure waves in a channel system at frequencies of audible sound and on microstructured elastic (achiral) metamaterial beams supporting transverse rotons at ultrasound frequencies. The latter experiment is illustrated in figure 28. Part of the manufactured metamaterial sample is illustrated in figure 28(a), where the parts mediating the third-nearest-neighbor interaction are highlighted in red. Importantly, these interactions unavoidably require a 3D metamaterial structure. Otherwise, crossings of the beams cannot be avoided [396]. The acoustical metamaterial phonon dispersion relation, measured on a sample containing 50 unit cells along the propagation direction is shown in panel (b), alongside a numerically calculated band structure for the same finite-size beam. The roton minimum is clearly visible in both, experiment and theory. For this particular structure, roton behavior occurs only for waves propagating along the z-direction. Other metamaterial realizations of third-nearest-neighbor interactions and beyond are conceptually possible in two dimensions [397]. If these can be realized experimentally, one has the possibility to obtain any shape of the lowest acoustical phonon dispersion relation in the sense of a Fourier expansion. Herein, the N-th Fourier coefficient is proportional to the strength of the Nth nearest-neighbor interaction [397].

4.1.9. Topologically protected states. The mature field of phononic crystals [11] has largely been driven by obtaining stop bands and complete band gaps for elastic wave propagation. Complete band gaps for bulk phonon modes can be accompanied by modes that exist at the surface of a phononic crystal. While the eigenfrequencies of such modes may accidentally lie inside of the phononic band gap, this condition is generally not guaranteed at all.

However, for a special class of band gaps called topological band gaps, this condition is guaranteed [404]. The notion of topological band gaps is connected to topological phases and was originally developed for quantum-mechanical electronic systems [405–407]. It has been argued that the associated surface or edge modes are robust against perturbations

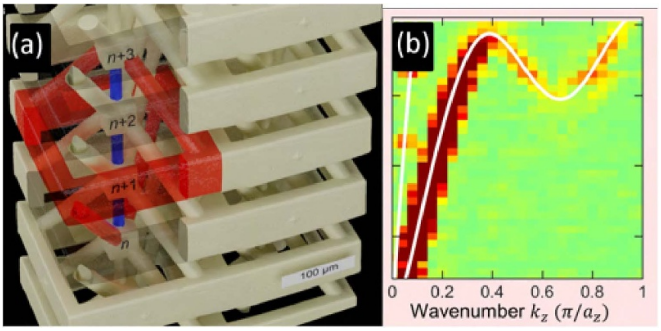

Figure 28. (a) Part of the manufactured metamaterial sample reconstructed by optical imaging with the parts mediating the third-nearest-neighbor interaction which is highlighted in red. (b) Experimentally measured dispersion relation for the fabricated sample. Reproduced from [396]. CC BY 4.0.

[400]. However, no metrics are available yet allowing for quantifying the robustness of an edge mode. In mechanics, such edge modes can also occur in the static regime [401, 408]. Theory has systematically classified the conditions for 1D, 2D, and 3D topological band gaps to occur in classical mechanical architectures [404, 409]. Envisioned applications include unidirectional propagating of edge modes in 2D systems [400] as robust elastic waveguides, analogous to the edge states in quantum-Hall-effect physics [410], and protected twist edge states for chiral resonant mechanical laser beam scanners [411].

A paradigmatic model for topological gaps is the quantum-mechanical Su–Schrieffer–Heeger (SSH) model for electrons [412]. A classical mechanical variant is the 1D diatomic mass-and-spring lattice illustrated in figure 30. In solid-state physics, one mostly discusses the case of unequal masses, $m_1 \neq m_2$, and equal Hooke's spring constants, $D_1 = D_2$. This leads to acoustical and optical phonon modes with a frequency gap in between. This gap turns out to be not topological. The opposite case of equal masses $m_1 = m_2$ and unequal spring constants $D_1 \neq D_2$ can lead to a topological band gap between the acoustical and the optical phonon modes for certain parameter combinations [404, 411, 413].

The diatomic basis of the SSH model has inspired a variety of topological mechanical metamaterials in different dimensions [404, 414].

However, diatomic unit cells (see figure 29) are not a necessary condition for topological band gaps. The circulating-airflow acoustical metamaterials [383] discussed in section 4.1.6. are an example. A selection of experimentally realized topological mechanical metamaterials and examples of edge states are depicted in figure 30. Further work can be found in [298, 398, 399, 409, 414–423]. It should be also noted that non-commutative differential geometry developed in the late 70s and 80s by Connes [424] (building upon the earlier work of Grothendieck, Atiyah and Hirzebruch on topological K-theory [425]), has been applied to the quantum Hall effect [426] and it offers an interesting avenue to study topological insulators in disordered and quasiperiodic systems [427–429]. From an engineering standpoint, group theoretic and topological concepts have been employed to geometrically design

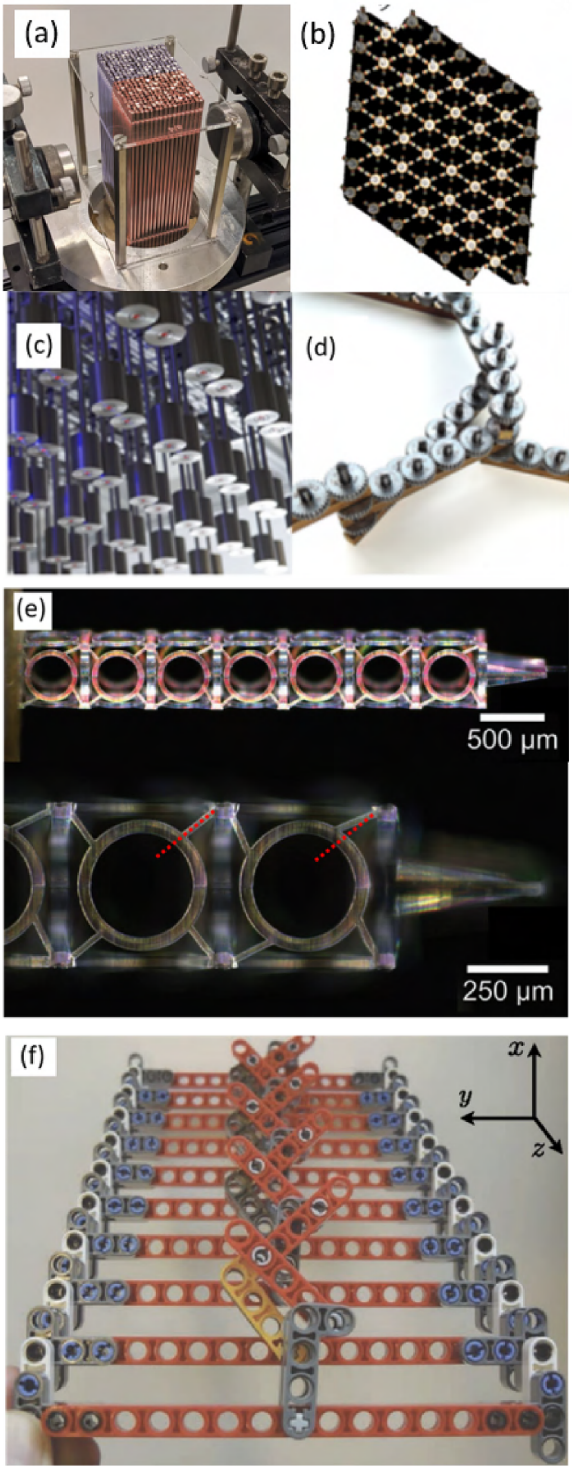

Figure 29. Examples of structures showing topological insulator behavior for elastic waves or deformations. (a) Topological waves guided by a glide-reflection symmetric crystal interface in underwater acoustics. Reprinted (figure) with permission from [398], Copyright (2022) by the American Physical Society. (b) Topological spinner metamaterial. Reprinted (figure) with permission from [399], Copyright (2020) by the American Physical Society. (c) Elastic topological metamaterial. From [400]. Reprinted with permission from AAAS. (d) Geared Topological Metamaterial. Reproduced from [401]. CC BY 3.0. (e) 3D chiral topological metamaterial. Reproduced from [402]. CC BY 4.0. (f) Nonlinear conduction via solitons in a topological mechanical insulator. Reproduced with permission from [403].

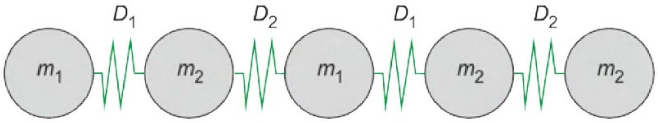

Figure 30. Mass-and-spring model analogous to the SSH model for electrons [412]. For $m_1 = m_2$ and $D_1 \neq D_2$, one obtains a topological band gap, whereas one does not obtain a topological band gap for $m_1 \neq m_2$ and $D_1 = D_2$.

interfacial wave networks that contain splitters which partition energy in two, three, four, or five directions for flexural waves in thin plates [241, 430, 431], surface water waves [432] and acoustic waves [433]. Figure 31 summarizes the recipe to design a topologically protected flexural edge wave propagating along the interface separating two regions of a thin elastic plate with doubly periodic arrays of square perforations rotated through opposite angles (counter-clockwise above the interface and clockwise below). Figure 32 further demonstrates the principle of a topological rainbow, wherein a gradual variation of the topological crystal plate thickness in figure 31 allows for the concentration of the edge wave energy in a desired region of the plate. An analogous elastic energy trapping via a topological rainbow has been proposed with a graded SHH system consisting of pillars of varying height atop a thin elastic plate [434]. Other effects including cloaking in graded metamaterials are discussed in section 5.

4.1.10. Active metamaterials. The definition of active mechanical metamaterials is that they require an external input to function. This input can, for example, be electrical, which makes the metamaterial hybrid in nature. Being active includes the possibility that energy is transferred from the external input to the mechanical/acoustical wave or vice versa [435].

In section 4.1.6, we have already mentioned two examples of non-reciprocal metamaterials (based on spinners and circulating air flows) that need active input or energy supply if friction is not zero. Another approach toward obtaining non-reciprocal and unidirectional acoustical sound propagation makes the active aspect more obvious: conceptually, one could mount an array of sub-wavelength microphones on one side of a rigid wall. These microphones transmit their signals electrically to an array of sub-wavelength loudspeakers on the other side of the wall. Obviously, the sound would only be transmitted through the wall in one direction (unidirectional) over a large frequency range. A single compact sub-wavelength active nonlinear non-reciprocal acoustic metamaterial unit cell performing such diode or rectifying function with about 10 dB isolation at around 3 kHz frequency has been demonstrated experimentally [437].

An immediate real-world application of active acoustical and mechanical metamaterials lies in noise cancelation and vibration cancelation, respectively. The underlying idea is similar to commercially available active-noise-cancelation headsets: a sub-wavelength detector senses local forces or pressures and an electrical feedback circuit combined with a sub-wavelength transducer (or loudspeaker) imposes a

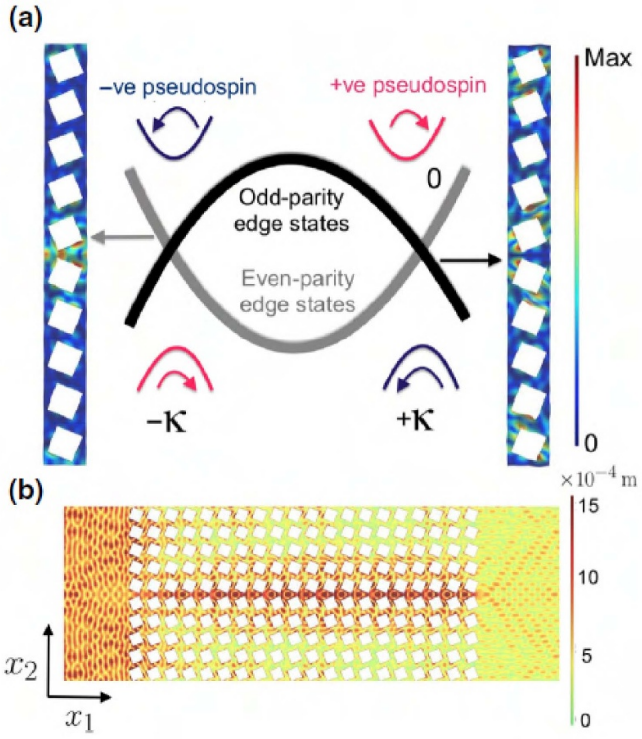

Figure 31. Topologically protected flexural edge waves in a plate with soft soil elastic parameters: panel (a) illustrates opposite parity edge states appearing inside the stop band of a periodic medium (a thin elastic plate with square stress-free perforations of sidelength 2m and center-to-center spacing 3m), when an interface is created in a ribbon thanks to a mirror symmetry of the geometry about the horizontal x_1 axis, half way from the top and bottom boundaries. Some periodic conditions are assumed on top and bottom, and Floquet–Bloch conditions on left and right boundaries. The two ribbon eigenmodes shown depict the absolute values of the out-of-plane components of the modes propagating along the interface between oppositely orientated squares. Periodic boundary conditions have been applied to the left- and right-hand sides of this ribbon with Floquet–Bloch conditions applied along the top and bottom boundaries. Panel (b) shows how an even-parity flexural edge state is excited in an elastic plate of constant thickness (10 cm) by a left-incident plane wave at frequency $\omega\kappa/(2\pi) = 16.5$ Hz. Reprinted (figure) with permission from [242], Copyright (2021) by the American Physical Society.

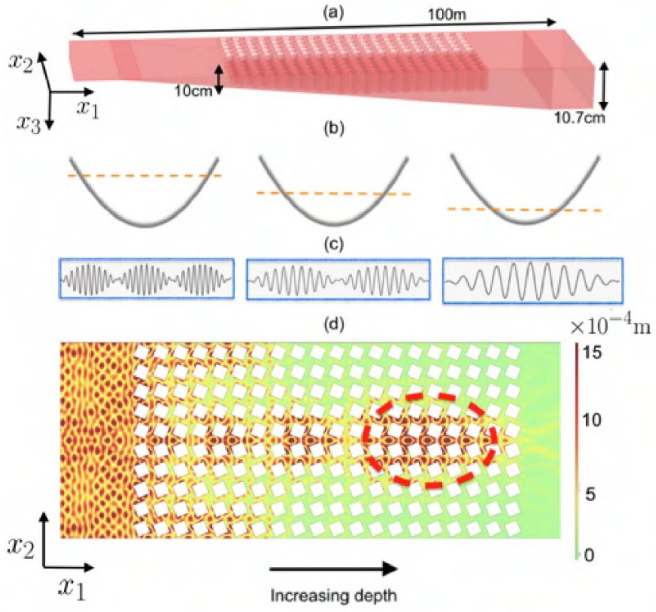

Figure 32. Panel (a) is a schematic of the periodically perforated soil plate that varies in depth (from 10 cm to 10.7 cm). By sending in a plane-wave source of fixed frequency $\omega_\kappa/(2\pi) = 17.3$ Hz, the rightward mode excited shifts its position along the even-parity dispersion curve (shown in figure 31(a)). The source amplitude has a magnitude of 1.6×10^{-4} m and the corresponding vertical displacement is of the order 10^{-4} m. As the depth of the elastic substrate increases, the curve shifts upwards (black solid line) whilst the excitation frequency (orange dashed line) remains unchanged. As the modal excitation approaches the standing wave at Γ point (minimum of the considered dispersion curve) the period of the envelope modulation decreases as shown in (c), hence a rainbow effect. The magnitude of the out-of-plane component of the displacement is shown in panel (d); the region of concentrated energy is highlighted by the red dashed circle. Reprinted (figure) with permission from [242], Copyright (2021) by the American Physical Society.

corresponding counter-force or pressure, leading to zero net force or pressure. Along these lines, an active acoustic liner for aircraft-engine noise reduction, based on a 2D array of 120 microphones and 30 loudspeakers (which might also be called a metasurface), operating at around 1 kHz frequency, has been designed and validated experimentally [438].

Using combinations of microphones and transducers in active metamaterials alternatively allows for amplifying sound or vibrations. Such gain can compensate for losses, leading to effectively lossless metamaterials. This compensation can, for example, be achieved by an alternation of unit cells with gain and loss. Such metamaterials can be designed to obey parity-time (PT) symmetry [439, 440]. There, both loss and gain individually violate time-inversion symmetry ($t \to -t$). The alternation also breaks parity or space-inversion symmetry $\vec{r} \to -\vec{r}$ (cf section 4.1.5). However, the PT-symmetric metamaterials are invariant under the combined operation $(\vec{r}, t) \to (-\vec{r}, -t)$. Such metamaterials are inherently unstable in the sense that precautions must be taken that the gain does not overcompensate the loss, in which case exponentially diverging wave amplitudes would result. Early work on macroscopic 1D acoustical metamaterials was based on discrete components in a cylindrical waveguide [441]. Using non-Foster electrical feedback circuits [442], demonstrated experimentally a non-invasive, shadow-free, invisible sensor for airborne sound waves at audible frequencies (see also [443] for an analogous effect of reflectionless and trapped modes in a waveguide with an obstacle satisfying certain symmetries). This sensor fully absorbs the impinging signal, without perturbing its own measurement and without creating an acoustic shadow. An interesting more integrated approach has been presented based on using the acousto-electric effect in piezoelectric semiconductors [444]. Here, by tuning the gate voltage applied to the piezoelectric materials, the 1D PT-symmetric metamaterial could theoretically be brought to

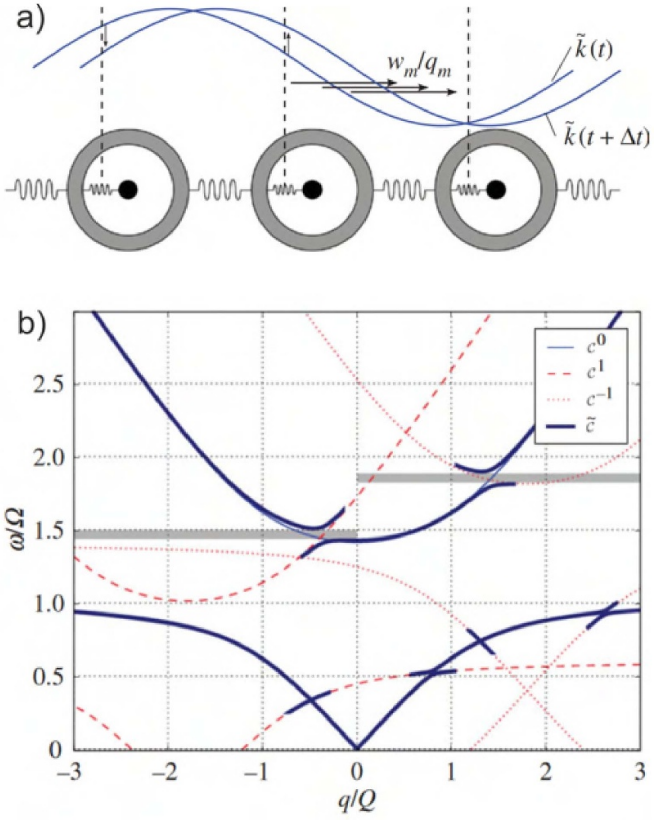

Figure 33. (a) Principle of modulated mechanical metamaterial. (b) Dispersion relation of a modulated mass-spring chain. Reproduced with permission from [436]. © 2017 The Author(s) Published by the Royal Society. All rights reserved.

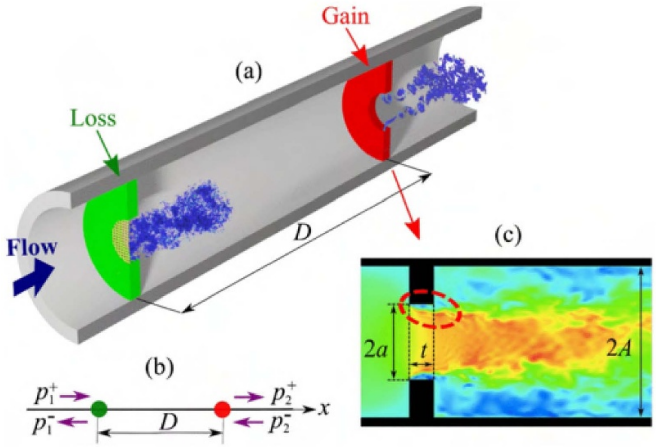

Figure 34. (a) Sketch of the acoustic $P-T$-symmetric system in an airflow duct. (b) Corresponding 1D model. (c) Numerical simulation with Large Eddies Simulation of the flow in the diaphragm in the presence of an acoustic wave. Reprinted (figure) with permission from [445], Copyright (2017) by the American Physical Society.

so-called exceptional points, allowing for unidirectional suppression of wave reflection (see also figure 34 for P-T a system in air acoustics).

Another specific opportunity of active metamaterials arises from modulation of the properties of the individual metamaterial unit cells. This modulation can, for example, be time-harmonic, with angular frequency ω_{mod}. A constant phase shift, ζ, between adjacent metamaterial unit cells, with fixed period or lattice constant a, leads to a modulation wave number $k_{\text{mod}} = \zeta/a$ and wavelength $\lambda_{\text{mod}} = 2\pi/k_{\text{mod}}$. The modulation wave propagates through the metamaterial with constant velocity $v_{\text{mod}} = \omega_{\text{mod}}/k_{\text{mod}}$. As a result, metamaterial phonons propagate in the presence of a metamaterial modulation wave. To avoid confusion, we emphasize that the metamaterial itself is not moving with respect to the laboratory inertial system.

A special case is that the properties of all unit cells are modulated with the same phase, i.e. zero phase difference $\zeta = 0$, which is equivalent to $\lambda_{\text{mod}} = \infty$. This setting simply corresponds to tunable mechanical metamaterial properties. We refer the reader to the experimental examples discussed in [446–450]. Tunability is distinct from programmability, which is discussed in section 3.2.

To get a first feeling for the generally very rich behavior arising from metamaterial modulation-waves, we consider the 1D mass-in-mass and spring model with lattice constant a in figure 33. Without temporal modulation, this model can describe a frequency-dependent effective dynamic mass density [451] (compare section 4.1.3). The inner spring constants $D_n(t)$ are modulated in time according to

$$D_n(t) = D + \delta D \cos(k_{\text{mod}} x - \omega_{\text{prop}} t),$$

with $x = na$ and the modulation amplitude $0 \neq \delta D \ll D$. All actual masses shall be constant in time. An example of the resulting metamaterial phonon dispersion relation $\omega(k)$ as obtained from perturbative Floquet–Bloch analysis is shown in figure 33. Obviously, $\omega(k) \neq \omega(-k)$, indicating non-reciprocal or unidirectional behavior (compare section 4.1.6). In particular, note the two narrow frequency intervals for which waves with wave number $k > 0$ $(k < 0)$ experience a stop band, whereas those with wave numbers $k < 0$ $(k > 0)$ do not. By tuning the modulation frequency and amplitude, these unidirectional stop bands could be adjusted dynamically.

A corresponding macroscopic 1D prototype experiment based on 15 metamaterial unit cells has been presented [452]. Herein, the tunable Hooke's springs have been realized by a permanent magnet inside of a magnetic coil in each metamaterial unit cell (see figure 35. By modulating the electrical current through the magnetic coil, the effective Hooke's spring constant could be modulated individually for each unit cell. Non-reciprocal wave propagation and unidirectional frequency conversion were observed experimentally at frequencies around 300 Hz [452].

4.2. Reversible nonlinear, multi-stable, and programmable elasticity

Nonlinear elastic behavior of a mechanical metamaterial may result from reversible elastic nonlinearities of its constituent material(s). This case shall not be discussed here (cf section 4.3). From the viewpoint of metamaterials, it is more interesting that the effective properties can also become nonlinear, multi-stable, and programmable due to geometrical

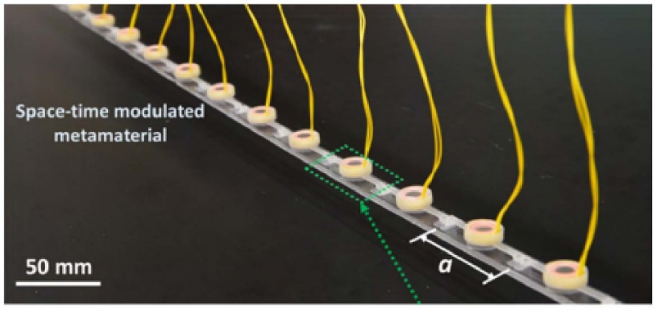

Figure 35. Photograph of fabricated modulated metamaterial samples containing an array of magnets and coils periodically distributed over the beam. Reprinted (figure) with permission from [452], Copyright (2019) by the American Physical Society.

nonlinearities of the metamaterial architecture. Conceptually, this is true even for strictly linear-elastic Hooke's behavior of the constituent material(s).

Within the linear elastic regime, all displacement components and strains are simply proportional to each other. Mechanical metamaterials have been constructed mathematically in which one strain component can be any wanted nonlinear function of another strain component [453, 454]. Such a feature follows from [29] that demonstrates that all of the elements of the deformation tensor for periodic non-linear affine unimode metamaterials constructed from rigid bars and pivots can be arbitrary functions of one element, subject to the natural restriction that the determinant of the deformation gradient remains positive. Experiments along this line have not been reported so far.

A paradigmatic motif that can be part of a different type of nonlinear mechanical metamaterial unit cells is the buckling beam [456–460]. A large variety of interesting metamaterials based on buckling have been realized experimentally over the years [455, 460, 461]. An example is shown in figure 36(d). A suspended single buckling beam exhibits an S-shaped behavior of the force F versus the beam displacement u. The region of negative slope is stable under displacement control, but unstable under force control. If an integer number, $N \geqslant 1$, of such buckling elements (with index i) are arranged in serial, the forces $F_i = F$ are the same for all unit cells and the individual displacements u_i add up to the total displacement, $u = \sum_i u_i$. When controlling the total displacement u in an experiment, this simple condition couples the different unit cells in a non-local manner: If, for example, the displacement of one particular unit cell, u_j, changes, all other unit cells with $i \neq j$ have to adjust accordingly, such that the sum of all displacements equals the predetermined value u. This means that the periodicity of a metamaterial that is periodic without external forces is spontaneously broken by individual buckling processes.

The consequences are illustrated in figure 36(c). The serial arrangement of buckling units leads to multi-stable behavior of the metamaterial under displacement control, connected to discontinuous switching processes, multiple stable solutions at a given displacement value, and hysteretic behavior. The area enclosed by the hysteresis curve in the force-displacement

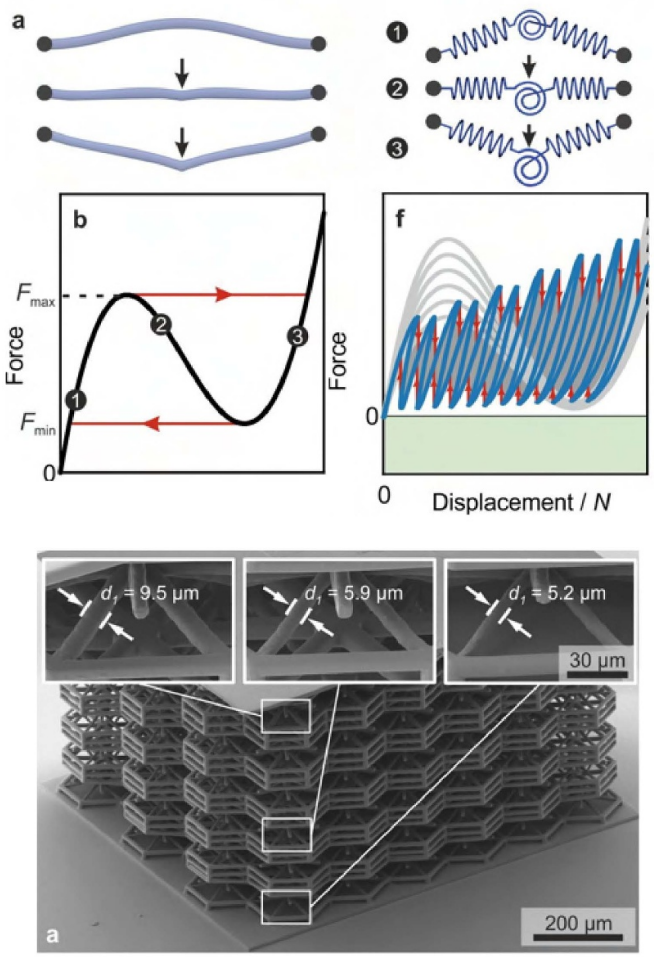

Figure 36. (a) Principle of buckling-based metamaterials. (a) Schematical representation of a buckling element in three states and corresponding springs model. (b) Schematic force–displacement curve of the previous buckling bar. As (b) but for 6 pairs of different bucling elements layed in a serial way. (d) Experimental realisation inspired from (c). [455] John Wiley & Sons. © 2016 WILEY-VCH Verlag GmbH & Co. KGaA, Weinheim.

diagram in figure 36(b) is equal to the energy dissipated in one cycle of loading and unloading the metamaterial. If the constituent material behaves linear elastically and shows no deterioration effects, this dissipation can be used for repeatable energy (shock) absorption [455]. Furthermore, if the S-shaped curve of a single buckling unit leads to absolute negative forces (rather than only to a negative slope), the metamaterial will stay in a certain state once the external force is released [455]. This possibility of choosing a stable state can be interpreted as programmability of the mechanical metamaterial [455]. For example, the effective Young's modulus with respect to the programmed position can be varied along these lines. A variation of a factor of five has been demonstrated experimentally [455].

Furthermore, researchers have fabricated meta-beams out of buckling metamaterials [462]. In figure 37, one can see a slender meta-beams that displays discontinuous buckling for large enough non-linearity and a negative post-buckling slope.

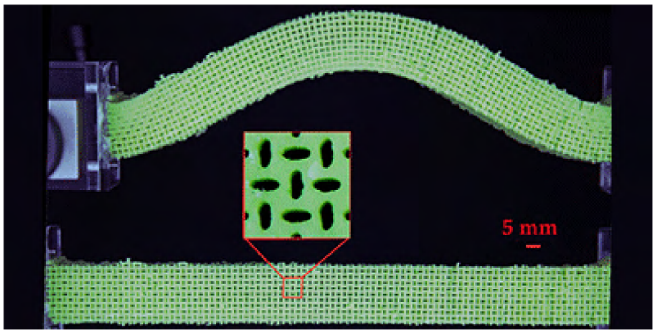

Figure 37. Example of buckling of a mechanical meta-beams under a compressive force. Reprinted (figure) with permission from [459], Copyright (2015) by the American Physical Society.

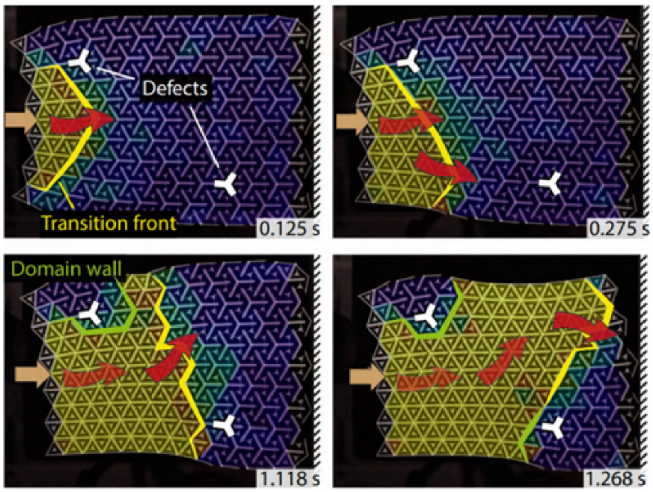

Figure 38. Transition based metamaterial: an impulse strain is propagating through the structure inducing transitions in the metamaterial. Reproduced with permission from [463].

Finally, designing successive buckling states can initiate some dissipative motion of topological defects such as phase and domain boundaries as illustrated in figure 38. Such multistable structures could be used for guided motion and reconfiguration in arbitrary dimensions and of arbitrary complexity. This opens an avenue towards extension of transformation elastodynamics to the strongly nonlinear transition front motion [463].

4.3. Irreversible mechanical behavior

Usual constituent materials follow Hooke's law for a certain range of strains, exhibit a small range of reversible elastic nonlinearity versus increasing strain, and then soon irreversibly deform plastically or fracture. For many real-world applications of materials, the maximum stress before irreversible failure, the strength $\widetilde{\sigma}$, is an important property. The strength of ordinary bulk materials is related to size effects such as the motion of dislocations and the nucleation of cracks [464].

Large metamaterial research efforts have been devoted towards keeping up the ratio $\widetilde{\sigma}_{\text{eff}}/\rho_{\text{eff}}$ with respect to σ/ρ of the

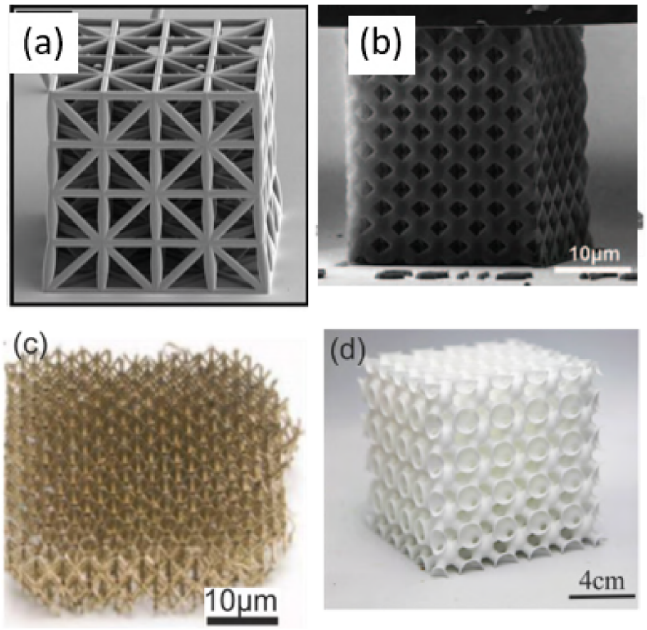

Figure 39. Gallery of electron micrographs of metamaterials with irreversible mechanical behavior. (a) High-strength cellular ceramic composites with 3D microarchitecture. Reproduced with permission from [465]. CC BY-NC-ND 4.0. (b) Strong, lightweight, and recoverable 3D ceramic nanolattices. From [466]. Reprinted with permission from AAAS. (c) Ultralight Metallic Microlattices. From [467]. Reprinted with permission from AAAS. (d) Closed tubular mechanical metamaterial. Reprinted from [453], Copyright (2020), with permission from Elsevier.

constituent material(s) [465] (for ρ_{eff} see section 4.1.1). Here, the buckling of beams and details of the nodes within truss lattices play a decisive role [465]. The experimental findings can be summarized by a scaling according to

$$\frac{\widetilde{\sigma}_{\text{eff}}}{\widetilde{\sigma}} \propto \left(\frac{\rho_{\text{eff}}}{\rho}\right)^{a},$$

with dimensionless coefficient a. Typically, this exponent lies between 1 and 2 [468]. For example, using a metamaterial based on a honeycomb topology and pyrolysis of the constituent polymer material to pure Carbon in the fabrication process, $\widetilde{\sigma}_{\text{eff}} = 1.2\,\text{GPa}$ and $\rho_{\text{eff}} = 600\,\text{kg}\,\text{m}^{-3}$ have been achieved [468]. Only diamond has a notably larger $\widetilde{\sigma}/\rho$ ratio [469].

It is interesting to ask how this irreversible mechanical behavior (see examples in figure 39) of a metamaterial is connected to its reversible linear-elastic regime. There, a related scaling has been found for the ratio $E_{\text{eff}}/\rho_{\text{eff}}$, with the effective metamaterial Young's modulus E_{eff}. The experimental findings can be lumped into the following general behavior

$$\frac{E_{\text{eff}}}{E} \propto \left(\frac{\rho_{\text{eff}}}{\rho}\right)^{b},$$

where E is the Young's modulus of the constituent material and b is a dimensionless coefficient. Typically, the exponent b lies between 1 and 3 [453]. We refer the reader to the following extensive reviews [460, 470], in which these issues have been emphasized.

5. Graded metamaterials

The fascination about cloaking and coordinate transformations (see section 5.1) was originally driven by the dream of making macroscopic objects under ambient conditions invisible with respect to light throughout the entire visible electromagnetic spectrum, for all viewing directions in transmission and reflection as well as for all polarizations of light [8, 471, 472]. In optics, a rather unwanted but unavoidable side effect is that a person inside of such an ideal cloak would literally stand in the dark. That is, a cloak isolates its inside electromagnetically from its outside. However, causality forbids the existence of such an ideal cloak [473]. Nevertheless, the idea of cloaking in optics raises the question: what is a meaningful counterpart of cloaking in mechanics? One immediate possibility is the idea of making macroscopic objects undetectable to airborne or waterborne sound for all relevant frequencies, e.g. for sonar applications. For the quasi-static case, consider a void or feedthrough in a supporting bulk material. The void would obviously make the system more compliant. An ideal quasi-static cloak around the hole makes the system material-void-cloak identical to the bulk material concerning all possible deformations. Concerning seismic waves on the earth's surface, an ideal cloaking structure would isolate seismically a sensitive infrastructure such as a nuclear power plant from the rest of the world, and thereby prevent damage or destruction. Here, the aspect of seismic invisibility is of no immediate importance for the power plant. However, a suitable graded metamaterial architecture could adiabatically guide enormous mechanical momentum and energy around the infrastructure, whereas any sort of localized reflector would fully swallow the momentum. An absorber would fully swallow the energy. Either would likely lead to destruction. Similar protective cloaks could be imagined for surface water waves. Despite of these interesting application possibilities, the truth is that many of the experiments to be discussed in this section were rather driven by scientific curiosity as to what is conceptually possible in mechanics. As discussed in section 2.2, the starting point in mechanics is different from electromagnetism. Whereas the Maxwell equations for continua are form invariant under arbitrary curvilinear spatial coordinate transformations [471, 474], classical textbook Cauchy continuum mechanics is generally not form invariant. At first sight, this mathematical fact appears to be a brutal showstopper. However, at least the following three different approaches remain.

- Investigate special cases of mechanics, for which the equations are form invariant (cf section 5.1).
- Search for approximate solutions (cf section 5.2).
- Consider generalized elastic continua beyond Cauchy elasticity (cf sections 2 and 3), for which the equations are form invariant.

5.1. Coordinate transformations

5.1.1. Spatial coordinate transformations. Inspired by the concepts of Einstein's theory of general relativity, transformation physics (optics [471, 472, 475–479], conductivity [480, 481], thermodynamics [482–484], acoustics [485–496] and elastodynamics [437, 497–505]) maps fictitious distortions of space onto actual spatially inhomogeneous and generally anisotropic media in Cartesian laboratory space. However, unlike for the covariant Maxwell's equations governing the propagation of electromagnetic waves, Navier's equations do not generally retain their form under coordinate transforms, especially if one wishes to preserve the symmetry of the elasticity tensor as noted by Milton, Briane and Willis fifteen years ago [497], in which case the transformed equation has the structure of modified Willis equations [506].

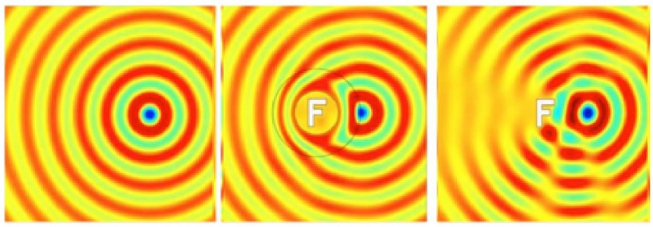

Figure 40. Wave pattern for a monopolar acoustic source radiating in (left) free space, (middle) in presence of a rigid obstacle surrounded by a transformed anisotropic heterogeneous medium (cloak), (right) in presence of a rigid obstacle. Wave patterns in left and middle panels are identical outside the cloak. One notes the wave undergoes a phase distortion inside the cloak, but without loss of amplitude.

The principle of the so-called transformational elastodynamics is to relate the change of material parameters in the physical domain to a spatial transformation. Indeed, the concept of material properties defined by transformation is not restricted to electromagnetism [471, 472, 507], as such coordinate changes can be applied to any governing equation in physics. Thus, this has stimulated research in other static and wave phenomena [19]. The paradigm of the area of wave physics known as transformational physics is so-called cloaking, whereby a scattering obstacle is concealed to acoustic, electromagnetic, surface water and even elastic waves thanks to an invisibility cloak. We illustrate the principle of a cloak in figure 40 for the case of pressure acoustic waves: a monopolar acoustic source radiates a concentric wave (left), which is distorted in phase and amplitude when it is located closeby a rigid 'F' obstacle (right). When the 'F' obstacle is surrounded by a ring of transformed medium', the concentric wavefront is restored outside the cloak (middle). The cloak could be viewed as a type of Perfectly Matched Layer (PML), without absorption: the wavefield has a phase which is smoothly distorted by the anisotropy inside the ring which is designed such that the ring's outer boundary is impedanced matched to free space, just like in a PML. However, the wave amplitude does not decrease inside the cloak, as it should inside a PML: If one replaces the cloak by a 'PML ring' in the middle panel, then one observes some damping of the wave on the exit of the cloak, which is analogous to 'the shadow region' in the right panel (although without phase distortion). Interestingly, some optical and acoustical 'black holes' have been proposed as another paradigm of transformational physics, that take their name from the Schwarzschild metric used to design the

transformed medium inside the ring. These devices trapped light/sound inside their core and could be viewed as advanced versions of 'PML rings'. The design of 'adaptative PMLs' for quasi-static fields and invisibility cloaks for the control of scattered field in elastodynamics has been studied in [508] in the framework of transformed media described by elasticity tensors without the minor symmetries (Cosserat media).

The main mechanism behind transformation optics was identified early in the sixties by Dolin [474] and used later in nineties for the construction of PMLs by Bérenger for electromagnetic problems [509]. In 2003, Greenleaf *et al* used a fundamental mathematical identity behind the transformational physics in their seminal work on making an object undetectable by electrostatic measurements [480, 510]. This fundamental mathematical identity is the equivalence of the heterogeneous Laplacian $\mathcal{L}$ in the original coordinates to a partial differential operator $\mathcal{L}'$ in the transformed coordinates (so-called transformed Laplace operator):

$$\begin{aligned} \mathcal{L} &:= \nabla_{\mathbf{X}} \cdot a \nabla_{\mathbf{X}} \mathbf{U} \\ \rightarrow \mathcal{L}' &:= \det(\mathbf{J})\, \nabla_{\mathbf{x}} \cdot \det(\mathbf{J})^{-1}\, \mathbf{J} a \mathbf{J}^T \nabla_{\mathbf{x}} \mathbf{u} \end{aligned} \tag{96}$$

with a an inhomogeneous parameter (a conductivity in the physical setup of [480, 510]), $\mathbf{J} := \mathbf{J}_{\mathbf{xX}} = \partial \mathbf{x} / \partial \mathbf{X}$ the deformation gradient of the transformation from transformed (say stretched Cartesian) coordinates $\{x, y, z\}$ to original (say Cartesian) coordinates $\{X, Y, Z\}$. The mathematical identity (96) holds if a is matrix valued.

In the work [480, 510], it is argued that to uniquely fix the solution u of the Laplace equation $\mathcal{L}(u) = 0$ in a domain Ω, it is enough to give u a value f on the boundary $\partial\Omega$. The uniqueness requires that a be a bounded and strictly positive function. Greenleaf, Lassas and Uhlmann thus introduce a singular coordinate transform (a blowup of a point)

$$\mathbf{x} = \left(\frac{|\mathbf{X}|}{2} + 1 \right) \frac{\mathbf{X}}{|\mathbf{X}|}\,, \; 0 < |\mathbf{X}| \leqslant 2 \tag{97}$$

that maps a ball of radius 2 centered on the origin (i.e. a disc in 2D and a sphere in 3D), onto a ring/shell of inner radius $|\mathbf{x}| = 1$ and outer radius $|\mathbf{x}| = 2$. This makes the parameter in $\mathcal{L}'$ singular anisotropic (eigenvalues of this parameter have no lower and/or upper bounds at $|\mathbf{x}| = 1$). Uniqueness of solution u then breaks down. For results on uniqueness depending upon various assumptions on a we refer to [511] and references therein. Closely related inverse problems are that of the reconstruction of a in the domain Ω from boundary measurements on $\partial\Omega$. Mathematically, one wishes to identify the Dirichlet to Neumann map DtN corresponding to a, i.e. the map taking the Dirichlet boundary values of the solution U to the Laplace equation $\mathcal{L}(U) = 0$ to the corresponding Neumann boundary values: $\mathrm{DtN} : U|_{\partial\Omega} \longmapsto \mathbf{n} \cdot a \nabla_{\mathbf{X}} U|_{\partial\Omega}$, with $\mathbf{n}$ the exterior unit normal to $\partial\Omega$. So-called Calderon's inverse problem (whose reprint of the original 1980 work can be found in [512]) is then to reconstruct a from the knowledge of the DtN map. This problem has been studied by numerous mathematicians, uniqueness results are available e.g. for an anisotropic conductivity a that is uniformly bounded from above and below. However, Kohn and Vogelius pointed out almost 40 years ago in [513] an observation of Tartar that for a diffeomorphism of a domain Ω fixing the boundary $\partial\Omega$, the Laplace equations $\mathcal{L}(U) = 0$ and $\mathcal{L}'(u) = 0$ have the same Dirichlet-to-Neumann map, thus producing infinite-dimensional families of indistinguishable conductivities. This can already be considered as a form of cloaking, since distinct conductivities in a domain are indistinguishable from boundary measurements, but further concealing an object requires the blowup transform introduced 20 years ago in [480, 510].

For the layman, invisibility is rather concealing an object or a person from an external observer, which concerns electromagnetic waves. Note that the aforementioned transform from stretched Cartesian coordinates $\{x, y, z\}$ to original Cartesian coordinates $\{X, Y, Z\}$ is known as a pull-back, and this has good properties for instance when using differential forms. Pendry, Schurig and Smith (unaware of the earlier work [480, 510]) applied the blowup transform (96) to the Maxwell's equations in their proposal of an invisibility cloak in [471]. This proposal is underpinned by a mathematical identity similar to (96) that holds for the transformed Maxwell's operator i.e. $\mathcal{M} : \nabla \times a \nabla \times \mathbf{u} \rightarrow \mathcal{M}' : \det(\mathbf{J}) \nabla \times \det(\mathbf{J})^{-1} \mathbf{J} a \mathbf{J}^T \nabla \times \mathbf{u}$, a being an inhomogeneous anisotropic parameter (the inverse of permittivity or permeability), as shown using the formalism of differential forms in [507]. However, as we shall see in the sequel, the transformed Navier operator is more involved. Before we move to the core of this section, which involves tensorial equations, we find it useful to recall the derivation of (96).

Let us now consider a map (a push forward) from a co-ordinate system $\{X, Y, Z\}$ to the co-ordinate system $\{x, y, z\}$ given by the transformation characterized by $x(X, Y, Z)$, $y(X, Y, Z)$ and $z(X, Y, Z)$. This change of co-ordinates is characterized by the transformation of the differentials through the Jacobian:

$$\begin{pmatrix} \mathrm{d}x \\ \mathrm{d}y \\ \mathrm{d}z \end{pmatrix} = \mathbf{J}_{xX} \begin{pmatrix} \mathrm{d}X \\ \mathrm{d}Y \\ \mathrm{d}Z \end{pmatrix}\,, \text{ with } \mathbf{J}_{xX} = \frac{\partial(x, y, z)}{\partial(X, Y, Z)}\,. \tag{98}$$

This Jacobian is the cornerstone of transformation physics. Before we study the case of transformed (tensorial) Navier equations for elastodynamic waves of any polarization, we would like to look at the simpler case of out-of-plane shear waves.

5.1.1.1. Transformation acoustics. A canonical example of transformed equation with physical interest is that of time-harmonic anti-plane shear waves propagating in an isotropic elastic medium with shear modulus μ_0 and density ρ_0:

$$\nabla_{\mathbf{X}} \cdot (\mu_0 \nabla_{\mathbf{X}} U) + \rho_0 \omega^2 U = 0 \tag{99}$$

where $\nabla_{\mathbf{X}}$ is the gradient in the coordinates $\{X, Y, Z\}$.

An elegant way to derive the so-called transformed Helmholtz equation is to multiply (99) by a test function Φ that is an infinitely differentiable and to further integrate by

parts over the domain Ω with particle location $\mathbf{X} = (X, Y, Z)$, which leads to:

$$\int_\Omega \mathrm{d}\mathbf{X}\left(\rho_0\omega^2 U\Phi\right) = \int_\Omega \mathrm{d}\mathbf{X}\left(\mu_0\nabla_{\mathbf{X}}U\cdot\nabla_{\mathbf{X}}\Phi\right) - \int_{\partial\Omega}\mathrm{d}\mathbf{S}\left(\mu_0\nabla_{\mathbf{X}}U\cdot\mathbf{N}\Phi - \mu_0\nabla_{\mathbf{X}}\Phi\cdot\mathbf{N}U\right) \tag{100}$$

where $\mathbf{N}$ is the unit outward normal to the boundary $\partial\Omega$ of the integration domain Ω. This equation is the variational form associated with (99) for out-of-plane displacement fields U of finite energy in Ω (in Hilbert space $H^1(\Omega;\mathbb{C})$ of complex valued functions which are square integrable and with square integrable gradient on Ω).

We now apply to (100) the coordinate change and noting that

$$\begin{aligned}\nabla_{\mathbf{x}} &= (\partial/\partial x, \partial/\partial y, \partial/\partial z)^T \\ &= \frac{\partial(X,Y,Z)}{\partial(x,y,z)}(\partial/\partial X, \partial/\partial Y, \partial/\partial Z)^T \\ &= \mathbf{J}_{\mathbf{X}\mathbf{x}}\nabla_{\mathbf{X}} = \mathbf{J}_{\mathbf{x}\mathbf{X}}^{-1}\nabla_{\mathbf{X}}\end{aligned}$$

or equivalently $\mathbf{J}_{\mathbf{x}\mathbf{X}}\nabla_{\mathbf{x}} = \nabla_{\mathbf{X}}$ where $\nabla_{\mathbf{x}}$ is the gradient in the new coordinates, we end up with

$$\begin{aligned}&\int_{\Omega'}\mathrm{d}\mathbf{x}\left(\rho_0\omega^2 u\phi\,|\det(\mathbf{J}_{\mathbf{X}\mathbf{x}})|\right) \\ &= \int_{\Omega'}\mathrm{d}\mathbf{x}\left\{\left(\mathbf{J}_{\mathbf{x}\mathbf{X}}\nabla_{\mathbf{x}}u\cdot\mu_0\mathbf{J}_{\mathbf{x}\mathbf{X}}\nabla\phi\right)|\det(\mathbf{J}_{\mathbf{X}\mathbf{x}})|\right\} \\ &\quad - \int_{\partial\Omega'}\mathrm{d}\mathbf{s}\left\{\left(\mu_0\mathbf{J}_{\mathbf{x}\mathbf{X}}\nabla_{\mathbf{x}}u\cdot\mathbf{n}\phi\right.\right. \\ &\quad \left.\left.-\mu_0\mathbf{J}_{\mathbf{x}\mathbf{X}}\nabla_{\mathbf{x}}\phi\cdot\mathbf{n}u\right)|\det(\mathbf{J}_{\mathbf{X}\mathbf{x}})|\right\}\end{aligned}$$

where $\mathbf{n}$ is the unit outward normal to the boundary $\partial\Omega'$ of the transformed integration domain Ω'. This is the variational form associated with the transformed Helmholtz equation. Further integrating by parts, we get that

$$\begin{aligned}&\int_{\Omega'}\mathrm{d}\mathbf{x}\left(\rho_0\omega^2 u\phi\,|\det(\mathbf{J}_{\mathbf{X}\mathbf{x}})|\right) \\ &= -\int_{\Omega'}\mathrm{d}\mathbf{x}\left\{\nabla_{\mathbf{x}}\cdot\left(|\det(\mathbf{J}_{\mathbf{X}\mathbf{x}})|\mathbf{J}_{\mathbf{x}\mathbf{X}}\mu_0\mathbf{J}_{\mathbf{x}\mathbf{X}}^T\nabla_{\mathbf{x}}u\right)\phi\right\}.\end{aligned}$$

Since this equation holds for any smooth function ϕ, one has

$$\nabla_{\mathbf{x}}\cdot\left(|\det(\mathbf{J}_{\mathbf{X}\mathbf{x}})|\mathbf{J}_{\mathbf{x}\mathbf{X}}\mu_0\mathbf{J}_{\mathbf{x}\mathbf{X}}^T\nabla_{\mathbf{x}}u\right) + \rho_0|\det(\mathbf{J}_{\mathbf{X}\mathbf{x}})|\omega^2 u = 0 \tag{101}$$

which we can also recast in operator form as $-\mathcal{L}'(u) = \rho_0\omega^2 u$ in agreement with (96) wherein $\mu_0 = 1$ and $\det(\mathbf{J}_{\mathbf{X}\mathbf{x}}) > 0$ (this excludes the case of space folding transforms).

When $\det(\mathbf{J}_{\mathbf{X}\mathbf{x}})$ is not a constant, this transformed equation (101) has not only a heterogeneous anisotropic shear modulus, but also a heterogeneous density. In the static limit when ω vanishes, the requirement on the spatially varying density can be relaxed. Similarly, in electromagnetics, transformed media have both spatially varying (and anisotropic) electric permittivity and magnetic permeability parameters [471], but in the static limit things also get simpler, when one need consider only (decoupled) transformed magnetostatic or electrostatic equations.

The non-uniqueness of the transformed material properties found by Greenleaf *et al* in electric impedance tomography [480] and then by Norris in acoustic cloaking theory [491] transfers to elastodynamics as we shall now see.

5.1.1.2. Transformation elastodynamics and cloak. The first study of the transformation of the elastodynamic equations by Milton *et al* [497] concluded that the appropriate class of constitutive equations for the transformed material is the Willis equations for material response. Indeed, these authors enforced the symmetry of the transformed elasticity tensor by considering a linear gauge between the displacement $\mathbf{U}$ at particle location $\mathbf{X}$ and the transformed displacement $\mathbf{u}$ at particle location $\mathbf{x}$:

$$\mathbf{U} = \mathbf{A}^T\mathbf{u} \tag{102}$$

where $\mathbf{A}$ is a non singular matrix. Note that the choice of a transpose matrix $\mathbf{A}^T$ in (102) means that $\mathbf{A}$ and the Jacobian matrix $\mathbf{J}_{\mathbf{x}\mathbf{X}}$ are similar mathematical objects (these are not rank-2 tensors as they are built with components of original and transformed domains).

Here, in the first paragraph, we will derive the transformation method for elastodynamics and then we will focus on the different problems derived in the general case.

5.1.1.3. General theory. The propagation of elastic waves in a domain Ω in a coordinate system $\{X, Y, Z, t\}$, where X, Y, Z are space variables and t is the time variable, is governed by the Navier equation

$$\nabla_{\mathbf{X}}\cdot\boldsymbol{\sigma} = \frac{\partial\mathbf{P}}{\partial t} \tag{103}$$

where $\nabla_{\mathbf{X}}$ is the gradient in the coordinates $\{X, Y, Z\}$, $\mathbf{P} = (P_J)$ the quantity of motion and $\boldsymbol{\sigma} = (\sigma_{IJ})$, $I, J = 1, 2, 3$, the stress tensor. Besides from that, $\mathbf{p}$ and $\boldsymbol{\sigma}$ are related to the displacement field $\mathbf{U} = (U_j)$ via

$$\boldsymbol{\sigma} = \mathbb{C} : \nabla_{\mathbf{X}}\mathbf{U}\ ,\ \mathbf{P} = \rho_0\frac{\partial\mathbf{U}}{\partial t}\ , \tag{104}$$

where $\mathbb{C} := (C_{IJKL})$ is the rank-four elasticity tensor, $\nabla_{\mathbf{X}}\mathbf{U}$ is the deformation rank-two tensor and ρ_0 the scalar density of the elastic medium.

Let us consider an isotropic homogeneous elastic medium with Lamé parameters λ and μ , so that $\mathbb{C}$ has the following 81 coefficients: $C_{IIII} = \lambda + 2\mu$ and if $I \neq J$, $C_{IIJJ} = \lambda$, $C_{IJIJ} = C_{IJJI} = \mu$.

Assuming time harmonic $\exp(-i\omega t)$ dependence, with ω as the angular wave frequency and t the time variable, allows us to work directly in the spectral domain, such as in the previous section. The time dependence is assumed henceforth and suppressed leading to

$$\nabla_{\mathbf{X}}\left(\mathbb{C} : \nabla_{\mathbf{X}}\mathbf{U}\right) + \rho_0\omega^2\mathbf{U} = \mathbf{0}\,. \tag{105}$$

Following [162, 307] (and also [514, 515] in the context of elastic near-cloaking theory), an elegant way to derive the so-called transformed time-harmonic Navier equation is to multiply (105) by a test function Φ that is infinitely differentiable and vanishes on the boundary $\partial\Omega$ of a domain Ω, and to further integrate by parts over the domain Ω with particle location $\mathbf{X} = (X, Y, Z)$, which leads to:

$$\int_\Omega \mathrm{d}\mathbf{X} \left(\rho_0 \omega^2 \mathbf{U} \cdot \Phi\right) = \int_\Omega \mathrm{d}\mathbf{X} \left(\mathbb{C} : \nabla_{\mathbf{X}} \mathbf{U} : \nabla_{\mathbf{X}} \Phi\right). \tag{106}$$

This equation is the variational form associated with (105) for displacement fields of finite energy that vanish on the boundary of Ω (in Hilbert space $H_0^1(\Omega; \mathbb{C}^3)$ of vector displacement fields of finite energy in Ω which vanish on the boundary $\partial\Omega$).

We now apply to (106) the coordinate change and noting that $\mathbf{J}_{\mathbf{xX}} \nabla_{\mathbf{x}} = \nabla_{\mathbf{X}}$ where $\nabla_{\mathbf{x}}$ is the gradient in the new coordinates, and using the same gauge (102) for both $\mathbf{U}$ and Φ, we end up with

$$\begin{aligned} &\int_{\Omega'} \mathrm{d}\mathbf{x} \left(\rho_0 \omega^2 \mathbf{A}^{\mathbf{T}} \mathbf{u} \cdot \mathbf{A}^{\mathbf{T}} \phi |\det(\mathbf{J}_{\mathbf{Xx}})|\right) \\ &\quad = \int_{\Omega'} \mathrm{d}\mathbf{x} \left\{ \left(\mathbb{C} : \mathbf{J}_{\mathbf{xX}} \nabla_{\mathbf{x}} \mathbf{A}^{\mathbf{T}} \mathbf{u} : \right.\right. \\ &\qquad \left.\left. \times \ \mathbf{J}_{\mathbf{xX}} \nabla_{\mathbf{x}} \mathbf{A}^{\mathbf{T}} \phi \right) |\det(\mathbf{J}_{\mathbf{Xx}})| \right\} \end{aligned}$$

which is the variational form associated with the transformed Navier equation. Further integrating by parts, we get that

$$\begin{aligned} &\int_{\Omega'} \mathrm{d}\mathbf{x} \left(\rho_0 \omega^2 \mathbf{A}^{\mathbf{T}} \mathbf{u} \cdot \mathbf{A}^{\mathbf{T}} \phi |\det(\mathbf{J}_{\mathbf{Xx}})|\right) \\ &\quad = -\int_{\Omega'} \mathrm{d}\mathbf{x} \left\{ \mathbf{A} \nabla_{\mathbf{x}} \cdot \left(|\det(\mathbf{J}_{\mathbf{Xx}})| \mathbb{C} : \right.\right. \\ &\qquad \left.\left. \times \ \mathbf{J}_{\mathbf{xX}} \nabla_{\mathbf{x}} (\mathbf{u}^{\mathbf{T}} \mathbf{A}) \mathbf{J}_{\mathbf{xX}}^T \right) \phi \right\} \end{aligned}$$

Since this equation holds for any smooth function ϕ, one has

$$\begin{aligned} &\mathbf{A} \nabla_{\mathbf{x}} \cdot \left(|\det(\mathbf{J}_{\mathbf{Xx}})| \mathbb{C} : \mathbf{J}_{\mathbf{xX}} \nabla_{\mathbf{x}} (\mathbf{u}^{\mathbf{T}} \mathbf{A}) \mathbf{J}_{\mathbf{xX}}^T \right) \\ &\quad + \rho_0 \mathbf{A} \mathbf{A}^T |\det(\mathbf{J}_{\mathbf{Xx}})| \omega^2 \mathbf{u} = \mathbf{0} \,. \end{aligned} \tag{107}$$

Following [500], we note that $\nabla_{\mathbf{x}} \cdot (\det(\mathbf{J}_{\mathbf{Xx}}) \mathbf{J}_{\mathbf{xX}}) = \mathbf{0}$, and introducing the fourth order quantity $\mathbf{Q}$ such that

$$Q_{ijIJ} = \det(\mathbf{J}_{\mathbf{Xx}}) (\partial x_i / \partial X_L) A_{jJ} \,, \tag{108}$$

one can recast (107) as

$$\begin{aligned} &\mathbf{Q} \nabla_{\mathbf{x}} \cdot \left(|\det(\mathbf{J}_{\mathbf{Xx}})| \mathbb{C} : \nabla_{\mathbf{x}} (\mathbf{u}^{\mathbf{T}} \mathbf{Q}) \right) \\ &\quad + \rho_0 \mathbf{A} \mathbf{A}^T |\det(\mathbf{J}_{\mathbf{Xx}})| \omega^2 \mathbf{u} = \mathbf{0} \,. \end{aligned} \tag{109}$$

The transformed equation (109) is equivalent to

$$\nabla_{\mathbf{x}} \cdot \boldsymbol{\sigma} = -i\omega \mathbf{p} \tag{110}$$

with transformed momentum $\mathbf{p} = (p_j)$, stress tensor $\boldsymbol{\sigma} = (\sigma_{ij})$, rank-four elasticity tensor $\mathbb{C} = (C_{ijkl})$ and density $\rho = (\rho_{ij})$, which are related to the transformed displacement $\mathbf{u} = \mathbf{u}(x, y, z)$, by

$$\begin{aligned} \sigma_{ij} &= C_{ijkl} \ (\nabla \mathbf{u})_{kl} + S_{ijl} u_l \,, \\ p_j &= D_{jkl} (\nabla \mathbf{u})_{kl} - i \ \omega \ \rho_{jl} u_l \,, \end{aligned} \tag{111}$$

where

$$\begin{aligned} C_{ijkl} &= |\det(\mathbf{J}_{\mathbf{Xx}})| C_{IJKL} Q_{ijIJ} Q_{klKL} \,, \\ S_{ijl} &= \frac{i}{\omega} |\det(\mathbf{J}_{\mathbf{Xx}})| C_{IJKL} Q_{ijIJ} \frac{\partial}{\partial x_k} Q_{klKL} \,, \\ \rho_{jl} &= \rho_0 |\det(\mathbf{J}_{\mathbf{Xx}})| \left(A_{iL} A_{jL} \right. \\ &\quad \left. + \frac{1}{\omega^2} C_{IJKL} \frac{\partial}{\partial x_i} Q_{ijIJ} \frac{\partial}{\partial x_k} Q_{jkKL} \right) . \end{aligned} \tag{112}$$

Note that the transformed elasticity tensor and the transformed density satisfy the general symmetries $C_{ijkl} = C_{klij}$ and $\rho_{jl} = \rho_{lj}$, but not the full symmetries.

5.1.1.4. Case of transformed Navier equations when $\boldsymbol{A} = \alpha \boldsymbol{I}$.

When the gauge $\mathbf{A}$ is constant, the fourth order quantity $\mathbf{Q}$ satisfies

$$\frac{\partial}{\partial x_i} Q_{ijIJ} = 0 \,, \tag{113}$$

and transformed equation (110) and associated constitutive parameters in (112) simplify (notably $\mathbf{S} = \mathbf{0}$), so that the transformed equation (111) take the following form:

$$\begin{aligned} \nabla_{\mathbf{x}} \cdot \boldsymbol{\sigma} &= -\omega^2 \rho \mathbf{u} \,, \rho = \rho_0 \mathbf{A} \mathbf{A}^T |\det(\mathbf{J}_{\mathbf{Xx}})| \,, \\ \sigma_{ij} &= C_{ijkl} \ (\nabla \mathbf{u})_{kl} \,, \\ C_{ijkl} &= |\det(\mathbf{J}_{\mathbf{Xx}})| C_{IJKL} Q_{ijIJ} Q_{klKL} \,, \end{aligned} \tag{114}$$

where $\mathbf{Q}$ is defined by (108). Importantly, the transformed elasticity tensor C_{ijkl} does not have the minor symmetries since

$$\begin{aligned} C_{ijkl} - C_{jikl} &= |\det(\mathbf{J}_{\mathbf{Xx}})| C_{IJKL} \frac{\partial x_k}{\partial X_K} \\ &\quad \times A_{lL} \left(\frac{\partial x_i}{\partial X_I} A_{jJ} - \frac{\partial x_j}{\partial X_I} A_{iJ} \right) \,, \end{aligned} \tag{115}$$

which does not vanish in general. This means that the stress is not necessarily symmetric, which is associated with Cosserat media [47].

In [498, 503, 508], the authors assumed that $\mathbf{A} = \mathbf{I}$ so that $\mathbf{u} = \mathbf{U}$, in which case

$$\begin{aligned} C_{ijkl} &= |\det(\mathbf{J}_{\mathbf{Xx}})| C_{iJkl} \frac{\partial x_i}{\partial X_I} \frac{\partial x_k}{\partial X_K} \,, \\ \rho &= \rho_0 |\det(\mathbf{J}_{\mathbf{Xx}})| \,, \end{aligned} \tag{116}$$

and one notes that the transformed density is now isotropic.

We give in figure 41, a numerical example of a 3D spherical Cosserat cloak.

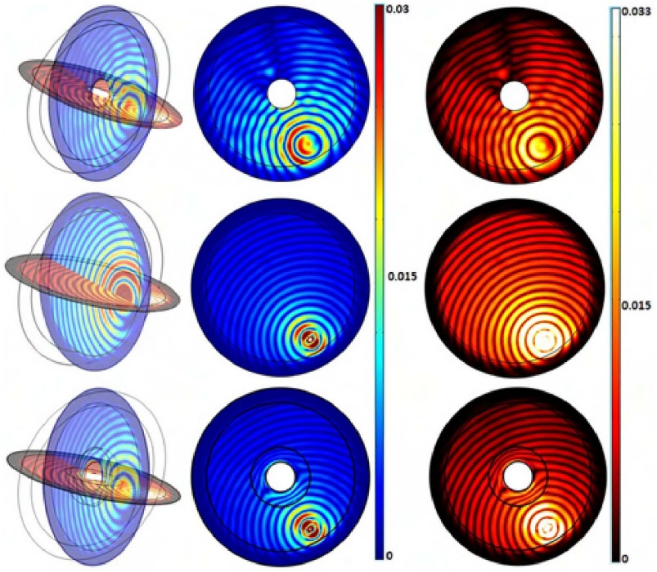

Figure 41. Slices of the 3D plot of the magnitude of the elastic displacement field, for the point force in presence of the void (upper panel), the void surrounded by the spherical Cosserat cloak (lower panel) and in the isotropic elastic medium (middle panel). Reproduced from [503]. CC BY 4.0.

5.1.1.5. Special case of acoustics with pentamode materials. Let us now assume that one has an acoustic fluid with elastic stiffness

$$\mathbf{C}_0 = K_0 \mathbf{I} \otimes \mathbf{I} \,, \tag{117}$$

known as pentamode material [27]. These media take their name from the 6×6 Voigt matrix associated with the elements $C_{IJKL} = K_0 \delta_{IJ} \delta_{KL}$, which have five zero eigenvalues.

Plugging the elastic stiffness (117) in (109) we get

$$\begin{aligned} &\mathbf{Q} \nabla_{\mathbf{x}} \cdot \left(|\det(\mathbf{J}_{\mathbf{Xx}})| K_0 \mathbf{I} \otimes \mathbf{I} : \right. \\ &\left. \nabla_{\mathbf{x}} (\mathbf{u}^{\mathbf{T}} \mathbf{Q}) \right) + \rho_0 \mathbf{A} \mathbf{A}^T |\det(\mathbf{J}_{\mathbf{Xx}})| \omega^2 \mathbf{u} = \mathbf{0} \,, \end{aligned} \tag{118}$$

with

$$\mathbf{Q} = |\det(\mathbf{J}_{\mathbf{xX}})| \frac{\partial \mathbf{x}}{\partial \mathbf{X}} \mathbf{A}^T \,. \tag{119}$$

Note that here $\mathbf{Q}$ is a second order quantity such that $Q_{ij} = |\det(\mathbf{J}_{\mathbf{xX}})| (\partial x_i / \partial X_I) A_{jI} = Q_{ijKK}$.

The general form of the governing equations can be once more identified to (111), but constitutive parameters (112) should be

$$\begin{aligned} C_{ijkl} &= K_0 |\det(\mathbf{J}_{\mathbf{xX}})| B_{ik} A_{jN} A_{lN} \,, \\ S_{ijl} &= i/\omega K_0 |\det(\mathbf{J}_{\mathbf{xX}})| B_{ik} A_{jN} \frac{\partial}{\partial x_k} A_{lN} \,, \\ \rho_{jl} &= \rho_0 |\det(\mathbf{J}_{\mathbf{xX}})| \left(A_{iL} A_{jL} \right. \\ &\left. + \frac{K_0}{\omega^2} B_{ik} \frac{\partial}{\partial x_i} A_{jN} \frac{\partial}{\partial x_k} A_{lN} \right) \end{aligned} \tag{120}$$

with $\mathbf{B} = (\partial \mathbf{x} / \partial \mathbf{X}) (\partial \mathbf{x} / \partial \mathbf{X})^T$.

As in the case of general elasticity theory, one can further simplify the equations by assuming that $\mathbf{A} = \alpha \mathbf{I}$ (Cosserat elasticity). In this case, (113) takes the simpler form

$$\frac{\partial}{\partial x_i} Q_{ij} = 0 \,, \tag{121}$$

in which case the transformed equations are of the Cosserat type (for a fluid)

$$\begin{aligned} &\nabla_{\mathbf{x}} \cdot \boldsymbol{\sigma} = -\omega^2 \rho \mathbf{u}, \boldsymbol{\rho} = \rho_0 \mathbf{Q}^T \mathbf{B}^{-1} \mathbf{Q} |\det(\mathbf{J}_{\mathbf{Xx}})| \,, \\ &\boldsymbol{\sigma} = \mathbf{C} : (\nabla \mathbf{u}) \,, \\ &\mathbf{C} = K_0 |\det(\mathbf{J}_{\mathbf{Xx}})| \mathbf{Q} \otimes \mathbf{Q} \,, \; \nabla_{\mathbf{x}} . \mathbf{Q} = 0 \,. \end{aligned} \tag{122}$$

We note that $\boldsymbol{\rho} = \boldsymbol{\rho}^T$ and $C_{ijkl} = C_{klij}$, but the minor symmetry $C_{ijkl} = C_{jikl}$ does not hold in general unless $\mathbf{Q} = \mathbf{Q}^T$.

Therefore, one notes that the transformed acoustics equations are some pentamode material of Cosserat type with anisotropic density.

However, since the transformed medium is still of pentamode type, it is possible to recast the transformed equation in a form reminiscent of the transformed acoustics theory, by using a scalar pseudo pressure field p and a bulk modulus $K = K_0 |\det(\mathbf{J}_{\mathbf{Xx}})|$. The transformed equations should thus have the form

$$i\omega \boldsymbol{\rho} = \mathbf{Q} \nabla p \,, \; i\omega p = -K \mathrm{Tr}(\mathbf{Q} \nabla \mathbf{v}) \,. \tag{123}$$

With this acoustic setup, one can still achieve (121) with a constant gauge $\mathbf{A}$. For instance, taking $\mathbf{A} = \mathbf{I}$, one has that

$$\begin{aligned} \boldsymbol{\rho} &= \rho_0 |\det(\mathbf{J}_{\mathbf{Xx}})| \,, \\ \mathbf{C} &= K_0 |\det(\mathbf{J}_{\mathbf{Xx}})| \mathbf{J}_{\mathbf{xX}} \otimes \mathbf{J}_{\mathbf{xX}} \,, \end{aligned} \tag{124}$$

which describes a medium with isotropic density and pentamode/Cosserat structure. More precisely, the stiffness is of pentamode type (with a single nonzero eigenstiffness [516]) and a single eigenstress of generally non-symmetric form (Cosserat type).

Norris noted in [491] that there is one case, which is of foremost practical importance, for which the transformed pentamode is purely pentamode with isotropic density with symmetric stress. This is possible for certain function $h(\mathbf{x})$ such that $\nabla_{\mathbf{x}} (h \mathbf{V}) = 0$. This function $h = |\det(\mathbf{J}_{\mathbf{Xx}})|$ corresponds to pure stretch $\mathbf{J}_{\mathbf{Xx}}| = \mathbf{V}$. In this case, one can recast (124) as

$$\boldsymbol{\rho} = \rho_0 |\det(\mathbf{J}_{\mathbf{Xx}})| \mathbf{I} \,, \; \mathbf{C} = K_0 |\det(\mathbf{J}_{\mathbf{Xx}})| \mathbf{V} \otimes \mathbf{V} \,, \tag{125}$$

with $\mathbf{V}$ a pure stretch.

Finally, it is remarkable that the free divergence condition on $\mathbf{Q}$ (121) can be also satisfied when $\mathbf{A}$ is not a constant matrix. Take for instance $\mathbf{A} = |\det(\mathbf{J}_{\mathbf{xX}})| (\mathbf{J}_{\mathbf{Xx}})^T$, this leads to $\mathbf{Q} = \mathbf{I}$ which is clearly divergence free. In this case, one has a transformed fluid

$$\begin{aligned} \boldsymbol{\rho} &= \rho_0 |\det(\mathbf{J}_{\mathbf{xX}})| \mathbf{B}^{-1} \,, \\ \mathbf{C} &= K_0 |\det(\mathbf{J}_{\mathbf{xX}})| \mathbf{I} \otimes \mathbf{I} \,, \end{aligned} \tag{126}$$

with isotropic (hydrostatic) stress, bulk modulus $K = K_0|\det(\mathbf{J}_{\mathbf{xX}})|$ and anisotropic density $\boldsymbol{\rho}$. This transformed acoustic medium was the first one unveiled by physicists [487, 488, 517]. Such a medium is made possible thanks to the simple structure of the second order quantity $\mathbf{Q}$ which can be divergence-free when $\mathbf{A}$ is non-constant, unlike its fourth-order counterpart. The full acoustic cloaking theory which has all the possible cases detailed is due to Norris [491], whereas the full elastodynamic cloaking theory is due to Shuvalov and Norris [500]. There is nonetheless a particular case of transformed plate equations that has been studied independently [499, 504, 505]. We shall come back on the latter in section 5.6.

5.1.1.6. Non-symmetric stress in the framework of small-on-large motion. We have already seen that when we consider a gauge $\mathbf{A} = \mathbf{I}$, we depart from symmetric stress, which is legitimate in Cosserat elasticity [47]. There is another framework, known as theory of small-on-large motion, within which stress need not be symmetric. In the tracks of Norris and Parnell, we now study this case. The solid medium is considered in two different states. First, a reference configuration Ω_1 under zero strain. The second, current, state of the solid medium is Ω. The hyperelastic theory of small motion superimposed on large depends on the initial, finite, large static pre-strain that maps $\mathbf{X} \in \Omega_1$ to $\mathbf{x} \in \Omega$. The small motion is defined by the mapping $\mathbf{X} \longmapsto \mathbf{x} + \tilde{\mathbf{u}}(\mathbf{x}, t)$. In what follows, following Ogden and Norris and Parnell, we assume that $\tilde{\mathbf{u}}$ and the associated strain are sufficiently small that tangent moduli can be used to derive the linear equations of motion for the small-on-large motion.

Let us introduce the deformation gradient of pre-strain $\mathbf{F} = \nabla_{\mathbf{X}}\mathbf{x}$ whose inverse is $\mathbf{F}^{-1} = \nabla_{\mathbf{x}}\mathbf{X}$. The polar decomposition of $\mathbf{F}$ is

$$\mathbf{F} = \mathbf{RU} = \mathbf{VR}\,, \tag{127}$$

where $\mathbf{RR}^T = \mathbf{R}^T\mathbf{R} = \mathbf{I}$ and $\det(\mathbf{R}) = 1$ ($\mathbf{R}$ is a rotation matrix). Also, the tensors $\mathbf{U}$ and $\mathbf{V}$ are such that $\mathbf{U}^2 = \mathbf{F}^T\mathbf{F}$ and $\mathbf{V}^2 = \mathbf{FF}^T$.

Under the hypothesis of hyperelasticity, there exists a strain energy function $\mathcal{W}$ per unit volume from which the static Cauchy pre-stress is defined as

$$\sigma = \det(\mathbf{F}^{-1})F_{iI}\frac{\partial \mathcal{W}}{\partial F_{iI}}. \tag{128}$$

The governing equation follows as

$$\frac{\partial}{\partial x_i}\det(\mathbf{F}^{-1})F_{iI}F_{kK}\frac{\partial^2 \mathcal{W}}{\partial F_{jI}\partial F_{lK}}\frac{\partial}{\partial x_k}\tilde{u}_l = \det(\mathbf{F}^{-1})\rho\frac{\partial^2}{\partial t^2}\tilde{u}_j. \tag{129}$$

This theory has been successfully applied in numerical wave simulations with pre-stressed materials (see figure 42 for the out-of-plane case and figure 43 for the in-plane case). We note nonetheless the criticism done by Yavari and Golgoon in this context [518].

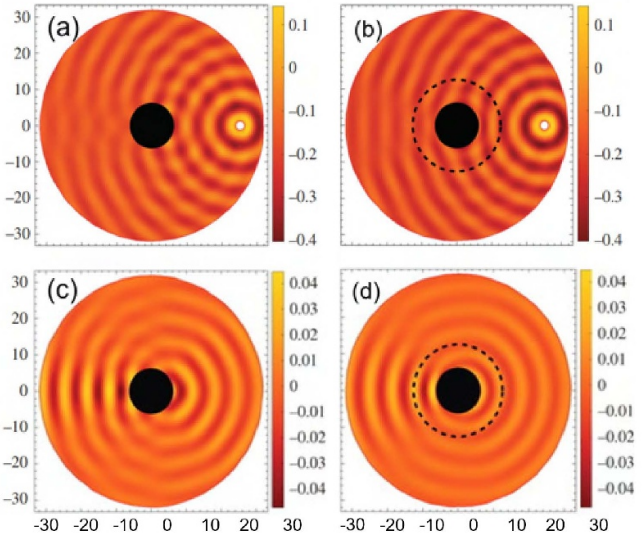

Figure 42. SH wave field. (a) Total (i) and scattered (ii) fields corresponding to an undeformed cavity; (b) total (i) and scattered (ii) fields corresponding to a conventional cloak generated via pre-stress. Reproduced with permission from [502].

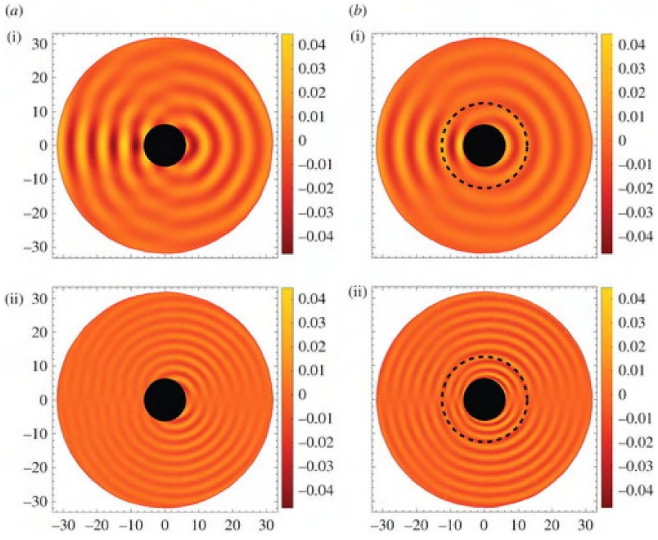

Figure 43. Scattered fields for the in-plane P/SV problem for an incident field generated by a compressional source (a) compressional (i) and shear (ii) fields corresponding to an undeformed cavity (b) compressional (i) and shear (ii) fields corresponding to a conventional cloak generated via pre-stress. Reproduced with permission from [502].

Let us pursue this review of cloaking theories by the space-time coordinate transforms. This research area remains a niche to this date, due to the lack of successfully implemented metamaterial cloak designs, with two exceptions we shall mention. We note space-time homogenization (section 3.1.8) might be a useful tool to achieve new designs of space-time cloaks in conjunction with the fast developing field of time-modulated metamaterials.

5.1.2. Space-time coordinate transformations. Ten years ago, McCall *et al* proposed a concept of a space-time cloak that can conceal events to electromagnetic waves [519] (also see [520–523]). Their bold proposal was based on the usual coordinate stretch $(X,Y) \longmapsto (x,y)$, followed by a rotation of that coordinate system to identify it to a stretched space-time coordinate system $(x,y) \longmapsto (x,ct)$. This route is easier to follow than that starting from a space-time coordinate frame (X,cT) and mapping it onto (x,ct), see figure 44. In the electromagnetic case, the space-time cloak requires a bianisotropic medium, which can be identified to a moving medium, which in turn can be generated by a time-modulated medium when its electric permittivity and its magnetic permeability have the same space-time variation [257]. An experimental demonstration of the history editor, as McCall *et al* coin their cloak, was performed with an optical fibre just one year after the theoretical proposal [524]. We note that the history editing cloak clearly involves temporal changes of material parameters. Their real and imaginary parts are connected by the Kramers–Kronig relations (see section 4.1.3). This means that history editing is inevitably connected with finite losses and hence energy dissipation. A natural extension is to adapt this concept to acoustic and elastodynamic space-time cloaks. However, it is not as easy to use McCall's algorithm as it might seem, even for the bare acoustic case. Thus, an alternative approach has been proposed in [525] using the idea of analogue spacetimes.

The latter approach considers the governing equation (99) for pressure waves in the time domain:

$$B\nabla_{\mathbf{X}} \cdot \left(\rho^{-1}\nabla_{\mathbf{X}} P(\mathbf{X},T)\right) = \frac{\partial^2}{\partial T^2} P(\mathbf{X},T)\,. \tag{130}$$

where $\nabla_{\mathbf{X}}$ is the gradient in the Cartesian coordinates $\{X,Y,Z\}$ and T is the time variable. From the transformation physics point of view, (130) has a set of drawbacks. First, its form is not form-invariant under coordinate transformations that mix space and time. Second, it breaks down for fluids flowing with a non-zero background velocity, which is the case in many physical situations. Finally, (130) assumes that the background (static) pressure is homogeneous. Thus, it does not hold for fluids with significant pressure gradients, such as when gravitational forces are relevant. Rather than starting from (130), one can look at the field of analogue gravity, where the formulation of a form-invariant equation has become a standard procedure. In terms of the velocity potential Φ, the equation for the acoustic perturbations of a barotropic and irrotational fluid can be expressed as

$$\begin{aligned}\frac{\partial}{\partial t}\left(\frac{\rho}{c^2}\frac{\partial}{\partial t}\Phi + \mathbf{V}\cdot\nabla_{\mathbf{X}}\Phi\right) + \nabla_{\mathbf{X}}\cdot\rho\nabla_{\mathbf{X}}\Phi \\ - \nabla_{\mathbf{X}}\cdot\left(\frac{\rho}{c^2}\frac{\partial}{\partial t}\Phi + \mathbf{V}\cdot\nabla_{\mathbf{X}}\Phi\right)\mathbf{V} = 0\,.\end{aligned} \tag{131}$$

with ρ the mass density, c the speed of sound, and $\mathbf{V}$ the fluid background velocity. This equation is still not form-invariant under transformations that mix space and time. Therefore, it is noted in [525] that equation (131) is structurally identical to

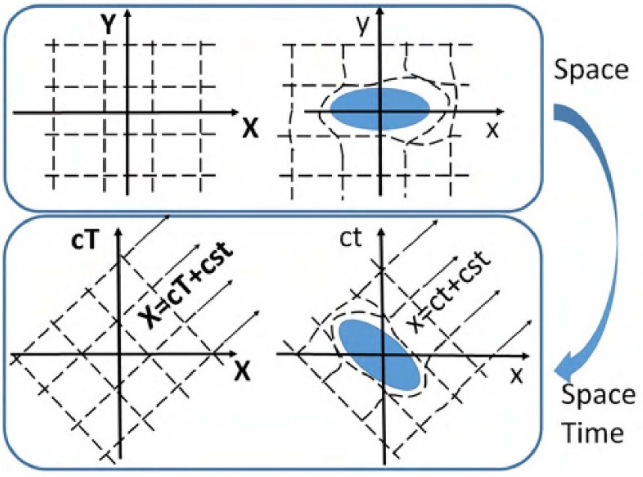

Figure 44. Principle of the space-time cloak (aka history editor [519]): A coordinate stretch $(X,Y) \longmapsto (x,y)$ (e.g. using the blow up transform in [471, 510]) is followed by a rotation in the plane leading to a stretched space-time coordinate system $(x,y) \longmapsto (x,ct)$. One can alternatively rotate (X,Y) coordinates into space-time coordinates (X,cT) and then apply the coordinate stretch to map (X,Y) onto (x,ct). The diagram is commutative. One notes that this makes a $1+1$ space-time cloak.

the equation describing a relativistic massless scalar field over a curved spacetime

$$\frac{1}{\sqrt{-g}}\frac{\partial}{\partial_\mu}\sqrt{-g}g^{\mu\nu}\frac{\partial}{\partial_\nu}\Phi = 0 \tag{132}$$

with a metric, see [525], which is given by

$$g^{\mu\nu} = \frac{\rho}{c}\begin{pmatrix} -1 & -v^j \\ \cdots & \cdots \\ -v^i & (c^2\delta^{ij} - v^i v^j)\end{pmatrix}\,, \tag{133}$$

with v^i, v^j the components of $\mathbf{V}$ and $\sqrt{-g} = \rho^2/c$. Note that $g^{\mu\nu}$ does not represent the metric of the laboratory space-time but corresponds to the abstract space-time in which the analog model is defined.

Equation (132) retains its form upon any coordinate transformation. Thus, using (131) as the laboratory equation and (132) as the analog equation, one can design a space-time cloak for acoustic waves. The first experimental proof of a space-time acoustic cloak is given in [525], see figure 45, together with the detailed derivation of (132) and (133). We note that a similar equation has been derived by other means by Kinsler and McCall [526].

Within the framework of transformation elastodynamics, following McCall's algorithm illustrated in figure 44, one would consider the space transformation $(X,Y) \to (x,y)$ and restrict to elastic waves propagating forwards along the x-axis. The spacetime transformation would be carried out in the (x,ct) plane that is analogous to the spatial transformation carried out in the (x,y) plane, up to a rotation in the xy-plane. In contrast to the spatial cloak, where the direction of propagation in the $x-y$ plane is arbitrary, the elastic wave ray

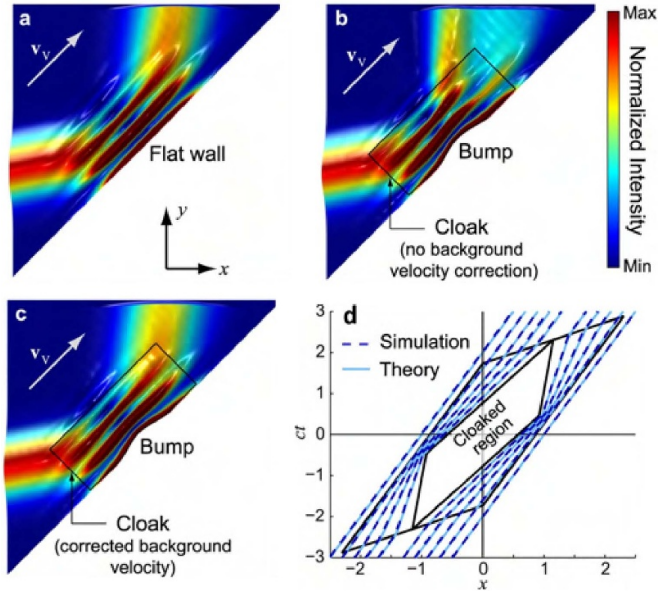

Figure 45. A Gaussian beam initially propagates along the positive x-direction. The wave is immersed in a fluid moving parallel to the aircraft wall (with speed 0.35 cV) and thus suffers a dragging effect that deviates it from its original trajectory. (a) Wave impinging onto a flat wall. (b) Wave impinges onto a wall with a bump surrounded by a carpet cloak within which the background fluid flows with the same velocity as outside the cloak. The wave outside the cloak is significantly distorted compared to the flat-wall case. (c) As in (b), but now the background fluid flows with a modified velocity calculated with the analogue transformation method. Outside the cloak, the wave recovers the form it had in the flat-wall case: the bump is perfectly cloaked. (d) Simulated acoustic rays. As can be seen, sound propagation is speeded up or slowed down in order to hide any acoustic event belonging to the cloaked region. Rays exit the cloak as if they had just passed through the background fluid. Reproduced with permission from [525]. CC BY-NC-ND 3.0.

trajectories must follow the straight lines $x = ct + \text{const}$. These rays are then mapped under the transformation to the curved rays. The space-time elastodynamic cloak might require some Willis type medium that might be achieved via space-time homogenization, see section 3.1.8.

Let us now turn to metamaterial cloaks that have been achieved in quasi-static and dynamic regimes.

5.2. Quasi-static cloaking

In general, quasi-static Cauchy elasticity is not form invariant under arbitrary coordinate transformations (cf section 5.1). This starting point asks for approximate cloaks.

Ideal pentamode metamaterials (cf section 3.1.1) approach the properties of fluids, for which the dynamic pressure-wave equation is form invariant (cf following section 4.1.1). Simple cylindrical core–shell cloaks made from 3D pentamode metamaterials have been realized experimentally (see figure 46). Cloaking with respect to uniaxial loading has been demonstrated explicitly [301]. Using the same architectures, cloaking with respect to shear deformations is expected theoretically. However, this demonstration is academic in that the surrounding, with respect to which the structure cloaks, needs

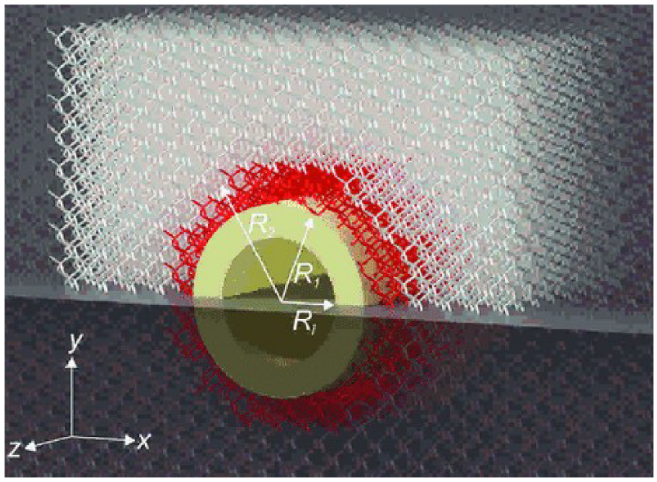

Figure 46. Illustration of a core–shell pentamode cloak. A stiff inclusion depicted in yellow is cloaked by a softer pentamode shell embedded in a pentamode environment. Reproduced from [301], with permission from Springer Nature.

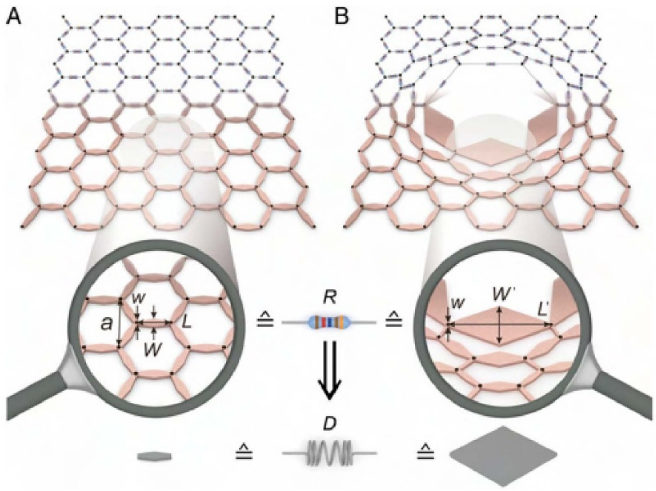

Figure 47. Direct lattice-transformation approach. (a) Inspired by a hexagonal lattice of identical Ohmic resistors the problem can equivalently be replaced by double-trapezoidal conductive elements going from a concept to a material design. (b) The lattice points of the lattice in (a) transformed to keep the resistors R identical. Same approach is used to keep the Hooke's spring constant for the mechanical counterpart. Reproduced with permission from [527].

to be a pentamode material, too. An approximate approach that has successfully worked for many different surrounding metamaterials or lattices is the direct lattice transformation [527].

It starts from a fictitious periodic lattice of points. These points are connected by identical elastic elements. Upon applying a wanted coordinate transformation to the lattice of points, leading to a change of the distance between the points, the shape of each connecting element is adjusted such that its Hooke's spring constant stays constant (see figure 47). While this simple ad-hoc ansatz completely ignores the shear forces, it has worked amazingly well for lattices covering a wide range of ratios of bulk modulus to shear modulus B/G. For example,

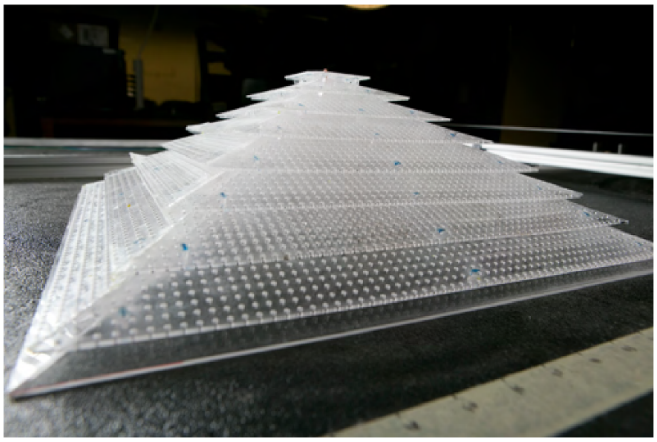

Figure 48. Schematic the fabricated acoustic cloak. Reproduced with permission from Steve Cummer, Duke University.

for a cylindrically symmetric cloak and for $B/G = 40$ of the starting lattice, the relative mean squared displacement difference, Δ, has been reduced by a factor of 34 from $\Delta = 738\%$ without cloak to $\Delta = 22\%$ with cloak [527].

5.3. Bulk acoustic pressure waves

The wave equation of airborne or waterborne sound propagation is form invariant under general coordinate transformations. This reduces the problem of realizing the resulting distributions of the bulk modulus and the mass density. This task is far from easy though. The problem starts with matching the effective acoustic impedance of the metamaterial in the cloak to the impedance of the surrounding, which is especially challenging for airborne sound. Otherwise, large reflections result. So far, the ideal of a 3D omnidirectional broadband acoustic cloak is elusive. For waterborne sound in two dimensions, an omnidirectional cloak has been designed and experimentally demonstrated in the frequency range from 52 kHz to 64 kHz [492]. However, the loss of 6 dB m^{-1} in the presence of the cloak led to a reduction of the transmitted power by about a factor of two with respect to the free-space surrounding. Later, a 2D carpet cloak based on piece-wise homogeneous laminate metamaterials was demonstrated [528]. The cloak reduced the total cross section by about a factor of 5 for frequencies in the range from 11 to 16 kHz. For airborne sound, the carpet cloak shown in figure 48 based on a piecewise homogeneous laminated effectively anisotropic metamaterial has been demonstrated [493]. The unit cell is a cube with a side length of 5 mm filled with a perforated plate of 1.6 mm thickness and 0.85 mm hole radius. These dimensions can be compared with the wavelength of 11 cm corresponding to the center frequency of 3 kHz in ambient air. Experiments were performed in reflection geometry by pulses impinging from three different directions and in the time domain, demonstrating the broadband performance. A related 2D acoustic carpet cloak was presented previously by the same group [485].

Using topology optimization (see section 3.2), the 3D unidirectional free-space airborne acoustic cloak shown in figure 49 has been achieved [529]. Scattering reduction was

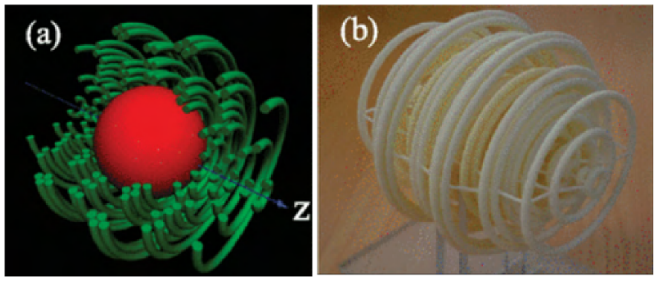

Figure 49. Schematic (a) and fabricated (b) acoustic cloak. Reprinted (figure) with permission from [529], Copyright (2013) by the American Physical Society.

observed experimentally for a single direction of incidence in the frequency range from 8.45 to 8.75 kHz. At the optimum frequency, scattering was reduced by about a factor of three. Outside of the mentioned frequency interval, scattering was increased by the cloak as compared to no cloak. Topology optimization led to other designs of optical [530, 531], acoustical [532] and water wave [533] cloaks with similar performances. Topology optimization has been also applied to carpet cloaks [534]. Alternatively, unidirectional cloaks, both in 2d and 3d, can be obtained for acoustics by putting two carpet cloaks back to back [535–537].

Finally, design of acoustic cloaks based on inverse homogenization making use of machine learning tools has been proposed in [505] with a genetic algorithm and in [538] with the advanced deep learning network approach. The latter is described in figure 50. This is a dynamic research area [539–541]. Interestingly, certain species of moths have evolved to achieve specific acoustic properties [542] and bio-inspiration [543] is yet another avenue towards design of acoustic and mechanical metamaterials.

5.4. Fluid surface waves

In water and other fluids, unlike for gases, surface waves play a tremendous role in addition to bulk waves. Depending on the conditions, these are dominated by gravity or by capillary forces due to surface tension [414]. The velocity of these surface waves can be modulated by varying the height, h, of the water surface above ground or by taking advantage of friction between the water (or another liquid) and a rigid wall. Under appropriate conditions, this friction can be mapped onto an effective spatially varying shear viscosity of the meta-liquid. Along these lines, early work [490] based on a linearized version of the Navier–Stokes equation that can be simplified into a Helmholtz-type equation at the free liquid–air interface, designed and demonstrated experimentally the cylindrical cloak shown in figure 51(a). Experiments using methoxynonafluorobutane as liquid and a cloak with an inner (outer) radius of $R_1 = 41$ mm ($R_2 = 100$ mm) were performed in the regime around 10 Hz, and demonstrated reduced backscattering for a rigid obstacle of radius $R_0 = 3.8$ mm. It was subsequently shown [494] that the same metamaterial cloak works for one linear polarization in the microwave regime, see figure 51, and for airborne pressure waves for frequencies

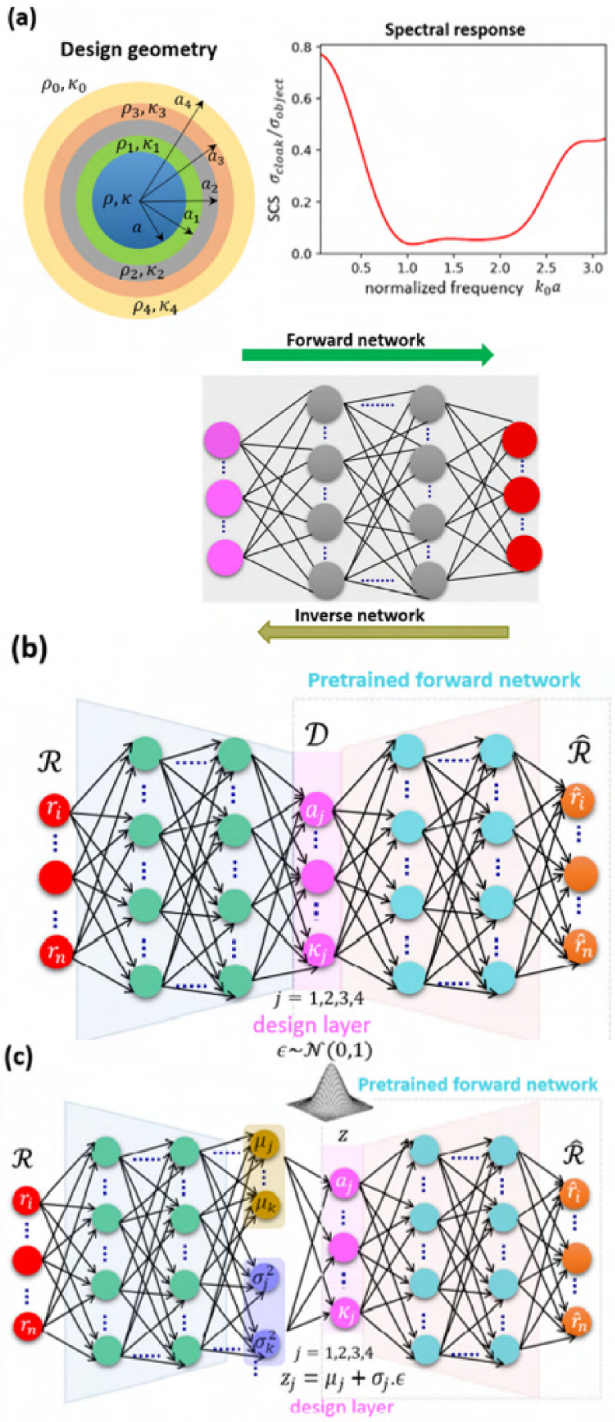

Figure 50. Framework of the deep learning network for inverse design of the acoustic cloak. (a) Schematic illustration of the core–shell acoustic cloak and its spectral response (ratio between total scattering cross-section spectra of the cloak and that of the object, i.e. object) where the neural network learns the relation from D (design parameters) to R (spectral response) and from R to D for forward and inverse design, respectively. (b), (c) Proposed deep learning models for inverse design of the cloak. (b) Deterministic model where the pre-trained forward network acts as a decoder to predict the spectral response. (c) Probabilistic model where the design space is transformed into the latent space z, with a standard Gaussian distribution $\mathcal{N}(0,1)$. The physical design parameters are sampled from that distribution in the form of latent variables to generate the desired spectral response. Reproduced from [538]. CC BY 4.0.

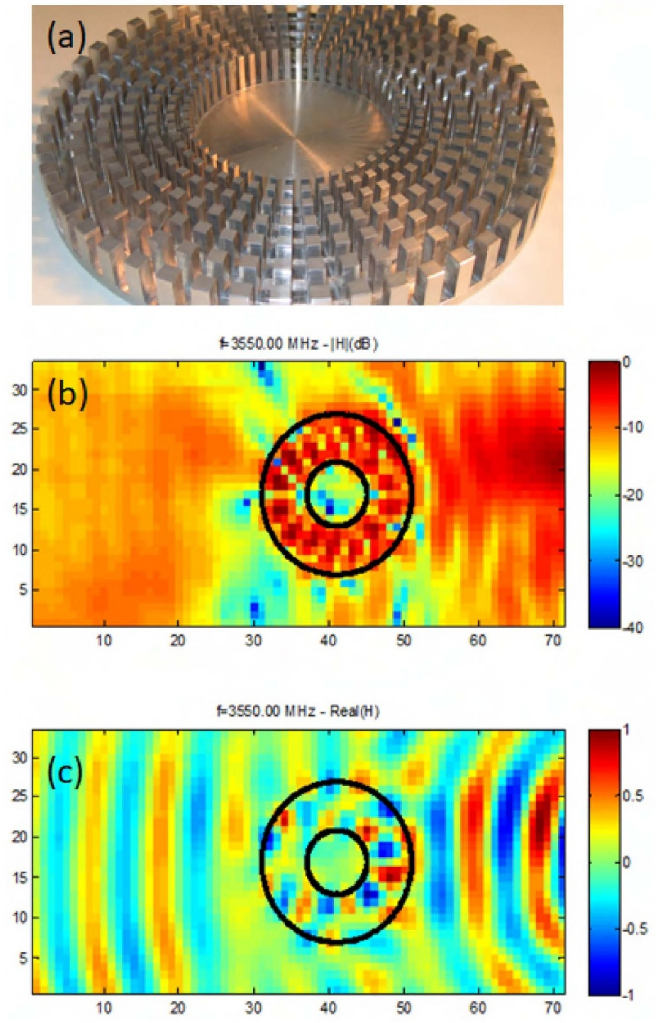

Figure 51. (a) Oblique-view photograph of the aluminium based cloak (20 cm in diameter) consisting of seven concentric rings of pillars with elongated cross-sections mimicking the anisotropic heterogeneous shell in middle panel of figure 40.
(b), (c) Experimental results in backward and forward scattering for microwaves when a square metallic obstacle is placed inside the invisibility region: The normalized modulus (b) and the normalized real part (c) of the magnetic field is measured within a rectangular domain. A ridged horn antenna generates transverse electric microwaves propagating from right to left at frequency 3.55 GHz. Similar results hold in the cloaking interval $[2.6, 7]$ GHz, and this translates in the frequency range $[8, 15]$ Hz for water waves and $[3, 8]$ kHz for airborne pressure waves. Reproduced from [494]. CC BY 4.0.

between 4 and 8 kHz. Indeed, the same Helmholtz equation supplied with homogeneous Neumann data on rigid/metallic obstacles holds for this metamaterial cloak for surface water waves, transverse magnetic waves (i.e. for magnetic field perpendicular to the plane in figure 51), and for transverse pressure waves. Moreover, microwave experiments have shown the field is reduced by 10–30 dB inside the invisibility region, which suggests the multi-wave cloak could be used as a protection against water, sonic or microwaves. Other routes towards a control of surface water waves include varying the bathymetry, using floating objects [544–558].

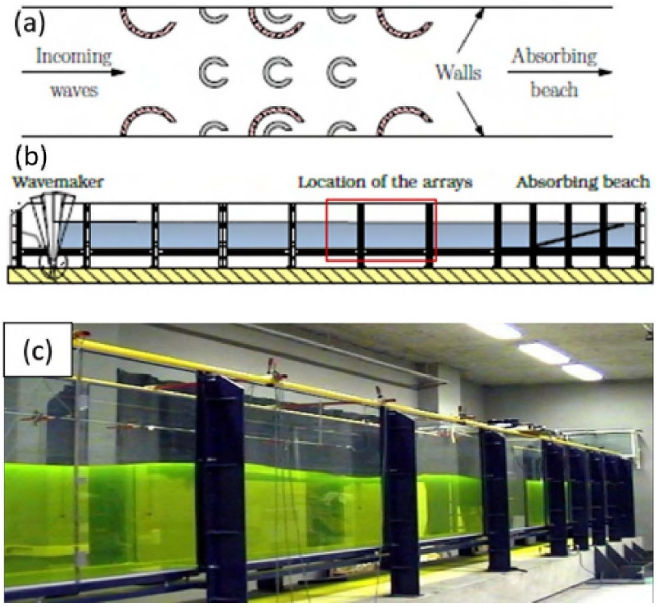

Figure 52. Water wave experiments in the 17 m long wave channel at Ecole Centrale Marseille. (a) Schematical top view of the experimentally tested arrays. (b) Side view of wave canal. (c) Photograph of the water channel. Reprinted (figure) with permission from [559], Copyright (2017) by the American Physical Society.

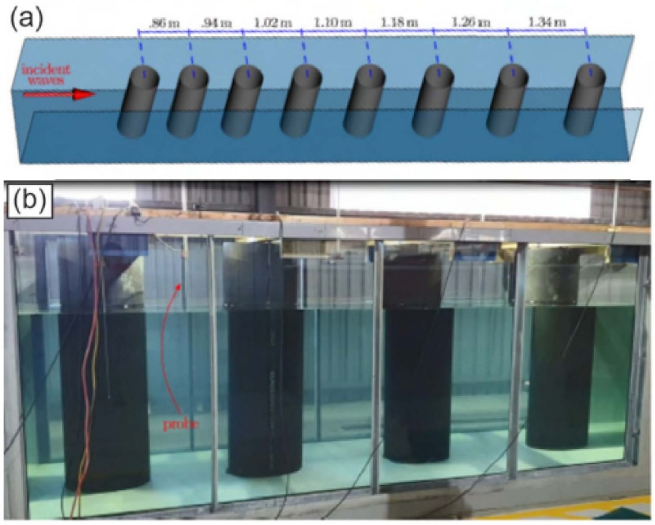

Figure 53. (a) Wave-flume experimental setup, involving a chirped array of eight identical cylinders, with spacing increasing in the incident wave direction. (b) Side-view photograph showing cylinders 3–6, including probes in cylinder spacings. Reprinted (figure) with permission from [561], Copyright (2020) by the American Physical Society.

It was experimentally demonstrated [559] that C-shaped vertical rigid cylinders of varying radii clamped to the bottom of a long water wave channel and perforating the water free surface (see figure 52) can filter out surface waves with long wavelengths (including with large wave heights) thanks to low frequency stop bands associated with a low transmission on a wide range of wavelengths. On the other hand, when the period of waves decreases, C-shaped vertical rigid cylinders so designed become inactive [559]. This makes it possible to design dykes attenuating waves associated with storm swell, without affecting coastline in other conditions. Another interesting effect was further proposed for a graded chain of such split ring resonators in a fluid [560]. Water waves in natural environments are typically broadband, nonlinear, and dynamic phenomena. Taking concepts developed for slow light in optics [360], it is possible to design arrays to control the spatial distribution of water wave energy and amplify specific frequencies from within target frequency bands at individual locations, as proposed in [560] Meter-scale wave-flume experiments, in which incident waves interact with a chirped array of eight vertical cylinders (see figure 53) demonstrate significant amplifications over a broad frequency range, as predicted numerically and theoretically in [561]. The water wave amplification locations, at which the group velocity slows to zero, aligns with the band structure of infinite periodic arrays using local cylinder spacings. The outcome suggests future strategies for ocean-wave-energy harvesting by arrays should consider taking advantage of the broadband response and precise control demonstrated in [561].

5.5. Bulk elastic waves

As discussed previously, a goal of cloaking is to control bulk elastic waves. One needs either Willis materials or non-symmetric tensors. However, losing minor symmetry is considered impossible without introducing artificial body torques (see figure 54). Research groups [255, 563] have demonstrated the feasibility of such exotic materials by introducing rotational resonances. Amplified rotational inertia of the microstructure can break the shear stress symmetry in response to dynamical loading. Researchers have thereby successfully tailored the elastic metamaterial structures to achieve the necessary effective material properties deduced from transformation elastodynamics. However, such exotic metamaterials have been inherently resonant. In order to achieve broadband cloaking of elastic waves, other routes need to be identified in the future. There is notably a proposal for a carpet cloak consisting of an isotropic elastic medium with a mild variation of the density that one might wish to further explore. This design is based on a compact form of the Navier equation in isotropic homogeneous media (10), that allows for the decoupling between shear and elastic components of the displacement field via the Helmholtz decomposition in the virtual space [30]. Careful manipulation of the form invariant wave equations satisfied by the scalar compressional potential and the vector shear potential both in virtual and real spaces, and specific treatment of the interface conditions that couple the potentials at the ground boundary in physical space, leads to the design of a 2D carpet cloak hiding surface defects from incoming compressional and shear waves, see figure 55. This carpet cloak also works surprisingly well for Rayleigh waves that propagate along the surface with a defect dressed by the

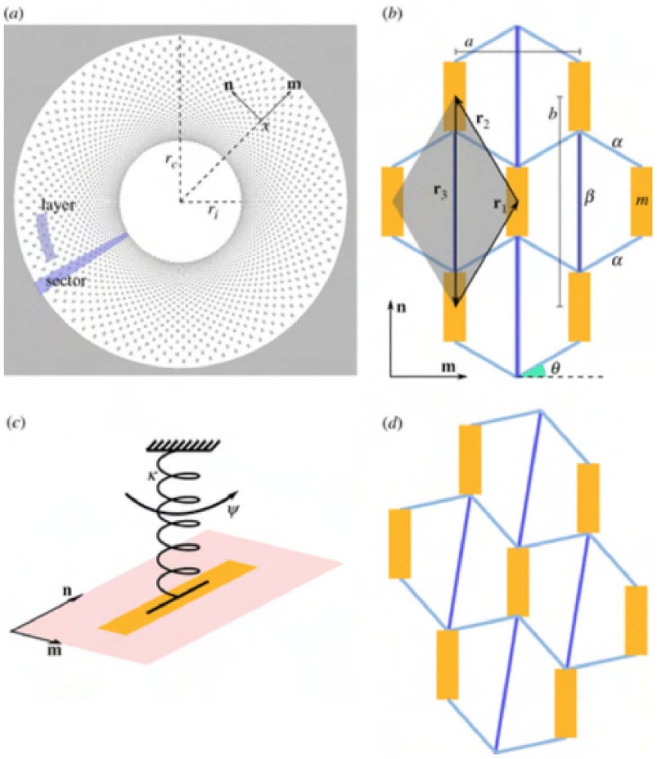

Figure 54. (a) Two-dimensional lattice elastic cloak designed by exact discrete transformation elastodynamics with torquing elements ('torque springs') as introduced in [562]. (b) Local lattice geometry with rectangles representing rigid masses; edges are springs with all contacts hinge-like. (c) A torque restoring mechanism. (d) First deformation mode. Reproduced with permission from [255].

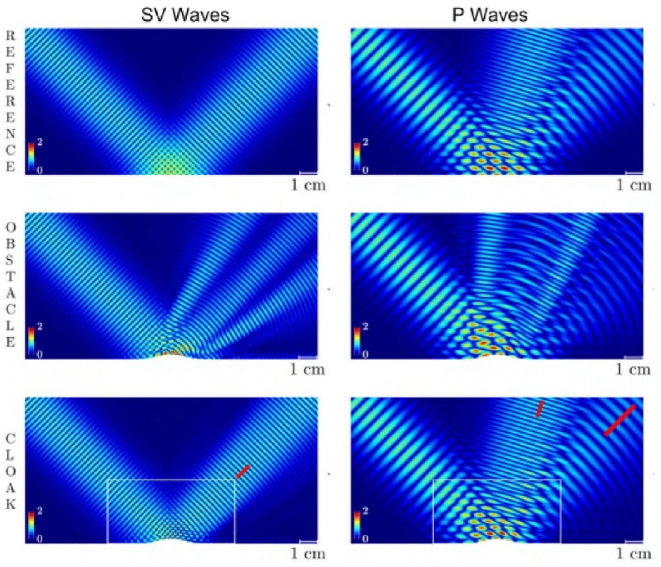

Figure 55. two-dimensional Carpet cloak for S waves on the left and P waves on the right. The reflection of both waves is shown for three configurations (reference: flat mirror, obstacle and cloak). The fields are normalized with respect to the amplitude of the incident wave. Reprinted from [30], Copyright (2021), with permission from Elsevier.

carpet with almost unnoticeable scattering [30]. One could envisage scaling up this design for the control of surface seismic waves in structured soils, by gradually varying the soil density e.g. with concrete columns. Other proposals for the control of bulk elastic waves include symmetrized Cosserat elasticity-tensors as originally proposed in [508]. Such symmetrization is not unique, but any chosen symmetrization must be physical in that all eigenvalues of the resulting elasticity tensor need to be real or complex valued with positive imaginary parts, at least for passive media. One can then approximate the ideal transformed medium with homogenized formulas in section 3.1.1, e.g. making use of Backus's formulae [73], as was done in [515] in order to achieve a layered cylindrical cloak for in-plane elasticity. The symmetrization of the Cosserat tensor was also employed in [564] to design a seismic cloak.

5.6. Flexural and Lamb waves

Propagation of time-harmonic flexural waves in a homogeneous isotropic elastic plate satisfies the Kirchhoff–Love equation

$$\Delta D_0 \Delta w(X_1,X_2) - \rho H \omega^2 w(X_1,X_2) = 0 \qquad (134)$$

with $w(X_1,X_2)$ the out-of-plane displacement, H the plate thickness, ρ its density and D_0 its flexural rigidity in units of Pa m^3 (even if the plate is homogeneous, it is safe to place D_0 in between the two Laplacians Δ since it is in general a rank-4 tensor if the plate is anisotropic). In 2009, Farhat *et al* [499] used the theory of acoustic cloaking developed by Norris [491] to make a change of coordinates $(X_1,X_2) \to (x_1,x_2)$ in (134) and obtained a transformed biharmonic equation, which was interpreted in terms of an anisotropic rigidity of the form

$$\mathbf{D} = D_0 F F^T F F^T |\det F|^{-1} \qquad (135)$$

with F the gradient of the considered transformation. However, this approach does not take into account the full complexity of flexural waves in anisotropic media described by a fourth order rigidity tensor. In 2014, Colquitt *et al* [504] corrected the transformed equation by considering an appropriate anisotropic rigidity and using again the theory developed in [491]. Especially the lemma (2.1) therein, was applied twice to account for the fourth order derivatives in (134). In [504], the Kirchoff–Love equation (134) is mapped onto a von-Karman equation:

$$\begin{aligned} &D_{ijkl} w_{,ijkl} + 2 D_{ijkl,i} w_{,jkl} + (D_{ijkl,ij} N_{kl}) w_{,kl} + S_l w_{,l} \\ &\quad = h \rho \omega^2 w \ , \ i,j,k,l = 1,2 \end{aligned} \qquad (136)$$

where we use Einstein's summation convention, the subscript $i \ldots l$ denoting partial derivatives with respect to space variables $x_i \ldots x_l$ and

$$\begin{cases} D_{ikjl} = D_0 F_{ip} F_{jp} F_{km} F_{lm} J^{-1} \\ N_{kl} = D_0 (J G_{kl} G_{ij,i} - J G_{jl} G_{ik,i})_{,j} \\ \qquad -D_0 G_{jk} (J G_{il,i})_{,j} \\ S_l = D_0 [G_{jk} (J G_{il,i})_{,j}]_{,k} \end{cases} \qquad (137)$$

with $J = \det F$, $G_{ij} = J^{-1} F_{ip} F_{jp}$ and $h = H |\det F|^{-1}$.

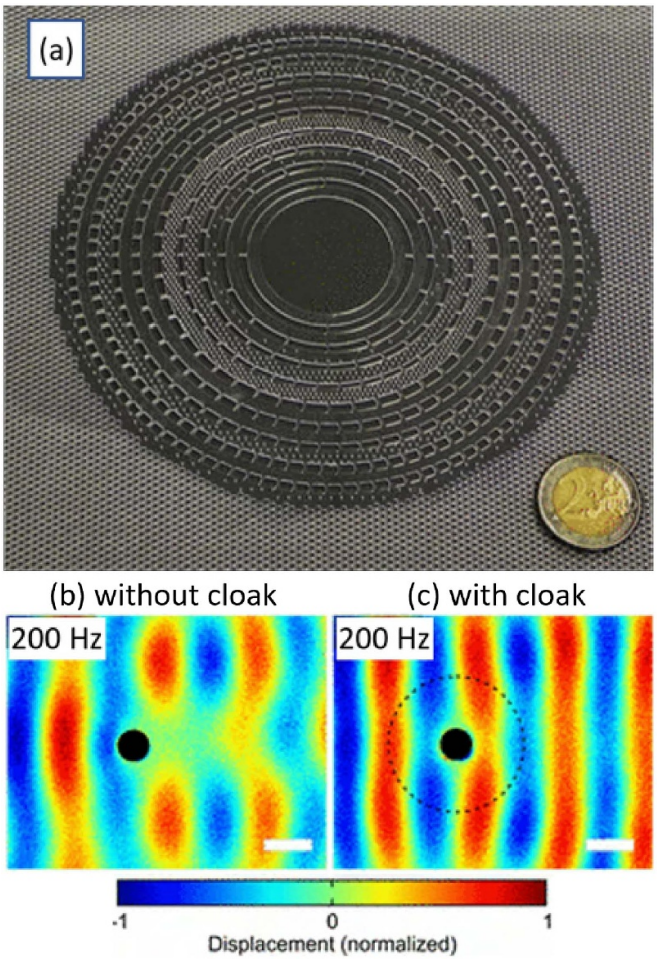

Figure 56. (a) Oblique-view photograph of the PVC based cloak before PDMS has been filled into the voids. The cloak is composed of 20 concentric rings made from 16 different metamaterial structures. (b) Measured displacement field shown on a false-color scale for the uncloaked clamped obstacle in the middle. (c) Same, but with cloak. Reprinted (figure) with permission from [501], Copyright (2012) by the American Physical Society.

However, Pomot *et al* [505] realized in 2018 that the transformed Kirchhoff–Love equation derived in [504] does not verify in general the equilibrium equation $N_{IJ,J} + S_I = 0$, and further allows for unphysical zero energy mode. This pitfall was attributed to the fact Colquitt *et al.* used a push forward $(X_1, X_2) \to (x_1, x_2)$ from the over simplified biharmonic equation (134), to get (136), whereas they should have started instead from the Kirchhoff–Love equation for an anisotropic heterogeneous plate, and then applied a pull-back transform to achieve the correct result, which was derived in [505]. One notes that in the latter, it was shown that experiments in [501] as suggested by the theory exposed in [499], are justified when the thickness if the cloak is large enough (in the limit when the outer radius of the cloak is large compared with the inner radius).

Consider propagation of elastic waves in a plate made from a material that can be described by Cauchy elasticity. If the plate is sufficiently thin, only one type of waves called flexural waves is left that can be described approximately by a 2D bi-harmonic wave equation. This wave equation is form-invariant under general coordinate transformations [499]. By drilling and machining holes into a polyvinyl-chloride plate in the spirit of a graded laminate metamaterial, and filling the holes with polydimethylsiloxane (PDMS), an anisotropic phase-velocity profile has been realized experimentally [501] (see figure 56). It should be noted though that, by adding holes, the velocity only gets smaller compared to the bulk plate, whereas an ideal cloak requires azimuthal components of the velocity vector that are (much) larger than in the isotropic surrounding. Therefore, the surrounding of the cloak was perforated as well to reduce the flexural-wave speed there. Experiments based on 20 concentric rings of 16 different perforated laminate metamaterials showed broadband omnidirectional cloaking for frequencies between 200 and 450 Hz. For 200 Hz frequency, the cloak reduced the distortions due to the clamped cloak interior by about a factor of 8. A directional and resonant variant with rods of varying heights (according to Pendry's transform) atop a thin homogeneous isotropic plate was published later [565]. Control of fleuxural waves in structured plates fueled the interest in soils structured at the meter scale (e.g. with boreholes or trees) for a control of surface Rayleigh waves, which were coined seismic metamaterials in [566].

5.7. Rayleigh waves and seismic protection

A test zone consisting of an array of vertical cylindrical voids was carried out by the soil dynamic laboratory of Stéphane Brûlé (Ménard Company, Lyon) on a selected site near the French Alpine city of Grenoble in 2012. The frequency of the vibrating source in the experiments (a crane, see figure 57) is 50 Hz. This frequency falls within the stop band of the corresponding periodic plate model [566], and thus leads to strong reflection of surface elastic waves by the large scale metamaterial (see photo in figure 57). The experimental mesh is made of three discontinuous lines of ten boreholes 0.32 m in diameter. The length of columns is about 5 m and the mesh spacing is 1.73 m. To capture the energy field, we set 20 three-component velocimeters (x, y, z) with a corner frequency of 4.5 Hz (-3 dB at 4.5 Hz) electronically corrected to 1 Hz. The sensors were used simultaneously with a common time-base. In order to map completely the energy field, the sensors were set four times on site before and after carrying out the boreholes.

In order to map completely the energy field, the sensors were set four times on site (green, blue, pink and orange grids in figure 58(a)) before and after carrying out the boreholes. These are consecutively normalized by the energy per second recorded by the sensors next to the source, so as to reconstruct a uniform energy field over the whole experimental area. The boreholes' effect on the energy field is given figure 58 that shows the difference $J_2 - J_1$ of the measured energy field after (J_2 and before (J_1)) carrying out the boreholes. This map is displayed with interpolation between sensors.

There is an alternative to drilling boreholes in soils: To evaluate forests of trees as potential natural metamaterials a geophysical survey on a small forest ($\approx 60{,}000\,\mathrm{m}^2$, mainly

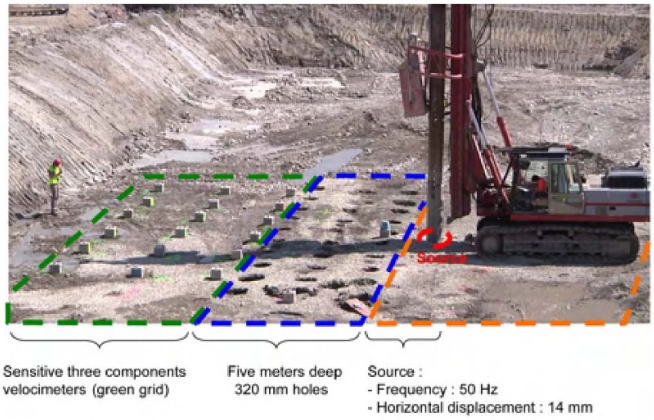

Figure 57. Photograph of the artificial seismic metamaterial experiment from Ménard company performed in a sedimentary basin near the French city of Grenoble in 2012 (Credit: S. Brûlé). Three dashed perimeters account for location of sensors (measuring the three components of wave velocity, green area on this photograph), seismic metamaterial (5 m deep self-stable holes of diameter 0.32 m with center-to-center spacing of 1.73 m, blue area), and rotating source (a vibrating probe set on a crane) with a horizontal displacement of 0.014 m generating an elastic wave at frequency 50 Hz. Reproduced from [566]. CC BY 3.0.

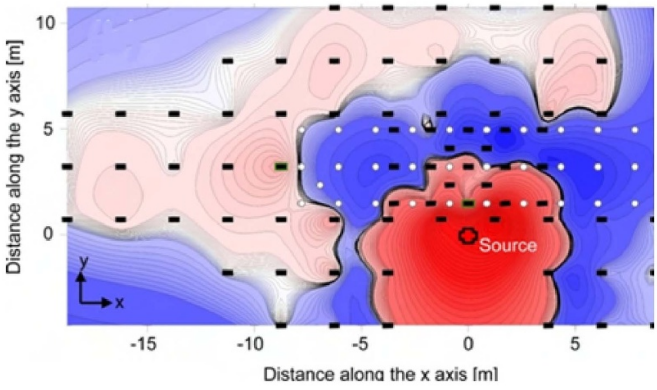

Figure 58. Seismic measurements for a monochromatic source at 50 Hz: experimental results' map after interpolation between sensors: difference $(J_2 - J_1)$ of measured energy field (arbitrary units) after (J_2) and before (J_1) carrying out the boreholes. Note the red region has twice more elastic energy after we carried out the boreholes. This is reminiscent of a source in presence of a mirror. Note also small values of J_1 about ten meters away from the source (viscoelastic soil) make $(J_2 - J_1)$ artificially high on the upper edge of the map, and should be disregarded. Black rectangles symbolize sensors, white circles, the holes and the red cross, the source. Reproduced from [566]. CC BY 3.0.

pine trees) located on the campus of the University of Joseph Fourier in Grenoble was carried out. Two three-component seismometers, S_1 and S_2, recorded, in continuous mode for 1 h, the ambient noise inside and outside the region occupied by the meta-forest (see figure 59(b)). The positioning was chosen so S_2 was far enough from the forest, whilst S_1 was well inside the forest so as to capture the different propagation properties. The total records were windowed in 10 min records and the averaged spectral ratio between S_1 and S_2 is depicted in blue in figure 59(c) for the horizontal displacement component u_x. Two large transmission minima can be seen in the frequency

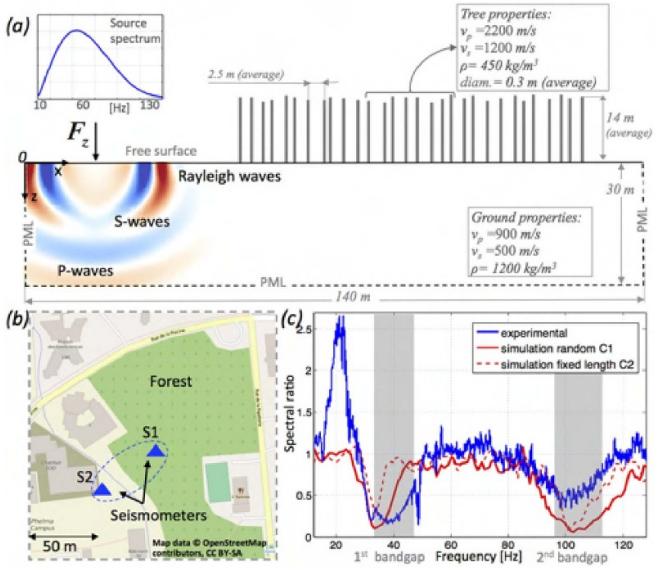

Figure 59. Natural seismic metamaterial experiment performed on the campus of University of Grenoble in 2015. (a) The 2D computational domain shows, in red-blue colorscale, the vertical displacement uz. (b) Map (reproduced from © OpenStreetMaps contributors. CC BY-SA 2.0) of the forest location, S1 and S2 are the seismometers. (c) Measured (blue) and simulated (red) spectral ratios. Dashed (solid) red line corresponds to the periodic C2 (random C1) model for the forest, see further details in [574]. Reproduced from [574]. CC BY 4.0.

intervals $[30, 45]$ Hz and $[90, 110]$ Hz. The energy transferred through the forest in these frequency intervals is reduced by a factor of 6. One notes that the second minimum occurs approximately at three times the frequency of the first minimum and hence is related to longitudinal vibrations of the trees. These minima are located inside band gaps induced by local resonances between trees and Rayleigh waves propagating in the soil and are explained notably in [567–569] by extending the beam-plate metamaterial theory of [570]. An analogous model has been proposed for Love waves in [571].

By varying the height of trees according to the geometry shown in figure 59, it is possible to convert Rayleigh surface waves (see figure 60) into mainly harmless downward propagating shear bulk waves [572], an effect akin to the seismic rainbow effect, which has been independently proposed for resonators of varying sizes buried in the soil in [573].

5.8. External cloaking

In 1994, it has been proposed that a resonant optical core–shell system [575] allows for some level of cloaking. This seminal work has inspired external cloaking based on anomalous resonances [576] in the quasi-static regime, and for a countable set of small dipoles [577–580]. We further note the result on perfect cloaking due to anomalous resonance of small objects, of size not dependent on the loss [581], in contrast to the numerical results of [577]. At elevated frequencies, the set of dipoles is no longer perfectly cloaked [582].

However, some space folding techniques based on non-monotonic transforms have been proposed to extend external

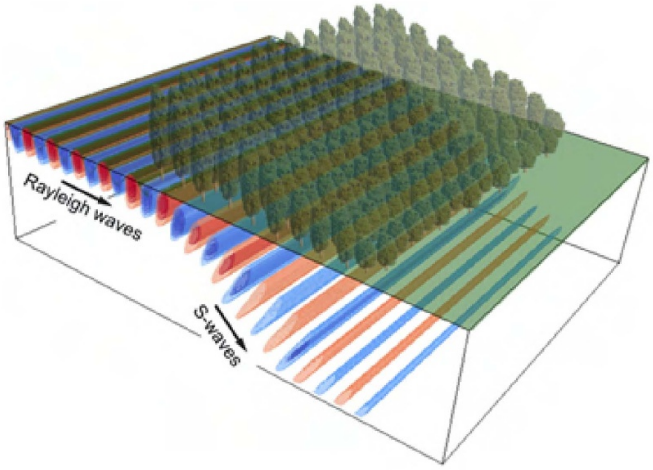

Figure 60. Artistic view of the conversion phenomenon made possible by a seismic metawedge consisting of a forest of trees of decreasing heights with respect to the incoming Rayleigh wave (Credit: A Colombi). The incident Rayleigh surface wave is converted into a downward propagating bulk shear wave. Taken from [572]. Reproduced from [572]. CC BY 4.0.

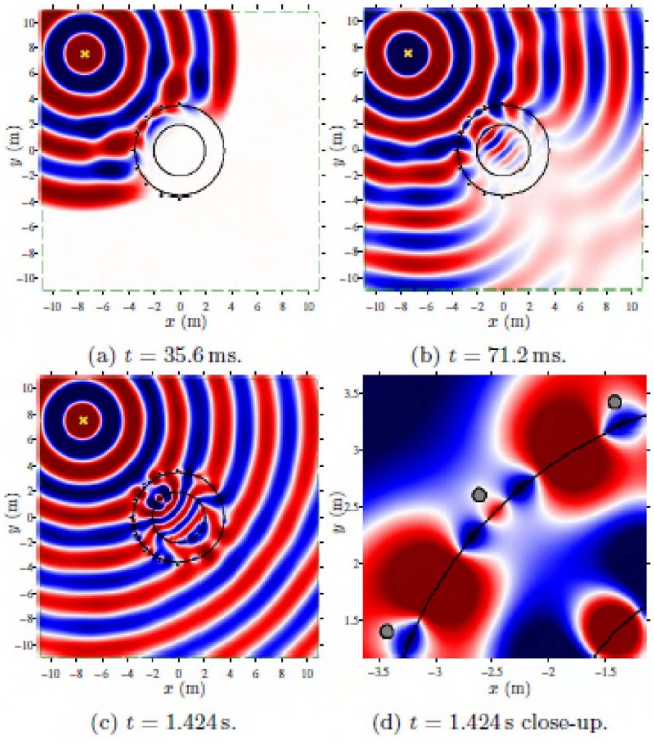

Figure 61. Snapshots of anti-plane shear wave at different times for small clamped scatterers placed just outside an external cloak. The yellow cross marks the source. Panel (d) is a close-up of (c) highlighting the interactions of the surface waves on the shell with the scatterers shown as grey dots. Reprinted from [585], with the permission of AIP Publishing.

cloaking in optics beyond the quasi-static regime [583] with a governing equation that holds true also for transverse electromagnetic, acoustic pressure, and anti-plane shear elastic waves. This concept has even been extended to bianisotropic media [584], for which correspondences can be drawn with in-plane elasticity. Such correspondences break down in the full 3D elastic case, such as for spherical cloaks.

Space folding techniques should thus open an interesting route to cloaking small objects for acoustic and elastic waves, at least in cylindrical geometries. Indeed, in the tracks of [583, 584], one can generate a new class of cylindrical isotropic acoustic cloaks with a constant negative density and a spatially varying negative bulk modulus [585]. More precisely, in figure 61, we consider an external cloak consisting of a core with a positive definite shear modulus and a positive mass density, and a shell with simultaneously negative density and shear modulus. Such a core–shell resonant system akin to that in [575] creates a virtual folded region outside the shell. To handle such negative physical parameters in the time-domain, a two-step strategy has been used in [585], first assuming resonant (Drude-type) effective parameters in the frequency-domain and then returning to the time-domain by applying the formalism of the auxiliary fields [586, 587]. One can see in figure 61 that after a transient regime for which the external cloak behaves like a super-scatterer (figure 61(b)) i.e. the external cloak scatters even more than the set of clamped scatterers on their own), a stationary regime is reached in which scattering by the small clamped scatterers is almost totally suppressed (figure 61(c)). The magnified view in figure 61(d) focuses on the anomalous resonance at the interface between the shell and ambient medium. This resonance appears due to sign-shifting shear and mass-density parameters across the interface. We note that phase and group velocity have opposite sign within the shell. Thus, the physics of negative refraction [588] plays a prominent role in external cloaking.

Interestingly, one can even envisage cloaking finite-size objects outside of an external cloak, making use of complementary media [589], but this route may be harder to implement in practice as it requires inserting the complementary version of the object to cloak within the shell.

5.9. Active cloaking

It was shown in [590] that within the accuracy of the first-order Born approximation there are neither deterministic nor random non-scattering scatterers that are invisible for all directions of incidence. However, Miller has shown in [473] that active sources can be used to cloak a region of space to make its contents transparent to waves. Miller's method uses sensors and active sources near the surface of the region, and could operate over finite bandwidths. This method is reminiscent of anti-sound devices [591], and can be described as follows. Consider first how to exclude a scalar wave from a volume V based only on surface sources deduced from local values of the field at the surface S. Assume that outside of

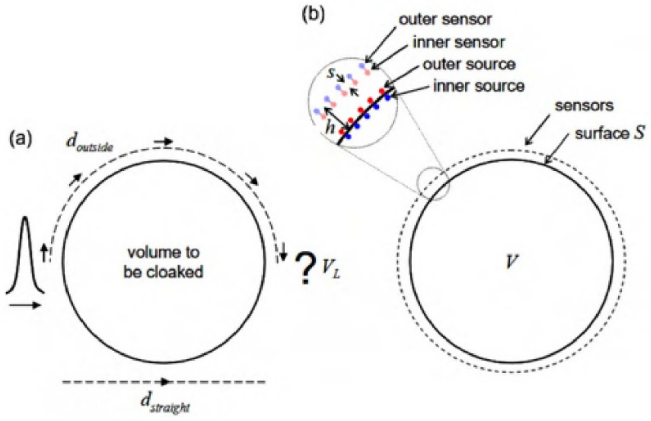

Figure 62. (a) Illustration of a pulse incident on a volume V to be cloaked solely on the basis of local response near the surface. (b) Arrangement of sources and sensors for cloaking of scalar waves. The challenge is to avoid the delay induced by the detoured wave trajectory d_{outside} compared with d_{straight}. Taken from [473]. Reprinted with permission from [473] © The Optical Society.

the volume V, the wavefield satisfies the homogeneous scalar wave equation $\Delta p + (1/c^2)\frac{\partial^2 p}{\partial t^2} = 0$ with c the wave velocity. To exclude the wave from V, Miller adds sources to the surface S of the volume V. For scalar waves of amplitude p, point sources and dipole sources oriented perpendicular to the surface S will exclude the field from the volume [591]. The wave equation is supplied with an initial incident field and surface sources are retarded and obey the radiation condition. Miller's sources behave as perfect absorbers for scalar waves, e.g. they make a large planar surface reflectionless for a normally incident plane wave.

Miller designed the scheme as shown in figure 62(b): pairs of sensors some small distance h outside V, oriented perpendicular to S, are aligned with corresponding pairs of sources located on either side of S. Without loss of generality, the same separations s are assumed in each pair. The difference between the measured waves at these two sensors gives the wave gradient $\partial p/\partial n$, with $\mathbf{n}$ the normal to the surface S pointing outward from V, whilst their average gives the amplitude p. Dipole sources are built with appropriate opposite values on the two sources in a pair, or alternatively point sources by assigning half of their value to each of the elements in the source pair. Miller then derives a formula for calculating the resulting inner and outer source amplitudes p_{in} and p_{out} respectively based on the inner and outer measured wave amplitudes f_{in} and f_{out} respectively from the corresponding sensor pair, namely $p_{\text{out}} = f_{\text{in}}\delta a/s$ and $p_{\text{in}} = -p_{\text{out}}\delta a/s$ where δa is the effective element of area on S occupied by a given source pair.

If the source and sensor pairs are sufficiently dense, such an active quasi-cloaking scheme of local measurements and resulting driven sources on S does indeed exclude all waves from the volume V.

However, Guevara, Milton and Onofrei further proposed some concept of active exterior cloaking whereby the object to cloak is not entirely surrounded by sources [562, 592].

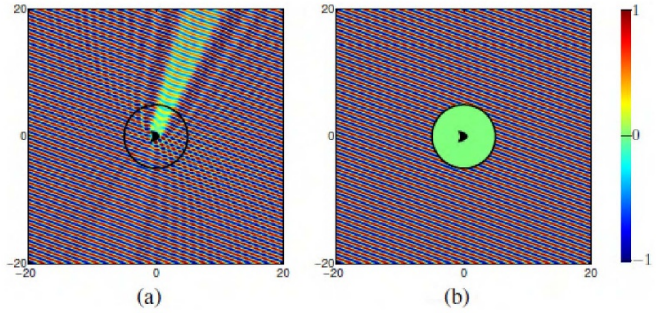

Figure 63. Active interior cloak (a) inactive and (b) active. The region D where Green's formula is applied is the circle of radius 5λ in thick lines. The field inside the cloaked region D is virtually zero, so that outside the cloaked region the field is indistinguishable from the incident plane wave with direction $5\pi/13$. The axis units are in wavelengths λ. Reprinted from [592], Copyright (2011), with permission from Elsevier.

The cloaking device consists of at least three multipolar point sources in 2D (resp. four in 3D) making use of the addition theorem and applying it to Miller's set of sources. This approach leads to a cloaking efficiency similar to that proposed by the same researchers in [593]. In the latter, the amplitudes of the wave-canceling sources are found numerically to ensure cloaking, yet with minimal disturbance to the field outside a given radius. The work [562, 592] has been extended to the Helmholtz equation with complex wavenumbers in [594].

The concept of active exterior cloaking (see Figure 63) has been extended to elastodynamics in [595], and this opens new avenues in the control of bulk and surface seismic waves: one can envision utilizing a set of seismic sources to counteract ground vibrations generated for instance by construction work. Indeed, placing a few vibrometers along the perimeter of the construction area, and adequately tuning their frequencies, might already reduce impact of ground vibrations on buildings surrounding the construction zone.

6. Conclusion

Mechanical metamaterials have advanced quite dramatically over the last decade, and that progress is accelerating. The advance from plywood panels, that are perhaps one of the oldest practical application of laminate metamaterials, through to 3D printed tailored graded polymer elastic lattices have entered designer sports-shoe soles, and the future where ultra-light weight and deployable mechanical metamaterials will likely enter space applications is driven by the deep understanding of metamaterials and exploiting their potential. Further examples are compact acoustical sound absorbers, as well as vibration absorbers, engineered for narrow-band and broadband operation that are now on their way into commercial applications, for example in cars. Vibration isolation of the mirrors in large-scale optical interferometers for gravitational-wave detection by metamaterial mirror holders is related and emerging as a scientific application. A different facet of vibration isolation by metamaterials is the guiding of seismic waves around sensitive buildings (cloaking) by

graded architectures, the design of which is based on spatial coordinate transformations—and these are just a snapshot of the applications that are emerging.

Other metamaterial properties are just fascinating scientifically, but still in search for real-world applications. Examples include backward waves, topological band gaps for robust wave guiding, unidirectional or nonreciprocal sound propagation, and means of manipulating the polarization of elastic waves. In many instances, mechanical metamaterials have also served as model systems for optics, where experimental realizations are often more demanding. A whole wealth of further possibilities arises in time-modulated mechanical metamaterials, but theory is far ahead of experiment in this field. Despite all of the advances described in this review, basic scientific questions are still open. Consider two examples.

(1) Suppose a metamaterial composed of two different ingredient materials A and B is discretized into a certain number of voxels per unit cell. What are the fundamental bounds for the resulting effective elastic properties? (2) Suppose a user requests certain effective elastic metamaterial properties for an application. What is a possible metamaterial microstructure that yields these properties? Both of these seemingly simple questions cannot even be answered efficiently for ordinary classical Cauchy elasticity, not to mention more advanced generalized forms of effective-medium elasticity that we have also covered in the first part of this review. Finally, mechanical properties are important and have been in the center of this review, but one must not forget that in most real-world applications of materials, a combination of mechanical, optical, electrical, and thermal properties matters. We refer the reader to correspondingly broader reviews on metamaterials [523, 596–601].

Data availability statement

No new data were created or analysed in this study.

Acknowledgments

We thank Vincent Laude, Laurent Hirsinger and Yi Chen for stimulating discussions. We also thank the two reviewers for their insightful and constructive comments that have helped significantly to improve this paper. This research has been funded by the Deutsche Forschungs gemeinschaft (DFG, German Research Foundation) under Germany's Excellence Strategy via the Excellence Cluster 3D Matter Made to Order (EXC-2082/1-390761711), which has also been supported by the CarlZeiss Foundation through the Carl-Zeiss-Foundation-Focus@HEiKA, by the State of Baden-Württemberg, and by the Karlsruhe Institute of Technology (KIT). We further acknowledge support by the Helmholtz program Materials Systems Engineering (MSE), and by the associated KIT project Virtual Materials Design (VIRTMAT). M K is grateful for support by the EIPHI Graduate School (Contract No. ANR-17-EURE-0002) and in part by the ANR PNanoBot (Contract No. ANR-21-CE33-0015).

ORCID iDs

Richard Craster https://orcid.org/0000-0001-9799-9639
Sébastien Guenneau https://orcid.org/0000-0002-5924-622X
Muamer Kadic https://orcid.org/0000-0002-4692-5696
Martin Wegener https://orcid.org/0000-0002-9770-2441

References

[1] Laughlin D E and Hono K 2014 *Physical Metallurgy* (Newnes)
[2] Castro Neto A H, Guinea F, Peres N M R, Novoselov K S and Geim A K 2009 *Rev. Mod. Phys.* **81** 109–62
[3] Honarvar H and Hussein M I 2018 *Phys. Rev.* B **97** 195413
[4] Hussein M I, Tsai C N and Honarvar H 2020 *Adv. Funct. Mater.* **30** 1906718
[5] Walser R M 2001 Electromagnetic metamaterials *Proc. SPIE* **4467** 1–15
[6] Caloz C and Itoh T 2005 *Electromagnetic Metamaterials: Transmission Line Theory and Microwave Applications* (Wiley)
[7] Soukoulis C M, Linden S and Wegener M 2007 *Science* **315** 47–49
[8] McCall M *et al* 2018 *J. Opt.* **20** 063001
[9] Soukoulis C and Wegener M 2011 *Nat. Photon.* **5** 523
[10] Xiao S, Wang T, Liu T, Zhou C, Jiang X and Zhang J 2020 *J. Phys. D: Appl. Phys.* **53** 503002
[11] Laude V 2015 *Phononic Crystals: Artificial Crystals for Sonic, Acoustic and Elastic Waves* vol 26 (Walter de Gruyter GmbH & Co. KG)
[12] Morse P M and Ingard K U 1968 *Theoretical Acoustics* (McGraw-Hill)
[13] Pierce A D 1989 *Acoustics: An Introduction to its Principles and Applications* (American Institute of Physics)
[14] Howe M S 1998 *Acoustics of Fluid-Structure Interactions* (Cambridge University Press)
[15] Hayward A 1969 *Nature* **221** 1047
[16] Milton G W 2002 *The Theory of Composites* (Cambridge University Press)
[17] Oerter R 2006 *The Theory of Almost Everything: The Standard Model, the Unsung Triumph of Modern Physics* (Penguin)
[18] Banerjee B 2011 *An Introduction to Metamaterials and Waves in Composites* (CRC Press)
[19] Kadic M, Schittny R, Bückmann T and Wegener M 2013 *New J. Phys.* **15** 023029
[20] Sommerfeld A 1950 *Mechanics of Deformable Bodies* (*Lectures on Theoretical Physics*) (Academic)
[21] Authier A 2003 *International tables for Crystallography Volume D: Physical Properties of Crystals* (Springer)
[22] Lecoutre G, Daher N, Devel M and Hirsinger L 2017 *Acta Mech.* **228** 1681–710
[23] Hirsinger L, Daher N, Devel M and Lecoutre G 2018 The principle of virtual power (PVP): application to complex media, extension to gauge and scale invariances and fundamental aspects *Generalized Models and Non-Classical Approaches in Complex Materials* vol 2 (Springer) pp 29–53
[24] Tadmor E B and Miller R E 2011 *Modeling Materials: Continuum, Atomistic and Multiscale Techniques* (Cambridge University Press)
[25] Song Y, Devel M and Wang Z 2021 *Physica* E **127** 114567
[26] Ting T T C 1996 *Anisotropic Elasticity: Theory and Applications* (Oxford University Press)
[27] Milton G W and Cherkaev A V 1995 *J. Eng. Mater. Technol.* **117** 483–93

[28] Sigmund O 1995 *Mech. Mater.* **20** 351–68
[29] Milton G W 2013 *J. Mech. Phys. Solids* **61** 1543–60
[30] Quadrelli D E, Craster R, Kadic M and Braghin F 2021 *Extreme Mech. Lett.* **44** 101262
[31] Sacha K and Zakrzewski J 2017 *Rep. Prog. Phys.* **81** 016401
[32] Kadic M, Milton G, van Hecke M and Wegener M 2019 *Nat. Rev. Phys.* **1** 198–210
[33] Ikeda T 1996 *Fundamentals of Piezoelectricity* (Oxford University Press)
[34] Kittel C 1996 *Introduction to Solid State Physics* (Wiley)
[35] Drebushchak V 2020 *J. Therm. Anal. Calorimetry* **142** 1097–113
[36] Alaee R, Christensen J and Kadic M 2018 *Phys. Rev. Appl.* **9** 014007
[37] Chen Y, Kadic M, Kaplan D E, Rajendran S, Sushkov A O and Wegener M 2020 arXiv:2007.07974
[38] Eringen A 1974 *Elastodynamics* vol II (Academic)
[39] Kadic M, Diatta A, Frenzel T, Guenneau S and Wegener M 2019 *Phys. Rev.* B **99** 214101
[40] Chen Y, Frenzel T, Guenneau S, Kadic M and Wegener M 2020 *J. Mech. Phys. Solids* **137** 103877
[41] Madeo A and Neff P 2017 *Handbook of Nonlocal Continuum Mechanics for Materials and Structures* (Springer) pp 713–39
[42] Barbagallo G, Madeo A, d'Agostino M V, Abreu R, Ghiba I D and Neff P 2017 *Int. J. Solids Struct.* **120** 7–30
[43] Willis J R 1980 *J. Mech. Phys. Solids* **28** 287–305
[44] Norris A, Shuvalov A and Kutsenko A 2012 *Proc. R. Soc.* A **468** 1629
[45] Mindlin R D and Tiersten H F 1962 *Arch. Ration. Mech. Anal.* **11** 415–488
[46] Koiter W T 1964 *Proc. Ned. Akad. Wet.* B **67** 17–44
[47] Cosserat E and Cosserat F 1909 *Theorie des Corps Deformables* (Hermann)
[48] Eringen A 1966 *J. Math. Mech.* **15** 909–23
[49] Mindlin R D and Eshel N 1968 *Int. J. Solids Struct.* **4** 109–24
[50] Ferretti M, Madeo A, dell'Isola F and Boisse P 2014 *Z. Angew. Math. Phys.* **65** 587–612
[51] Cordero N, Forest S and Busso E 2016 *J. Mech. Phys. Solids* **97** 92–124
[52] Smyshlyaev V and Fleck N 1994 *J. Mech. Phys. Solids* **42** 1851–1382
[53] Boutin C 1996 *Int. J. Solids Struct.* **33** 1023–51
[54] dell'Isola F, Sciarra G and Vidoli S 2009 *Proc. R. Soc.* A **465** 2177–96
[55] Casolo S 2004 *Int. J. Solids Struct.* **41** 3625–41
[56] Auffray N, He Q and Le Quang H 2019 *Int. J. Solids Struct.* **159** 197–210
[57] Kroener E 1959 *Arch. Ration. Mech. Anal.* **4** 273–334
[58] Hall E 1951 *Proc. Phys. Soc.* B **64** 747
[59] Petch N 1953 *J. Iron Steel Inst.* **173** 25
[60] Aifantis K and Willis J 2005 *J. Mech. Phys. Solids* **53** 1047–70
[61] Acharya A and Bassani J 2000 *J. Mech. Phys. Solids* **48** 1565–1595
[62] Guha S, Sangal S and Basu S 2015 *Sadhana* **40** 1205–40
[63] Niordson C 2008 *Phil. Mag.* **88** 3731–45
[64] Biot M A 1956 *J. Appl. Mech.* **23** 91–96
[65] Biot M A 1956 *J. Acoust. Soc. Am.* **28** 179–91
[66] Rice J R and Cleary M P 1976 *Rev. Geophys.* **14** 227–41
[67] Bensoussan A, Lions J L and Papanicolaou G 1978 *Asymptotic Analysis for Periodic Structures* (*Studies in Mathematics and its Applications* vol 5) (North-Holland Publishing Co.)
[68] Sánchez-Palencia E 1980 *Non-Homogeneous Media and Vibration Theory* (*Lecture Notes in Physics* vol 127) (Springer)
[69] Zhikov V V, Kozlov S M and Oleinik O A 1994 *Homogenization of Differential Operators and Integral Functionals* (Springer)
[70] Bakhvalov N S and Panasenko G 2012 *Homogenisation: Averaging Processes in Periodic Media: Mathematical Problems in the Mechanics of Composite Materials* vol 36 (Springer Science & Business Media)
[71] Bytner S and Gambin B 1986 *Arch. Mech. Stosow.* **38** 289–99
[72] Laude V, Iglesias M J A, Wang Y F and Kadic M 2021 *J. Appl. Phys.* **129** 215106
[73] Backus G E 1962 *J. Geophys. Res.* **67** 4427–40
[74] Postma G 1955 *Geophysics* **20** 780–806
[75] Francfort G A and Murat F 1986 *Arch. Ration. Mech. Anal.* **94** 307–34
[76] Tartar L 1977 *Séminaire Équations aux Dérivées Partielles (Polytechnique) dit Aussi" Séminaire Goulaouic–Schwartz* pp 1–12
[77] Murat F 1978 *Ann. Scuola Norm. Super. Pisa Cl. Sci.* **5** 489–507
[78] Wright S, Mikelic A and Bourgeat A 1994 *J. Reine Angew. Math.* **1994** 19–52
[79] Abddaimi Y, Michaille G and Licht C 1997 *Asymptotic Anal.* **15** 183–202
[80] Bourgeat A and Piatnitski A 2004 *Ann. Inst. Henri Poincare* B **40** 153–65
[81] Bourgeat A, Mikelić A and Piatnitski A 2003 *Asymptotic Anal.* **34** 311–32
[82] Zhikov V V and Pyatnitskii A 2006 *Izv. Math.* **70** 19–67
[83] Boukrouche M and Ciuperca I 2006 *Q. Appl. Math.* **64** 561–91
[84] Ambrosio L and Frid H 2009 *Arch. Ration. Mech. Anal.* **192** 37–85
[85] Heida M 2011 *Asymptotic Anal.* **72** 1–30
[86] Sango M 2014 *Commun. Math. Sci.* **12** 345–82
[87] Mohammed M and Sango M 2015 *Asymptotic Anal.* **91** 341–71
[88] Ptashnyk M 2015 *Multiscale Model. Simul.* **13** 1061–105
[89] Calvo-Jurado C, Casado-Díaz J and Luna-Laynez M 2016 *Nonlinear Anal.* **133** 250–74
[90] Neukamm S and Varga M 2018 *Multiscale Model. Simul.* **16** 857–99
[91] Pardoux E 1999 *J. Funct. Anal.* **167** 498–520
[92] Papanicolaou G and Varadhan S 1979 Boundary value problems with rapidly oscillating random coefficients *Colloquia Mathematica Societatis János Bolyai* vol 27 (North-Holland) pp 835–73
[93] Bourgeat A and Piatnitski A 1999 *Asymptotic Anal.* **21** 303–15
[94] Le Bris C 2014 *ESAIM Proc. Surv.* **45** 18–31
[95] Anantharaman A and Le Bris C 2011 *Multiscale Model. Simul.* **9** 513–44
[96] Blanc X, Le Bris C and Lions P L 2007 *J. Math. Pures Appl.* **88** 34–63
[97] Kozlov S 1979 *Math. USSR Sbornik* **35** 481
[98] Oleinik O and Zhikov V 1982 *Semin. Mat. Fis. Milano* **52** 149–66
[99] Braides A 1992 *Appl. Anal.* **47** 259–77
[100] De Arcangelis R 1992 *Appl. Anal.* **43** 77–98
[101] Casado-Díaz J and Gayte I 2002 *Proc. R. Soc.* A **458** 2925–46
[102] Sango M, Svanstedt N and Woukeng J L 2011 *Nonlinear Anal.* **74** 351–79
[103] Douanla H and Svanstedt N 2011 *Commun. Math. Anal.* **11** 61–93
[104] Silva J 2015 *Calc. Var. PDE* **54** 3623–41
[105] Jäger W, Tambue A and Woukeng J L 2019 arXiv:1906.11501
[106] Nguetseng G 1989 *SIAM J. Math. Anal.* **20** 608–23
[107] Allaire G 1992 *SIAM J. Math. Anal.* **23** 1482–518

[108] Lukkassen D, Nguetseng G and Wall P 2002 *Int. J. Pure Appl. Math.* **2** 35–86
[109] Bouchitté G, Guenneau S and Zolla F 2010 *Multiscale Model. Simul.* **8** 1862–81
[110] Duneau M and Katz A 1985 *Phys. Rev. Lett.* **54** 2688–91
[111] Ferreira R, Fonseca I and Venkatraman R 2021 *SIAM J. Math. Anal.* **53** 1785–817
[112] Wellander N, Guenneau S and Cherkaev E 2022 *Eur. J. Mech.* A **100** 104796
[113] Wellander N, Guenneau S and Cherkaev E 2018 *Math. Methods Appl. Sci.* **41** 1101–6
[114] Chen Y, Kadic M, Guenneau S and Wegener M 2020 *Phys. Rev. Lett.* **124** 235502
[115] O'Brien S and Pendry J B 2002 *J. Phys.: Condens. Matter* **14** 4035
[116] Bouchitté G and Felbacq D 2004 *C. R. Math.* **339** 377–82
[117] Guenneau S and Zolla F 2000 *Prog. Electromagn. Res.* **27** 91–127
[118] Kristensson G and Wellander N 2003 *SIAM J. Appl. Math.* **64** 170–95
[119] Barbatis G and Stratis I 2003 *Math. Methods Appl. Sci.* **26** 1241–53
[120] Guenneau S and Zolla F 2007 *Physica* B **394** 145–7
[121] Andryieuski A, Menzel C, Rockstuhl C, Malureanu R, Lederer F and Lavrinenko A 2010 *Phys. Rev.* B **82** 235107
[122] Milton G and Willis R 2007 *Proc. R. Soc.* A **463** 855–80
[123] Liu Y, Gralak B and Guenneau S 2016 *Opt. Express* **24** 26479–93
[124] Zhikov V V 2000 *Sbornik Math.* **191** 973
[125] Zhikov V V 2004 *Algebr. Anal.* **16** 34–58
[126] Auriault J 1983 *Int. J. Heat Mass Transfer* **26** 861–9
[127] Auriault J and Bonnet G 1985 *Arch. Mech.* **37** 269–84
[128] Auriault J 1994 *Curr. Top. Acoust. Res.* **1** 63–90
[129] Auriault J and Boutin C 1994 *Transp. Porous Media* **14** 143–62
[130] Ávila A, Griso G and Miara B 2005 *C. R. Math.* **340** 933–8
[131] Avila A, Griso G, Miara B and Rohan E 2008 *Multiscale Model. Simul.* **7** 1–21
[132] Bellieud M and Bouchitté G 1998 *Ann. Scuola Norm. Super. Pisa Cl. Sci.* **26** 407–36
[133] Briane M and Tchou N 2001 *Ann. Scuola Norm. Super. Pisa Cl. Sci.* **30** 681–711
[134] Parnell W J and Abrahams I D 2006 *Wave Motion* **43** 474–98
[135] Briane M and Camar-Eddine M 2007 *J. Math. Pures Appl.* **88** 483–505
[136] Andrianov I V, Bolshakov V I, Danishevs'kyy V V and Weichert D 2007 *Int. J. Mech. Sci.* **49** 1344–54
[137] Guillot L, Capdeville Y and Marigo J J 2010 *Geophys. J. Int.* **182** 1438–54
[138] Parnell W and Abrahams I 2008 *J. Mech. Phys. Solids* **56** 2521–40
[139] Smyshlyaev V P 2009 *Mech. Mater.* **41** 434–47
[140] Ramírez-Torres A, Penta R, Rodríguez-Ramos R, Grillo A, Preziosi L, Merodio J, Guinovart-Díaz R and Bravo-Castillero J 2019 *Comput. Vis. Sci.* **20** 85–93
[141] Smith M J and Abrahams I D 2022 *Proc. R. Soc.* A **478** 20220124
[142] Cherdantsev M, Cherednichenko K and Velčić I 2019 *Appl. Anal.* **98** 91–117
[143] Decoopman T, Tayeb G, Enoch S, Maystre D and Gralak B 2006 *Phys. Rev. Lett.* **97** 073905
[144] Pierre R and Gralak B 2008 *J. Mod. Opt.* **55** 1759
[145] Liu Y, Guenneau S and Gralak B 2013 *Phys. Rev.* B **88** 165104
[146] Herzig Sheinfux H, Kaminer I, Plotnik Y, Bartal G and Segev M 2014 *Phys. Rev. Lett.* **113** 243901
[147] Maurel A and Marigo J 2018 *Phys. Rev.* B **98** 024306
[148] Liu Y, Guenneau S and Gralak B 2013 *Proc. R. Soc.* A **469** 20130240
[149] Gorlach M A and Lapine M 2020 *Phys. Rev.* B **101** 075127
[150] Novitsky D V, Shalin A S and Novitsky A 2019 *Phys. Rev.* A **99** 043812
[151] Hossain A S and Tsukerman I 2021 *Phys. Lett.* **398** 127278
[152] Cornaggia R and Guzina B B 2020 *Int. J. Solids Struct.* **188** 88–102
[153] Lannebère S, Morgado T A and Silveirinha M G 2020 *C. R. Physique* **21** 367–88
[154] Zhukovsky S V, Andryieuski A, Takayama O, Shkondin E, Malureanu R, Jensen F and Lavrinenko A V 2015 *Phys. Rev. Lett.* **115** 177402
[155] Willis J R 2009 *Mech. Mater.* **41** 385–93
[156] Shuvalov A, Kutsenko A, Norris A and Poncelet O 2011 *Proc. R. Soc.* A **467** 1749–69
[157] Sheinfux H H, Lumer Y, Ankonina G, Genack A Z, Bartal G and Segev M 2017 *Science* **356** 953–6
[158] Coppolaro M, Castaldi G and Galdi V 2020 *Phys. Rev.* B **102** 075107
[159] Frenzel T, Kadic M and Wegener M 2017 *Science* **358** 1072–4
[160] Birman M and Suslina T 2001 Threshold effects near the lower edge of the spectrum for periodic differential operators of mathematical physics *Systems, Approximation, Singular Integral Operators and Related Topics: Int. Workshop on Operator Theory and Applications, IWOTA 2000* (Springer) pp 71–107
[161] Birman M and Suslina T 2004 *St. Petersburg Math. J.* **15** 639–714
[162] Shuvalov A, Kutsenko A and Norris A N 2010 *Wave Motion* **47** 370–82
[163] Brillouin L 1926 *Z. Phys.* **39** U840
[164] Kramers H A 1926 *Z. Phys.* **39** 828–40
[165] Wentzel G 1926 *Z. Phys.* **38** 518–29
[166] Jeffreys H 1925 *Proc. London Math. Soc.* **2** 428–36
[167] Bretherton F 1968 *Proc. R. Soc.* A **302** 555–76
[168] Smith R 1977 *SIAM J. Appl. Math.* **33** 39–50
[169] Gridin D and Craster R V 2003 *Proc. R. Soc.* A **459** 2909–31
[170] Gridin D, Craster R V and Adamou A T 2005 *Proc. R. Soc.* A **461** 1181–97
[171] Kaplunov J, Rogerson G and Tovstik P 2005 *Q. J. Mech. Appl. Math.* **58** 645–64
[172] Postnova J and Craster R V 2007 *Wave Motion* **44** 205–21
[173] Adams S D, Craster R V and Guenneau S 2008 *Proc. R. Soc.* A **464** 2669–92
[174] Adams S D, Craster R V and Guenneau S 2009 *Waves Random Complex Media* **19** 321–46
[175] Craster R, Guenneau S and Adams S 2009 *Phys. Rev.* B **79** 045129
[176] Adams S D, Cherednichenko K D, Craster R and Guenneau S 2010 *Eur. J. Appl. Math.* **21** 557–90
[177] March N H and Stoddart J 1968 *Rep. Prog. Phys.* **31** 533
[178] Stoddart J, March N and Stott M 1969 *Phys. Rev.* **186** 683
[179] Forstmann F and Pendry J 1970 *Z. Phys.* A **235** 75–84
[180] Pendry J and Gurman S 1975 *Surf. Sci.* **49** 87–105
[181] Haydock R, Heine V, Kelly M and Pendry J 1972 *Phys. Rev. Lett.* **29** 868
[182] Rousseau J, Stoddart J and March N 1970 *Proc. R. Soc.* A **317** 211–25
[183] John S 1987 *Phys. Rev. Lett.* **58** 2486
[184] Page J H, Schriemer H P, Jones I, Sheng P and Weitz D A 1997 *Physica* A **241** 64–71
[185] Wu F, Hou Z, Liu Z and Liu Y 2001 *Phys. Lett.* A **292** 198–202
[186] Fistul M and Page J 2001 *Phys. Rev.* E **64** 036609
[187] Yang S, Page J H, Liu Z, Cowan M L, Chan C T and Sheng P 2002 *Phys. Rev. Lett.* **88** 104301
[188] Martinsson P and Movchan A 2003 *Q. J. Mech. Appl. Math.* **56** 45–64

[189] Pennec Y, Djafari-Rouhani B, Larabi H, Vasseur J and Hladky-Hennion A 2008 *Phys. Rev.* B **78** 104105
[190] Gei M, Movchan A and Bigoni D 2009 *J. Appl. Phys.* **105** 063507
[191] Krushynska A O, Kouznetsova V G and Geers M G 2014 *J. Mech. Phys. Solids* **71** 179–96
[192] He Y, Wu F, Yao Y, Zhang X, Mu Z, Yan S and Cheng C 2013 *Phys. Lett.* A **377** 889–94
[193] Mermin N D 1979 *Rev. Mod. Phys.* **51** 591
[194] Figotin A and Kuchment P 1996 *SIAM J. Appl. Math.* **56** 68–88
[195] Figotin A and Kuchment P 1996 *SIAM J. Appl. Math.* **56** 1561–620
[196] Figotin A and Klein A 1997 *J. Stat. Phys.* **86** 165–77
[197] Allaire G and Conca C 1998 *J. Math. Pure Appl.* **77** 153–208
[198] Hempel R and Lienau K 2000 *Commun. PDE* **25** 1445–70
[199] Movchan A B, Movchan N V and Poulton C G 2002 *Asymptotic Models of Fields in Dilute and Densely Packed Composites* (World Scientific)
[200] Wilcox S, Botten L, McPhedran R, Poulton C and de Sterke C M 2005 *Phys. Rev.* E **71** 056606
[201] Ammari H, Fitzpatrick B, Hiltunen E O and Yu S 2018 *SIAM J. Appl. Math.* **78** 3316–35
[202] Nazarov S A 2010 *Math. Notes* **87** 738–56
[203] Poulton C, Movchan A, Movchan N and McPhedran R C 2012 *Proc. R. Soc.* A **468** 1196–216
[204] Cherednichenko K D, Cooper S and Guenneau S 2015 *Multiscale Model. Simul.* **13** 72–98
[205] Wang K, Zhou J, Cai C, Xu D and Ouyang H 2019 *Appl. Math. Modelling* **73** 581–97
[206] Craster R V and Davies B 2022 arXiv:2202.07324
[207] Craster R V, Kaplunov J and Pichugin A V 2010 *Proc. R. Soc.* A **466** 2341–62
[208] Birman M 2004 *St. Petersburg Math. J.* **15** 507–13
[209] Birman M S and Suslina T 2006 *J. Math. Sci.* **136** 3682–90
[210] Antonakakis T, Craster R and Guenneau S 2014 *J. Mech. Phys. Solids* **71** 84–96
[211] Nemat-Nasser S, Willis J R, Srivastava A and Amirkhizi A V 2011 *Phys. Rev.* B **83** 104103
[212] Boutin C, Rallu A and Hans S 2014 *J. Mech. Phys. Solids* **70** 362–81
[213] Rallu A, Hans S and Boutin C 2017 *Proc. Eng.* **199** 1501–6
[214] Zalipaev V, Movchan A, Poulton C and McPhedran R 2002 *Proc. R. Soc.* A **458** 1887–912
[215] Antonakakis T, Craster R V and Guenneau S 2013 *Proc. R. Soc.* A **469** 20120533
[216] Antonakakis T, Craster R V and Guenneau S 2014 *Europhys. Lett.* **105** 54004
[217] Achaoui Y, Ungureanu B, Enoch S, Brûlé S and Guenneau S 2016 *Extreme Mech. Lett.* **8** 30–37
[218] Nicorovici N, McPhedran R and Botten L 1995 *Phys. Rev. Lett.* **75** 1507
[219] Bouchitté G and Picard C 1996 *Appl. Anal.* **61** 307–41
[220] Movchan A, Poulton C G, Botten L C, Nicorovici N and McPhedran R C 2001 *SIAM J. Appl. Math.* **61** 1706–30
[221] Cabib E, Freddi L, Morassi A and Percivale D 2001 *J. Elast. Phys. Sci. Solids* **64** 157–78
[222] Guenneau S, Poulton C and Movchan A 2003 *Proc. R. Soc.* A **459** 2215–63
[223] Bellieud M and Cooper S 2017 *SIAM J. Math. Anal.* **49** 4275–317
[224] Aziz A and Na T Y 1984 *Perturbation Methods in Heat Transfer* (Springer)
[225] Shivamoggi B K 2003 *Perturbation Methods for Differential Equations* (Springer)
[226] Verhulst F 2005 *Methods and Applications of Singular Perturbations* (Springer)
[227] Watts R G 2012 Introduction to perturbation methods *Essentials of Applied Mathematics for Engineers and Scientists* (Springer) pp 153–62
[228] Kevorkian J K and Cole J D 2012 *Multiple Scale and Singular Perturbation Methods* vol 114 (Springer Science & Business Media)
[229] Kanaun S and Levin V 2007 *Self-Consistent Methods for Composites: Vol. 1: Static Problems* vol 148 (Springer Science & Business Media)
[230] Andrianov I V, Bolshakov V I, Danishevs'kyy V V and Weichert D 2008 *Proc. R. Soc.* A **464** 1181–201
[231] Martin P, Maurel A and Parnell W 2010 *J. Acoust. Soc. Am.* **128** 571–7
[232] Ammari H, Fitzpatrick B, Kang H, Ruiz M, Yu S and Zhang H 2018 *Mathematical and Computational Methods in Photonics and Phononics* vol 235 (American Mathematical Society)
[233] Meng S and Guzina B B 2018 *Proc. R. Soc.* A **474** 20170638
[234] Russell P S J, Marin E, Diez A, Guenneau S and Movchan A 2003 *Opt. Express* **11** 2555–60
[235] Dainese P, Russell P S J, Joly N, Knight J, Wiederhecker G, Fragnito H L, Laude V and Khelif A 2006 *Nat. Phys.* **2** 388–92
[236] Lefebvre G, Antonakakis T, Achaoui Y, Craster R V, Guenneau S and Sebbah P 2017 *Phys. Rev. Lett.* **118** 254302
[237] Guzina B B, Meng S and Oudghiri-Idrissi O 2019 *Proc. R. Soc.* A **475** 20180547
[238] Assier R C, Touboul M, Lombard B and Bellis C 2020 *Proc. R. Soc.* A **476** 20200402
[239] Moukhomodiarov R, Pichugin A and Rogerson G 2010 *Math. Mech. Solids* **15** 462–90
[240] Antonakakis T and Craster R 2012 *Proc. R. Soc.* A **468** 1408–27
[241] Tang K, Makwana M, Craster R V and Sebbah P 2020 *Phys. Rev.* B **102** 214103
[242] Ungureanu B, Makwana M P, Craster R V and Guenneau S 2021 *Phys. Rev. Appl.* **15** 014057
[243] Bellis C, Lombard B, Touboul M and Assier R 2021 *J. Mech. Phys. Solids* **149** 104321
[244] Li X M 2018 *J. Math. Soc. Japan* **70** 519–72
[245] Hairer M and Pardoux E 2021 *Arch. Ration. Mech. Anal.* **239** 151–217
[246] Tip A, Moroz A and Combes J 2000 *J. Phys. A: Math. Gen.* **33** 6223
[247] Combes J M, Gralak B and Tip A 2002 Spectral properties of absorptive photonic crystals *Waves in Periodic and Random Media* (*Contemporary Mathematics* vol 339) (American Mathematical Society) p 1
[248] Hussein M I and Frazier M J 2013 *Acoustic Metamaterials and Phononic Crystals* (Springer) pp 201–15
[249] Frazier M J and Hussein M I 2015 *J. Acoust. Soc. Am.* **138** 3169–80
[250] Wang Y F, Wang Y S and Laude V 2015 *Phys. Rev.* B **92** 104110
[251] Miniaci M, Krushynska A, Gliozzi A S, Kherraz N, Bosia F and Pugno N M 2018 *Phys. Rev. Appl.* **10** 024012
[252] Parnell W J and De Pascalis R 2019 *Phil. Trans. R. Soc.* A **377** 20180072
[253] Harutyunyan D, Milton G W and Craster R V 2016 *Proc. R. Soc.* A **472** 20160066
[254] Martin P 2020 *Mech. Res. Commun.* **105** 103502
[255] Nassar H, Chen Y Y and Huang G L 2018 *Proc. R. Soc.* A **474** 20180523
[256] Nassar H, Yousefzadeh B, Fleury R, Ruzzene M, Alù A, Daraio C, Norris A N, Huang G and Haberman M R 2020 *Nat. Rev. Mater.* **5** 667–85
[257] Huidobro P A, Galiffi E, Guenneau S, Craster R V and Pendry J 2019 *Proc. Natl Acad. Sci. USA* **116** 24943–8

[258] Torrent D, Poncelet O and Batsale J C 2018 *Phys. Rev. Lett.* **120** 125501
[259] Camacho M, Edwards B and Engheta N 2020 *Nat. Commun.* **11** 3733
[260] Lurie K A 1997 *Int. J. Solids Struct.* **34** 1633–43
[261] Lurie K A *et al* 2007 *An Introduction to the Mathematical Theory of Dynamic Materials* vol 15 (Springer)
[262] Holmbom A, Svanstedt N and Wellander N 2005 *Appl. Math.* **50** 131–51
[263] Flodén L and Olsson M 2007 *Appl. Math.* **52** 431–46
[264] Ariel G, Engquist B, Kim S J and Tsai R 2014 *Commun. Math. Sci.* **12** 791–824
[265] Dehamnia A and Haddadou H 2022 *Applications of Mathematics* (Springer) pp 1–17
[266] Nassar H, Xu X, Norris A and Huang G 2017 *J. Mech. Phys. Solids* **101** 10–29
[267] Melnikov A, Chiang Y K, Quan L, Oberst S, Alù A, Marburg S and Powell D 2019 *Nat. Commun.* **10** 1–7
[268] Leymarie N, Aristégui C, Audoin B and Baste S 2002 *J. Acoust. Soc. Am.* **111** 1232–44
[269] Sigmund O 1994 *Int. J. Solids Struct.* **31** 2313–29
[270] Allaire G and Kohn R V 1993 *Eur. J. Mech.* A **12** 839–78
[271] Cherkaev E 2001 *Inverse Problems* **17** 1203
[272] Bendsoe M P and Sigmund O 2013 *Topology Optimization: Theory, Methods and Applications* (Springer Science & Business Media)
[273] Cherkaev A 2012 *Variational Methods for Structural Optimization* vol 140 (Springer Science & Business Media)
[274] Allaire G 2012 *Shape Optimization by the Homogenization Method* vol 146 (Springer Science & Business Media)
[275] Chen W and Huang X 2019 *J. Mech. Phys. Solids* **131** 372–86
[276] Nash C and Sen S 1988 *Topology and Geometry for Physicists* (Elsevier)
[277] Mitchell T M and Mitchell T M 1997 *Machine Learning* (McGraw-Hill)
[278] Carleo G, Cirac I, Cranmer K, Daudet L, Schuld M, Tishby N, Vogt-Maranto L and Zdeborová L 2019 *Rev. Mod. Phys.* **91** 045002
[279] Yang Z, Yu C H and Buehler M J 2021 *Sci. Adv.* **7** eabd7416
[280] Zheng L, Kumar S and Kochmann D M 2021 *Comput. Methods Appl. Mech. Eng.* **383** 113894
[281] Li Y, Zhang J, Yi J and Zhang K 2022 *Adv. Intell. Syst.* **4** 2100187
[282] Kollmann H T, Abueidda D W, Koric S, Guleryuz E and Sobh N A 2020 *Mater. Des.* **196** 109098
[283] Mao Y, He Q and Zhao X 2020 *Sci. Adv.* **6** eaaz4169
[284] Lakes R 1987 *Science* **235** 1038–41
[285] Milton G W 1992 *J. Mech. Phys. Solids* **40** 1105–37
[286] Bückmann T, Schittny R, Thiel M, Kadic M, Milton G W and Wegener M 2014 *New J. Phys.* **16** 033032
[287] Xin X, Liu L, Liu Y and Leng J 2020 *Adv. Funct. Mater.* **30** 2004226
[288] Lei M, Hong W, Zhao Z, Hamel C, Chen M, Lu H and Qi H J 2019 *ACS Appl. Mater. Interfaces* **11** 22768–76
[289] Teng X C, Ren X, Zhang Y, Jiang W, Pan Y, Zhang X G, Zhang X Y and Xie Y M 2022 *Int. J. Mech. Sci.* **229** 107524
[290] Lvov V A, Senatov F S, Veveris A A, Skrybykina V A and Díaz Lantada A 2022 *Materials* **15** 1439
[291] Wilt J K, Yang C and Gu G X 2020 *Adv. Eng. Mater.* **22** 1901266
[292] Gao J, Xue H, Gao L and Luo Z 2019 *Comput. Methods Appl. Mech. Eng.* **352** 211–36
[293] Yang H and Ma L 2020 *Compos. Struct.* **249** 112560
[294] Wang L, Ulliac G, Wang B, Iglesias M J A, Dudek K K, Laude V and Kadic M 2022 *Adv. Sci.* **9** 2204721
[295] Kadic M, Bückmann T, Stenger N, Thiel M and Wegener M 2012 *Appl. Phys. Lett.* **100** 191901
[296] Mohammadi K, Movahhedy M R, Shishkovsky I and Hedayati R 2020 *Appl. Phys. Lett.* **117** 061901
[297] Dong H W, Zhao S D, Miao X B, Shen C, Zhang X, Zhao Z, Zhang C, Wang Y S and Cheng L 2021 *J. Mech. Phys. Solids* **152** 104407
[298] Li S and Yang J 2021 *Phys. Rev. Appl.* **15** 014058
[299] Martin A, Kadic M, Schittny R, Bückmann T and Wegener M 2012 *Phys. Rev.* B **86** 155116
[300] Schittny R, Bückmann T, Kadic M and Wegener M 2013 *Appl. Phys. Lett.* **103** 231905
[301] Bückmann T, Thiel M, Kadic M, Schittny R and Wegener M 2014 *Nat. Commun.* **5** 1–6
[302] Kadic M, Bückmann T, Schittny R, Gumbsch P and Wegener M 2014 *Phys. Rev. Appl.* **2** 054007
[303] Layman C N, Naify C J, Martin T P, Calvo D C and Orris G J 2013 *Phys. Rev. Lett.* **111** 024302
[304] Milton G, Briane M and Harutyunyan D 2017 *Math. Mech. Complex Syst.* **5** 41–94
[305] Phani A S and Hussein M I 2017 *Dynamics of Lattice Materials* (Wiley)
[306] Camar-Eddine M and Seppecher P 2003 *Arch. Ration. Mech. Anal.* **170** 211–45
[307] Guevara Vasquez F, Milton G W and Onofrei D 2011 *J. Elast.* **102** 31–54
[308] Radman A, Huang X and Xie Y 2013 *Eng. Optim.* **45** 1331–48
[309] Los J, Janssen T and Gähler F 1993 *J. Physique* I **3** 107–34
[310] Janot C 1994 Quasicrystals *Neutron and Synchrotron Radiation for Condensed Matter Studies* (Springer) pp 197–211
[311] Herz-Fischler R 2013 *A Mathematical History of the Golden Number* (Courier Corporation)
[312] Gummelt P 1996 *Geom. Dedicata* **62** 1–17
[313] Zheng X *et al* 2014 *Science* **344** 1373–7
[314] Dong Z, Schumann M F, Hokkanen M J, Chang B, Welle A, Zhou Q, Ras R H, Xu Z, Wegener M and Levkin P A 2018 *Adv. Mater.* **30** 1803890
[315] Barthlott W *et al* 2010 *Adv. Mater.* **22** 2325–8
[316] Tricinci O, Terencio T, Mazzolai B, Pugno N M, Greco F and Mattoli V 2015 *ACS Appl. Mater. Interfaces* **7** 25560–7
[317] Tang P and Sirignano W 1973 *J. Sound Vib.* **26** 247–62
[318] Lee S H, Park C M, Seo Y M, Wang Z G and Kim C K 2010 *Phys. Rev. Lett.* **104** 054301
[319] Xie Y, Popa B I, Zigoneanu L and Cummer S A 2013 *Phys. Rev. Lett.* **110** 175501
[320] Liang Z and Li J 2012 *Phys. Rev. Lett.* **108** 114301
[321] Chan C T, Li J and Fung K H 2005 *J. Zhejiang Univ. Sci.* A **7** 24–28
[322] Li J and Chan C T 2004 *Phys. Rev.* E **70** 055602
[323] Mei J, Liu Z, Wen W and Sheng P 2006 *Phys. Rev. Lett.* **96** 024301
[324] Ding Y, Liu Z, Qiu C and Shi J 2007 *Phys. Rev. Lett.* **99** 093904
[325] Cheng Y, Xu J Y and Liu X J 2008 *Phys. Rev.* B **77** 045134
[326] Liu Z, Zhang X, Mao Y, Zhu Y Y, Yang Z, Chan C T and Sheng P 2000 *Science* **289** 1734–6
[327] Liu Z, Chan C T and Sheng P 2005 *Phys. Rev.* B **71** 014103
[328] Craster R V and Guenneau S 2013 *Acoustic Metamaterials* (*Springer Series in Materials Science*) (Springer)
[329] Wu Y, Lai Y and Zhang Z Q 2011 *Phys. Rev. Lett.* **107** 105506
[330] Frenzel T, David Brehm J, Bückmann T, Schittny R, Kadic M and Wegener M 2013 *Appl. Phys. Lett.* **103** 061907
[331] Li Y, Yu G, Liang B, Zou X, Li G, Cheng S and Cheng J 2014 *Sci. Rep.* **4** 6830
[332] Yu N and Capasso F 2014 *Nat. Mater.* **13** 139–50
[333] Ball J and James R 1987 *Arch. Ration. Mech. Anal.* **100** 13
[334] Qu J, Kadic M and Wegener M 2017 *Appl. Phys. Lett.* **110** 171901

[335] Qu J, Gerber A, Mayer F, Kadic M and Wegener M 2017 *Phys. Rev.* X **7** 041060
[336] Biot M A and Willis D 1957 *J. Appl. Mech.* **15** 594–601
[337] Qu J, Kadic M, Naber A and Wegener M 2017 *Sci. Rep.* **7** 40643
[338] Lakes R 1996 *J. Mater. Sci. Lett.* **15** 475–7
[339] Gatt R and Grima J N 2008 *Phys. Status Solidi* **2** 236–8
[340] Grima J N, Ellul B, Gatt R and Attard D 2013 *Phys. Status Solidi* b **250** 2051–6
[341] Ni X, Guo X, Li J, Huang Y, Zhang Y and Rogers J A 2019 *Adv. Mater.* **31** 1905405
[342] Zhang Y, Liang Y, Liu S and Su Y 2019 *Acta Mech. Sin.* **35** 507–17
[343] Guo X *et al* 2021 *Adv. Mater.* **33** 2004919
[344] Xu W, Xiao X, Chen J, Han Z and Wei K 2022 *Thin-Walled Struct.* **174** 109147
[345] Yang H and Ma L 2020 *Mater. Des.* **188** 108430
[346] Bai Y, Liu C, Li Y, Li J, Qiao L, Zhou J and Bai Y 2022 *ACS Appl. Mater. Interfaces* **14** 35905–16
[347] Chen X, Moughames J, Ji Q, Martínez J A I, Tan H, Ulliac G, Laude V and Kadic M 2022 *J. Mech. Phys. Solids* **169** 105057
[348] Chen X, Ji Q, Martinez J A I, Tan H, Ulliac G, Laude V and Kadic M 2022 *J. Mech. Phys. Solids* **167** 104957
[349] Jiang B, Chen X, Yu J, Zhao Y, Xie Z and Tan H 2022 *Thin-Walled Struct.* **180** 109765
[350] Grima J N, Farrugia P S, Gatt R and Zammit V 2007 *Proc. R. Soc.* A **463** 1585–96
[351] Grima J N, Bajada M, Scerri S, Attard D, Dudek K and Gatt R 2015 *Proc. R. Soc.* A **471** 20150188
[352] Wang Q, Jackson J A, Ge Q, Hopkins J B, Spadaccini C M and Fang N X 2016 *Phys. Rev. Lett.* **117** 175901
[353] Dudek K K, Attard D, Caruana-Gauci R, Wojciechowski K W and Grima J N 2016 *Smart Mater. Struct.* **25** 025009
[354] Chen J, Xu W, Wei Z, Wei K and Yang X 2021 *Int. J. Mech. Sci.* **202** 106527
[355] Chen J, Wang H, Wang K, Wei Z, Xu W and Wei K 2022 *Mech. Mater.* **165** 104176
[356] Münchinger A, Hsu L Y, Fürniß F, Blasco E and Wegener M 2022 *Mater. Today* **59** 9–17
[357] Yang M, Chen S, Fu C and Sheng P 2017 *Mater. Horiz.* **4** 673–80
[358] Yang M, Ma G, Yang Z and Sheng P 2015 *EPJ Appl. Metamater.* **2** 10
[359] Jiménez N, Huang W, Romero-García V, Pagneux V and Groby J P 2016 *Appl. Phys. Lett.* **109** 121902
[360] Jiménez N, Romero-García V, Pagneux V and Groby J P 2017 *Sci. Rep.* **7** 1–12
[361] Tang Y, Ren S, Meng H, Xin F, Huang L, Chen T, Zhang C and Lu T J 2017 *Sci. Rep.* **7** 43340
[362] Ryoo H and Jeon W 2018 *Appl. Phys. Lett.* **113** 121903
[363] Huang S, Fang X, Wang X, Assouar B, Cheng Q and Li Y 2019 *J. Acoust. Soc. Am.* **145** 254–62
[364] Donda K, Zhu Y, Fan S W, Cao L, Li Y and Assouar B 2019 *Appl. Phys. Lett.* **115** 173506
[365] Meng H, Chronopoulos D, Fabro A, Elmadih W and Maskery I 2020 *J. Sound Vib.* **465** 115005
[366] Xiang X, Wu X, Li X, Wu P, He H, Mu Q, Wang S, Huang Y and Wen W 2020 *Extreme Mech. Lett.* **39** 100786
[367] Kadic M, Frenzel T and Wegener M 2018 *Nat. Phys.* **14** 8–9
[368] Ziemke P, Frenzel T, Wegener M and Gumbsch P 2019 *Extreme Mech. Lett.* **32** 100553
[369] Reinbold J, Frenzel T, Münchinger A and Wegener M 2019 *Materials* **12** 3527
[370] Coulais C, Kettenis C and van Hecke M 2018 *Nat. Phys.* **14** 40
[371] Frenzel T, Köpfler J, Jung E, Kadic M and Wegener M 2019 *Nat. Commun.* **10** 3384
[372] Portigal D and Burstein E 1968 *Phys. Rev.* **170** 673
[373] Pine A 1970 *Phys. Rev.* B **2** 2049
[374] Bhagwat K and Subramanian R 1988 *Acta Crystallogr.* A **44** 551–4
[375] Lindell I, Sihvola A, Tretyakov S and Viitanen A 1994 *Electromagnetic Waves in Chiral and Bi-Isotropic Media* (Artech House)
[376] Plum E, Liu X, Fedotov V, Chen Y, Tsai D and Zheludev N 2009 *Phys. Rev. Lett.* **102** 113902
[377] Barron L D 2009 *Molecular Light Scattering and Optical Activity* (Cambridge University Press)
[378] Nienhuis G, Woerdman J and Kuščer I 1992 *Phys. Rev.* A **46** 7079
[379] Nieves M, Carta G, Jones I, Movchan A and Movchan N 2018 *J. Mech. Phys. Solids* **121** 387–408
[380] Carta G, Colquitt D, Movchan A, Movchan N and Jones I 2020 *Phil. Trans. R. Soc.* A **378** 20190350
[381] Carta G, Jones I, Movchan N, Movchan A and Nieves M 2017 *Sci. Rep.* **7** 1–11
[382] Carta G, Jones I, Movchan N, Movchan A and Nieves M 2017 *Proc. R. Soc.* A **473** 20170136
[383] Fleury R, Sounas D L, Sieck C F, Haberman M R and Alù A 2014 *Science* **343** 516–9
[384] Zeeman P 1897 *London, Edinburgh Dublin Phil. Mag. J. Sci.* **43** 226–39
[385] Xiao R C, Shao D F, Zhang Z Q and Jiang H 2020 *Phys. Rev. Appl.* **13** 044014
[386] Shorter P J and Langley R S 2005 *J. Acoust. Soc. Am.* **117** 85–95
[387] Coulais C, Sounas D and Alù A 2017 *Nature* **542** 461–4
[388] Bigoni D, Guenneau S, Movchan A B and Brun M 2013 *Phys. Rev.* B **87** 174303
[389] Wang P, Lu L and Bertoldi K 2015 *Phys. Rev. Lett.* **115** 104302
[390] Liu X, Hu G, Huang G and Sun C 2011 *Appl. Phys. Lett.* **98** 251907
[391] Ma G, Fu C, Wang G, Del Hougne P, Christensen J, Lai Y and Sheng P 2016 *Nat. Commun.* **7** 1–8
[392] Kishine J, Ovchinnikov A and Tereshchenko A 2020 *Phys. Rev. Lett.* **125** 245302
[393] Chen Y, Kadic M and Wegener M 2021 *Nat. Commun.* **12** 1–8
[394] Landau L 1941 *Phys. Rev.* **60** 356
[395] Godfrin H, Meschke M, Lauter H J, Sultan A, Böhm H M, Krotscheck E and Panholzer M 2012 *Nature* **483** 576–9
[396] Iglesias Martínez J A, Groß M F, Chen Y, Frenzel T, Laude V, Kadic M and Wegener M 2021 *Sci. Adv.* **7** eabm2189
[397] Wang K, Chen Y, Kadic M, Wang C and Wegener M 2022 *Nat. Commun.* **3** 1–11
[398] Martínez J A I, Laforge N, Kadic M and Laude V 2022 *Phys. Rev.* B **106** 064304
[399] Qian K, Zhu L, Ahn K H and Prodan C 2020 *Phys. Rev. Lett.* **125** 225501
[400] Süsstrunk R and Huber S D 2015 *Science* **349** 47–50
[401] Meeussen A S, Paulose J and Vitelli V 2016 *Phys. Rev.* X **6** 041029
[402] Köpfler J, Frenzel T, Schmalian J and Wegener M 2021 *Adv. Mater.* **33** 2103205
[403] Chen B G g, Upadhyaya N and Vitelli V 2014 *Proc. Natl Acad. Sci. USA* **111** 13004–9
[404] Süsstrunk R and Huber S D 2016 *Proc. Natl Acad. Sci. USA* **113** E4767–75
[405] Pancharatnam S 1956 *Proc. Indian Acad. Sci.* A **44** 398–417
[406] Berry M V 1984 *Proc. R. Soc.* A **392** 45–57
[407] Zak J 1989 *Phys. Rev. Lett.* **62** 2747–50
[408] Zhang Y, Li B, Zheng Q, Genin G M and Chen C 2019 *Nat. Commun.* **10** 1–8
[409] Xin L, Siyuan Y, Harry L, Minghui L and Yanfeng C 2020 *Curr. Opin. Solid State Mater. Sci.* **24** 100853

[410] Janßen M, Viehweger O, Fastenrath U and Hajdu J 1994 *Introduction to the Theory of the Integer Quantum Hall Effect* ed J Hajdu (Wiley-VCH)
[411] Köpfler J, Frenzel T, Kadic M, Schmalian J and Wegener M 2019 *Phys. Rev. Appl.* **11** 034059
[412] Su W P, Schrieffer J R and Heeger A J 1979 *Phys. Rev. Lett.* **42** 1698–701
[413] Xiao M, Zhang Z Q and Chan C T 2014 *Phys. Rev.* X **4** 021017
[414] Laforge N, Laude V, Chollet F, Khelif A, Kadic M, Guo Y and Fleury R 2019 *New J. Phys.* **21** 083031
[415] Sirota L, Ilan R, Shokef Y and Lahini Y 2020 *Phys. Rev. Lett.* **125** 256802
[416] Al-Ketan O and Abu Al-Rub R K 2019 *Adv. Eng. Mater.* **21** 1900524
[417] Zheng S, Man X, Kong Z L, Lin Z K, Duan G, Chen N, Yu D, Jiang J H and Xia B 2022 *Sci. Bull.* **67** 2069–75
[418] Guo X F and Ma L 2020 *Int. J. Mech. Sci.* **175** 105555
[419] Lera N, Torrent D, San-Jose P, Christensen J and Alvarez J V 2019 *Phys. Rev.* B **99** 134102
[420] Huang H, Chen J and Huo S 2021 *J. Phys.: Condens. Matter* **33** 503002
[421] Fan X, Xia T, Qiu H, Zhang Q and Qiu C 2022 *Phys. Rev. Lett.* **128** 216403
[422] Miniaci M and Pal R 2021 *J. Appl. Phys.* **130** 141101
[423] Cheng W, Prodan E and Prodan C 2020 *Phys. Rev. Lett.* **125** 224301
[424] Connes A 1985 *Publ. Math. Inst. Hautes Etudes Sci.* **62** 41–144
[425] Atiyah M 2018 *K-Theory* (CRC Press)
[426] Bellissard J, van Elst A and Schulz-Baldes H 1994 *J. Math. Phys.* **35** 5373–451
[427] Prodan E 2010 *New J. Phys.* **12** 065003
[428] Prodan E 2011 *J. Phys. A: Math. Theor.* **44** 113001
[429] Liu Y, Santos L F and Prodan E 2022 *Phys. Rev.* B **105** 035115
[430] Makwana M P and Craster R V 2018 *Phys. Rev.* B **98** 235125
[431] Makwana M P and Craster R V 2018 *Phys. Rev.* B **98** 184105
[432] Makwana M P, Laforge N, Craster R V, Dupont G, Guenneau S, Laude V and Kadic M 2020 *Appl. Phys. Lett.* **116** 131603
[433] Laforge N, Wiltshaw R, Craster R V, Laude V, Martínez J A I, Dupont G, Guenneau S, Kadic M and Makwana M P 2021 *Phys. Rev. Appl.* **15** 054056
[434] Chaplain G J, De Ponti J M, Aguzzi G, Colombi A and Craster R V 2020 *Phys. Rev. Appl.* **14** 054035
[435] Zangeneh-Nejad F and Fleury R 2019 *Rev. Phys.* **4** 100031
[436] Nassar H, Chen H, Norris A, Haberman M and Huang G 2017 *Proc. R. Soc.* A **473** 20170188
[437] Cummer S A, Christensen J and Alù A 2016 *Nat. Rev. Mater.* **1** 16001
[438] Boulandet R, Lissek H, Karkar S, Collet M, Matten G, Ouisse M and Versaevel M 2018 *J. Sound Vib.* **426** 19–33
[439] Zhu X, Ramezani H, Shi C, Zhu J and Zhang X 2014 *Phys. Rev.* X **4** 031042
[440] Liu T, Zhu X, Chen F, Liang S and Zhu J 2018 *Phys. Rev. Lett.* **120** 124502
[441] Rivet E, Brandstötter A, Makris K G, Lissek H, Rotter S and Fleury R 2018 *Nat. Phys.* **14** 942–7
[442] Fleury R, Sounas D and Alu A 2015 *Nat. Commun.* **6** 1–7
[443] Dhia A S B B, Chesnel L and Pagneux V 2018 *Proc. R. Soc.* A **474** 20180050
[444] Christensen J, Willatzen M, Velasco V and Lu M H 2016 *Phys. Rev. Lett.* **116** 207601
[445] Aurégan Y and Pagneux V 2017 *Phys. Rev. Lett.* **118** 174301
[446] Tateo F, Collet M, Ouisse M, Ichchou M, Cunefare K and Abbe P 2015 *J. Intell. Mater. Syst. Struct.* **26** 952–64
[447] Ouisse M, Collet M and Scarpa F 2016 *Smart Mater. Struct.* **25** 115016
[448] Collet M, Ouisse M and Ichchou M 2012 *J. Intell. Mater. Syst. Struct.* **23** 1661–77
[449] Karkar S, De Bono E, Collet M, Matten G, Ouisse M and Rivet E 2019 *Phys. Rev. Appl.* **12** 054033
[450] Yi K, Ouisse M, Sadoulet-Reboul E and Matten G 2019 *Smart Mater. Struct.* **28** 065025
[451] Banerjee B 2011 *An Introduction to Metamaterials and Waves in Composites* (CRC Press)
[452] Chen Y, Li X, Nassar H, Norris A N, Daraio C and Huang G 2019 *Phys. Rev. Appl.* **11** 064052
[453] Chen X, Ji Q, Wei J, Tan H, Yu J, Zhang P, Laude V and Kadic M 2020 *Int. J. Mech. Sci.* **169** 105288
[454] Chen X, Laforge N, Ji Q, Tan H, Liang J, Ulliac G, Moughames J, Adrar S, Laude V and Kadic M 2020 *C. R. Physique* **21** 751–65
[455] Frenzel T, Findeisen C, Kadic M, Gumbsch P and Wegener M 2016 *Adv. Mater.* **28** 5865–70
[456] Jones R M 2006 *Buckling of Bars, Plates and Shells* (Bull Ridge Corporation)
[457] Dixon J C 2008 *The Shock Absorber Handbook* (Wiley)
[458] Lakes R and Lakes R S 2009 *Viscoelastic Materials* (Cambridge University Press)
[459] Coulais C, Overvelde J T B, Lubbers L A, Bertoldi K and van Hecke M 2015 *Phys. Rev. Lett.* **115** 044301
[460] Bertoldi K, Vitelli V, Christensen J and van Hecke M 2017 *Nat. Rev. Mater.* **2** 1–11
[461] Bertoldi K, Reis P M, Willshaw S and Mullin T 2010 *Adv. Mater.* **22** 361–6
[462] Coulais C, Teomy E, De Reus K, Shokef Y and van Hecke M 2016 *Nature* **535** 529–32
[463] Jin L, Khajehtourian R, Mueller J, Rafsanjani A, Tournat V, Bertoldi K and Kochmann D M 2020 *Proc. Natl Acad. Sci.* **117** 2319–25
[464] Bauer J, Meza L R, Schaedler T A, Schwaiger R, Zheng X and Valdevit L 2017 *Adv. Mater.* **29** 1701850
[465] Bauer J, Hengsbach S, Tesari I, Schwaiger R and Kraft O 2014 *Proc. Natl Acad. Sci. USA* **111** 2453–8
[466] Meza L R, Das S and Greer J R 2014 *Science* **345** 1322–6
[467] Schaedler T A, Jacobsen A J, Torrents A, Sorensen A E, Lian J, Greer J R, Valdevit L and Carter W B 2011 *Science* **334** 962–5
[468] Bauer J, Schroer A, Schwaiger R and Kraft O 2016 *Nat. Mater.* **15** 438–43
[469] Berger J, Wadley H and McMeeking R 2017 *Nature* **543** 533–7
[470] Christensen J, Kadic M, Kraft O and Wegener M 2015 *MRS Commun.* **5** 453–62
[471] Pendry J B, Schurig D and Smith D R 2006 *Science* **312** 1780–2
[472] Leonhardt U 2006 *Science* **312** 1777–80
[473] Miller D A B 2006 *Opt. Express* **14** 12457–66
[474] Dolin L 1961 *Izv. Vyssh. Uchebn. Zaved. Radiofiz.* **4** 964–7
[475] Schurig D, Mock J J, Justice B J, Cummer S A, Pendry J B, Starr A F and Smith D R 2006 *Science* **314** 977–80
[476] Chen H, Chan C T and Sheng P 2010 *Nat. Mater.* **9** 387–96
[477] Guenneau S, McPhedran R C, Enoch S, Movchan A B, Farhat M and Nicorovici N A P 2010 *J. Opt.* **13** 024014
[478] Qiu C W, Hu L, Zhang B, Wu B I, Johnson S G and Joannopoulos J D 2009 *Opt. Express* **17** 13467–78
[479] Novitsky A, Qiu C W and Zouhdi S 2009 *New J. Phys.* **11** 113001
[480] Greenleaf A, Lassas M and Uhlmann G 2003 *Math. Res. Lett.* **10** 685–93
[481] Kohn R, Shen H, Vogelius M and Weinstein M 2008 *Inverse Problems* **24** 015016
[482] Guenneau S, Amra C and Veynante D 2012 *Opt. Express* **20** 8207–18
[483] Schittny R, Kadic M, Guenneau S and Wegener M 2013 *Phys. Rev. Lett.* **110** 195901

[484] Guenneau S and Puvirajesinghe T 2013 *J. R. Soc. Interface* **10** 20130106
[485] Popa B I, Zigoneanu L and Cummer S A 2011 *Phys. Rev. Lett.* **106** 253901
[486] Torrent D and Sánchez-Dehesa J 2008 *New J. Phys.* **10** 063015
[487] Chen H and Chan C 2007 *Appl. Phys. Lett.* **91** 183518
[488] Cummer S A, Popa B I, Schurig D, Smith D R, Pendry J, Rahm M and Starr A 2008 *Phys. Rev. Lett.* **100** 024301
[489] Dupont G, Farhat M, Diatta A, Guenneau S and Enoch S 2011 *Wave Motion* **48** 483–96
[490] Farhat M, Enoch S, Guenneau S and Movchan A B 2008 *Phys. Rev. Lett.* **101** 134501
[491] Norris A N 2008 *Proc. R. Soc.* A **464** 2411–34
[492] Zhang S, Xia C and Fang N 2011 *Phys. Rev. Lett.* **106** 024301
[493] Xie Y, Wang W, Chen H, Konneker A, Popa B I and Cummer S A 2014 *Nat. Commun.* **5** 1–5
[494] Xu J, Jiang X, Fang N, Georget E, Abdeddaim R, Geffrin J, Farhat M, Sabouroux P, Enoch S and Guenneau S 2015 *Sci. Rep.* **5** 10678
[495] Chang T, Dupont G, Enoch S and Guenneau S 2012 *New J. Phys.* **14** 035011
[496] Torrent D and Sánchez-Dehesa J 2011 *Wave Motion* **48** 497–504
[497] Milton G W, Briane M and Willis J R 2006 *New J. Phys.* **8** 248
[498] Brun M, Guenneau S and Movchan A B 2009 *Appl. Phys. Lett.* **94** 061903
[499] Farhat M, Guenneau S and Enoch S 2009 *Phys. Rev. Lett.* **103** 024301
[500] Norris A N and Shuvalov A L 2011 *Wave Motion* **48** 525–38
[501] Stenger N, Wilhelm M and Wegener M 2012 *Phys. Rev. Lett.* **108** 014301
[502] Norris A N and Parnell W J 2012 *Proc. R. Soc.* A **468** 2881–903
[503] Diatta A and Guenneau S 2014 *Appl. Phys. Lett.* **105** 021901
[504] Colquitt D J, Brun M, Gei M, Movchan A B, Movchan N V and Jones I S 2014 *J. Mech. Phys. Solids* **72** 131–43
[505] Pomot L, Bourgeois S, Payan C, Remillieux M and Guenneau S 2018 arXiv:1901.00067
[506] Willis J R 1981 *Adv. Appl. Mech.* **21** 1–78
[507] Nicolet A, Remacle J F, Meys B, Genon A and Legros W 1994 *J. Appl. Phys.* **75** 6036–8
[508] Diatta A, Kadic M, Wegener M and Guenneau S 2016 *Phys. Rev.* B **94** 100105
[509] Berenger J P 1994 *J. Comput. Phys.* **114** 185–200
[510] Greenleaf A, Lassas M and Uhlmann G 2003 *Physiol. Meas.* **24** 413
[511] Greenleaf A, Kurylev Y, Lassas M and Uhlmann G 2008 *J. Phys.: Conf. Ser.* **124** 012005
[512] Calderón A P 2006 *Comput. Appl. Math.* **25** 133–8
[513] Kohn R and Vogelius M 1984 *Commun. Pure Appl. Math.* **37** 289–98
[514] Diatta A and Guenneau S 2013 arXiv:1306.4647
[515] Craster R, Diatta A, Guenneau S and Hutridurga H 2021 *Multiscale Model. Simul.* **19** 633–64
[516] Thomson W 1856 *Phil. Trans. R. Soc.* **146** 481–98
[517] Torrent D, Håkansson A, Cervera F and Sánchez-Dehesa J 2006 *Phys. Rev. Lett.* **96** 204302
[518] Yavari A and Golgoon A 2019 *Arch. Ration. Mech. Anal.* **234** 211–316
[519] McCall M W, Favaro A, Kinsler P and Boardman A 2010 *J. Opt.* **13** 024003
[520] Caloz C and Deck-Léger Z L 2019 *IEEE Trans. Antennas Propag.* **68** 1569–82
[521] Caloz C and Deck-Leger Z L 2019 *IEEE Trans. Antennas Propag.* **68** 1583–98
[522] Huidobro P A, Silveirinha M G, Galiffi E and Pendry J 2021 *Phys. Rev. Appl.* **16** 014044
[523] Engheta N 2021 *Nanophotonics* **10** 639–42
[524] Fridman M, Farsi A, Okawachi Y and Gaeta A L 2012 *Nature* **481** 62–65
[525] García-Meca C, Carloni S, Barceló C, Jannes G, Sánchez-Dehesa J and Martínez A 2013 *Sci. Rep.* **3** 1–5
[526] Kinsler P and McCall M W 2014 *Phys. Rev.* A **89** 063818
[527] Bückmann T, Kadic M, Schittny R and Wegener M 2015 *Proc. Natl Acad. Sci. USA* **112** 4930–4
[528] Bi Y, Jia H, Lu W, Ji P and Yang J 2017 *Sci. Rep.* **7** 1–10
[529] Sanchis L, García-Chocano V M, Llopis-Pontiveros R, Climente A, Martínez-Pastor J, Cervera F and Sánchez-Dehesa J 2013 *Phys. Rev. Lett.* **110** 124301
[530] Andkjær J and Sigmund O 2011 *Appl. Phys. Lett.* **98** 021112
[531] Vial B and Hao Y 2015 *Opt. Express* **23** 23551–60
[532] Yang Z and Huang X 2022 *J. Acoust. Soc. Am.* **152** 3510–21
[533] Hua Y, Qian C, Chen H and Wang H 2022 *Mater. Today Phys.* **27** 100754
[534] Nakamoto K, Isakari H, Takahashi T and Matsumoto T 2017 *Mech. Eng. J.* **4** 16-00268
[535] Landy N and Smith D R 2013 *Nat. Mater.* **12** 25–28
[536] Jiang Z, Liang Q, Li Z, Chen T, Li D and Hao Y 2020 *Adv. Opt. Mater.* **8** 2000827
[537] Zhu J, Chen T, Liang Q, Wang X, Xiong J and Jiang P 2015 *J. Phys. D: Appl. Phys.* **48** 305502
[538] Ahmed W W, Farhat M, Zhang X and Wu Y 2021 *Phys. Rev. Res.* **3** 013142
[539] Donda K, Zhu Y, Merkel A, Fan S W, Cao L, Wan S and Assouar B 2021 *Smart Mater. Struct.* **30** 085003
[540] Lai P, Amirkulova F and Gerstoft P 2021 *J. Acoust. Soc. Am.* **150** 4362–74
[541] Ji Q, Chen X, Liang J, Fang G, Laude V, Arepolage T, Euphrasie S, Martinez J A I, Guenneau S and Kadic M 2022 *Int. J. Heat Mass Transfer* **196** 123149
[542] Neil T R, Shen Z, Robert D, Drinkwater B W and Holderied M W 2020 *Proc. Natl Acad. Sci.* **117** 31134–41
[543] Bosia F *et al* 2022 *Matter* **5** 3311–40
[544] Berraquero C, Maurel A, Petitjeans P and Pagneux V 2013 *Phys. Rev.* E **88** 051002
[545] Newman J 2014 *Eur. J. Mech.* B **47** 145–50
[546] Porter R and Newman J 2014 *J. Fluid Mech.* **750** 124–43
[547] Dupont G, Kimmoun O, Molin B, Guenneau S and Enoch S 2015 *Phys. Rev.* E **91** 023010
[548] Zareei A and Alam M R 2015 *J. Fluid Mech.* **778** 273–87
[549] Dupont G, Guenneau S, Kimmoun O, Molin B and Enoch S 2016 *J. Fluid Mech.* **796** R1
[550] Zhang Z, He G, Kashiwagi M and Wang Z 2018 *Appl. Ocean Res.* **71** 1–10
[551] Wang Z, Li C, Zatianina R, Zhang P and Zhang Y 2017 *Phys. Rev.* E **96** 053107
[552] Maurel A, Marigo J J, Cobelli P, Petitjeans P and Pagneux V 2017 *Phys. Rev.* B **96** 134310
[553] Iida T and Kashiwagi M 2018 *J. Fluid Mech.* **849** 90–110
[554] Zou S *et al* 2019 *Phys. Rev. Lett.* **123** 074501
[555] Zhang Z, He G, Wang Z, Liu S, Gou Y and Liu Y 2019 *Ocean Eng.* **183** 305–17
[556] Zhang Z, Liu S, Luan Z, Wang Z and He G 2020 *Phys. Fluids* **32** 081701
[557] Maurel A, Pham K and Marigo J J 2019 *J. Fluid Mech.* **871** 350–76
[558] Iida T, Zareei A and Alam M R 2023 *J. Fluid Mech.* **954** A4
[559] Dupont G, Remy F, Kimmoun O, Molin B, Guenneau S and Enoch S 2017 *Phys. Rev.* B **96** 180302
[560] Bennetts L G, Peter M A and Craster R V 2018 *J. Fluid Mech.* **854** R4
[561] Archer A J, Wolgamot H A, Orszaghova J, Bennetts L G, Peter M A and Craster R V 2020 *Phys. Rev. Fluids* **5** 062801
[562] Guevara Vasquez F, Milton G W, Onofrei D and Seppecher P 2013 Transformation elastodynamics and active exterior

acoustic cloaking *Acoustic Metamaterials* (Springer) pp 289–318
[563] Zhang H, Chen Y, Liu X and Hu G 2020 *J. Mech. Phys. Solids* **135** 103796
[564] Sklan S R, Pak R Y and Li B 2018 *New J. Phys.* **20** 063013
[565] Colombi A, Roux P, Guenneau S and Rupin M 2015 *J. Acoust. Soc. Am.* **137** 1783–9
[566] Brûlé S, Javelaud E, Enoch S and Guenneau S 2014 *Phys. Rev. Lett.* **112** 133901
[567] Colquitt D, Colombi A, Craster R, Roux P and Guenneau S 2017 *J. Mech. Phys. Solids* **99** 379–93
[568] Marigo J J, Pham K, Maurel A and Guenneau S 2020 *J. Mech. Phys. Solids* **143** 104029
[569] Pu X, Palermo A and Marzani A 2022 *Proc. R. Soc.* A **478** 20210669
[570] Williams E G, Roux P, Rupin M and Kuperman W 2015 *Phys. Rev.* B **91** 104307
[571] Maurel A, Marigo J J, Pham K and Guenneau S 2018 *Phys. Rev.* B **98** 134311
[572] Colombi A, Colquitt D, Roux P, Guenneau S and Craster R V 2016 *Sci. Rep.* **6** 1–6
[573] Palermo A, Krödel S, Marzani A and Daraio C 2016 *Sci. Rep.* **6** 1–10
[574] Colombi A, Roux P, Guenneau S, Gueguen P and Craster R V 2016 *Sci. Rep.* **6** 1–7
[575] Nicorovici N, McPhedran R C and Milton G W 1994 *Phys. Rev.* B **49** 8479
[576] Milton G W and Nicorovici N A P 2006 *Proc. R. Soc.* A **462** 3027–59
[577] Bruno O P and Lintner S 2007 *J. Appl. Phys.* **102** 124502
[578] Bouchitté G and Schweizer B 2010 *Q. J. Mech. Appl. Math.* **63** 437–63
[579] Ammari H, Ciraolo G, Kang H, Lee H and Milton G W 2013 *Arch. Ration. Mech. Anal.* **208** 667–92
[580] Kohn R V, Lu J, Schweizer B and Weinstein M I 2014 *Commun. Math. Phys.* **328** 1–27
[581] Nguyen H M 2017 *SIAM J. Math. Anal.* **49** 3208–32
[582] Nicorovici N P, McPhedran R, Enoch S and Tayeb G 2008 *New J. Phys.* **10** 115020
[583] Milton G W, Nicorovici N A P, McPhedran R C, Cherednichenko K and Jacob Z 2008 *New J. Phys.* **10** 115021
[584] Liu Y, Gralak B, McPhedran R C and Guenneau S 2014 *Opt. Express* **22** 17387–402
[585] Guenneau S, Lombard B and Bellis C 2021 *Appl. Phys. Lett.* **118** 191102
[586] Gralak B and Tip A 2010 *J. Math. Phys.* **51** 052902
[587] Bellis C and Lombard B 2019 *Wave Motion* **86** 175–94
[588] Ramakrishna S A 2005 *Rep. Prog. Phys.* **68** 449
[589] Lai Y, Chen H, Zhang Z Q and Chan C T 2009 *Phys. Rev. Lett.* **102** 093901
[590] Wolf E and Habashy T 1993 *J. Mod. Opt.* **40** 785–92
[591] Ffowcs Williams J 1984 *Proc. R. Soc.* A **395** 39563–88
[592] Guevara Vasquez F, Milton G W and Onofrei D 2011 *Wave Motion* **48** 515–24
[593] Guevara Vasquez F, Milton G W and Onofrei D 2009 *Phys. Rev. Lett.* **103** 073901
[594] Cassier M, DeGiovanni T, Guenneau S and Guevara Vasquez F 2022 *Phil. Trans. R. Soc.* A **380** 20220073
[595] Norris A N, Amirkulova F A and Parnell W J 2014 *Math. Mech. Solids* **19** 603–25
[596] Kadic M, Bückmann T, Schittny R and Wegener M 2013 *Rep. Prog. Phys.* **76** 126501
[597] Chen H T, Taylor A J and Yu N 2016 *Rep. Prog. Phys.* **79** 076401
[598] Zangeneh-Nejad F, Sounas D L, Alù A and Fleury R 2021 *Nat. Rev. Mater.* **6** 207–25
[599] Brûlé S, Enoch S and Guenneau S 2020 *Phys. Lett.* **384** 126034
[600] Li Y, Li W, Han T, Zheng X, Li J, Li B, Fan S and Qiu C W 2021 *Nat. Rev. Mater.* **6** 488–507
[601] Galiffi E, Tirole R, Yin S, Li H, Vezzoli S, Huidobro P A, Silveirinha M G, Sapienza R, Alù A and Pendry J 2022 *Adv. Photonics* **4** 014002